

CWPAN: Coupled Wavelength Postbuckling Analysis



Thesis submitted in fulfilment of the requirement for the degree of
Doctor of Philosophy

By

Kai Zhao

October 2021

School of Engineering
Cardiff University

I dedicate this thesis to my parents

Abstract

Laminated composite plates are used extensively in the aerospace industry because of their light weight, high strength and stiffness. Additionally, the use of panel structures leads to a reserve of postbuckling strength which allows more load to be carried than the initial critical buckling load. This enables the weight of the aircraft to be further reduced by fully utilising this stable postbuckling phase.

Postbuckling is a highly nonlinear process incurring high computational costs for conventional numerical methods particularly when the plate is manufactured from composite material or subject to shear loading. For many years, researchers and engineers have been searching for a fast yet reliable analysis technique to extend the design envelope as far as possible into the postbuckling region. However, most of the commercial design software is characterized by either low computational efficiency or lack of accuracy. This work is motivated by the need for an alternative to such software.

The coupled wavelength postbuckling analysis (CW PAN) presented in this thesis is based on the use of a series of sinusoidal solutions representing in-plane displacements, strains and stresses for a composite plate under any combination of in-plane loading based on the exact strip method. By incorporating classical plate theory and large deflection theory, the governing equilibrium equations are assembled and solved analytically at each postbuckling equilibrium state. The in-plane distributions of displacements, strains and stresses are therefore obtained as a means of observing postbuckling behaviour.

A convergence procedure consisting of a modified Newton iteration scheme and its supporting strategies is also developed to capture progressive postbuckling behaviour. With such a procedure, successive equilibrium states can be connected and enabling a full postbuckling analysis considering postbuckling stiffness. Postbuckling behaviours such as stress redistribution can therefore be observed.

CW PAN is illustrated using appropriate practical examples and numerical results including symmetric balanced, unsymmetric, unbalanced composite plates under in-plane compression, shear and combined loading under three different in-plane boundary conditions, and is validated against the most widely used numerical technique, finite element analysis (FEA).

Acknowledgements

First and foremost, I would like to express my sincere gratitude to my supervisors Prof. David Kennedy and Prof. Carol Featherston, for their continuous guidance, invaluable advice and continued support throughout my PhD study. The completion of this research could not have been possible without their excellent supervision and consistent encouragement.

I wish to thank Dr. Che Bin and Dr. Chi Zhang who developed the VIPASA postbuckling analysis providing a detailed account which inspires the research in this thesis. I am also thankful to my colleagues and friends for their kind support and accompany over the years.

Last but not least, I would like to thank my family, especially my parents, Suting Zhao and Qingrun Li, for their unconditional support and great confidence in me. It was their great love and sacrifice that made the completion of this thesis possible.

Contents

Abstract.....	i
Acknowledgements	ii
Contents	iii
List of figures.....	vi
List of tables.....	xi
Chapter 1. Introduction.....	1
1.1 Background	1
1.2 Thesis scope	3
1.3 Thesis aims and objectives	4
1.4 Thesis overview	4
1.5 Publications arising from this thesis.....	6
Chapter 2. Background Theory and Literature Review.....	7
2.1. Review of thin plate buckling theory.....	7
2.2. Buckling of plates.....	9
2.3. Review of composite material	12
2.4. Review of postbuckling theory.....	15
Chapter 3. Exact Finite Strip Method and VICONOPT	25
3.1. Exact strip method	25
3.2. Wittrick-Williams algorithm	27
3.3. VIPASA.....	28
3.4. VICON	31
3.5. Exact strip software VICONOPT.....	35
3.6. VIPASA Postbuckling.....	36
3.7. Newton iteration scheme	42
3.8. Improved exact strip postbuckling analysis	43

Chapter 4. CWPAN: In-plane Solutions	46
4.1. Description and assumptions of the analysis	46
4.2. Displacement assumptions	49
4.3. Calculation of strains and derivatives of strains	52
4.4. Calculation of stresses and derivatives of stresses	60
4.5. Equilibrium equations	65
4.6. Boundary and loading conditions	67
4.7. Conclusions	72
Chapter 5. CWPAN: Newton Iteration and Convergence Procedure.....	73
5.1. Overview	73
5.2. Convergence procedure overview.....	75
5.3. Convergence procedure	76
5.4. Pre-defined variables	79
5.5. Newton Iteration scheme	80
5.6. Approximate buckling mode amplitude.....	83
5.7. Stress resultants calculation	86
5.8. Conclusions	88
Chapter 6. Parameter Selection	90
6.1. Number of half-wavelengths	90
6.2. Number of nodes/strips.....	98
6.3. The ratio of linear strain increment α and the number of cycles	100
6.4. The tolerance for Newton iteration scheme β.....	100
6.5. Conclusions	101
Chapter 7. Illustrative Results and Validation	103
7.1. Overview	103
7.2. Isotropic plate under combined loading	105
7.3. Composites loaded in compression.....	121
7.4. Composite loaded under combined load	127

7.5. Composite loaded in pure shear	134
7.6. Unbalanced and unsymmetric composites.....	140
7.7. Computational Efficiency Evaluation	149
7.8. Conclusion	152
Chapter 8. Conclusions and future work	153
8.1. General conclusions	153
8.2. Future work	155
References.....	158
Appendices.....	164
Appendix A	164
Appendix B	174

List of figures

Figure 2.1. Deformation of a typical transverse normal line in various plate theories (Wang, 2007)	9
Figure 2.2. Laminated composite.....	13
Figure 2.3. Load-displacement graph for postbuckling problem (Zhao, 2019).....	15
Figure 2.4. Load-deflection curves for single-mode bifurcation behaviour (Hutchinson and Koiter, 1970).....	16
Figure 2.5. Von Kármán’s effective width concept: (a) non-uniform distribution of axial stress in the postbuckling stage and (b) assumed uniform stress distribution over an effective width b_{ee}	17
Figure 3.1(a) Examples of prismatic plate assemblies. (b) a component strip, showing the applied uniform stress resultants N_l , N_t and N_s (Wittrick and Williams, 1971).....	28
Figure 3.2 A strip of a component plate, showing the perturbation edge forces and displacements, and nodal lines (Wittrick and Williams, 1971)	30
Figure 3.3 An infinitely long plate. Nodal lines in (a) are straight and perpendicular to the longitudinal direction, which is consistent with simply supported end conditions. Nodal lines in (b) are skewed due to anisotropy or shear loads, approximating the simply supported end condition.	30
Figure 3. 4 Load and strain paths of VICON and VIPASA for shear or anisotropy	32
Figure 3.5 Graphic explanation of an infinitely long plate assembly with the end supports repeating at longitudinal intervals of the panel length l (a) plan view (b) isometric view (Anderson et al., 1983).....	33
Figure 3.6 Buckling analysis, out-of-plane displacement contours from (a)VIPASA analysis and (b) VICON analysis(Williams and Anderson, 1983).....	35
Figure 3.7 Typical flat plate of width b , subdivided into n_s strips of width b_s (Powell et al. 1998).	37
Figure 3.8 Cross-section of part of a thin rectangular plate having an initial imperfection w_0 with maximum value γ_0 : (a) unloaded; (b) loaded(Powell et al. 1998).....	38
Figure 3.9 Variation of stress resultants across a plate(Powell et al. 1998).	40
Figure 3.10 Typical applications for postbuckling analysis: (a) cross-section of a perfect isotropic infinitely wide panel with simply supported ends, showing the local buckling mode, and dimensions of a typical repeating portion (ABCA_); (b) curved simply supported panel, showing repeating portion and local buckling mode; and (c) longitudinally stiffened cylindrical shell(Powell et al. 1998).	41

Figure 3.11 Implementation scheme of the improved VIPASA postbuckling analysis (Zhang 2018).	45
Figure 4.1. Diagram showing the full process for one iteration of postbuckling analysis	48
Figure 4.2. An example square plate with width a divided into $n-1$ strips of equal width b , showing the datum and axes used in this thesis	50
Figure 4.3. Initial postbuckling of a rectangular plate with longitudinal free edges under combined uniform compressive and shear stresses. The black rectangles indicate rigid bodies that control the displacements applied to the plate in the postbuckling analysis.....	68
Figure 4.4. Initial postbuckling of a rectangular plate with longitudinal fixed edges under combined uniform compressive and shear stresses	69
Figure 4.5. Initial postbuckling of a rectangular plate with longitudinal straight edges under combined uniform compressive and shear stresses	70
Figure 5.1. Postbuckling mode shape analysed by CWPAN at cycles 1,10 and 20, showing contour plots of growing out-of-plane displacements. (a) Isotropic plate under compression, no skewing at any point of postbuckling cycles. (b) Composite plate under compression with small amount of shear, growing skewed mode.	74
Figure 5.2. Flow of diagram for the method of analysis: red boxes indicate in-plane solutions, yellow boxes indicate Newton Iteration scheme	78
Figure 5.3. Three wavelength stiffness matrix transverse boundary conditions example	81
Figure 5.4. Implementation of Newton iteration in CWPAN	82
Figure 5.5. Flow diagram for the method of analysis	85
Figure 5.6. Stress distribution of a postbuckling analysis from a rectangular flat plate where solid line indicates normal stress distribution and dashed line is the equivalent uniform stress distribution.	86
Figure 6.1. Out-of-plane deflections calculated using different numbers of half-wavelengths for a composite plate under combined loading, divided into 10 strips	95
Figure 6.2. Execution time for different numbers of half-wavelengths from a composite plate under combined loading, divided into 10 strips.....	95
Figure 6.3. Out-of-plane deflections calculated by different half-wavelengths from a composite plate under shear loading, divided into 10 strips.....	96
Figure 6.4. Execution time of different half-wavelengths from a composite plate under shear loading, divided by 10 strips.....	97
Figure 6.5. Max out-of-plane deflections calculated based on 3 half-wavelengths for a composite plate under combined loading, divided into different numbers of strips.....	98

Figure 6.6. Execution time of 3 half-wavelengths for a composite plate under combined loading, divided into different numbers of strips.....	99
Figure 7.1.The CWPAN model: in-plane boundary conditions and loading conditions.....	104
Figure 7.2. Load and boundary conditions for isotropic plate under combined load.....	106
Figure 7.3. Contour plots of (a) out-of-plane displacements $w(m)$; (b) in-plane displacements $u(m)$; (c) in-plane displacements $v(m)$; (d) strain ϵ_x ; (e) strain ϵ_y ; (f) strain γ_{xy} ; (g) stress resultant N_x ; (h) stress resultant $N_y(N/m)$; (i) stress resultant $N_{xy}(N/m)$, under compression and shear with free in-plane edge conditions, at cycle 10 (200% of initial end shortening strain).....	111
Figure 7.4 Postbuckling behaviour of load strain curve.....	113
Figure 7.5 Equivalent uniform longitudinal stress at strip vs normalized end shortening strains.....	113
Figure 7.6. Equivalent uniform shear stress at strip vs normalized end shortening strains...	113
Figure 7.7. Equivalent uniform stress distribution at each postbuckling cycle.....	114
Figure 7.8 Equivalent uniform shear stress distribution at each postbuckling cycle.....	115
Figure 7.9. Contour plots of out-of-plane displacements at cycles 1 to 20, showing the progressive buckling mode.....	116
Figure 7.10. v displacement contour plots (m) from (a) free edges, (b) fixed edges and (c) straight edges.....	117
Figure 7.11. Uniform longitudinal stress distribution at each postbuckling cycle for in-plane longitudinal straight edges.....	118
Figure 7.12. Equivalent uniform longitudinal stress distribution at each postbuckling cycle for in-plane longitudinal fixed edges.....	119
Figure 7.13. Equivalent uniform transverse stress distribution N_y at each postbuckling cycle for in-plane longitudinal fixed edges.....	120
Figure 7.14. Postbuckling load paths for all boundary conditions for metal plate.....	121
Figure 7.15 Laminate orientation example.....	122
Figure 7.16. Contour plots of displacements (m) at cycle 8 of the composite plate under compression: (a) out-of-plane w , CWPAN (b) out-of-plane w , ABAQUS (c) in-plane u , CWPAN (d) in-plane u , ABAQUS (e) in-plane v , CWPAN (f) in-plane v , ABAQUS.....	124
Figure 7.17. Contour plots of stress resultants N_x at cycle 8 of composite plate under compression (N/m): (a) series solution (b) improved exact strip method (Zhang, 2018) (c) ABAQUS solution.....	125

Figure 7.18. Contour plots of stress resultants N_y at cycle 8 of the composite plate under compression (N/m): (a) series solution (b) improved exact strip method (Zhang 2018) (c) ABAQUS solution	126
Figure 7.19. Normalized applied compressive load(P/P_{cr}) vs non-dimensional maximum deflection w/h	126
Figure 7.20. Load and boundary conditions	128
Figure 7.21. Combined loading case contour plots of: (a) out-of-plane displacement w (m) (b) in-plane displacement u (m) (c) in-plane displacement v (m) (d) strain ϵ_x (e) strain ϵ_y (f) strain γ_{xy} (g) stress resultant N_x (N/m) (h) stress resultant N_y (N/m) (i) stress resultant N_{xy} (N/m)	130
Figure 7.22 Postbuckling load paths and tabulation of shear and compression for a composite plate under combined loading and in-plane fixed boundary conditions	131
Figure 7. 23 Equivalent uniform longitudinal stress distribution at each postbuckling cycle for a composite plate under combined loading and in-plane longitudinal fixed edges	132
Figure 7.24. Arc length procedure for specific iteration (Memon, 2004).....	133
Figure 7.25. The inputs and outputs of a postbuckling analysis using: (a) the ABAQUS Riks method; (b) CWPAN	134
Figure 7.26 Contour plots of out-of-plane displacements w at initial buckling for pure shear case (m): (a) CWPAN. (b) ABAQUS	135
Figure 7.27. Contour plots of out-of-plane displacements u for pure shear case at cycle 5 (m): (a) CWPAN. (b) ABAQUS.....	135
Figure 7.28. Contour plots of out-of-plane displacements v for pure shear case at cycle 5 (m): (a) CWPAN. (b) ABAQUS.....	136
Figure 7.29. Contour plots of strain ϵ_x for pure shear case at cycle 5: (a) CWPAN. (b) ABAQUS	136
Figure 7.30. Contour plots of strain ϵ_y for pure shear case at cycle 5: (a) CWPAN. (b) ABAQUS	137
Figure 7.31. Contour plots of strain γ_{xy} for pure shear case at cycle 5: (a) CWPAN. (b) ABAQUS	137
Figure 7.32. Initial buckling solution from VICON for pure shear case	139
Figure 7.33. Shear stress redistribution from pure shear model	140
Figure 7.34. Symmetric unbalanced laminated composite under in-plane compression and fixed boundary condition at cycle 1 (110% of buckling end shortening strain), contour plots of: (a) out-of-plane deflection w (m); (b) in-plane longitudinal deflection u (m); (c) in-plane transverse	

deflection v (m); (d) strain ϵ_x ; (e) strain ϵ_y ; (f) strain γ_{xy} ; (g) stress resultant N_x (N/m); (h) stress resultant N_y (N/m); (i) stress resultant N_{xy} (N/m)..... 143

Figure 7.35. Equivalent shear uniform stress distribution at each postbuckling cycle..... 144

Figure 7.36. Postbuckling load paths for unbalanced symmetric composite under compression, free edges 144

Figure 7.37. Unsymmetric unbalanced laminated composite model under in-plane compression and fixed boundary conditions at cycle 1 (110% of buckling end shortening strain), contour plots of: (a) out-of-plane deflection w (m); (b) in-plane longitudinal deflection u (m); (c) in-plane transverse deflection v (m); (d) strain ϵ_x ; (e) strain ϵ_y ; (f) strain γ_{xy} ; (g) stress resultant N_x (N/m); (h) stress resultant N_y (N/m); (i) stress resultant N_y (N/m). 147

Figure 7.38. Unsymmetric unbalanced laminated composite model under in-plane compression and fixed boundary condition at cycle 1 (110% of buckling end shortening strain), contour plots of: (a) curvature κ_x ; (b) curvature κ_y ; (c) curvature κ_{xy} ; (d) bending moment M_x (Nm); (e) bending moment M_y (Nm); (f) bending moment M_{xy} (Nm). 148

Figure B.1. Input data for balanced and symmetric composite plate under combined loading, straight edges. 174

Figure B. 2. Contour plots of (a) out-of-plane displacements w (m); (b) in-plane displacements u (m); (c) in-plane displacements v (m); (d) strain ϵ_x ; (e) strain ϵ_y ; (f) strain γ_{xy} ; (g) stress resultant N_x (N/m); (h) stress resultant N_y (N/m); (i) stress resultant N_y (N/m), for composite plate under compression and shear with free in-plane edge conditions, at cycle 10 (200% of initial end shortening strain) 176

Figure B.3. Contour plots of in-plane displacements v at cycles 1 to 20, showing the progressive buckling mode..... 177

Figure B.4. Uniform stress resultant distribution at each postbuckling cycle for composite plate under combined loading, in-plane longitudinal straight edges 178

Figure B.5. Input data for unbalanced and symmetric composite plate under compression, free edges. 179

Figure B.6. Contour plots of (a) out-of-plane displacements w (m); (b) in-plane displacements u (m); (c) in-plane displacements v (m); (d) strain ϵ_x ; (e) strain ϵ_y ; (f) strain γ_{xy} ; (g) stress resultant N_x (N/m); (h) stress resultant N_y (N/m); (i) stress resultant N_y (N/m), for unbalanced symmetric composite under compression with free in-plane edge conditions, at cycle 10 (200% of initial end shortening strain) 181

Figure B.7. Contour plots of (a) Moment M_x (Nm); (b) Moment M_y (Nm); (c) Moment M_{xy} (Nm); (d) curvature κ_x ; (e) curvature κ_y ; (f) curvature κ_{xy} for unbalanced symmetric composite under compression with free in-plane edge conditions, at cycle 10 (200% of initial end shortening strain)..... 182

Figure B.8. Equivalent uniform longitudinal stress resultant distribution at each postbuckling cycle 182

List of tables

Table 4.1. Summations of half-wavelengths l/m and l/n , $m, n = (1,3,5)$	58
Table 4.2. Subtractions of half-wavelengths l/m and l/n , $m, n = (1,3,5)$	58
Table 6.1. Summations of half-wavelengths l/m and l/n , $m, n = (1,3,5)$	91
Table 6.2. Subtractions of half-wavelengths l/m and l/n , $m, n = (1,3,5)$	91
Table 6.3. Out-of-plane half-wavelengths l/m , $m = (1,3,5)$	91
Table 6.4. Summations of half-wavelengths l/m and l/n , $m, n = (0,2,4)$	92
Table 6.5. Subtractions of half-wavelengths l/m and l/n , $m, n = (0,2,4)$	92
Table 6.6. Out-of-plane half-wavelengths l/m , $m = (0,2,4)$	92
Table 6.7. Summations of half-wavelengths l/m and l/n , $m, n = (\xi, \xi \pm 2, \xi \pm 4)$	93
Table 6.8. Subtractions of half-wavelengths l/m and l/n , $m, n = (\xi, \xi \pm 2, \xi \pm 4)$	93
Table 6.9. Out-of-plane half-wavelengths l/m $m = (\xi, \xi \pm 2, \xi \pm 4)$	93
Table 6.10. Relationships between in-plane and out-of-plane half-wavelengths	94
Table 7.1. End shortening strains at postbuckling cycles, 0 indicates critical buckling point	106
Table 7.2. Amplitudes of nodal in-plane displacement u from CWPAN for an isotropic plate under compression and shear with in-plane free edges at cycle 10	107
Table 7.3. Amplitudes of nodal in-plane displacement v from CWPAN for an isotropic plate under compression and shear with in-plane free edges at cycle 10	108
Table 7.4. Amplitudes of nodal out-plane displacement w (left) and rotation φ (right) by Newton iteration scheme for an isotropic plate under compression and shear with in-plane free edges at cycle 10.....	109
Table 7.5. Laminate stiffness of balanced and symmetric laminates	122
Table 7.6. Normalized deflections from CWPAN and ABAQUS.....	126
Table 7.7 Approximate computational efficiency of CWPAN, showing iteration counts and solution times.	150

Nomenclature

$\mathbf{A}_{ij}, \mathbf{B}_{ij}, \mathbf{D}_{ij}$	membrane, bending-membrane and flexural stiffness elements
a	length of plate
b	width of strip
\mathbf{D}	displacement vector
\mathbf{d}^*	displacement adjustment vector
E	Young's modulus
\mathbf{f}	matrix of first order finite difference approximation
f	eigen-parameter
f^*	trial value of f
h	thickness of plate
\mathbf{H}	right hand side vector of equilibrium equations
\mathbf{I}	identity matrix
J	number of eigenvalues below f^*
J_0	number of fixed end eigenvalues below f^*
J_m	number of fixed end eigenvalues of member m below f^*
\mathbf{K}_m	member stiffness matrix
$\mathbf{K}(f)$	global stiffness matrix
k	longitudinal in-plane half-wavelengths

K	unique value of in-plane half-wavelengths
l	length of plate
\mathbf{L}	matrix of left hand side of equilibrium equations
L	repeating interval length of plate
M_x, M_y, M_{xy}	bending moments
m	unique value of out-of-plane half-wavelengths
n	number of nodes
N_x, N_y, N_{xy}	stress resultants
\mathbf{P}	applied load vector
\mathbf{s}	matrix of second order finite difference approximation
$s\{\mathbf{K}(f)\}$	sign count of $\mathbf{K}(f)$
u, v	in-plane displacements
V_x, V_y, V_{xy}	work done by applied loads
w, ψ	out-of-plane displacements and rotations
x, y, z	longitudinal, transverse and lateral directions
α	constant strain increment ratio
β	tolerance of modified Newton iteration scheme
γ	constant shear strain increment ratio
$\bar{\gamma}$	constant shear strain

$\bar{\epsilon}$	constant normal strain
$\epsilon_x, \epsilon_y, \gamma_{xy}$	middle surface strain
$\kappa_x, \kappa_y, \kappa_{xy}$	curvatures
λ	longitudinal out-of-plane half-wavelength
ξ	longitudinal repetition parameter
$\mathbf{0}$	null matrix

Subscripts

c	cosine terms
k	sequence of in-plane half-wavelengths
i	node reference number
j, m, n	half-wavelength reference number
s	sine terms
x, y, xy	longitudinal, transverse, shear

Superscripts

-1	inverse matrix
'	derivative with respect to transverse direction

Chapter 1. Introduction

1.1 Background

Mass minimisation is a crucial objective in aircraft design to reduce the cost of manufacturing, environmental impact and fuel consumption (Che et al., 2010). Industrial strategic research objectives demand a reduction in aviation fuel consumption and CO₂ emission by 1.39% per annum to 2045 and 21% reduction in full flight nitrogen oxide in the long term (Fleming and Lepinay, 2019). This objective can be realized in many ways.

Firstly, materials such as composites which exhibit better performance than traditional metals in terms of strength and stiffness to weight ratio can be used to reduce the amount of material needed and thus the weight of an aircraft. They may also have additional benefits such as a high resistance to fatigue and corrosion. Composites are increasingly adopted in industries including aerospace, shipbuilding and the automotive sector. However, such materials often incur significantly high manufacturing costs.

From a structural perspective, the use of panels is well known to increase the critical buckling strength whilst reducing weight. More than this however they have the potential to provide a postbuckling reserve of strength, allowing compressive and shear loads exceeding the initial buckling load to be carried (Anderson and Kennedy, 2008). If this reserve can be employed safely, the weight of composite structures can be further reduced and the structure becomes even more efficient.

Postbuckling analysis however is characterized by non-linearity and is therefore computationally expensive. On the other hand it is almost impossible to conduct the analytical and numerical analysis of non-linear composite plates using algebraic expressions manually, especially for increasingly complex structures. An efficient computer aided engineering (CAE) software for non-linear problems therefore becomes exceedingly valuable. Researchers and

designers have been searching for such reliable computational theories and techniques to increase design efficiency for many decades.

CAE software including finite element analysis (FEA) is widely used in industry. However, when it comes to highly non-linear problems, FEA often results in high computational costs with discretisation problems due to the large stiffness matrices used. In this context, alternative approaches such as the finite strip and exact strip methods which reduce degrees of freedom and levels of discretisation have proved particularly valuable.

VICONOPT is a software for designing prismatic structural components developed at Cardiff University in 1990. By utilizing the exact strip method and Wittrick-Williams algorithm, VICONOPT can solve critical buckling and free vibration problems analytically with considerably high speed. However, for postbuckling analysis, an incomplete capture of in-plane behaviour leads to conservative results for composite materials or shear. Previous authors including Che (2010) and Zhang (2018), have begun to address this by developing an exact solution to capture in-plane distributions. This new approach however is still relatively inaccurate for composite material and shear loaded plate problems.

In this thesis, a new numerical method, coupled wavelength postbuckling analysis (CW PAN) based on the exact strip method is presented to overcome these limitations and allow accurate postbuckling analysis for a wider range of load and boundary conditions, and for anisotropic materials. The method uses classical plate theory and von Kármán large deflection theory to account for the additional strains generated from lateral deflection. By assuming displacements can be represented using a series of trigonometric terms, equilibrium equations can be solved analytically and in-plane displacements, stresses and strains can be identified. To find the postbuckling equilibrium path, a modified Newton-type iteration scheme and corresponding convergence method is developed. The method is validated against results obtained using the finite element method to further understand its advantages and limitations.

1.2 Thesis scope

This thesis addresses the limitations of the previous postbuckling analysis (Che 2010; Zhang 2018) based on improved exact strip analysis and VICONOPT.

The ‘Improved exact strip analysis’ developed by (Zhang, 2018) provides an efficient approach to postbuckling analysis for isotropic plate assemblies in the preliminary design of aircraft structures. It improves previous exact strip postbuckling analysis by capturing in-plane displacements. However it has drawbacks when it comes to isotropic material or shear loading cases resulting skewed mode shape, as it gives unrealistic results or fails to solve the equilibrium equations. This is because it represents the postbuckling mode with one single half-wavelength which despite being efficient is often inaccurate. In this thesis, a series based postbuckling analysis is presented which successfully overcome previous limitations utilising a number of half wavelengths and therefore more accurately representing the postbuckling for composite materials and shear loaded plates.

VICONOPT uses a Newton type iteration scheme to capture the changing mode from previous postbuckling analysis. It can successfully obtain the mode shape for regular and symmetric mode shapes but has not thus far considered any circumstances under which the mode shape is skewed due to composite material or shear loading. The previous improved analysis does not implement the Newton iteration from VICONOPT and can only therefore analyse a postbuckling scenario at one particular equilibrium point. Therefore for a plate that has a skewed mode shape, none of the above methods could achieve a full postbuckling analysis. In this thesis, a series based Newton iteration scheme and corresponding convergence scheme are developed to allow a full postbuckling analysis.

1.3 Thesis aims and objectives

The aim of this thesis is to develop an accurate and efficient methodology for predicting the postbuckling behaviour of composites under combined loading.

The objectives are as follows:

1. To review the composite postbuckling theories of other researchers and understand their limitations when analysing composite plates or for shear loading.
2. To develop a postbuckling analysis which addresses these limitations while retaining the advantages of the fast and reliable VICONOPT.
3. To develop a convergence procedure allowing the equilibrium path to be found.
4. To investigate the sensitivity of the developed method 'CW PAN' based on a series of parametric studies.
5. To validate CW PAN against the finite element method by modelling using the commercial software ABAQUS.

1.4 Thesis overview

The thesis is presented in the following Chapters.

Chapter 2: Background theory and literature review

This chapter provides a review of the postbuckling analysis of plates. Formulations for buckling and postbuckling based on classical plate theory are presented to establish a basic understanding of the methods utilized in this thesis. A review of composite material and its mechanisms is included. Finally, a review of recent advances in the postbuckling analysis of composite plates is presented.

Chapter 3: Exact strip method and VICONOPT

This chapter presents the exact strip method and its implementation through the VIPASA and VICON analysis options of VICONOPT. Formulations are given for each method highlighting the differences between the basic theories of the two. The previous ‘Improved exact strip analysis’ postbuckling method developed based on VIPASA analysis is presented and its limitations highlighted.

Chapter 4: CWPAN: in-plane solutions

This chapter develops a coupled wavelength postbuckling analysis (CWPAN) for composite plates using VICON analysis to address the limitations of the previous method. Inspired by Stein’s assumptions and employing VICON analysis, a series of trigonometric functions are developed based on von Kármán large deflection theory and finite difference approximations. By solving the governing in-plane equilibrium equations analytically, accurate in-plane variables can be obtained.

Chapter 5: CWPAN: Newton iteration and convergence procedure

This chapter introduces a modified Newton iteration scheme and its supporting convergence procedure into CWPAN. The postbuckling analysis requires the buckling mode to be provided as an input to each cycle. Whilst accurate representation of this mode requires plate deformation to be represented as varying sinusoidally with a series of half-wavelengths the previously implemented Newton iteration schemes only calculate the buckling mode for a single half-wavelength. A new Newton iteration is therefore developed.

Chapter 6: Parameter selection

Four parameters influence the proposed analysis significantly and suitable values for them are required to be selected. This chapter studies the sensitivity of the results to each of these parameters.

Chapter 7: Illustrative results and validation

As the most widely used finite element software, results from analyses carried out using the ABAQUS Riks method for nonlinear analysis are used to validate the method. For cases where this is not possible, differences in the two modelling approaches are discussed.

Chapter 8: Conclusions and future work

The final chapter concludes the thesis and summarises contributions made to the research area. It also provides suggestions for future work.

1.5 Publications arising from this thesis

Zhao, K., Kennedy, D. and Featherston, C.A., 2019. Exact strip postbuckling analysis of composite plates under compression and shear. *Aeronautical Journal*, 123(1263), pp.658-677.

Zhao, K., Kennedy, D. and Featherston, C.A., 2021. Postbuckling analysis of Composite plate under shear loading. Submitted to *Composite Structures*.

Zhao, K., Kennedy, D. and Featherston, C., 2019. Postbuckling analysis of composite panel under shear load. *Proceedings of 6th Aircraft Structural Design Conference*, Bristol, U.K.

Chapter 2. Background Theory and Literature Review

Problems relating to the stability of plate and shell structures have drawn a great deal of attention from industry and academia since the 1880s. Driven by increasing shell structure applications, large numbers of studies and experiments from isotropic metal plates to laminated composite panels, have been conducted and published. On one hand, researchers are searching for suitable theories and techniques to efficiently and accurately capture buckling and postbuckling behaviour. On the other, using these techniques, materials such as composites can be optimised to meet certain requirements. In this chapter, a comprehensive summary of previous research on the stability of laminated composite plates including basic structural buckling and postbuckling theory is given. The chapter is organised as follows: Section 2.1 reviews some of the most widely used thin plate theories. Section 2.2 provides basic formulations for the buckling analysis of plates. Section 2.3 summarises the development of composite materials and their basic mechanisms. Section 2.4 discusses some of the important literature on the postbuckling of composite plates.

2.1. Review of thin plate buckling theory

Thin walled plates, defined as 3-dimensional structures having a thickness which is small compared to their other two dimensions (Timoshenko, 1959), are very common engineering structural components. Such structures when subject to in-plane loading can be analysed using two-dimensional stress theory. Since the 19th century, numerous plate theories have been developed, of which two are the most widely used:

- 1) The Kirchhoff-Love theory, also called Classical Plate Theory (CPT) (Love, 1888).
- 2) The Reissner-Mindlin theory, also called First-order Shear Deformation Theory (FSDT) (Uflyand 1948).

If deflections in the plate's lateral direction are small compared to its thickness, classical plate theory is usually applied. This makes the following assumptions:

1. The midplane is considered to be the neutral plane.

In-plane deformations of the mid-plane of the plate due to bending are zero. Subsequently, in-plane stresses/strains due to bending are zero as well. The bending of a plate only causes the plane above and below this mid-plane to deform in-plane, see Figure 2.1.

2. Line elements normal to the mid-plane remain normal to it after deformation

Line elements are the straight lines normal to the mid-plane which remain straight after bending. Such a hypothesis can be applied when the transverse shear force is small in comparison with compression. A larger transverse shear force will cause the element lines to skew (first-order shear deformation theory) or even become curved (higher-order shear deformation theory, and example being third-order shear deformation theory (TSDT)). In this case, other plate theories need to be applied.

3. Strains and stresses in the thickness direction remain zero

The lengths of line elements remain the same after deformation.

When the ratio of plate thickness to width is comparably large, first-order shear plate theory is normally applied. As with the Kirchhoff-Love theory, first-order shear deformation theory assumes the plate's thickness remains unchanged after deformation and its midplane is taken as the neutral plane. However, the element lines may not remain normal to the neutral plane due to transverse shear forces (Uflyand, 1948, Mindlin, 1951), see Figure 2.1.

Higher-order shear deformation theory is a further extension of classical plate theory where element lines are no longer straight after deformation due to the nonlinear distribution of in-plane displacements in the lateral direction (D'Ottavio and Polit, 2017), see Figure 2.1. Higher-order theory was first studied by Vlasov (1957a, 1957b). Later, in 1977 Lo, Christensen and Wu developed the required formulations by considering the variation of displacements and stresses in the thickness direction. Such theory is naturally suitable for analysing laminated composite where plies are stacked in the thickness direction (Hanna and Leissa, 1994). The development of higher-order plate theory for composite plates has continued ever since.

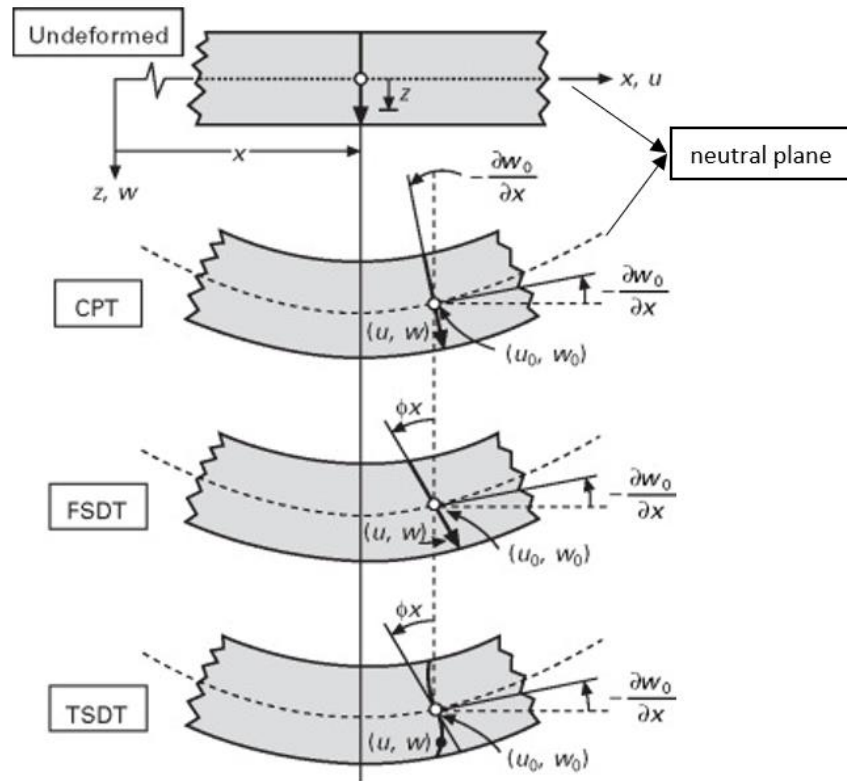


Figure 2.1. Deformation of a typical transverse normal line in various plate theories (Wang, 2007)

2.2. Buckling of plates

Combining Kirchhoff-Love and Euler buckling theory (1759), Bryan (1890) investigated the buckling of a simply supported rectangular plate under axial compression using an energy approach. Timoshenko (1936) extended this plate stability analysis to include more boundary conditions and presented the theory with kinematic behaviour.

Applying classical plate theory, in-plane deflections can be represented in terms of lateral deflection w as follows

$$u = u_0 - z \frac{\partial w}{\partial x}, \quad v = v_0 - z \frac{\partial w}{\partial y} \quad \dots(2.1)$$

where w , u and v represent displacements within the plate and u_0 and v_0 are in-plane displacements of the neutral plane. Based on these in-plane displacements, direct strains ε_x , ε_y and shear strain γ_{xy} can be obtained by plane elasticity theory

$$\varepsilon_x = \frac{\partial u}{\partial x}, \quad \varepsilon_y = \frac{\partial v}{\partial y}, \quad \gamma_{xy} = \frac{\partial u}{\partial y} + \frac{\partial v}{\partial x} \quad \dots(2.2)$$

Substituting Equations 2.1 into Equations 2.2,

$$\varepsilon_x = \varepsilon_x^0 - z\kappa_x, \quad \varepsilon_y = \varepsilon_y^0 - z\kappa_y, \quad \gamma_{xy} = \gamma_{xy}^0 - z\kappa_{xy} \quad \dots(2.3)$$

where ε_x^0 , ε_y^0 and γ_{xy}^0 are the strains in the neutral plane and κ_x , κ_y and κ_{xy} are the changing curvature with respect to x , y and shear directions

$$\varepsilon_x^0 = \frac{\partial u_0}{\partial x}, \quad \varepsilon_y^0 = \frac{\partial v_0}{\partial y}, \quad \gamma_{xy}^0 = \frac{\partial u_0}{\partial y} + \frac{\partial v_0}{\partial x} \quad \dots(2.4)$$

$$\kappa_x = \frac{\partial^2 w}{\partial x^2}, \quad \kappa_y = \frac{\partial^2 w}{\partial y^2}, \quad \kappa_{xy} = 2 \frac{\partial^2 w}{\partial x \partial y} \quad \dots(2.5)$$

According to classical plate theory, the stress and moment resultants can be obtained by integrating strains through the thickness, as follows

$$N_x = \int_{-h/2}^{h/2} \sigma_x dz, \quad N_y = \int_{-h/2}^{h/2} \sigma_y dz, \quad N_{xy} = \int_{-h/2}^{h/2} \gamma_{xy} dz \quad \dots(2.6)$$

$$M_x = \int_{-h/2}^{h/2} \kappa_x z dz, \quad M_y = \int_{-h/2}^{h/2} \kappa_y z dz, \quad M_{xy} = \int_{-h/2}^{h/2} \kappa_{xy} z dz \quad \dots(2.7)$$

Simplifying Equations 2.6 and 2.7, the relationship between strains and stresses in the neutral plane can be written in matrix form as

$$\begin{bmatrix} N_x \\ N_y \\ N_{xy} \\ M_x \\ M_y \\ M_{xy} \end{bmatrix} = \begin{bmatrix} A_{11} & A_{12} & A_{16} & B_{11} & B_{12} & B_{16} \\ A_{12} & A_{22} & A_{26} & B_{12} & B_{22} & B_{26} \\ A_{16} & A_{26} & A_{66} & B_{16} & B_{26} & B_{66} \\ B_{11} & B_{12} & B_{16} & D_{11} & D_{12} & D_{16} \\ B_{12} & B_{22} & B_{26} & D_{12} & D_{22} & D_{26} \\ B_{16} & B_{26} & B_{66} & D_{16} & D_{26} & D_{66} \end{bmatrix} \begin{bmatrix} \varepsilon_x \\ \varepsilon_y \\ \varepsilon_{xy} \\ \kappa_x \\ \kappa_y \\ \kappa_{xy} \end{bmatrix} \quad \dots(2.8)$$

where the matrix containing A_{ij} , B_{ij} and D_{ij} is known as the stiffness matrix which is related only to the properties of the structure. There are many characteristics of this matrix. For

example, it is perfectly symmetric. For particular materials, certain terms in the above matrix may be equal to zero which can significantly reduce the complexity of the analysis.

Having the stresses in the neutral plane, the equilibrium equations can be assembled as follows

$$\frac{\partial N_y}{\partial y} + \frac{\partial N_{xy}}{\partial x} = 0 \quad \dots(2.9)$$

$$\frac{\partial N_{xy}}{\partial y} + \frac{\partial N_x}{\partial x} = 0 \quad \dots(2.10)$$

$$\frac{\partial^2 M_x}{\partial x^2} + 2 \frac{\partial^2 M_{xy}}{\partial x \partial y} + \frac{\partial^2 M_y}{\partial y^2} + N_x \frac{\partial^2 w}{\partial x^2} + 2N_{xy} \frac{\partial^2 w}{\partial x \partial y} + N_y \frac{\partial^2 w}{\partial y^2} = 0 \quad \dots(2.11)$$

Substituting Equations 2.6-2.7 into Equation 2.11, the governing equation can be obtained

$$D \left(\frac{\partial^4 w}{\partial x^4} + 2 \frac{\partial^4 w}{\partial x^2 \partial y^2} + \frac{\partial^4 w}{\partial y^4} \right) + N_x \frac{\partial^2 w}{\partial x^2} + 2N_{xy} \frac{\partial^2 w}{\partial x \partial y} + N_y \frac{\partial^2 w}{\partial y^2} = 0 \quad \dots(2.12)$$

where D is the flexural rigidity of the plate

$$D = \frac{Eh^2}{12(1-\nu^2)} \quad \dots(2.13)$$

where E is the Young's modulus, ν is the Poisson's ratio and h the thickness of the plate. Equations 2.11 and 2.12 describe a case in which stress resultants N_x , N_y and N_{xy} are constant throughout the plate and no body forces are applied within. For a plate that is simply supported and uniformly axially loaded, the function of out-of-plane displacement can be assumed to be a series of trigonometrical functions

$$w = \sum_{m=1}^{\infty} \sum_{n=1}^{\infty} A_{mn} \sin \frac{m\pi x}{a} \sin \frac{n\pi y}{b} \quad \dots(2.14)$$

where m and n are the integer numbers of half-waves of a buckling response in the x and y -directions respectively. Out-of-plane assumptions are made regarding the boundary conditions and loading conditions. Substituting Equation 2.14 into Equation 2.12 the equation can be

solved analytically, noting that $N_{xy} = N_y = 0$ if the plate is loaded only in compression. The critical stress resultant N_x can therefore be achieved

$$N_x = \frac{kD\pi^2}{b^2} \quad \dots(2.15)$$

where k is the critical buckling load factor

$$k = \left(\frac{mb}{a} + \frac{n^2 a}{mb}\right)^2 \quad \dots(2.16)$$

. From Equation 2.16 it can be seen that the buckling load depends on a/b , m and n .

2.3. Review of composite material

A composite material is two or more different materials which are brought together to achieve properties such as high strength and stiffness to weight ratios but remain separate and distinct (Gibson, 2016). The advantages of composites have enabled them to make a significant contribution to engineering development, especially in the aerospace industry. The use of composite material before the 19th century was mainly in structural constructions and masonry such as bricks and Japanese swords to achieve desirable properties (Nagavally, 2017), while modern laminated composites cover a much wider range of engineering applications, e.g. aerospace structures, biomedical products, sports equipment, automotive components and many others.

The first use of glass fibre reinforced composite was at the time of the Second World War in 1942 on a boat. Reinforced plastic was invented in the same year and utilised in the electrical components of aircraft. Later in the 1960s, boron and high strength carbon fibres, considered as the basis of today's advanced composites were developed, and have been used in aircraft components since 1970 (Herakovich, 2012).

The mechanics of laminated composites have been developed alongside their introduction. Lekhnitskii in 1947 derived the earliest form of constitutive equations for composites,

demonstrating the number of independent constant required to describe different materials e.g. a monoclinic material has 13 independent constants, an orthotropic one has 9, and an isotropic material has two independent constants, etc.

The general form of these constitutive equations is

$$\begin{bmatrix} \sigma_{xx} \\ \sigma_{yy} \\ \sigma_{zz} \\ \tau_{yz} \\ \tau_{zx} \\ \tau_{xy} \end{bmatrix} = \begin{bmatrix} C_{11} & C_{12} & C_{13} & C_{14} & C_{15} & C_{16} \\ C_{21} & C_{22} & C_{23} & C_{24} & C_{25} & C_{26} \\ C_{31} & C_{32} & C_{33} & C_{34} & C_{35} & C_{36} \\ C_{41} & C_{42} & C_{43} & C_{44} & C_{45} & C_{46} \\ C_{51} & C_{52} & C_{53} & C_{54} & C_{55} & C_{56} \\ C_{61} & C_{62} & C_{63} & C_{64} & C_{65} & C_{66} \end{bmatrix} \begin{bmatrix} \varepsilon_{xx} \\ \varepsilon_{yy} \\ \varepsilon_{zz} \\ \gamma_{yz} \\ \gamma_{zx} \\ \gamma_{xy} \end{bmatrix} \quad \dots(2.17)$$

where ε_{ij} , γ_{ij} , σ_{ij} and τ_{ij} are normal and shear strains and stresses, respectively. C_{ij} are the 21 unique components of a symmetric stiffness matrix.

The mechanics of laminated composites became mature when classic lamination theory (CLT) was developed. Based on the work of Pister and Dong(1959), Reissner and Stavsky(1961) and Dong et.al. (1962), CLT describes the properties of an assembly of laminae, which are unidirectional fibrous composites with fibres in the k th layer oriented at an angle θ_k , see Figure 2.2.

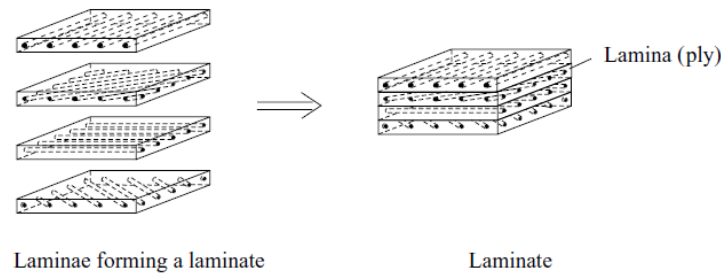


Figure 2.2. Laminated composite

Considering laminated composites are comparably thin such that classical plate theory is valid, the strains that relate to the lateral direction i.e. ε_{zz} , γ_{yz} and γ_{zx} are zero, and taking bending effects into account the stiffness matrix can be written as

$$\begin{bmatrix} N_x \\ N_y \\ N_{xy} \\ M_x \\ M_y \\ M_{xy} \end{bmatrix} = \begin{bmatrix} A_{11} & A_{12} & A_{16} & B_{11} & B_{12} & B_{16} \\ A_{21} & A_{22} & A_{26} & B_{12} & B_{22} & B_{26} \\ A_{16} & A_{26} & A_{66} & B_{16} & B_{26} & B_{66} \\ B_{11} & B_{12} & B_{16} & D_{11} & D_{12} & D_{16} \\ B_{12} & B_{22} & B_{26} & D_{12} & D_{22} & D_{26} \\ B_{16} & B_{26} & B_{66} & D_{16} & D_{26} & D_{66} \end{bmatrix} \begin{bmatrix} \varepsilon_x \\ \varepsilon_y \\ \gamma_{xy} \\ \kappa_x \\ \kappa_y \\ \kappa_{xy} \end{bmatrix} \quad \dots(2.18)$$

Here N_i and M_i are stress and moment resultants within the plate and ε_i , γ_i and κ_i are the corresponding strains and curvatures. A_{ij} , B_{ij} , D_{ij} are components of the stiffness matrix related to stiffness, thickness and lateral location of each ply.

In Equation 2.18, A_{ij} are in-plane stiffnesses relating to in-plane strains ε_x , ε_y , γ_{xy} to stresses N_x , N_y , N_{xy} ; D_{ij} are out-of-plane stiffnesses relating moments M_x , M_y , M_{xy} to curvatures κ_x , κ_y , κ_{xy} ; B_{ij} couple in-plane and out-of-plane stiffness relating in-plane stresses N_x , N_y , N_{xy} to curvatures κ_x , κ_y , κ_{xy} and moments M_x , M_y , M_{xy} to in-plane strains ε_x , ε_y , γ_{xy} .

Within the stiffness matrix, A_{16} , A_{26} describe shear extension coupling, i.e. if A_{16} , A_{26} are zeros, normal strains ε_x and ε_y do not cause shear stresses N_{xy} , and shear strains γ_{xy} do not cause extension stresses N_x , N_y . D_{16} , D_{26} represent bend twist coupling. If these terms are zeros, the twist of a composite κ_{xy} does not cause bending moments M_x , M_y , and vice versa. The stiffness elements B_{ij} describe in-plane and out-of-plane coupling, i.e., in-plane strains causing bending moments M_x , M_y , M_{xy} and out-of-plane curvatures κ causing in-plane stresses N_x , N_y , N_{xy} .

From the material point of view, laminated composites are normally categorized according to the arrangement of their plies which has consequences in terms of their behaviours e.g. symmetrical, balanced and orthotropic laminates. In a symmetric laminate, plies arranged in symmetric positions with respect to the mid-plane are identical. Such laminates have no in-plane-out-of-plane coupling and stiffness matrix \mathbf{B} is a null matrix. If a laminate is balanced every unidirectional ply has a ply with the opposite direction to balance it. It is characterized by having no extension-shear coupling and stiffness elements A_{16} and A_{26} are zero. For an orthotropic laminate, plies run in two mutually perpendicular directions meaning that forces and bending moments applied in those directions don't cause any shear or twist. In other words, there are no bend twist, extension shear or extension twist couplings. A laminated composite is often characterised by combinations of these characteristics for example being balanced and symmetric and therefore having neither out-of-plane-in-plane coupling nor extension-shear coupling. It is worth noting that for unsymmetric unbalanced layups, all of the stiffness elements can be non-zeros.

2.4. Review of postbuckling theory

It is well known that after a plate reaches its critical buckling load, increasing the applied load does not instantly cause failure (Bloom and Coffin, 2009). Instead, the plate starts to undergo a lateral deflection which is relatively large compared to its thickness. Most plate structures have such postbuckling reserve of strength, allowing them to carry compressive and shear loads exceeding the initial buckling load. If this reserve can be fully exploited, the weight of a structure can be reduced by different amounts depending on their properties. This would be exceptionally beneficial for the aerospace industry where saving a small amount of mass could result in reducing manufacturing cost, environmental impact and fuel consumption (Mrazova, 2013).

Figure 2.3 shows the behaviour of plate structures during buckling and postbuckling. With increasing in-plane load P , a perfect plate follows path A which shows no out-of-plane displacement until the critical buckling load is reached. After the bifurcation point B, the curve follows path C for a linear idealization. For large deflection analysis, the curve follows the non-linear path D with an increasing slope. Path E indicates the buckling and postbuckling behaviour of an imperfect plate.

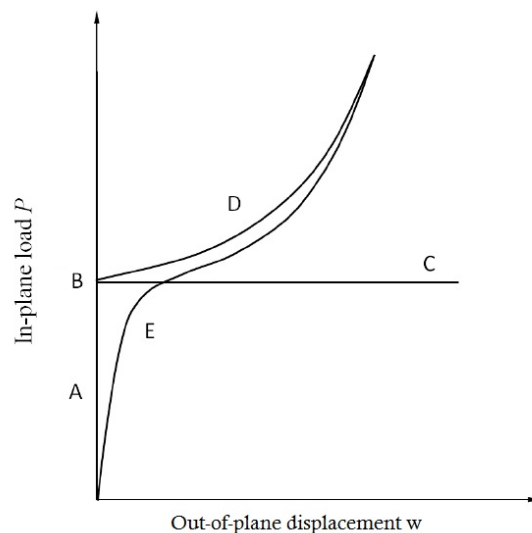


Figure 2.3. Load-displacement graph for postbuckling problem (Zhao, 2019).

As reported by Hutchinson and Koiter (1970) different types of postbuckling phenomena can occur. Figure 2.4 shows typical load-deflection curves for structures with a unique buckling

mode corresponding to their classical buckling load. In all three cases the perfect structure remains stable prior to buckling, i.e. $P < P_{cr}$, becoming unstable in postbuckling (indicated by the solid curve). The first case illustrates a structure with a stable postbuckling path which can support loads in excess of the critical load. The dashed curve indicates the behaviour of the same structure with a slight imperfection. The second case depicts a structure which can follow into either a stable or an unstable postbuckling path resulting in the load either increasing or decreasing after the critical buckling load. This is an example of asymmetric postbuckling where the route taken after buckling depends on factors such as initial imperfections. The path for an imperfect structure is again shown by the dashed line. The third case is an example for a structure which has possible postbuckling paths which are symmetric with respect to buckling deflection. In this case postbuckling behaviour is always unstable.

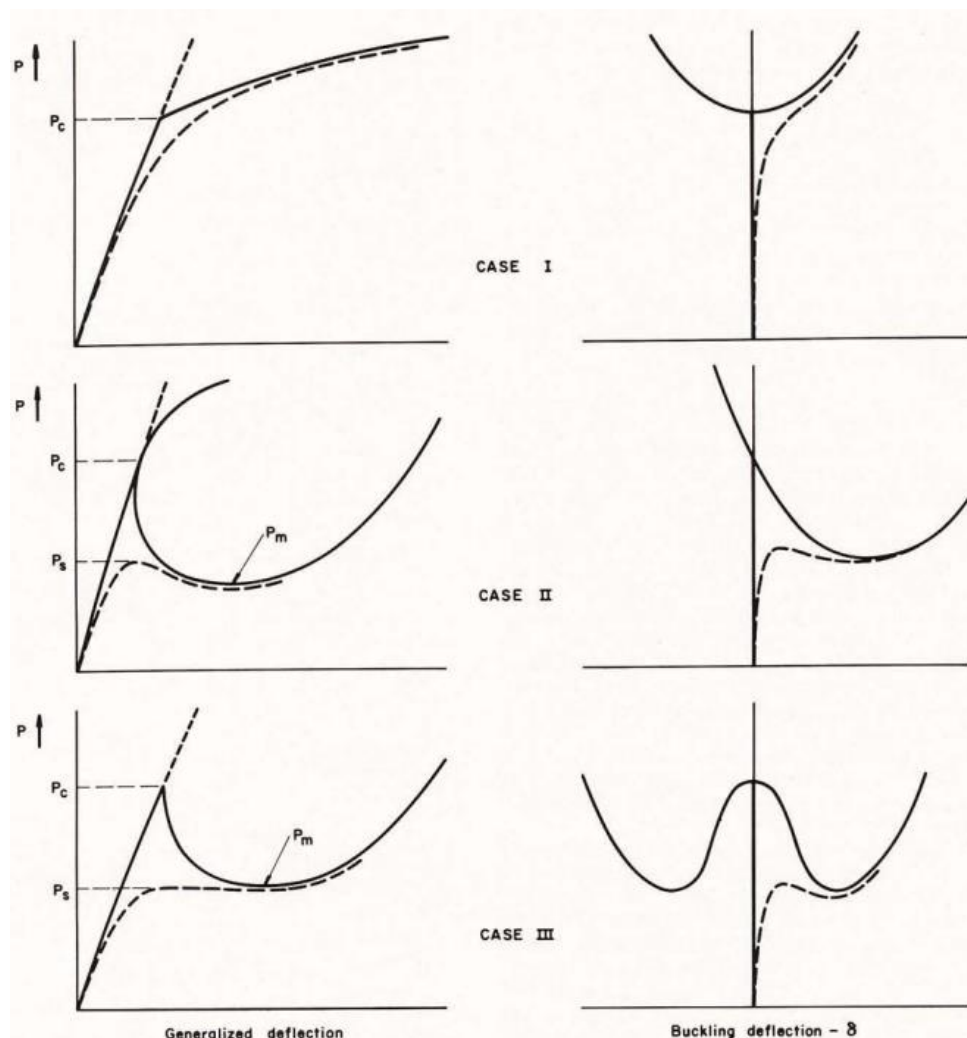


Figure 2.4. Load-deflection curves for single-mode bifurcation behaviour (Hutchinson and Koiter, 1970)

Research into the postbuckling phenomenon has been carried out for more than a century. As lateral deflection during postbuckling cannot be neglected, i.e. it is relatively large compared to the structure's thickness, the key difference between prebuckling and postbuckling, based on the work of von Kármán et al. (1932) who established large deflection theory, lies in the compatibility equations.

$$\begin{bmatrix} \varepsilon_x \\ \varepsilon_y \\ \varepsilon_{xy} \end{bmatrix} = \begin{bmatrix} \frac{\partial u}{\partial x} + \frac{1}{2} \left(\frac{\partial w}{\partial x} \right)^2 \\ \frac{\partial v}{\partial y} + \frac{1}{2} \left(\frac{\partial w}{\partial y} \right)^2 \\ \frac{\partial u}{\partial y} + \frac{\partial v}{\partial x} + \frac{\partial w}{\partial x} \frac{\partial w}{\partial y} \end{bmatrix} \quad \dots(2.19)$$

Compared to Equation 2.2, the extra terms in Equation 2.19 are due to the elongation related to out-of-plane deflection w . Substituting Equations 2.19 into the equilibrium equations, the postbuckling equations can be solved analytically. By establishing the interaction between membrane and flexural effects computational cost can be reduced significantly.

Another important postbuckling phenomenon discovered by von Kármán is the stress redistribution that occurs in a plate loaded with a uniformly distributed load (von Kármán et al. 1932; Winter 1947). The out-of-plane deflection in the postbuckling regime reduces the axial stiffness, redistributing the compression towards the edges of the plate. Under von Kármán's effective width theory these compressive forces at the edges of the plate are assumed to be uniformly distributed and concentrated within a width b_e , while the forces in the middle are assumed to be zero or near zero, see Figure 2.5.

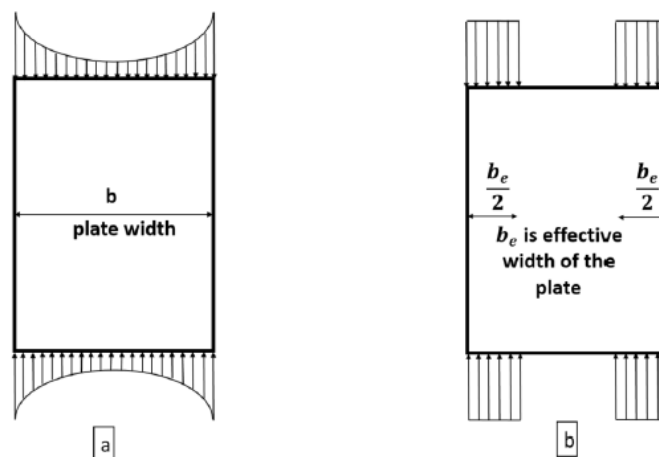


Figure 2.5. Von Kármán's effective width concept: (a) non-uniform distribution of axial stress in the postbuckling stage and (b) assumed uniform stress distribution over an effective width b_e

Based on von Kármán's large deflection theory, Cox et al. (1933) used energy considerations to determine postbuckling behaviour. In their research, the total potential energy is expressed in terms of in-plane and out-of-plane displacements which are then evaluated by minimizing total energy.

Later Koiter (1943), proving that large deflections which cause stiffness reductions cannot be ignored, developed classical nonlinear bifurcation theory, accelerating the development of nonlinear buckling analysis.

Prior to numerical analysis becoming mature, analytical methods were widely used. Levy (1942) continued von Kármán's large deflection theory utilizing double Fourier trigonometric functions which could be broken down and solved individually. Following on from Levy's research, Coan (1951) took imperfections into consideration, analysing the postbuckling of a plate under axial compression. Yamaki (1960) extended this work to cover rectangular and circular plates under different boundary and loading conditions.

Johns (1970) studied the shear buckling of isotropic and orthotropic plates. Both infinitely long and short plates under uniform shear and compression were investigated based on classic plate theory. Although analytical equations were assembled, equations were only found for possible buckling stress by thresholding shear and compression.

Marshall et al (1977) studied the postbuckling behaviour of thin orthotropic panels under compression. Based on von Kármán large deflection theory, they derived the non-linear equilibrium equations along the postbuckling path by representing deflections and forces with general Fourier series. To solve such complex equations, the Ritz technique was used to minimize the total energy in the midplane although the extent of the nonlinearity between the applied load and the lateral deflection resulted in a large number of deflection function coefficients and a high computational cost. Their method was successful in following the snap-through of the load-deflection curve which was validated experimentally.

During World War II, advanced fibres drew great attention in the aerospace industry, leading to the development of the theoretical and applied mechanics of composite materials and structures. Pister (1959) and Reissner (1961) developed a system to determine the elements of the compliance matrix for laminated composites known as Classical Lamination theory.

The buckling and vibration of cross-ply laminated composites were investigated by Jones (1973). An exact solution and numerical results were presented for simply supported composite plates. Harris (1975) derived the in-plane postbuckling stiffness of a rectangular composite plate immediately after critical buckling. He accounted for the coupling effects between bending and extension when a biaxial load is applied in the longitudinal direction and found the reduction of stiffness due to the change in postbuckling mode shape.

Stein (1983, 1985) formulated large-deflection equations based on von Kármán theory for orthotropic composite plates under compression based on earlier work on the buckling and postbuckling of isotropic materials employing von Kármán strains in an infinite set (Stein, 1959a, 1959b). Following this idea, lateral deflections were assumed to be in the form of trigonometric functions in the loading direction.

$$\begin{aligned}
 u &= -\bar{u}_{cn} \left(\frac{x}{a} - \frac{1}{2} \right) + u_0(y) + u_s(y) \sin \frac{2\pi x}{\lambda} + u_c(y) \cos \frac{2\pi x}{\lambda} \\
 v &= v_0(y) + v_s(y) \sin \frac{2\pi x}{\lambda} + v_c(y) \cos \frac{2\pi x}{\lambda} \quad \dots(2.20) \\
 w &= w_s(y) \sin \frac{\pi x}{\lambda} + w_c(y) \cos \frac{\pi x}{\lambda}
 \end{aligned}$$

where $-\bar{u}_{cn}$ is the applied longitudinal end shortening displacement, lateral deflection w is sinusoidally periodic with half-wavelength λ , and in-plane deflections u and v are sinusoidally periodic with half-wavelength $\lambda/2$. This work enabled the equilibrium equations to be converted into ordinary nonlinear differential equations which were solved numerically using a two-point boundary problem solution by Lentini and Pereyra (1977). The results were validated against experimental results and the work of other researchers' and shown to be efficient and accurate for certain problems. The displacement assumptions however were found to adequately represent the buckling mode only for isotropic and orthotropic plates. In addition to this, the twenty unknowns led to a large number of differential equations resulting in difficulties in implementing different boundary conditions. Despite these limitations, this work has provided a basis for further research into postbuckling by Che (2010) and Zhang (2018) who performed postbuckling analyses based on Stein's method for composite plates (more detail on this can be found in Chapter 3). In this thesis, Stein's work also plays an important role in the displacement assumptions.

Research into postbuckling analysis of composite material after 1990 is mostly based around the search for suitable plate theories to incorporate into either the finite element or finite strip methods. Librescu and Stein (1991) developed a higher-order geometrically non-linear theory for postbuckling analysis. By modifying the first-order shear deformation theory, their method analysed transversely isotropic symmetrically laminated composite plates focussing particularly on transverse shear deformation, transverse normal stress and higher-order effects. However, the equations derived from this work were limited to simply supported shear-deformable plates and did not consider the effect of in-plane boundary conditions.

Sundaresan et al. (1996) employed first-order shear deformation theory and von Kármán displacement assumptions to investigate the postbuckling of a moderately thick laminated composite plate. The resulting formulations were incorporated into eight-noded isoparametric plate finite elements with five degrees of freedom per node and used to solve the problem of a plate subject to uniform or biaxial compression in which the plate edges are allowed to move in the loading direction. Results showed good agreement with Dym (1974) for simply supported isotropic plates under compression. Three conclusions were drawn from this research. It was found that the postbuckling characteristics of the composite plate were very sensitive to boundary conditions, which was also shown by Librescu and Stein (1991), thick plates can withstand large loads after buckling and orthotropic plates exhibit a higher post-buckling strength compared to angle-ply plates. These conclusions made are not surprising, and validate the use of first-order shear deformation theory in finite elements for these particular boundary conditions, although more investigation is needed for general boundary conditions and materials.

Kim and Voyiadjis (1999) studied the non-linear behaviour of composite shell structures using an eight-noded shell element formulated based on a Lagrangian method. Unlike the previous finite element methods, the transverse shear deformation effect was considered and included in the linear stiffness matrix. Thus large deflections and small strains could be considered for postbuckling analysis. The advantage of this method is that it increases the accuracy of highly nonlinear problems and allows the modelling of relatively thick plates. It does not however consider the reduction of buckling capability caused by geometric imperfections. Note however that for thin plates, the use of shear deformation theory does not make much difference compared to CPT while the complexity of the method is increased to another level.

The arc length method in finite element was first proposed by Riks (1972; 1979) and Wempner (1971) to solve snap-through problems which the Newton-Raphson method was unable to solve. In this method, at each iteration, the load factor is perturbed to converge on an equilibrium path where iterative changes are made orthogonal to the predicted solution. Ramm (1981) adjusted such changes to secant iteration changes. These techniques however, linearise the arc-length method where constraint equations lead to unique solutions i.e. where there are no selection of root issues. This may result in missing the equilibrium path and causing numerical difficulties (Memon and Su, 2004). Therefore, Fafard and Massicotte (1993) modified the arc-length method based on Ramm (1981) and updated the hyper-plane technique to evaluate the arc length. Later, Teng and Luo (1998) extended the method using an accumulated arc length to optimize the convergence. Ferreira and Serpa (2005) found that the conventional arc length method obtains a limit point for snap-back and snap-through phenomenon due to the highly nonlinear load-displacement path. Therefore, Sousa and Pimenta (2010) introduced a new parameter with a function to add all previous arc lengths and generate a new load step. This efficiently overcomes the difficulties in the control of the load increment to reach convergence at specific locations of the equilibrium path.

Weaver (2004, 2006) observed that a skewed buckling mode is induced by anisotropy for infinitely long laminated composite plates subject to compression or shear loading and formed a closed-form solution. Later Diaconu and Weaver (2005, 2006), extended this solution for the postbuckling of such plates with both symmetric and unsymmetric laminate configurations. Their method represents the postbuckling mode using non-dimensional parameters to cover a wide range of dimensions and material properties with the solutions then written in terms of non-dimensional buckling coefficients and load factors. By doing so, the importance of the terms appearing in the equations or solutions can be easily clarified. The method was validated for an infinitely long plate with two long edges simply supported and compared with solutions obtained from a finite element method. The paper also highlighted that ‘postbuckling results for infinitely long plates are important because they provide a practical estimation and useful information on the postbuckling behaviour of finite length rectangular plates’.

Bisagni and Vescovini (2009) developed an analytical formulation for the buckling and postbuckling of isotropic and laminated stiffened panels subjected to axial compression. For buckling, two approaches were proposed employing the Kantorovich method (Kantorovich and Krylov, 1958) and a rigorous closed-form solution. Following critical buckling analysis, a localized postbuckling problem was formulated based on trigonometric shape functions and

non-linear governing equations derived by the Ritz method. The whole analytical technique was further coded into a computer program called Stiffened Panels Analysis (StiPAn) (Bisagni and Vescovini, 2009). The authors later refined the postbuckling part of the analysis (Vescovini and Bisagni, 2012) to cover curved stiffened panels and combined loading. In Vescovini and Bisagni (2006), this analysis was further developed into a semi-analytical procedure. By implementing the arc-length method, the analysis was able to solve for unsymmetric laminates. An optimization technique based on a genetic algorithm was also developed and employed.

Developments in postbuckling analysis techniques in recent years have examined novel materials or manufacturing approaches. Raju et al. (2013) used first-order shear deformation theory to derive the postbuckling equilibrium equations for a functionally graded plate and variable angle tow composite. Raju et al. (2013, 2015) developed a postbuckling technique based on the differential quadrature method (DQM) for variable angle tow composite plates under in-plane shear loading. Compared to the conventional finite element method, DQM showed good agreements and required few grid points and hence less computational effort to achieve converged results. Raju et al. (2015) developed a semi-analytical variational approach to investigate linear variable angle tow composite plates. Based on this approach and the Rayleigh-Ritz method, nonlinear equilibrium equations were assembled and solved analytically using trigonometric functions or Legendre polynomials. The load-end shortening curves and load-transverse deflection curves for such plates were drawn under uniform axial compression loading.

Song et al. (2017) investigated the postbuckling behaviour of functionally graded multilayer composite plates reinforced with randomly oriented graphene nanoplatelets (GPLs) uniformly dispersed in the polymer matrix. The analysis was formulated based on von Kármán nonlinear kinematics to take into account geometric imperfections and first-order shear deformation theory. The method used a two-step perturbation technique to find the postbuckling equilibrium paths of composite plates with all edges simply supported.

The Rayleigh-Ritz solution is one of the most successful methods for the analysis of the postbuckling of composite plates. Oliveri and Milazzo (2018) investigated the postbuckling of variable angle tow composite stiffened panels using a Rayleigh-Ritz method. Postbuckling equilibrium equations were found based on first-order shear deformation theory and von Kármán's large displacement assumptions. Penalty techniques were used to enforce the

structural continuity of the assembled thin-walled structures and the kinematical boundary conditions. The solution was further validated by the finite element method.

Li et al. (2020) developed an element-free Galerkin method for the postbuckling analysis of variable stiffness composite plates with circular cut-outs. Their method used weighted orthogonal basis functions to represent of the field of displacements. Classical laminate plate theory and von Kármán large deflection theory were then employed to find nonlinear strain components on the midplane. The postbuckling equilibrium path was found by an incremental loading step control method. The method was validated against conventional finite element analysis and achieved good agreement.

Chen and Qiao (2021) investigated the postbuckling behaviour of rotationally-restrained laminated composite plates under shear based on the Galerkin method. The trigonometric function proposed by Beslin and Nicolas (1997) and two other kinds of series functions based on the Airy functions were combined to uniquely satisfy the arbitrary rotationally-restrained boundary conditions.

Wang and Qiao (2021) investigated the postbuckling behaviour of stiffened laminated composite plates using a spline finite strip method. The method formulated the plates and stiffeners individually using first-order shear deformation theory and Timoshenko beam theory respectively. As the stiffeners were modelled as beams attached to the plate they did not add any extra additional degrees of freedom thereby increasing computational efficiency. Nonlinear governing equations were solved based on the Newton-Raphson method. Such a beam-plate model is capable of analysing both global and local postbuckling for both transversely- and orthogonally-stiffened plates.

The exact strip method was first proposed by Wittrick (1968a) to determine the elastic stability of plate assemblies. The buckling mode is assumed to vary sinusoidally in the longitudinal direction. Wittrick and Williams (1971) developed the W-W algorithm to overcome the transcendental problem arising from the exact strip method by counting the number of eigenvalues which lie between zero and any trial value without obtaining them explicitly.

Using the exact strip method and incorporating the W-W algorithm to overcome the transcendental eigenvalue problem, in the 1970s. VIPASA was developed to carry out vibration and buckling analyses for a range of prismatic plate assemblies (Wittrick and Williams, 1973). However, results are very conservative for panels with anisotropy or shear loading (Wittrick and Williams, 1974). VICON (VIPASA with Constraints) is an enhanced version of VIPASA

which couples together sinusoidal modes to represent more complicated waveforms (Anderson et al., 1983). In the 1990s, VICONOPT, developed at Cardiff University in cooperation with Airbus, BAE Systems and NASA combined VIPASA and VICON analyses with optimum design to carry out initial buckling, free vibration and optimisation design of prismatic plate assemblies. The first non-linear local postbuckling analysis in VICONOPT was developed by Powell et al. (1998). Kennedy and Anderson (2008) created the Newton iteration method for accurate convergence on the postbuckling mode for VICONOPT postbuckling. Later on, Che (2010) and Zhang (2018) developed an improved VIPASA postbuckling method by solving the differential equations analytically to determine in-plane displacement distributions. However, the postbuckling analysis in VICONOPT remains limited to isotropic material and compressive loading.

Research on the stability of laminated composite plates has continued for centuries. Postbuckling of the shell structures in particular draw attention among designers and engineers in recent years. However, most of the postbuckling analysis techniques are characterized by either low computational efficiency or lack of accuracy. To address those limitations, this thesis proposes a fast yet reliable postbuckling analysis technique for preliminary design.

Chapter 3. Exact Finite Strip Method and VICONOPT

This chapter introduces the computer program VICONOPT, its fundamental theories and applications for buckling and postbuckling analysis. It is organized as follows: Section 3.1 presents a general review of the basic theory for the exact strip method. Section 3.2 reviews the theory of the Wittrick-Williams algorithm (W-W algorithm) and its application in the exact strip method. Sections 3.3-3.5 introduce the theory underpinning the buckling and vibration analysis software VIPASA, VICON and VICONOPT, the platforms used in this research. Sections 3.6-3.8 review recent research into postbuckling analysis based on VIPASA, addressing the limitations of the methods developed and introduce the research background to this thesis.

3.1. Exact strip method

The exact strip method is an alternative numerical analysis method to the finite strip method (Wittrick, 1968a, 1968b) for buckling and undamped natural frequency analysis of prismatic plate assemblies, providing faster and more accurate analysis by reducing the partial differential governing equations to ordinary differential equations which are solved analytically. The method assumes plates to be divided into strips with arbitrary width in the longitudinal direction, as identified by the n nodes at the strip edges. At each node, the out-of-plane deflection \mathbf{D} is assumed to vary in a series of trigonometric terms. According to classical plate theory, the governing equations of each node, therefore, are transformed into transcendental ordinary differential equations. As in many structural analysis methods, a global stiffness matrix \mathbf{K} is assembled using element stiffness matrices. The elements of \mathbf{K} are highly

transcendental functions of the loads and/or vibration frequency. The relationship between nodal displacements, global stiffness matrix and perturbation loads vector \mathbf{P} is then:

$$\mathbf{KD} = \mathbf{P} \quad \dots(3.1)$$

Thus critical buckling loads and natural frequencies can be determined explicitly by solving the eigenvalue problem

$$\mathbf{KD} = \mathbf{0} \quad \dots(3.2)$$

where the displacement amplitude vector \mathbf{D} contains four degrees of freedom, as explained Section 3.3.

Wittrick and Curzon (1968) later extended the exact strip method to include the effect of in-plane shear loading leading to skewed nodal lines and mode shapes. To address the spatial phase differences across the transverse direction of the plate caused by these skewed nodal lines, displacements are represented by complex quantities. Later on, Viswanathan et al. (1973;1974) extended the research to cover anisotropic material in flat and curved plate assemblies which also causes skewed nodal lines.

In the exact strip method, the sinusoidal variation assumption converts a buckling problem to a single-term type analysis at the node level. It provides accurate results by assuming the plate to be infinitely long with no anisotropy or shear loading and solving the governing equations explicitly rather than using the energy approach. In this way, the global stiffness matrix is reduced to a much lower order than that of the finite element method. The computational effort is therefore reduced significantly, with an accuracy that is more than enough for preliminary aircraft design. A disadvantage compared to finite element and finite strip methods is that buckling or free vibration requires the solution of a transcendental, rather than linear eigenvalue problem. However transcendental eigenvalue problems can be solved accurately, quickly and reliably using the Wittrick-William algorithm (Wittrick and Williams, 1971, 1973).

3.2. Wittrick-Williams algorithm

Solving eigenvalue problems is essential to finding the natural frequencies or the critical buckling loads of plate and shell structures. Techniques for finding the eigenvalues of a matrix are widely developed. However, the solution of transcendental eigenvalue problems can be computationally expensive. Wittrick and Williams (1971) developed the Wittrick-Williams algorithm (W-W algorithm) which efficiently finds the transcendental eigenvalues needed to determine the undamped natural frequencies of vibration problems or the critical buckling load factor for elastic structures.

Rather than finding the eigenvalues directly, the W-W algorithm counts the number of eigenvalues that lie below any trial value f^* of f , the load factor or frequency of the vibration from Equation 3.2. The general form of the algorithm can be written as

$$J = J_0 + s\{\mathbf{K}(f^*)\} \quad \dots(3.3)$$

where J is the number of eigenvalues lying between zero and the trial value f^* ; J_0 is the number of eigenvalues which would still be exceeded by f^* if constraints were imposed so as to make all the displacements \mathbf{D} zero and $s\{\mathbf{K}(f^*)\}$ is known as the sign count of \mathbf{K} , i.e. the number of negative diagonal elements of the upper triangular matrix $\mathbf{K}^\Delta(f^*)$ obtained from $\mathbf{K}(f^*)$ by Gauss elimination (Wittrick and Williams, 1973). J_0 can be calculated from

$$J_0 = \sum_m J_m \quad \dots(3.4)$$

where J_m is the number of eigenvalues of member m exceeded at the trial value f^* when its ends are fully restrained, which can be obtained analytically or by numerical procedures (Wittrick and Williams, 1974).

After obtaining J_0 and $s\{\mathbf{K}(f^*)\}$, eigenvalues can be found by using parabolic interpolation or the bisection method within any desired accuracy and consequently the structures' natural frequencies or critical buckling load factors can be obtained.

3.3. VIPASA

VIPASA is a powerful analysis program developed in the 1970s. By using the exact strip method incorporating the W-W algorithm to solve the transcendental eigenvalue problem, VIPASA can solve vibration and buckling problems for prismatic plate assemblies under pure or combined loadings such as those shown in Figure 3.1. The characteristic simple form calculation of the exact strip method with the W-W algorithm allows fast and reliable analysis in VIPASA within any acceptable level of accuracy (Stroud et al. 1984). It has been proven that for certain component plates, VIPASA is 1000 times faster than the conventional finite element program STAGS (Almroth et al. 1981).

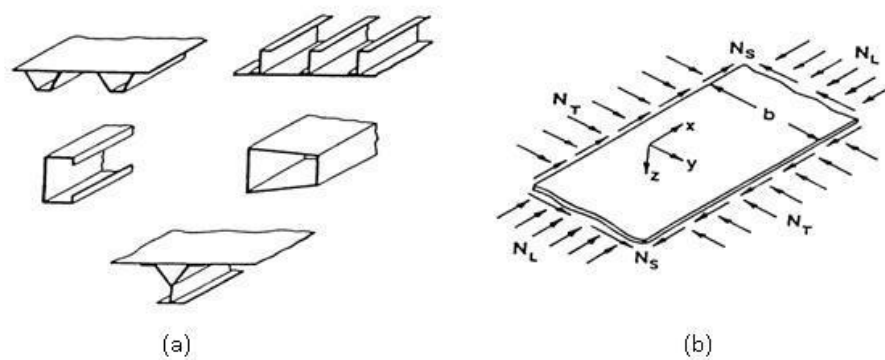


Figure 3.1(a) Examples of prismatic plate assemblies. (b) a component strip, showing the applied uniform stress resultants N_L , N_T and N_S (Wittrick and Williams, 1971)

VIPASA analysis assumes the displacements u , v and w in the x , y and z directions respectively vary sinusoidally in the longitudinal direction with half-wavelength λ as shown in Figure 3.2. The amplitudes of the perturbation force and displacement vectors \mathbf{P}_j and \mathbf{d}_j at edges of $j=1$ or 2 of a strip are defined by;

$$\mathbf{P}_j = [m_j, p_{zj}, p_{vj}, ip_{xj}] \quad \dots(3.5)$$

$$\mathbf{d}_j = [\psi_j, w_j, v_j, iu_j]$$

Terms in the above vectors are multiplied by $\exp(i\pi x/\lambda)\cos(2\pi nx)$ to allow for possible phase differences. Solving the transcendental eigenvalue problem in Equation 3.2, substituting Equation 3.5 leads to;

$$\mathbf{P}_1 = \mathbf{k}_{11}\mathbf{d}_1 + \mathbf{k}_{12}\mathbf{d}_2 \quad \dots(3.6)$$

$$\mathbf{P}_2 = \mathbf{k}_{21}\mathbf{d}_1 + \mathbf{k}_{22}\mathbf{d}_2$$

The stiffness matrices \mathbf{k}_{ij} can be further expanded to give

$$\mathbf{k}_{11} = \begin{bmatrix} S_{MM} & -S_{MQ} & 0 & 0 \\ -\bar{S}_{MQ} & S_{QQ} & 0 & 0 \\ 0 & 0 & S_{NN} & -S_{NT} \\ 0 & 0 & -S_{NT} & S_{TT} \end{bmatrix} \quad \dots(3.7)$$

$$\mathbf{k}_{22} = \begin{bmatrix} S_{MM} & \bar{S}_{MQ} & 0 & 0 \\ S_{MQ} & S_{QQ} & 0 & 0 \\ 0 & 0 & S_{NN} & S_{NT} \\ 0 & 0 & S_{NT} & S_{TT} \end{bmatrix} \quad \dots(3.8)$$

$$\mathbf{k}_{12} = \bar{\mathbf{k}}_{12}^t = \begin{bmatrix} f_{MM} & f_{MQ} & 0 & 0 \\ -f_{MQ} & -f_{QQ} & 0 & 0 \\ 0 & 0 & -f_{NN} & -f_{NT} \\ 0 & 0 & f_{NT} & f_{TT} \end{bmatrix} \quad \dots(3.9)$$

where superscript t denotes the transpose of a matrix and the bar denotes the possible complex conjugate. Explicit expressions for the coefficients in the stiffness matrix of the strip are explained and can be found in the work by Wittrick and Williams (1971) .

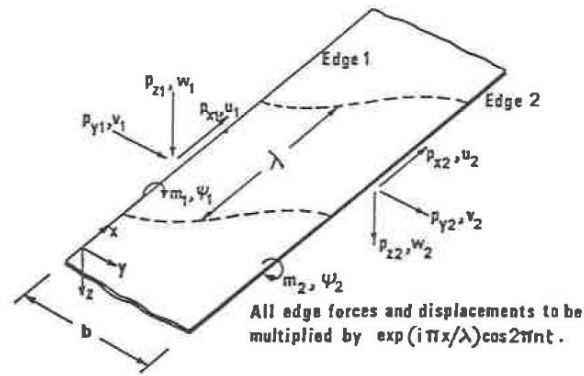


Figure 3.2 A strip of a component plate, showing the perturbation edge forces and displacements, and nodal lines (Wittrick and Williams, 1971)

For an orthotropic panel with simply supported boundary conditions (shown in Figure 3.3), straight nodal lines (nodes with zero displacements) are located at sinusoidal intervals equal to the half-wavelength λ . Therefore simply supported end conditions are automatically satisfied if λ divides exactly into the panel length l .

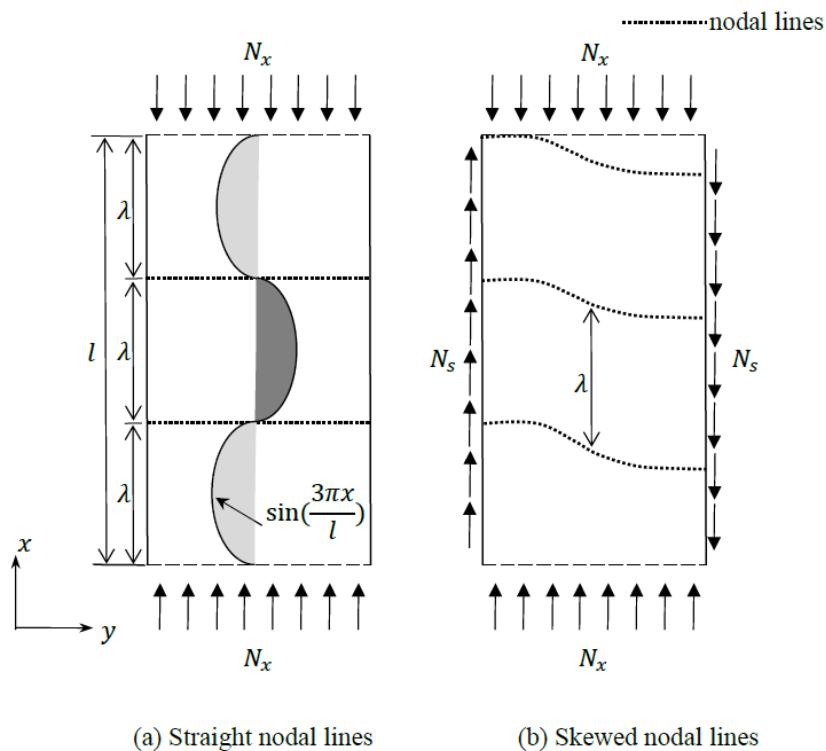


Figure 3.3 An infinitely long plate. Nodal lines in (a) are straight and perpendicular to the longitudinal direction, which is consistent with simply supported end conditions. Nodal lines in (b) are skewed due to anisotropy or shear loads, approximating the simply supported end condition.

VIPASA also allows other boundary conditions, which can be any combination of degrees of freedom, i.e. in-plane u and v and out-of-plane w and ψ , to be applied to the transverse edges of the panel by adding line supports in the longitudinal direction. A limitation of VIPASA analysis is that it is restricted to isotropic plates or composites with symmetric and balanced layups, i.e. those for which in-plane membrane stiffness matrix terms A_{16} and A_{26} are zero and there is no coupling with the out-of-plane bending stiffness matrix \mathbf{D} (Wittrick and Williams, 1974). Anisotropy or the application of shear however results in solutions which are increasingly inaccurate, because such plates have skewed mode shapes which lead to skewed nodal lines as shown in Figure 3.3(b) so that the simply supported end conditions implied by VIPASA are not satisfied. These skewed nodal lines cannot be satisfied by the single sine wave assumption. To overcome this VIPASA allows the terms s_{MQ} , f_{MM} , f_{MQ} and f_{QQ} to be complex. However, this presents increasingly conservative results.

Buckling loads can be found for a range of half-wavelengths λ which divide into the panel length l . The smallest such buckling load is taken as the critical buckling load. To ensure that all possible overall and local buckling possibilities have been considered, analysis should be performed for $\lambda = l, l/2, l/3, \dots, l/m$, where l/m is smaller than the width of the narrowest component plate.

3.4. VICON

Inheriting all the capabilities and functionalities of VIPASA, VICON (VIPASA with CONstraints) analysis was developed to overcome the limitations of VIPASA analysis in relation to shear load and anisotropy. Instead of representing mode shapes using one half-wavelength, VICON analysis couples the stiffness matrices of different half-wavelengths using Lagrangian multipliers to minimise the total energy of a panel subject to point constraints, to approximate the required end conditions. It can therefore handle assemblies of plates which carry shear load or are made from anisotropic material, or which have a variety of boundary conditions including attachments to beam-type supporting structures (Anderson et al., 1983).

As illustrated in the previous section, due to the simple support assumption, VIPASA presents conservative results for shear load and anisotropy, representing mode shapes with one single term analysis. VICON however presents more accurate solutions. Figure 3.4 shows the differences between VIPASA and VICON at initial buckling and a prediction of the VICON postbuckling path when shear or anisotropy is present.

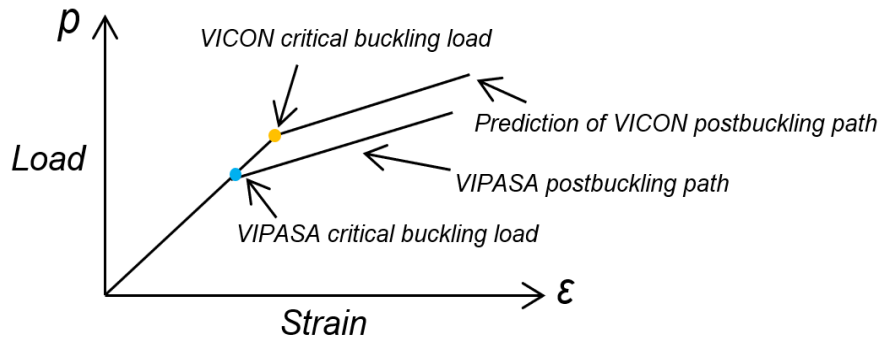


Figure 3. 4 Load and strain paths of VICON and VIPASA for shear or anisotropy

To interpolate infinitely long plate assemblies with point supports along their transverse edges, Fourier series of combinations of several half-wavelengths are chosen

$$\mathbf{D}_a = \sum_{m=-\infty}^{\infty} \mathbf{D}_m \exp\left(\frac{i\pi x}{\lambda_m}\right) \quad \dots(3.10)$$

$$\mathbf{P}_a = \sum_{m=-\infty}^{\infty} \mathbf{K}_m \mathbf{D}_m \exp\left(\frac{i\pi x}{\lambda_m}\right) \quad \dots(3.11)$$

where \mathbf{D}_a is the nodal deflection vector of an infinitely long plate assembly consisting of a series of deflection modes \mathbf{D}_m from VIPASA analyses. \mathbf{P}_a is the force vector applied at nodes. \mathbf{K}_m is the stiffness matrix for half-wavelength λ_m .

An infinitely long panel, with end supports repeating at longitudinal intervals of the panel length l , is shown in Figure 3.5. Its mode shapes are assumed to repeat in the longitudinal direction at intervals of $L = 2l/\xi$, where ξ is a parameter in the range $0 \leq \xi \leq 1$. Mode shapes can therefore be represented (Anderson et al., 1983) by a series of responses with half-

wavelengths $l/(\xi + 2m)$ where m is any integer. Sufficient accuracy is obtained by considering a finite series of half-wavelengths:

$$\lambda_m = \frac{l}{(\xi + 2m)} \quad (m = 0, \pm 1, \pm 2, \dots, \pm q) \quad \dots(3.12)$$

where the integer q determines the number of terms in the series.

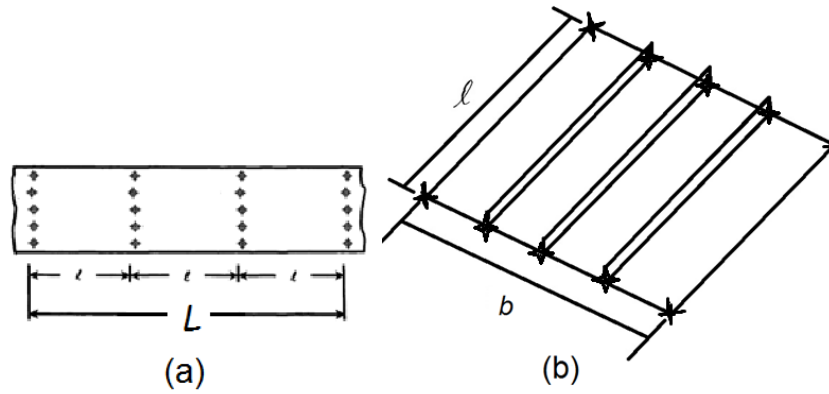


Figure 3.5 Graphical explanation of an infinitely long plate assembly with the end supports repeating at longitudinal intervals of the panel length l (a) plan view (b) isometric view (Anderson et al., 1983).

To couple multiple half-wavelengths, Lagrangian multipliers (Williams and Anderson, 1983) are applied. The total energy can be written as the energy of the plate without constraints plus the Lagrangian multipliers times the energy of the constraints. It can be written as a target function in terms of the nodal deflections \mathbf{D}_m and the stiffness matrices \mathbf{K}_m :

$$\varphi = \sum_{m=-\infty}^{\infty} \frac{1}{2} \mathbf{D}_m^T \mathbf{K}_m \mathbf{D}_m + \mathbf{P}_L^T \sum_{m=-\infty}^{\infty} \mathbf{E}_m \mathbf{D}_m \quad (m = 0, \pm 1, \pm 2, \dots, \pm q) \quad \dots(3.13)$$

where \mathbf{P}_L is the vector of Lagrangian multipliers, \mathbf{E}_m are matrices of the constraints and the superscript T denotes the transpose.

To find the minimum energy, setting the derivatives of the energy function φ with respect to the stiffness matrices \mathbf{K}_m and the Lagrangian multipliers \mathbf{P}_L equal to zero gives

$$L\mathbf{K}_m\mathbf{D}_m + \mathbf{E}_m^H\mathbf{P}_L = \mathbf{0} \quad \dots(3.14)$$

$$\sum_{m=-\infty}^{\infty} \mathbf{E}_m\mathbf{D}_m = \mathbf{0} \quad \dots(3.15)$$

where H denotes the Hermitian transpose.

For programming purposes, Equations 3.14 and 3.15 can be written as

$$\begin{bmatrix} L\mathbf{K}_0 & & & & & & & \mathbf{E}_0^H \\ & L\mathbf{K}_1 & & & & & & \mathbf{E}_1^H \\ & & L\mathbf{K}_{-1} & & & & & \mathbf{E}_{-1}^H \\ & & & L\mathbf{K}_2 & & & & \mathbf{E}_2^H \\ & & & & L\mathbf{K}_{-2} & & & \mathbf{E}_{-2}^H \\ & & & & & \ddots & & \vdots \\ \mathbf{E}_0 & \mathbf{E}_1 & \mathbf{E}_{-1} & \mathbf{E}_2 & \mathbf{E}_{-2} & \dots & \mathbf{0} & \mathbf{0} \end{bmatrix} \begin{bmatrix} \mathbf{D}_0 \\ \mathbf{D}_1 \\ \mathbf{D}_{-1} \\ \mathbf{D}_2 \\ \mathbf{D}_{-2} \\ \vdots \\ \mathbf{P}_L \end{bmatrix} = \mathbf{0} \quad \dots(3.16)$$

where the negative sign in the subscript denotes the complex conjugate. The reorganized stiffness matrix consists of a block matrix comprising the stiffness matrix \mathbf{K}_m and a block matrix of all the constraints \mathbf{E}_m added to the right and bottom of the main matrix. A similar approach to organizing the stiffness matrix will be used again in the VICON type Newton iteration scheme, presented in Chapter 5.

To obtain the eigenvalues from the complex transcendental matrix in equation 3.16 efficiently, a modified form of the W-W algorithm in VICON is developed and given by

$$J = \sum_m (J_{0m} + s\{\mathbf{K}_m\}) + s\{\mathbf{R}\} - r \quad \dots(3.17)$$

where J_{0m} and $s\{\mathbf{K}_m\}$ are the sign count of the eigenvalues for each half-wavelength λ_m , and \mathbf{R} is given by

$$\mathbf{R} = -\frac{1}{L} \sum_m \mathbf{E}_m \mathbf{K}_m^{-1} \mathbf{K}_m^H \quad \dots(3.18)$$

r is the number of constraints, i.e. the order of \mathbf{R} , and s denotes the sign count of a matrix.

Then similar to VIPASA's W-W algorithm, the eigenvalues can be found by bisection or parabolic interpolation.

By coupling more half-wavelengths through the use of Lagrangian multipliers, VICON analysis improves the accuracy of the buckling problem for plate assemblies with shear loading or anisotropy, as shown in Figure 3.6. The results are more accurate than those obtained using VIPASA analysis although this is at the sacrifice of computational time. However, it is still 150 times faster than the finite element program STAGS [Butler and Williams 1992].

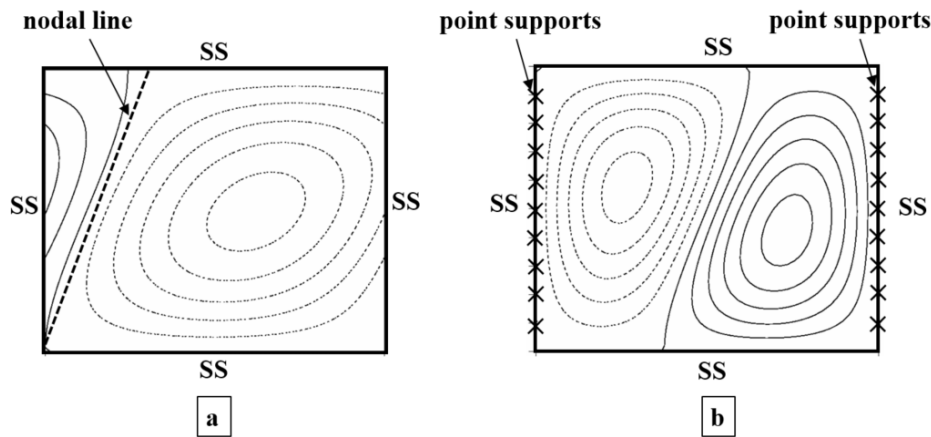


Figure 3.6 Buckling analysis, out-of-plane displacement contours from (a)VIPASA analysis and (b) VICON analysis(Williams and Anderson, 1983).

3.5. Exact strip software VICONOPT

VICONOPT (VIpasa with CONstraints and OPTimization) is a Fortran 77 computer software consisting of more than 50,000 lines of code developed at Cardiff University in 1990 in cooperation with NASA and Airbus (William et al. 1990, 1991). It incorporates VIPASA and VICON to cover the analysis of elastic buckling and undamped natural frequencies for prismatic assemblies including isotropic and anisotropic material under any combination of in-plane loadings and constraints. It also features multi-level optimization analysis enabling it to

minimise panel mass subject to buckling, stiffness and geometric constraints. The development of VICONOPT has never stopped. Continuous design optimization was introduced and coded into VICONOPT in 1992 by Butler and Williams. Later on, Kennedy *et al.* developed discrete optimisation for VICONOPT. In 1998, Powell developed the first non-linear local postbuckling analysis for shell structure assemblies and in 2008, Kennedy and Anderson created the Newton iteration for accurate convergence on postbuckling modes for VICONOPT postbuckling analysis. Later on, Che (2010) and Zhang (2018) developed an improved VIPASA postbuckling method to capture in-plane displacements for each postbuckling increment by solving the in-plane equilibrium equations analytically.

Overall, as a numerical modelling software, VICONOPT is highly efficient, taking advantage of a smaller stiffness matrix compared to finite element software. Implementing the exact strip method in VICONOPT means it is less likely to have discretization problems and enables it to perform much faster analyses of prismatic assemblies for both buckling and postbuckling analysis. The combination of VIPASA and VICON enables accurate results to be obtained for any material, loading and boundary conditions for critical buckling analysis. However, the postbuckling analysis in VICONOPT is at present unable to handle anisotropy and shear loading due to the limitations of VIPASA.

3.6. VIPASA Postbuckling

Stiffened wing and fuselage panels often have a post-buckling reserve of strength, enabling them to carry loads far in excess of their critical buckling loads. Therefore allowing for postbuckling in design can reduce the weight of such structures, and hence fuel consumption and environmental impact. The feature of postbuckling analysis is therefore of paramount importance for VICONOPT (Zhao, 2019).

Powell *et al.* (1998) developed the first postbuckling analysis for thin-walled structures as an extension of VICONOPT. Assuming the component plates are isotropic or anisotropic, infinitely wide and simply supported, the plate buckles locally with a half-wavelength λ which

divides exactly into the panel length l . As shown in Figure 3.7, a plate with width b and uniform thickness t is divided equally into n_s strips along the longitudinal direction.

$$b_s = \frac{b}{n_s} \quad \dots(3.19)$$

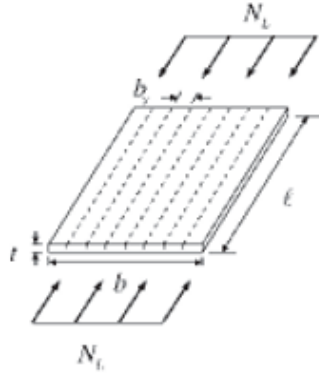


Figure 3.7 Typical flat plate of width b , subdivided into n_s strips of width b_s (Powell et al. 1998).

It is well known that postbuckling behaviour is significantly influenced by geometric imperfections. To account for this the method assumes a plate with geometric imperfections defined by its maximum out-of-plane displacement γ_0 . At the buckling load P_c , the initial stress resultant at each strip is calculated by

$$N_{xs} = N_L = \frac{P_c}{b} \quad \dots(3.20)$$

The analysis consists of a user-defined number of cycles. At each cycle, the out-of-plane displacement γ_2 is increased by a user-defined ratio and the applied load P and longitudinal end-shortening strain ϵ_x are obtained. Because the postbuckling mode is represented by a single wavelength, the mode shape stays the same as the buckling mode at each cycle. So the applied load at each cycle is

$$P = \left(1 - \frac{\gamma_0}{\gamma_2}\right) P_c \quad \dots(3.21)$$

The longitudinal strain due to the applied load P is P/S_1 , where S_1 is given by

$$S_1 = b(A_{11} - \frac{A_{12}^2}{A_{22}}) \quad \dots(3.22)$$

where A_{ij} are the in-plane elastic properties.

Thus the longitudinal strain ϵ_{x0} at the buckling load P_c is given by

$$\epsilon_{x0} = \frac{P_c}{S_1} \quad \dots(3.23)$$

Now consider the flexural strain ϵ_{Fx} due to bending at out-of-plane displacement w_2 . As shown in Figure 3.8, the change in projected length of a linear element of length dx in the longitudinal direction can be written as $(\partial w_2 / \partial x)^2 dx$. Thus the flexural strain ϵ_{Fx} can be obtained by differentiating the change between the initial and final projected lengths from 0 to the half-wavelength λ :

$$\epsilon_{Fx} = \frac{1}{2\lambda} \int_0^\lambda \left[\left(\frac{\partial w_2}{\partial x} \right)^2 + \left(\frac{\partial v_2}{\partial x} \right)^2 - \left(\frac{\partial w_0}{\partial x} \right)^2 - \left(\frac{\partial v_0}{\partial x} \right)^2 \right] \quad \dots(3.24)$$

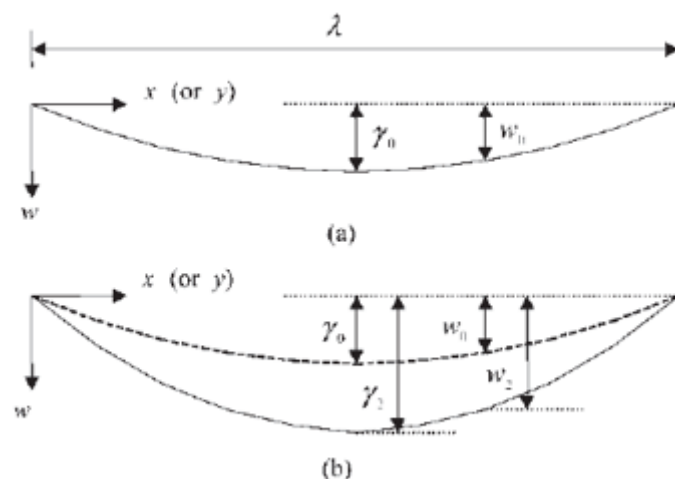


Figure 3.8 Cross-section of part of a thin rectangular plate having an initial imperfection w_0 with maximum value γ_0 : (a) unloaded; (b) loaded (Powell et al. 1998).

where the v displacement is included to allow for the alignment of stiffeners along the v direction.

Similar to the exact strip method, the mode can be written as a sinusoidal function

$$w_2 = \bar{w}_2 \sin (\pi x / \lambda) \quad \dots(3.25)$$

where \bar{w}_2 is the amplitude of the mode shape. Thus Equation 3.24 can be further simplified as

$$\varepsilon_{Fx} = \left(\frac{\pi^2}{4\lambda^2}\right)(\bar{w}_2^2 + \bar{v}_2^2 - \bar{w}_0^2 - \bar{v}_0^2) \quad \dots(3.26)$$

From Equation 3.23, the stress resultant due to flexure is

$$N_{Fx} = \varepsilon_{Fx} \frac{S_1}{b} \quad \dots(3.27)$$

After initial buckling, the stresses along the transverse edges are no longer uniform i.e. stress redistribution takes place. As shown in Figure 3.9, N_{Fxs} is the mean value of N_{Fx} along the two edges of strip s and N_L is the average stress resultant which equals P/b . At the edges where the stress resultants for flexure are zero, the stress is taken as $S_2 N_L$, where

$$S_2 = 1 + \left(\frac{1}{P}\right) \sum_s (b_s N_{Fs}) \quad \dots(3.28)$$

The overall stress resultant N_{xs} for each strip is given by;

$$N_{xs} = S_2 N_L - N_{Fxs} \quad \dots(3.29)$$

The end shortening strain at the same cycle can be obtained by;

$$\varepsilon_x = \frac{S_2 P}{S_1} \quad \dots(3.30)$$

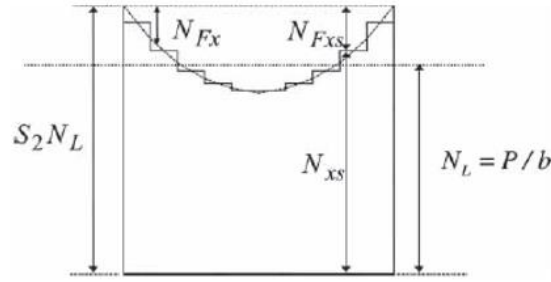


Figure 3.9 Variation of stress resultants across a plate(Powell et al. 1998).

To ensure accurate results, a convergence procedure is required to converge on the maximum displacement γ_2 , applied load P and end shortening strain ϵ_x . At each iteration of the procedure, the above calculations are executed and the convergence of the iteration is assumed to occur when the following criterion is met.

$$\frac{P_i - P_{pi}}{P_c} \leq \beta \quad \dots(3.31)$$

where P_i is the current applied load, P_{pi} is the previous iteration's applied load and β is a predefined small positive number.

For each new cycle, the previous converged mode is considered as the new imperfection, representing the worst possible shape and the maximum out-of-plane displacement is rescaled by increasing the value of γ_2 . For the new buckling load P_{cx} , instead of using VIPASA, a simple linear extrapolation based on the previous two buckling loads is applied to calculate P_{cx} . Hence by substituting P_{cx} into Equation 3.21 the applied load can be obtained for the first iteration of the new cycle.

An alternative boundary condition - simply supported with longitudinal edges able to move in the transverse direction but required to remain straight is also considered in Powell's method. Such a condition requires the transverse load obtained by integrating the transverse stress resultant to equal zero.

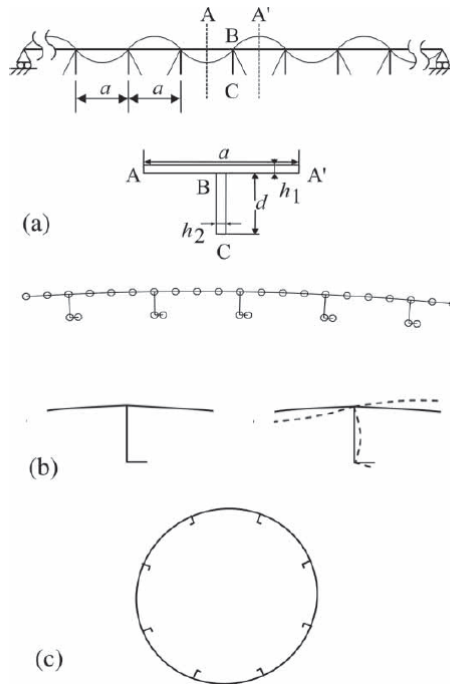


Figure 3.10 Typical applications for postbuckling analysis: (a) cross-section of a perfect isotropic infinitely wide panel with simply supported ends, showing the local buckling mode, and dimensions of a typical repeating portion (ABCA_); (b) curved simply supported panel, showing repeating portion and local buckling mode; and (c) longitudinally stiffened cylindrical shell (Powell et al. 1998).

The method can be applied not just to plates but to panels. In the application shown in Figure 3.10(a), the panel is divided into repeating portions of identical geometry. Since the panel is a perfect isotropic infinitely wide panel with simply supported ends, the calculation of one divided plate can normally represent the overall structure. Stiffened panels can also be analysed by altering the out-of-plane displacement of the plate to the in-plane displacement of the stiffeners as illustrated in Figure 3.10(b). Figure 3.10(c) shows a longitudinally stiffened cylindrical shell that can also be analyzed by VICONOPT.

Powell's method provides a lower bound local postbuckling analysis based on VIPASA and implemented into VICONOPT. It uses a simple linear extrapolation to obtain the buckling load for each cycle. It, therefore, assumes the buckling load paths follow an approximately linear relationship through the cycles. Such an assumption gives poor accuracy in terms of mode shape and follow-up calculations. To overcome this limitation, Kennedy and Anderson (2008)

created a Newton iteration scheme for accurate convergence on the critical buckling mode for VICONOPT postbuckling.

3.7. Newton iteration scheme

Instead of obtaining the buckling load and associated mode shape using the exact strip method and the W-W algorithm, a convergence scheme using Newton type iteration was developed for local postbuckling analysis.

The buckling problem for the exact strip method is to solve the transcendental eigenvalue problem;

$$\mathbf{K} \mathbf{D} = \mathbf{0} \quad \dots(3.32)$$

Here, $\mathbf{D} = \{D_j; j = 1, \dots, n\}$ is the mode vector for the structure, which includes displacements and rotations at the longitudinal plate edges. \mathbf{D} also includes displacements and rotations at the strip edges within each plate, and is ordered to permit elimination of these internal degrees of freedom by substructuring. $\mathbf{K} = \{K_{ij}; i, j = 1, \dots, n\}$ is the corresponding exact stiffness matrix, which is a transcendental function of the stress resultants in each strip, and hence also of \mathbf{D} . Note that, although \mathbf{K} and \mathbf{D} have finite order n , the formulation effectively retains an infinite number of internal degrees of freedom because the governing differential equations for each strip are solved exactly. Suppose that

$$\mathbf{D} = \mathbf{D}^* + \mathbf{d} \quad \dots(3.33)$$

where \mathbf{D}^* is a trial mode vector and $\mathbf{d} = \{d_j; j = 1, \dots, n\}$ is the adjustment to \mathbf{D}^* needed to solve Equation 3.32, The Newton iteration is expressed in matrix form as

$$\left(\mathbf{K}^* + \sum_{j=1}^n \frac{\partial \mathbf{K}^*}{\partial D_j} d_j\right) (\mathbf{D}^* + \mathbf{d}) = \mathbf{0} \quad \dots(3.34)$$

where $\mathbf{K}^* = \mathbf{K}(\mathbf{D}^*)$. Neglecting higher order terms, Equation 3.34 becomes

$$\sum_{j=1}^n (K_{ij}^* + \sum_{k=1}^n \frac{\partial K_{ik}^*}{\partial D_j} D_k^*) d_j = - \sum_{j=1}^n K_{ij}^* D_j^* \quad (i = 1, \dots, n) \quad \dots(3.35)$$

Equation 3.35 is solved to obtain d , and substitution in Equation 3.33 gives a new trial mode vector \mathbf{D} , which is used as \mathbf{D}^* in the next Newton iteration. The derivatives needed in Equation 3.35 are found using finite difference approximations using suitably small perturbations about the trial values $D_j = D_j^*$. It should be noted that when an element D_j is perturbed, the only non-zero derivatives in Equation 3.35 are those of the plates (or for some loading conditions, strips) immediately adjacent to D_j , and this is allowed for in the logic of the computer coding.

The Newton iteration reduces the level of approximation when performing postbuckling cycles. It gives accurate predictions of overall postbuckling stiffness and the stress distribution among plate assemblies. However, both this method and the previous local postbuckling analyses assume that in-plane deflections vary sinusoidally with the same half-wavelength λ as the out-of-plane displacements resulting in a failure to predict the in-plane displacements and strain distributions accurately.

3.8. Improved exact strip postbuckling analysis

The previous analysis can efficiently predict the postbuckling path and mode shape at each cycle approximately. However, there is a lack of deeper exploration of in-plane displacements, strains and stresses within the plates. Che (2010) and Zhang (2018) developed an improved VIPASA postbuckling method by assuming in-plane displacement to vary in a sinusoidal mode with half-wavelengths λ and $\lambda/2$. By solving the differential equations analytically, in-plane displacements and follow-up calculations for strains and stresses are captured more accurately.

This ‘Improved exact strip method’ is a VIPASA postbuckling analysis method aimed at obtaining more accurate stress resultant distributions and capturing in-plane displacements along the plate by extending the Stein method (1985). In the same way as for VIPASA initial buckling analyses, the plate is divided into longitudinal strips and all displacements vary

sinusoidally along the length with wavelength λ . Therefore the out-of-plane displacements at node i can be written as

$$w_i = w_{ic} \cos\left(\frac{\pi x}{\lambda}\right) + w_{is} \sin\left(\frac{\pi x}{\lambda}\right); \quad \psi_i = \psi_{ic} \cos\left(\frac{\pi x}{\lambda}\right) + \psi_{is} \sin\left(\frac{\pi x}{\lambda}\right) \quad \dots(3.36)$$

The in-plane displacements are assumed to vary as the sums of linear, constant and sinusoidal terms with two half-wavelengths λ and $\lambda/2$.

$$u_i = \bar{\varepsilon} \left(x - \frac{a}{2}\right) + u_{i0} + u_{ic} \cos\left(\frac{\pi x}{\lambda}\right) + u_{is} \sin\left(\frac{\pi x}{\lambda}\right) + u_{ic} \cos\left(\frac{2\pi x}{\lambda}\right) + u_{is} \sin\left(\frac{2\pi x}{\lambda}\right) \quad \dots(3.37)$$

$$v_i = v_{i0} + u_{ic} \cos\left(\frac{\pi x}{\lambda}\right) + v_{is} \sin\left(\frac{\pi x}{\lambda}\right) + v_{ic} \cos\left(\frac{2\pi x}{\lambda}\right) + v_{is} \sin\left(\frac{2\pi x}{\lambda}\right) \quad \dots(3.38)$$

where the linear term $\bar{\varepsilon} \left(x - \frac{a}{2}\right)$ denotes the end shortening strain due to compression and the constant term u_{i0} denotes a product related only to w which is considered as a known value from VICONOPT.

Using von Kármán large deflection theory (von Kármán et al., 1932), expressions for the neutral surface strains and curvatures can be obtained. Then the stresses and derivatives of these stresses can be obtained by introducing the membrane stiffness matrix. Since the method assumes the displacements vary sinusoidally along the longitudinal direction, any of the derivatives with respect to the longitudinal direction can be obtained analytically, but those with respect to the transverse direction in the calculation are required to be computed by first or second order finite difference approximation. Hence the equilibrium equations can be assembled using previous expressions and solved analytically. Figure 3.11 shows the improved method embedded into VIPASA postbuckling analysis.

VIPASA type exact strip postbuckling analysis provides an efficient approach to postbuckling analysis for isotropic plate assemblies in the preliminary design of aircraft structures (Zhang 2018). Instead of representing the in-plane mode with a single term, the improved exact strip method couples not just half-wavelengths from the out-of-plane displacement assumptions but also half-wavelengths generated by von Kármán large deflection theory. The new postbuckling analysis improves previous exact strip analyses by capturing in-plane displacements. However,

it has very similar drawbacks to VIPASA in term of buckling analysis. When it comes to anisotropic material or shear loading cases which lead to skewed mode shapes, it gives unrealistic results or fails to converge. Furthermore, although previous research provided explicit formulations for in-plane displacements and equivalent uniform stress resultants calculations, the improved exact strip method still predicts out-of-plane displacements and end shortening strains based on linear extrapolation from the critical buckling load. Subsequent chapters describe how the ‘Improved exact strip method’ has been implemented into the Newton iteration scheme and extended to VICON analysis.

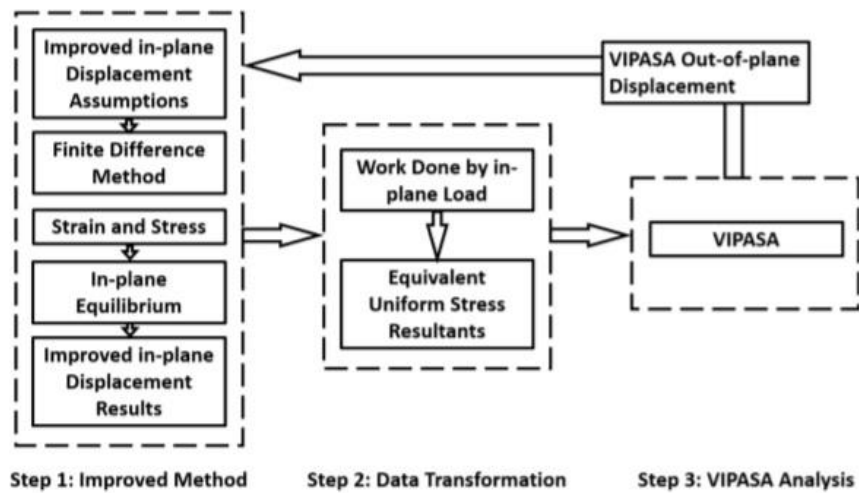


Figure 3.11 Implementation scheme of the improved VIPASA postbuckling analysis (Zhang 2018).

Chapter 4. CWPAN: In-plane Solutions

This chapter introduces a novel postbuckling simulation technique for flat plate structures – a series solution for postbuckling analysis. The proposed approach takes the previous exact strip postbuckling analysis and extends it, covering much more general cases, e.g. plates under pure shear or anisotropy, by representing modes using a series of any number of predefined half-wavelengths. The chapter is organized as follows: Section 4.1 outlines the main aims of the proposed method and the calculation process. Section 4.2 introduces the assumptions made in relation to out-of-plane and in-plane displacements. Sections 4.3 and 4.4 outline the development of explicit expressions for strains, curvatures, stress resultants and bending moments including a detailed explanation of the in-plane displacement assumption and finite difference approximation. Sections 4.5 and 4.6 outline the formulation of the equilibrium equations and boundary conditions for the proposed method. Section 4.7 concludes the chapter.

4.1. Description and assumptions of the analysis

The ‘Improved exact strip postbuckling method’ (Che, 2012) agrees well with other simulation techniques for flat plate structures for isotropic plates in the absence of shear loading. It reduces the computational modelling time significantly by discretising the structure into longitudinal strips rather than rectangular elements. By incorporating expressions for in-plane displacements and solving the corresponding equilibrium equations analytically, the sinusoidal variation of stress resultants and strains can be predicted. It does not, however, provide accurate results for anisotropic plates or when shear loads are applied due to the resulting skewing in the mode shape which cannot be represented by the assumption of sinusoidal variation by

longitudinal half-wavelengths λ and $\lambda/2$. In such cases, the solutions tend to be conservative compared with the finite element method. For extreme cases like pure shear, the method fails even to converge.

In this chapter, a series solutions for prismatic plate assemblies is presented. Whilst maintaining the advantage of smaller meshes from the exact strip method, the method improves accuracy when solving prismatic plates with anisotropy or under shear load, and enables the study of composite plates under pure shear which cannot be analysed using the improved exact strip postbuckling method. Inheriting the functionality of the previous postbuckling analysis, this new approach adopts VICON analysis and the method developed by Stein (1983; 1985) to enable the coupling of any number of half-wavelengths to represent the variation of in-plane displacements in the longitudinal direction. In this way, in-plane displacements and distributions of strains, curvatures, stress resultants and bending moments for any load condition or material can be captured with the desired level of accuracy.

As described in Chapter 3, VICON can solve buckling analyses for shear loaded and anisotropic plates more accurately than VIPASA by coupling responses with more than one half-wavelength. The new approach utilizes out-of-plane displacements and buckling loads from VICON buckling analyses to calculate in-plane displacements with a series of corresponding half-wavelengths. As in VICON analysis, the plate is assumed to be infinitely long and the modes are assumed to repeat at regular intervals along the longitudinal direction at the node level. Once expressions for the in-plane displacements are obtained, expressions for strains, curvatures, stress resultants and bending moments are calculated using von Kármán large deflection theory. Derivatives with respect to the transverse direction are calculated using finite difference approximations, enabling the in-plane equilibrium equations to be assembled. Finally, different boundary conditions including free edges, fixed edges and straight edges are applied on the longitudinal edges by modifying the in-plane equilibrium equations. Hence a full iteration of postbuckling analysis for a particular end shortening strain stage is solved analytically, see Figure 4.1.

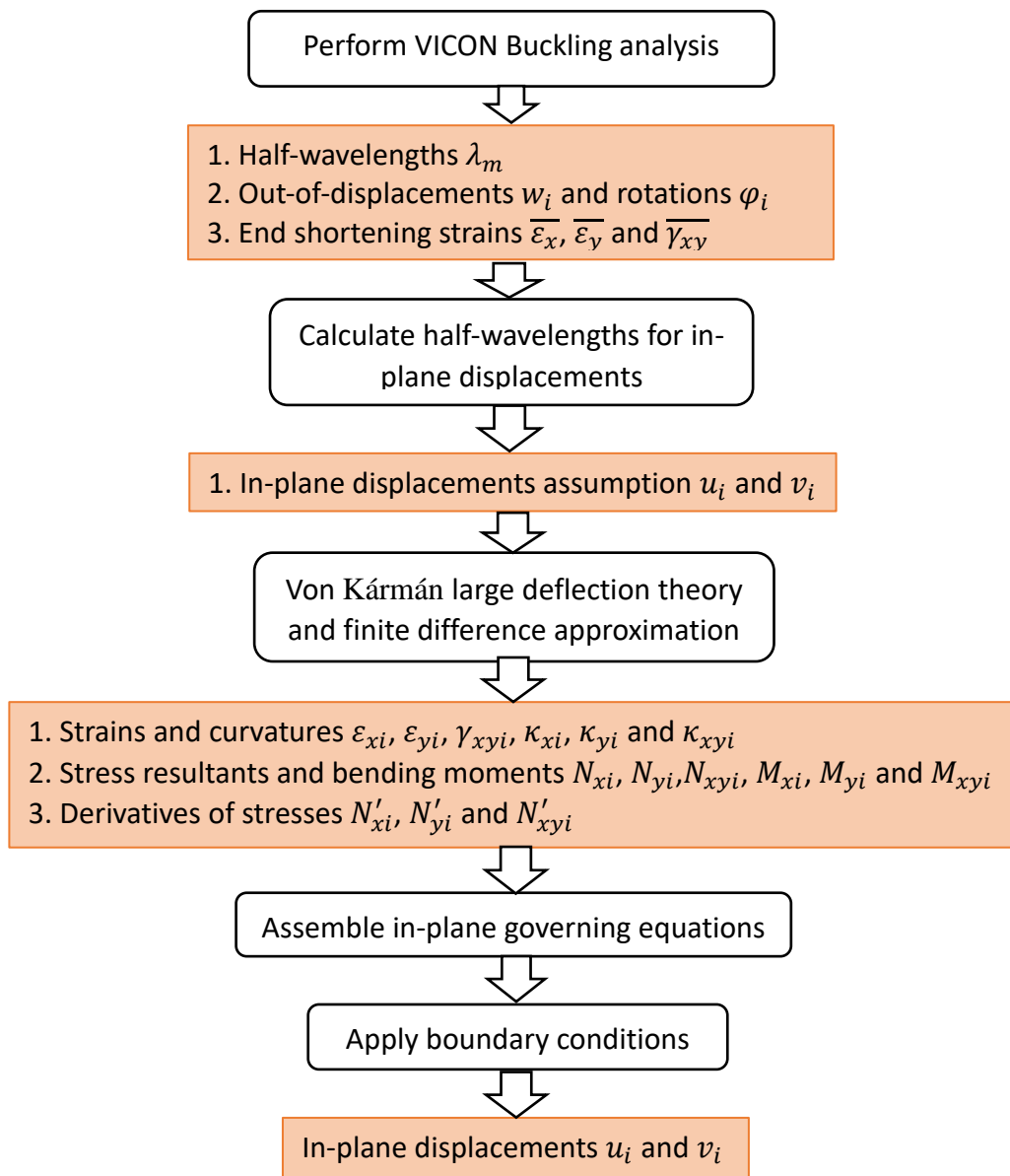


Figure 4.1. Diagram showing the full process for one iteration of postbuckling analysis

The main purpose of this process is to find the in-plane displacements and distributions of in-plane and out-of-plane forces at cycle one along the postbuckling path. It is worth noting that the process shown in Figure 4.1 is only for the first cycle of postbuckling after the critical buckling point. For the following cycles, the displacements are calculated by a Newton type iteration scheme and a corresponding convergence procedure, more detail of which will be presented in Chapter 5.

The following assumptions are made:

1. The series solutions are based on classical plate theory in which transverse shear deformation is assumed to be zero.
2. No imperfections are introduced.
3. The plate is assumed to be infinitely long in the longitudinal direction. The mode shapes repeat regularly in the longitudinal direction in a pattern which can be represented by a series of sinusoidal terms with predefined half-wavelengths.
4. If shear and compression are applied to the plate at the same time, the ratio between compressive end shortening strains and constant shear strains remains unchanged throughout all the postbuckling cycles.

The first assumption is justified when the plate is comparably thin (more detail is described in Chapter 2) and is mostly suitable for thin laminated composites. Having made such an assumption, the von Kármán large deflection theory can be applied and equilibrium equations can be assembled by neglecting higher order derivatives. As displacements along the plate's longitudinal direction vary in a regular pattern, the plates are naturally assumed to be perfectly flat. Hence the modelling in the proposed analysis has to assume the plate without any imperfections. The third assumption is inherited from the VICON analysis, and more detail will be illustrated in Chapter 7. The fourth assumption is based on the nature of CWPAN. More investigation has been presented in Chapter 7.

4.2. Displacement assumptions

Assume the plates are divided into $n-1$ strips with arbitrary width, as identified by the n nodes at the strip edges, as shown in Figure 4.2. At each node i , the out-of-plane deflections w_i and rotations φ_i about the x axis are assumed to vary as the sum of the sinusoidal responses in the longitudinal direction with half-wavelengths λ_m , and can be written in the form

$$\begin{bmatrix} w_i \\ \varphi_i \end{bmatrix} = \begin{bmatrix} \sum_m w_{imc} \cos \frac{\pi x}{\lambda_m} + w_{ims} \sin \frac{\pi x}{\lambda_m} \\ \sum_m \varphi_{imc} \cos \frac{\pi x}{\lambda_m} + \varphi_{ims} \sin \frac{\pi x}{\lambda_m} \end{bmatrix} \quad \dots(4.1)$$

where the amplitudes w_{imc} , w_{ims} , φ_{imc} and φ_{ims} are obtained from a VICON eigenvalue analysis at the previous iteration.

According to classical plate theory, it is assumed that $\varphi_i = w_i'$, where the prime indicates the derivative with respect to the transverse direction y . The subscript m denotes the sequence of out-of-plane half-wavelengths.

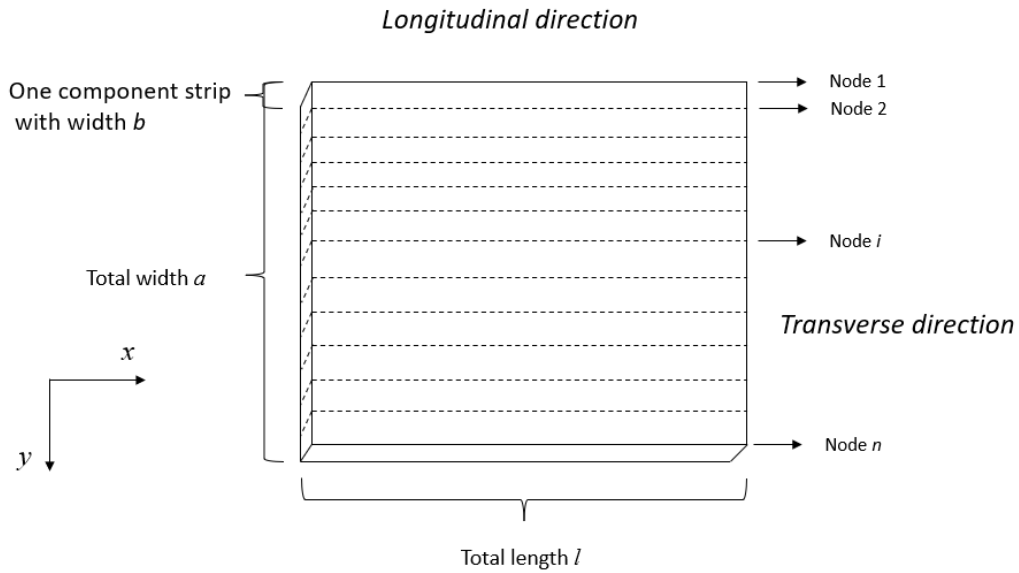


Figure 4.2. An example square plate with width a divided into $n-1$ strips of equal width b , showing the datum and axes used in this thesis

In terms of the in-plane displacements, when applying von Kármán large deflection theory, the calculations for strains and curvatures will lead to squared trigonometric terms which can be simplified to summations or subtractions of out-of-plane trigonometric terms, e.g. $\cos(\alpha) * \cos(\beta) = [\cos(\alpha + \beta) + \cos(\alpha - \beta)]/2$. In-plane displacements, therefore, have to be assumed to have all the terms that could appear in the expressions for strains and stress resultants. A detailed explanation and calculation will be addressed in the Section 4.3.

As described above, the in-plane displacements are assumed to be:

$$\begin{bmatrix} u_i \\ v_i \end{bmatrix} = \begin{bmatrix} \overline{\varepsilon}_x \left(x - \frac{l}{2} \right) + \overline{\gamma}_{xy} \left(y - \frac{a}{2} \right) + \sum_k u_{ikc} \cos \frac{\pi x}{\lambda_k} + u_{iks} \sin \frac{\pi x}{\lambda_k} \\ \overline{\varepsilon}_y \left(y - \frac{a}{2} \right) + \overline{\gamma}_{xy} \left(x - \frac{l}{2} \right) + \sum_k v_{ikc} \cos \frac{\pi x}{\lambda_k} + v_{iks} \sin \frac{\pi x}{\lambda_k} \end{bmatrix} \quad \dots(4.2)$$

where the linear terms $\overline{\varepsilon}_x$, $\overline{\varepsilon}_y$ and $\overline{\gamma}_{xy}$ denote the progressive uniform longitudinal, transverse and shear strains respectively. The subscript k denotes the sequence of in-plane half-wavelengths, subscript c denotes cosine terms and subscript s denotes sine terms. l is the plate length and a is its width.

In contrast to VIPASA postbuckling, CWPAN considers not only compressive loading but also shear loading and combined loading i.e. $\overline{\gamma}_{xy}$ is not zero. It is worth noting that the linear strain terms are pre-defined values based on the end shortening strains at the critical buckling load i.e. the postbuckling analysis is controlled by the ratio of the linear strain increments α , so if the linear strain at initial buckling is $\overline{\varepsilon}_x$, the first postbuckling cycle's linear strain will be $(1 + \alpha)\overline{\varepsilon}_x$. This assumption is very similar to that implemented in the deflection controlled simulation of the finite element method, where the structure is subject to proportional progressive in-plane displacements rather than uniform stresses or concentrated forces. It is actually considered to be closer to the approach taken in experiments in the laboratory where displacements are much easier to control compared to the application of uniform stress resultants. Moreover, in terms of complexity during experiments, running a test under load control leads to the possibility of the test machine to suddenly accelerating if the stiffness reduces in order to try to maintain constant load which can lead to accidents or potentially cause the machine to break, particularly for unstable responses like postbuckling. The term $\overline{\varepsilon}_y$ denotes the transverse end shortening strain resulting from transverse compressive loading. In this thesis, this is considered to be zero. In terms of strain, it should be noted that as we move further into the postbuckling analysis, the ratio between the longitudinal strain and the shear strain will remain the same as the ratio at initial buckling e.g. if the plate is loaded in combined compression in equal amounts ($N_x/N_{xy} = 1$) along the transverse edges, the ratio of end shortening compressive strain and end shortening shear strain for the whole postbuckling analysis will remain the same ($\overline{\varepsilon}_x/\overline{\gamma}_{xy} = 1$).

Postbuckling analysis starts from solutions obtained from a VICON analysis for which the number of half-wavelengths can be any predefined integer. Hence the half-wavelengths for the

out-of-plane deflections naturally become those from the coupled wavelength postbuckling analysis. However increasing the number of wavelengths can affect the calculation speed of the whole postbuckling analysis significantly. Adding one more half-wavelength into the out-of-plane deflection may lead to a doubling of the computational time. Therefore choosing the number of wavelengths can be crucial to balancing the desired accuracy with computational effort. More detailed on this is presented in the factor affecting both the results of the analysis and the computational efficiency Chapter 6.

Another factor affecting both the results of the analysis and the computational efficiency is the number of strips the plates are divided into. This can range from a minimum of five strips to an unlimited number of strips where the minimum is defined by the use of the finite difference approximation. The decision on a suitable number of strips must be made at the beginning of the analysis. More detail on this is presented in the Chapter 6.

4.3. Calculation of strains and derivatives of strains

Based on von Kármán's large deflection theory, strains and curvature at the neutral surface are given by

$$\begin{bmatrix} \varepsilon_{xi} \\ \varepsilon_{yi} \\ \gamma_{xyi} \\ \kappa_{xi} \\ \kappa_{yi} \\ \kappa_{xyi} \end{bmatrix} = \begin{bmatrix} \frac{\partial u_i}{\partial x} + \frac{1}{2} \left(\frac{\partial w_i}{\partial x} \right)^2 \\ \frac{\partial v_i}{\partial y} + \frac{1}{2} \left(\frac{\partial w_i}{\partial y} \right)^2 \\ \frac{\partial u_i}{\partial y} + \frac{\partial v_i}{\partial x} + \frac{\partial w_i}{\partial x} \frac{\partial w_i}{\partial y} \\ -\frac{\partial^2 w_i}{\partial x^2} \\ -\frac{\partial^2 w_i}{\partial y^2} \\ -2 \frac{\partial^2 w_i}{\partial x \partial y} \end{bmatrix} = \begin{bmatrix} \varepsilon_{xi0} & \varepsilon_{xi1c} & \varepsilon_{xi1s} & \dots \\ \varepsilon_{yi0} & \varepsilon_{yi1c} & \varepsilon_{yi1s} & \dots \\ \gamma_{xyi0} & \gamma_{xyi1c} & \gamma_{xyi1s} & \dots \\ \kappa_{xi0} & \kappa_{xi1c} & \kappa_{xi1s} & \dots \\ \kappa_{yi0} & \kappa_{yi1c} & \kappa_{yi1s} & \dots \\ \kappa_{xyi0} & \kappa_{xyi1c} & \kappa_{xyi1s} & \dots \end{bmatrix} \begin{bmatrix} 1 \\ \cos\left(\frac{\pi x}{\lambda_1}\right) \\ \sin\left(\frac{\pi x}{\lambda_1}\right) \\ \cos\left(\frac{\pi x}{\lambda_2}\right) \\ \sin\left(\frac{\pi x}{\lambda_2}\right) \\ \cos\left(\frac{\pi x}{\lambda_3}\right) \\ \sin\left(\frac{\pi x}{\lambda_3}\right) \\ \vdots \end{bmatrix} \quad \dots(4.3)$$

Substituting from Equation 4.2 into Equation 4.3 gives

$$\boldsymbol{\varepsilon}_i = \boldsymbol{\varepsilon}_0(\mathbf{w}_i) + \boldsymbol{\varepsilon}_1 \mathbf{u}_i + \boldsymbol{\varepsilon}_2 * \mathbf{f} * \mathbf{u}_i \quad \dots(4.4)$$

$$\boldsymbol{\kappa}_i = \boldsymbol{\kappa}_0(\mathbf{w}_i) \quad \dots(4.5)$$

$$\mathbf{w}_i = \begin{bmatrix} w_{i1c} \\ w_{i1s} \\ w_{i2c} \\ w_{i2s} \\ \vdots \end{bmatrix}, \mathbf{u}_i = \begin{bmatrix} u_{1,0} \\ u_{1,1c} \\ u_{1,1s} \\ u_{1,2c} \\ \vdots \\ v_{1,0} \\ v_{1,1c} \\ v_{1,1s} \\ v_{1,2c} \\ \vdots \\ u_{2,0} \\ u_{2,1c} \\ u_{2,1s} \\ u_{2,2c} \\ \vdots \\ v_{2,0} \\ v_{2,1c} \\ v_{2,1s} \\ v_{2,2c} \\ \vdots \\ u_{n,0} \\ u_{n,1c} \\ u_{n,1s} \\ u_{n,2c} \\ \vdots \\ v_{n,0} \\ v_{n,1c} \\ v_{n,1s} \\ v_{n,2c} \\ \vdots \end{bmatrix}, \boldsymbol{\varepsilon}_i = \begin{bmatrix} \varepsilon_{x1,0} \\ \varepsilon_{x1,1c} \\ \varepsilon_{x1,1s} \\ \varepsilon_{x1,2c} \\ \vdots \\ \varepsilon_{y1,0} \\ \varepsilon_{y1,1c} \\ \varepsilon_{y1,1s} \\ \varepsilon_{y1,2c} \\ \vdots \\ \gamma_{xy1,0} \\ \gamma_{xy1,1c} \\ \gamma_{xy1,1s} \\ \gamma_{xy1,2c} \\ \vdots \\ \varepsilon_{xn,0} \\ \varepsilon_{xn,1c} \\ \varepsilon_{xn,1s} \\ \varepsilon_{xn,2c} \\ \vdots \\ \varepsilon_{yn,0} \\ \varepsilon_{yn,1c} \\ \varepsilon_{yn,1s} \\ \varepsilon_{yn,2c} \\ \vdots \\ \gamma_{xyn,0} \\ \gamma_{xyn,1c} \\ \gamma_{xyn,1s} \\ \gamma_{xyn,2c} \\ \vdots \end{bmatrix}, \boldsymbol{\kappa}_i = \begin{bmatrix} \kappa_{x1,0} \\ \kappa_{x1,1c} \\ \kappa_{x1,1s} \\ \kappa_{x1,2c} \\ \vdots \\ \kappa_{y1,0} \\ \kappa_{y1,1c} \\ \kappa_{y1,1s} \\ \kappa_{y1,2c} \\ \vdots \\ \kappa_{xy1,0} \\ \kappa_{xy1,1c} \\ \kappa_{xy1,1s} \\ \kappa_{xy1,2c} \\ \vdots \\ \kappa_{xn,0} \\ \kappa_{xn,1c} \\ \kappa_{xn,1s} \\ \kappa_{xn,2c} \\ \vdots \\ \kappa_{yn,0} \\ \kappa_{yn,1c} \\ \kappa_{yn,1s} \\ \kappa_{yn,2c} \\ \vdots \\ \kappa_{xyn,0} \\ \kappa_{xyn,1c} \\ \kappa_{xyn,1s} \\ \kappa_{xyn,2c} \\ \vdots \end{bmatrix} \quad \dots(4.6(a),(b),(c))$$

In Equation 4.4,

$$\overline{\boldsymbol{\varepsilon}}_1 = \begin{bmatrix} \mathbf{J} & \mathbf{0}_{2K-1} \\ \mathbf{0}_{2K-1} & \mathbf{0}_{2K-1} \\ \mathbf{0}_{2K-1} & \mathbf{J} \end{bmatrix}, \overline{\boldsymbol{\varepsilon}}_2 = \begin{bmatrix} \mathbf{0}_{2K-1} & \mathbf{0}_{2K-1} \\ \mathbf{0}_{2K-1} & \mathbf{I}_{2K-1} \\ \mathbf{I}_{2K-1} & \mathbf{0}_{2K-1} \end{bmatrix} \quad \dots(4.7(a), (b))$$

$$\boldsymbol{\varepsilon}_1 = \begin{bmatrix} \overline{\boldsymbol{\varepsilon}}_1 & \mathbf{0}_{3K*2K} & \dots & \mathbf{0}_{3K*2K} \\ \mathbf{0}_{3K*2K} & \overline{\boldsymbol{\varepsilon}}_1 & \dots & \mathbf{0}_{3K*2K} \\ \vdots & \vdots & \ddots & \mathbf{0}_{3K*2K} \\ \mathbf{0}_{3K*2K} & \mathbf{0}_{3K*2K} & \mathbf{0}_{3K*2K} & \overline{\boldsymbol{\varepsilon}}_1 \end{bmatrix}, \quad \dots(4.8(a), (b))$$

$$\boldsymbol{\varepsilon}_2 = \begin{bmatrix} \overline{\boldsymbol{\varepsilon}}_2 & \mathbf{0}_{3K \times 2K} & \dots & \mathbf{0}_{3K \times 2K} \\ \mathbf{0}_{3K \times 2K} & \overline{\boldsymbol{\varepsilon}}_2 & \dots & \mathbf{0}_{3K \times 2K} \\ \vdots & \vdots & \ddots & \mathbf{0}_{3K \times 2K} \\ \mathbf{0}_{3K \times 2K} & \mathbf{0}_{3K \times 2K} & \mathbf{0}_{3K \times 2K} & \overline{\boldsymbol{\varepsilon}}_2 \end{bmatrix}$$

where \mathbf{I}_{2K-1} and $\mathbf{0}_{2K-1}$ are one and zero matrices of order of $2K - 1$, respectively and K is the number of unique values of k found from Tables 4.1 and 4.2.

Where $\mathbf{0}_{3K \times 2K}$ is a zero matrix having the same size as $\overline{\boldsymbol{\varepsilon}}_1$ and $\overline{\boldsymbol{\varepsilon}}_2$ i.e. $3K * 2K$.

$$J = \begin{bmatrix} \lambda_1 \frac{\pi}{l} & 0 & 0 & 0 & 0 & \dots & 0 & 0 \\ 0 & 0 & \lambda_2 \frac{\pi}{l} & 0 & 0 & \dots & 0 & 0 \\ 0 & -\lambda_2 \omega_i & 0 & 0 & 0 & \dots & 0 & 0 \\ 0 & 0 & 0 & 0 & \lambda_3 \frac{\pi}{l} & \dots & 0 & 0 \\ 0 & 0 & 0 & -\lambda_3 \frac{\pi}{l} & 0 & \dots & 0 & 0 \\ \vdots & \vdots & \vdots & \vdots & \vdots & \ddots & 0 & 0 \\ 0 & 0 & 0 & 0 & 0 & 0 & \pi \lambda_k \frac{\pi}{l} & 0 \\ 0 & 0 & 0 & 0 & 0 & 0 & -\lambda_k \frac{\pi}{l} & 0 \end{bmatrix} \quad \dots(4.9)$$

Derivatives with respect to the transverse direction y in the terms ε_{yi} and ε_{xyi} in Equation 4.4 are calculated at target nodes using a finite difference approximation. At node i , the derivative is expressed as the central difference:

$$u_i' = \frac{u_{i+1} - u_{i-1}}{2b} \quad \dots(4.10)$$

This expression works for all nodes where there are adjacent nodes before and after the central node. For the first and last nodes, at which an adjacent node is missing on one side, derivatives are found using the backward difference expression. For the first node:

$$u_i' = u_{i+\frac{b'}{2}} - \frac{1}{2} \left(u_{i+\frac{3b'}{2}} - u_{i+\frac{b'}{2}} \right)$$

$$u_i' = \frac{u_{i+1} - u_i}{b} - \frac{1}{2} \left(\frac{u_{i+2} - u_{i+1}}{b} - \frac{u_{i+1} - u_i}{b} \right) \quad \dots(4.11)$$

$$u_i' = \frac{-3u_i + 4u_{i+1} - u_{i+2}}{2b}$$

Similarly for the last node

$$u_i' = \frac{3u_i - 4u_{i-1} + u_{i-2}}{2b} \quad \dots(4.12)$$

Applying Equations 4.10 to 4.12 with von Kármán large deflection theory gives:

$f =$

$$\frac{1}{2b} \begin{bmatrix} -3 * I_{2K*2K} & 4 * I_{2K*2K} & -I_{2K*2K} & \mathbf{0}_{2K*2K} & \mathbf{0}_{2K*2K} & \dots & \mathbf{0}_{2K*2K} \\ I_{2K*2K} & \mathbf{0}_{2K*2K} & -I_{2K*2K} & \mathbf{0}_{2K*2K} & \mathbf{0}_{2K*2K} & \dots & \mathbf{0}_{2K*2K} \\ \mathbf{0}_{2K*2K} & I_{2K*2K} & \mathbf{0}_{2K*2K} & -I_{2K*2K} & \mathbf{0}_{2K*2K} & \dots & \mathbf{0}_{2K*2K} \\ \mathbf{0}_{2K*2K} & \mathbf{0}_{2K*2K} & I_{2K*2K} & \mathbf{0}_{2K*2K} & -I_{2K*2K} & \dots & \mathbf{0}_{2K*2K} \\ \mathbf{0}_{2K*2K} & \mathbf{0}_{2K*2K} & \mathbf{0}_{2K*2K} & I_{2K*2K} & \mathbf{0}_{2K*2K} & \dots & \mathbf{0}_{2K*2K} \\ \vdots & \vdots & \vdots & \vdots & \vdots & \ddots & \mathbf{0}_{2K*2K} \\ \mathbf{0}_{2K*2K} & \mathbf{0}_{2K*2K} & \mathbf{0}_{2K*2K} & \mathbf{0}_{2K*2K} & \mathbf{0}_{2K*2K} & I_{2K*2K} & \mathbf{0}_{2K*2K} \\ \mathbf{0}_{2K*2K} & \mathbf{0}_{2K*2K} & \mathbf{0}_{2K*2K} & \mathbf{0}_{2K*2K} & \mathbf{0}_{2K*2K} & -I_{2K*2K} & 4 * I_{2K*2K} \end{bmatrix} \quad \dots(4.13)$$

where f denotes the first order finite difference approximation matrix and I_{2K*2K} and $\mathbf{0}_{2K*2K}$ denote the identity matrix and a zero matrix of size $2K * 2K$ respectively.

The vectors $\boldsymbol{\varepsilon}_0(\mathbf{w}_i)$ and $\boldsymbol{\kappa}_0(\mathbf{w}_i)$ are functions of the out-of-displacements w which can be obtained by substituting w into von Kármán large deflection theory. These displacements are obtained by the modified Newton iteration scheme and can be considered as constant values when solving the in-plane equilibrium equations.

The vector $\boldsymbol{\varepsilon}_0(\mathbf{w}_i)$ in Equation 4.4 can be written $\begin{bmatrix} \boldsymbol{\varepsilon}_{0x}(\mathbf{w}_i) \\ \boldsymbol{\varepsilon}_{0y}(\mathbf{w}_i) \\ \boldsymbol{\varepsilon}_{0xy}(\mathbf{w}_i) \end{bmatrix}$, where

$$\begin{aligned} \epsilon_{0x}(\mathbf{w}_i) &= \frac{1}{2} \left(\frac{\partial w}{\partial x} \right)^2 = \\ & \frac{1}{2} \sum_m \sum_n \left(\begin{array}{l} -w_{imc} w_{inc} \frac{\pi^2}{\lambda_m \lambda_n} \sin \left(\frac{\pi x}{\lambda_m} \right) \sin \left(\frac{\pi x}{\lambda_n} \right) \\ + w_{ims} w_{ins} \frac{\pi^2}{\lambda_m \lambda_n} \cos \left(\frac{\pi x}{\lambda_m} \right) \cos \left(\frac{\pi x}{\lambda_n} \right) \\ - w_{imc} w_{ins} \frac{\pi^2}{\lambda_m \lambda_n} \sin \left(\frac{\pi x}{\lambda_m} \right) \cos \left(\frac{\pi x}{\lambda_n} \right) \\ - w_{ims} w_{inc} \frac{\pi^2}{\lambda_m \lambda_n} \cos \left(\frac{\pi x}{\lambda_m} \right) \sin \left(\frac{\pi x}{\lambda_n} \right) \end{array} \right) \end{aligned} \quad \dots(4.14)$$

$$\begin{aligned} \epsilon_{0y}(\mathbf{w}_i) &= \frac{1}{2} \left(\frac{\partial w}{\partial y} \right)^2 = \\ & \frac{1}{2} \sum_m \sum_n \left(\begin{array}{l} \varphi_{imc} \varphi_{inc} \frac{\pi^2}{\lambda_m \lambda_n} \cos \left(\frac{\pi x}{\lambda_m} \right) \cos \left(\frac{\pi x}{\lambda_n} \right) \\ + \varphi_{ims} \varphi_{ins} \frac{\pi^2}{\lambda_m \lambda_n} \sin \left(\frac{\pi x}{\lambda_m} \right) \sin \left(\frac{\pi x}{\lambda_n} \right) \\ + \varphi_{imc} \varphi_{ins} \frac{\pi^2}{\lambda_m \lambda_n} \cos \left(\frac{\pi x}{\lambda_m} \right) \sin \left(\frac{\pi x}{\lambda_n} \right) \\ + \varphi_{ims} \varphi_{inc} \frac{\pi^2}{\lambda_m \lambda_n} \sin \left(\frac{\pi x}{\lambda_m} \right) \cos \left(\frac{\pi x}{\lambda_n} \right) \end{array} \right) \end{aligned} \quad \dots(4.15)$$

$$\begin{aligned} \epsilon_{0xy}(\mathbf{w}_i) &= \frac{\partial w}{\partial x} \cdot \frac{\partial w}{\partial y} = \\ & \sum_m \sum_n \frac{\pi}{\lambda_m} \left(\begin{array}{l} w_{ims} \varphi_{inc} \frac{\pi^2}{\lambda_m \lambda_n} \cos \left(\frac{\pi x}{\lambda_m} \right) \cos \left(\frac{\pi x}{\lambda_n} \right) \\ - w_{imc} \varphi_{inc} \frac{\pi^2}{\lambda_m \lambda_n} \sin \left(\frac{\pi x}{\lambda_m} \right) \cos \left(\frac{\pi x}{\lambda_n} \right) \\ + w_{ims} \varphi_{ins} \frac{\pi^2}{\lambda_m \lambda_n} \cos \left(\frac{\pi x}{\lambda_m} \right) \sin \left(\frac{\pi x}{\lambda_n} \right) \\ - w_{imc} \varphi_{ins} \frac{\pi^2}{\lambda_m \lambda_n} \sin \left(\frac{\pi x}{\lambda_m} \right) \sin \left(\frac{\pi x}{\lambda_n} \right) \end{array} \right) \end{aligned} \quad \dots(4.16)$$

Substituting $\lambda_m = l/m$, $\lambda_n = l/n$ into Equations (4.14)-(4.16) and simplifying,

$$\begin{aligned} \boldsymbol{\varepsilon}_{0x}(\mathbf{w}_i) = & \\ & \frac{\pi^2}{4l^2} \sum_m \sum_n mn \begin{pmatrix} (w_{imc}w_{inc} + w_{ims}w_{ins})\cos[(m-n)\frac{\pi x}{l}] \\ +(w_{ims}w_{ins} - w_{imc}w_{inc})\cos[(m+n)\frac{\pi x}{l}] \\ +(-w_{ims}w_{inc} - w_{imc}w_{ins})\sin[(m+n)\frac{\pi x}{l}] \\ +(-w_{imc}w_{inc} + w_{ims}w_{ins})\sin[(m-n)\frac{\pi x}{l}] \end{pmatrix} \end{aligned} \quad \dots(4.17)$$

$$\boldsymbol{\varepsilon}_{0y}(\mathbf{w}_i) = \frac{1}{4} \sum_m \sum_n \begin{pmatrix} (\varphi_{imc}\varphi_{inc} + \varphi_{ims}\varphi_{ins})\cos[(m-n)\frac{\pi x}{l}] \\ +(\varphi_{imc}\varphi_{inc} - \varphi_{ims}\varphi_{ins})\cos[(m+n)\frac{\pi x}{l}] \\ +(\varphi_{ims}\varphi_{inc} - \varphi_{imc}\varphi_{ins})\sin[(m-n)\frac{\pi x}{l}] \\ +(\varphi_{imc}\varphi_{ins} + \varphi_{ims}\varphi_{inc})\sin[(m+n)\frac{\pi x}{l}] \end{pmatrix} \quad \dots(4.18)$$

$$\boldsymbol{\varepsilon}_{0xy}(\mathbf{w}_i) = \frac{\pi}{2l} \sum_m \sum_n m \begin{pmatrix} (w_{imc}\varphi_{inc} + w_{ims}\varphi_{ins})\cos[(m-n)\frac{\pi x}{l}] \\ +(w_{ims}\varphi_{inc} - w_{imc}\varphi_{ins})\cos[(m+n)\frac{\pi x}{l}] \\ +(-w_{imc}\varphi_{inc} + w_{ims}\varphi_{ins})\sin[(m+n)\frac{\pi x}{l}] \\ +(-w_{imc}\varphi_{inc} + w_{ims}\varphi_{ins})\sin[(m-n)\frac{\pi x}{l}] \end{pmatrix} \quad \dots(4.19)$$

Here c and s denote the cosine and sin components respectively. The values of $(m-n)$ and $(m+n)$ define the number of in-plane half-wavelengths λ_m to be used, which are generalized from summations and subtractions of the out-of-plane wavelength terms. For example, if $\xi = 1$ and $q = 2$ in Equation 3.12, the out-of-plane half-wavelengths are $\lambda_m=l/m$, $m=(1,3,5)$ and the summations and subtractions are shown in Tables 4.1 and 4.2, respectively.

Considering the unique values in Tables 4.1 and 4.2, the half-wavelengths for the in-plane displacements will be $\lambda_j = l/k_j$, $\mathbf{k} = (0,1,2,3,4,5,6,8,10)$. When $(m-n) = 0$, i.e. the half-wavelength $\lambda_j = \infty$, its cosine term is a constant term while its sine term is zero and is omitted from the analysis.

<i>Summations</i>	$n=1$	$n=3$	$n=5$
$m=1$	2	4	6
$m=3$	4	6	8
$m=5$	6	8	10

Table 4.1. Summations of half-wavelengths l/m and l/n , $m, n = (1,3,5)$

<i>Subtractions</i>	$n=1$	$n=3$	$n=5$
$m=1$	0	-2	-4
$m=3$	2	0	-2
$m=5$	4	2	0

Table 4.2. Subtractions of half-wavelengths l/m and l/n , $m, n = (1,3,5)$

The vector $\boldsymbol{\kappa}_0(\mathbf{w}_i)$ in Equation 4.5 can be written $\begin{bmatrix} \boldsymbol{\kappa}_{0x}(\mathbf{w}_i) \\ \boldsymbol{\kappa}_{0y}(\mathbf{w}_i) \\ \boldsymbol{\kappa}_{0xy}(\mathbf{w}_i) \end{bmatrix}$, where

$$\boldsymbol{\kappa}_{0x}(\mathbf{w}_i) = -\frac{\partial^2 w_i}{\partial x^2} = \sum_m \frac{\pi^2}{\lambda^2} (w_{imc} \cos \frac{m\pi x}{l} + w_{ims} \sin \frac{m\pi x}{l}) \quad \dots(4.20)$$

$$\boldsymbol{\kappa}_{0y}(\mathbf{w}_i) = -\frac{\partial^2 w_i}{\partial y^2} = \sum_m (\varphi'_{imc} \cos \frac{m\pi x}{l} + \varphi'_{ims} \sin \frac{m\pi x}{l}) \quad \dots(4.21)$$

$$\boldsymbol{\kappa}_{0xy}(\mathbf{w}_i) = -2 \frac{\partial^2 w_i}{\partial x \partial y} = \sum_m 2 \frac{\pi}{\lambda} (\varphi_{imc} \sin \frac{m\pi x}{l} + \varphi_{ims} \cos \frac{m\pi x}{l}) \quad \dots(4.22)$$

An analogous procedure can be used to find the curvatures $\boldsymbol{\kappa}_i$ as shown in Equations 4.20-4.22. Observing Equations 4.5, 4.20-4.22, curvatures $\boldsymbol{\kappa}_i$ are functions only of out-of-plane deflection w which is equivalent to $\boldsymbol{\varepsilon}_0(\mathbf{w}_i)$. Their calculation therefore only requires the half-wavelengths for out-of-plane displacement which are pre-defined in VICON. Therefore the half-wavelengths for the in-plane displacement are considered as pre-defined for the whole postbuckling analysis.

If $\lambda_m = l/m$, $m = [1]$, i.e. the plate is assumed to vary with one single sinusoidal term along the longitudinal direction, the half-wavelengths for the in-plane variations are, based on the above calculation procedure, (0, 1, 2). This is the assumption made for the previous ‘Improved exact strip method’ (Che, 2010; Zhang 2018) for in-plane displacements. Therefore, the improved exact strip method can be considered as a special case in CWPAN which is appropriate when the plate is loaded only in compression and is made from isotropic material.

The following calculations for the derivatives with respect to y of strains and curvatures will be involved in the equilibrium equations that will be described in the next chapter. These derivatives can be directly calculated from Equations 4.17-4.19 and Equations 4.20-4.22.

$$\varepsilon_{0x}(\mathbf{w}_i) = \frac{\pi^2}{4l^2} \sum_m \sum_n mn * \begin{pmatrix} (\varphi_{imc}w_{inc} + w_{imc}\varphi_{inc} + \varphi_{ims}w_{ins} + w_{ims}\varphi_{ins})\cos[(m-n)\frac{\pi x}{l}] \\ +(\varphi_{ims}w_{ins} + w_{ims}\varphi_{ins} - \varphi_{imc}w_{inc} + w_{imc}\varphi_{inc})\cos[(m+n)\frac{\pi x}{l}] \\ +(-\varphi_{ims}w_{inc} - w_{ims}\varphi_{inc} - \varphi_{imc}w_{ins} - w_{imc}\varphi_{ins})\sin[(m+n)\frac{\pi x}{l}] \\ +(-\varphi_{imc}w_{inc} - w_{imc}\varphi_{inc} + \varphi_{ims}w_{ins} + w_{ims}\varphi_{ins})\sin[(m-n)\frac{\pi x}{l}] \end{pmatrix} \quad \dots(4.23)$$

$$\varepsilon_{0x}(\mathbf{w}_i) = \frac{1}{4} \sum_m \sum_n \begin{pmatrix} (\varphi'_{imc}\varphi_{inc} + \varphi_{imc}\varphi'_{inc} + \varphi'_{ims}\varphi_{ins} + \varphi_{ims}\varphi'_{ins})\cos[(m-n)\frac{\pi x}{l}] \\ +(\varphi'_{imc}\varphi_{inc} + \varphi_{imc}\varphi'_{inc} - \varphi'_{ims}\varphi_{ins} - \varphi_{ims}\varphi'_{ins})\cos[(m+n)\frac{\pi x}{l}] \\ +(\varphi'_{ims}\varphi_{inc} + \varphi_{ims}\varphi'_{inc} - \varphi'_{imc}\varphi_{ins} - \varphi_{imc}\varphi'_{ins})\sin[(m-n)\frac{\pi x}{l}] \\ +(\varphi'_{imc}\varphi_{ins} + \varphi_{imc}\varphi'_{ins} + \varphi'_{ims}\varphi_{inc} + \varphi_{ims}\varphi'_{inc})\sin[(m+n)\frac{\pi x}{l}] \end{pmatrix} \quad \dots(4.24)$$

$$\varepsilon_{0xy}(\mathbf{w}_i) = \frac{\pi}{4l} \sum_m \sum_n m \left(\begin{array}{l} (\varphi_{imc}\varphi_{inc} + w_{imc}\varphi'_{inc} + \varphi_{ims}\varphi_{ins} + w_{ims}\varphi'_{ins})\cos[(m-n)\frac{\pi x}{l}] \\ +(\varphi_{ims}\varphi_{inc} + w_{ims}\varphi'_{inc} - \varphi_{imc}\varphi_{ins} - w_{imc}\varphi'_{ins})\cos[(m+n)\frac{\pi x}{l}] \\ +(-\varphi_{imc}\varphi_{inc} - w_{imc}\varphi'_{inc} + \varphi_{ims}\varphi_{ins} + w_{ims}\varphi'_{ins})\sin[(m+n)\frac{\pi x}{l}] \\ +(-\varphi_{imc}\varphi_{inc} - w_{imc}\varphi'_{inc} + \varphi_{ims}\varphi_{ins} + w_{ims}\varphi'_{ins})\sin[(m-n)\frac{\pi x}{l}] \end{array} \right) \quad \dots(4.25)$$

$$\kappa'_{0x}(\mathbf{w}_i) = \sum_m \frac{\pi^2}{\lambda^2} (\varphi_{imc}\cos\frac{m\pi x}{l} + \varphi_{ims}\sin\frac{m\pi x}{l}) \quad \dots(4.26)$$

$$\kappa'_{0y}(\mathbf{w}_i) = \sum_m (\varphi''_{imc}\cos\frac{m\pi x}{l} + \varphi''_{ims}\sin\frac{m\pi x}{l}) \quad \dots(4.27)$$

$$\kappa'_{0xy}(\mathbf{w}_i) = \sum_m 2\frac{\pi}{\lambda} (\varphi'_{imc}\sin\frac{m\pi x}{l} + \varphi'_{ims}\cos\frac{m\pi x}{l}) \quad \dots(4.28)$$

where φ'_{imc} , φ'_{inc} and φ''_{imc} , φ''_{inc} are calculated by multiplying φ by the first and second order of finite difference approximations.

4.4. Calculation of stresses and derivatives of stresses

The stress resultants N_{xi} , N_{yi} , N_{xyi} and bending moment M_{xi} , M_{yi} , M_{xyi} are needed for the equilibrium equations and final analysis

$$\begin{bmatrix} N_{xi} \\ N_{yi} \\ N_{xyi} \\ M_{xi} \\ M_{yi} \\ M_{xyi} \end{bmatrix} = \begin{bmatrix} A_{i11} & A_{i12} & A_{i16} & B_{i11} & B_{i12} & B_{i16} \\ A_{i12} & A_{i22} & A_{i26} & B_{i12} & B_{i22} & B_{i26} \\ A_{i16} & A_{i26} & A_{i66} & B_{i16} & B_{i26} & B_{i66} \\ B_{i11} & B_{i12} & B_{i16} & D_{i11} & D_{i12} & D_{i16} \\ B_{i12} & B_{i22} & B_{i26} & D_{i12} & D_{i22} & D_{i26} \\ B_{i16} & B_{i26} & B_{i66} & D_{i16} & D_{i26} & D_{i66} \end{bmatrix} \begin{bmatrix} \varepsilon_{xi} \\ \varepsilon_{yi} \\ \varepsilon_{xyi} \\ \kappa_{xi} \\ \kappa_{yi} \\ \kappa_{xyi} \end{bmatrix} \quad \dots(4.29)$$

Substituting Equation 4.29 into Equations 4.4 and 4.5 gives

$$\mathbf{N}_i = \mathbf{A} * [\boldsymbol{\varepsilon}_0(\mathbf{w}_i) + \boldsymbol{\varepsilon}_1 \mathbf{u}_i + \boldsymbol{\varepsilon}_2 * \mathbf{f} * \mathbf{u}_i] + \mathbf{B} * \boldsymbol{\kappa}_0(\mathbf{w}_i) \quad \dots(4.30)$$

$$\mathbf{M}_i = \mathbf{B} * [\boldsymbol{\varepsilon}_0(\mathbf{w}_i) + \boldsymbol{\varepsilon}_1 \mathbf{u}_i + \boldsymbol{\varepsilon}_2 * \mathbf{f} * \mathbf{u}_i] + \mathbf{D} * \boldsymbol{\kappa}_0(\mathbf{w}_i) \quad \dots(4.31)$$

where

$$\mathbf{N}_i = \begin{bmatrix} N_{x1,0} \\ N_{x1,1c} \\ N_{x1,1s} \\ N_{x1,2c} \\ \vdots \\ N_{y1,0} \\ N_{y1,1c} \\ N_{y1,1s} \\ N_{y1,2c} \\ \vdots \\ N_{xy1,0} \\ N_{xy1,1c} \\ N_{xy1,1s} \\ N_{xy1,2c} \\ \vdots \\ N_{xn,0} \\ N_{xn,1c} \\ N_{xn,1s} \\ N_{xn,2c} \\ \vdots \\ N_{yn,0} \\ N_{yn,1c} \\ N_{yn,1s} \\ N_{yn,2c} \\ \vdots \\ N_{xyn,0} \\ N_{xyn,1c} \\ N_{xyn,1s} \\ N_{xyn,2c} \\ \vdots \end{bmatrix}, \quad \mathbf{M}_i = \begin{bmatrix} M_{x1,0} \\ M_{x1,1c} \\ M_{x1,1s} \\ M_{x1,2c} \\ \vdots \\ M_{y1,0} \\ M_{y1,1c} \\ M_{y1,1s} \\ M_{y1,2c} \\ \vdots \\ M_{xy1,0} \\ M_{xy1,1c} \\ M_{xy1,1s} \\ M_{xy1,2c} \\ \vdots \\ M_{xn,0} \\ M_{xn,1c} \\ M_{xn,1s} \\ M_{xn,2c} \\ \vdots \\ M_{yn,0} \\ M_{yn,1c} \\ M_{yn,1s} \\ M_{yn,2c} \\ \vdots \\ M_{xyn,0} \\ M_{xyn,1c} \\ M_{xyn,1s} \\ M_{xyn,2c} \\ \vdots \end{bmatrix} \quad \dots(4.32(a),(b))$$

$$\bar{\mathbf{A}} = \begin{bmatrix} A_{11} * \mathbf{0}_{2K-1*2K-1} & A_{12} * \mathbf{0}_{2K-1*2K-1} & A_{16} * \mathbf{0}_{2K-1*2K-1} \\ A_{21} * \mathbf{0}_{2K-1*2K-1} & A_{22} * \mathbf{0}_{2K-1*2K-1} & A_{26} * \mathbf{0}_{2K-1*2K-1} \\ A_{61} * \mathbf{0}_{2K-1*2K-1} & A_{62} * \mathbf{0}_{2K-1*2K-1} & A_{66} * \mathbf{0}_{2K-1*2K-1} \end{bmatrix}, \quad \dots(4.33(a),(b))$$

$$\mathbf{A} = \begin{bmatrix} \bar{\mathbf{A}} & \mathbf{0}_{6K-3*6K-3} & \dots & \mathbf{0}_{6K-3*6K-3} \\ \mathbf{0}_{6K-3*6K-3} & \bar{\mathbf{A}} & \dots & \mathbf{0}_{6K-3*6K-3} \\ \vdots & \vdots & \ddots & \mathbf{0}_{6K-3*6K-3} \\ \mathbf{0}_{6K-3*6K-3} & \mathbf{0}_{6K-3*6K-3} & \mathbf{0}_{6K-3*6K-3} & \bar{\mathbf{A}} \end{bmatrix}$$

where $\mathbf{0}_{6K-3*6K-3}$ is a zero matrix with the same size as $\bar{\mathbf{A}}$

Similarly

$$\bar{\mathbf{B}} = \begin{bmatrix} B_{11} * \mathbf{0}_{2K-1*2K-1} & B_{12} * \mathbf{0}_{2K-1*2K-1} & B_{16} * \mathbf{0}_{2K-1*2K-1} \\ B_{21} * \mathbf{0}_{2K-1*2K-1} & B_{22} * \mathbf{0}_{2K-1*2K-1} & B_{26} * \mathbf{0}_{2K-1*2K-1} \\ B_{61} * \mathbf{0}_{2K-1*2K-1} & B_{62} * \mathbf{0}_{2K-1*2K-1} & B_{66} * \mathbf{0}_{2K-1*2K-1} \end{bmatrix},$$

...(4.34(a),(b))

$$\mathbf{B} = \begin{bmatrix} \bar{\mathbf{B}} & \mathbf{0}_{6K-3*6K-3} & \dots & \mathbf{0}_{6K-3*6K-3} \\ \mathbf{0}_{6K-3*6K-3} & \bar{\mathbf{B}} & \dots & \mathbf{0}_{6K-3*6K-3} \\ \vdots & \vdots & \ddots & \mathbf{0}_{6K-3*6K-3} \\ \mathbf{0}_{6K-3*6K-3} & \mathbf{0}_{6K-3*6K-3} & \mathbf{0}_{6K-3*6K-3} & \bar{\mathbf{B}} \end{bmatrix}$$

$$\bar{\mathbf{D}} = \begin{bmatrix} D_{11} * \mathbf{0}_{2K-1*2K-1} & D_{12} * \mathbf{0}_{2K-1*2K-1} & D_{16} * \mathbf{0}_{2K-1*2K-1} \\ D_{21} * \mathbf{0}_{2K-1*2K-1} & D_{22} * \mathbf{0}_{2K-1*2K-1} & D_{26} * \mathbf{0}_{2K-1*2K-1} \\ D_{61} * \mathbf{0}_{2K-1*2K-1} & D_{62} * \mathbf{0}_{2K-1*2K-1} & D_{66} * \mathbf{0}_{2K-1*2K-1} \end{bmatrix},$$

...(4.35(a),(b))

$$\mathbf{D} = \begin{bmatrix} \bar{\mathbf{D}} & \mathbf{0}_{6K-3*6K-3} & \dots & \mathbf{0}_{6K-3*6K-3} \\ \mathbf{0}_{6K-3*6K-3} & \bar{\mathbf{D}} & \dots & \mathbf{0}_{6K-3*6K-3} \\ \vdots & \vdots & \ddots & \mathbf{0}_{6K-3*6K-3} \\ \mathbf{0}_{6K-3*6K-3} & \mathbf{0}_{6K-3*6K-3} & \mathbf{0}_{6K-3*6K-3} & \bar{\mathbf{D}} \end{bmatrix}$$

The derivatives of the stress resultants are given by

$$\mathbf{N}'_i = \mathbf{A} * [\boldsymbol{\varepsilon}'_0(\mathbf{w}_i) + \boldsymbol{\varepsilon}_1 * \mathbf{f} * \mathbf{u}_i + \boldsymbol{\varepsilon}_2 * \mathbf{s} * \mathbf{u}_i] + \mathbf{B} * \boldsymbol{\kappa}'_0(\mathbf{w}_i) \quad \dots(4.36)$$

where

$$\mathbf{N}'_i = \begin{bmatrix} N_{x1,0}' \\ N_{x1,1c}' \\ N_{x1,1s}' \\ N_{x1,2c}' \\ \vdots \\ N_{y1,0}' \\ N_{y1,1c}' \\ N_{y1,1s}' \\ N_{y1,2c}' \\ \vdots \\ N_{xy1,0}' \\ N_{xy1,1c}' \\ N_{xy1,1s}' \\ N_{xy1,2c}' \\ \vdots \\ N_{xn,0}' \\ N_{xn,1c}' \\ N_{xn,1s}' \\ N_{xn,2c}' \\ \vdots \\ N_{yn,0}' \\ N_{yn,1c}' \\ N_{yn,1s}' \\ N_{yn,2c}' \\ \vdots \\ N_{xyn,0}' \\ N_{xyn,1c}' \\ N_{xyn,1s}' \\ N_{xyn,2c}' \\ \vdots \end{bmatrix} \quad \dots(4.37)$$

s is the matrix of second order finite differences

$\mathbf{s} =$

$$= \frac{1}{b^2} \begin{bmatrix} 2 * I_{2K*2K} & -5 * I_{2K*2K} & 4 * I_{2K*2K} & -I_{2K*2K} & \mathbf{0}_{2K*2K} & \dots \\ I_{2K*2K} & -2 * I_{2K*2K} & -I_{2K*2K} & \mathbf{0}_{2K*2K} & \mathbf{0}_{2K*2K} & \dots \\ \mathbf{0}_{2K*2K} & I_{2K*2K} & -2 * I_{2K*2K} & -I_{2K*2K} & \mathbf{0}_{2K*2K} & \dots \\ \mathbf{0}_{2K*2K} & \mathbf{0}_{2K*2K} & I_{2K*2K} & -2 * I_{2K*2K} & -I_{2K*2K} & \dots \\ \mathbf{0}_{2K*2K} & \mathbf{0}_{2K*2K} & \mathbf{0}_{2K*2K} & I_{2K*2K} & -2 * I_{2K*2K} & \dots \\ \vdots & \vdots & \vdots & \vdots & \vdots & \ddots \\ \mathbf{0}_{2K*2K} & \mathbf{0}_{2K*2K} & \mathbf{0}_{2K*2K} & \mathbf{0}_{2K*2K} & \mathbf{0}_{2K*2K} & I_{2K*2K} \\ \mathbf{0}_{2K*2K} & \mathbf{0}_{2K*2K} & \mathbf{0}_{2K*2K} & \mathbf{0}_{2K*2K} & -I_{2K*2K} & 4 * I_{2K*2K} \end{bmatrix} \dots(4.38)$$

$$\begin{bmatrix} \mathbf{0}_{2K*2K} & \mathbf{0}_{2K*2K} \\ -2 * I_{2K*2K} & -1 * I_{2K*2K} \\ -5 * I_{2K*2K} & 2 * I_{2K*2K} \end{bmatrix}$$

This matrix is obtained by differentiation of Equation 4.10 at node i . Similar to the previous differentiations the middle nodes are given by

$$u_i'' = \frac{u_{i+\frac{b}{2}}' - u_{i-\frac{b}{2}}'}{b}$$

$$u_i'' = \frac{\frac{u_{i+1} - u_i}{b} - \frac{u_i - u_{i-1}}{b}}{b} \dots(4.39)$$

$$u_i'' = \frac{u_{i+1} - 2u_i + u_{i-1}}{b^2}$$

For the first node

$$u_i'' = u_{i+1}'' - (u_{i+2}'' - u_{i+1}'')$$

$$u_i'' = 2u_{i+1}'' - u_{i+2}'' \dots(4.40)$$

$$u_i'' = \frac{2u_i - 5u_{i+1} + 4u_{i+2} - u_{i+3}}{b^2}$$

And for the last node:

$$u_i'' = \frac{-u_{i-3} + 4u_{i-2} - 5u_{i-1} + 2u_i}{b^2} \quad \dots(4.41)$$

Finite difference approximation is a numerical technique that is widely used for solving differential equations in modern numerical analysis. It aims to find the derivatives at discrete points based on finite difference and the values from adjacent points. It is proven to be reliable in solving complex differential equations for buckling and postbuckling analysis (Groosmann et.al. 2007). However the accuracy of the finite difference approximation depends largely on the distance between neighbouring nodes (b) (Liszka and Orkisz, 1980). It can be seen from the above equations that decreasing the distance can lead to a better accuracy, especially for the second derivative which has a quadratic relation with b^2 . On the contrary, increasing the spacing can lead to less accurate solutions. The number of nodes and therefore the width of the strips b is another predefined value for the whole of the postbuckling analysis, increases or decreases to which can affect the accuracy and computational efficiency of the calculation significantly. More investigation and discussion on the effect of changes to the number of nodes and the width of the strips is presented Chapter 6.

4.5. Equilibrium equations

According to classical plate theory the equilibrium equations at the neutral surface are written as

$$\frac{\partial N_{yi}}{\partial y} + \frac{\partial N_{xyi}}{\partial x} = 0 \quad \dots(4.42)$$

$$\frac{\partial N_{xyi}}{\partial y} + \frac{\partial N_{xi}}{\partial x} = 0 \quad \dots(4.43)$$

which can be simplified in matrix form as

$$\mathbf{T} * \mathbf{N}'_i + \mathbf{R} * \mathbf{N}_i = 0 \quad \dots(4.44)$$

where

$$\bar{\mathbf{T}} = \begin{bmatrix} \mathbf{0}_{2K-1*2K-1} & \mathbf{0}_{2K-1*2K-1} & \mathbf{I}_{2K-1*2K-1} \\ \mathbf{0}_{2K-1*2K-1} & \mathbf{I}_{2K-1*2K-1} & \mathbf{0}_{2K-1*2K-1} \end{bmatrix},$$

$$\bar{\mathbf{R}} = \begin{bmatrix} \mathbf{J} & \mathbf{0}_{2K-1} & \mathbf{0}_{2K-1} \\ \mathbf{0}_{2K-1} & \mathbf{0}_{2K-1} & \mathbf{J} \end{bmatrix}$$

$$\mathbf{T} = \begin{bmatrix} \bar{\mathbf{T}} & \mathbf{0}_{3K*2K} & \dots & \mathbf{0}_{3K*2K} \\ \mathbf{0}_{3K*2K} & \bar{\mathbf{T}} & \dots & \mathbf{0}_{3K*2K} \\ \vdots & \vdots & \ddots & \mathbf{0}_{3K*2K} \\ \mathbf{0}_{3K*2K} & \mathbf{0}_{3K*2K} & \mathbf{0}_{3K*2K} & \bar{\mathbf{T}} \end{bmatrix}, \quad \dots(4.45(a),(b),(c),(d))$$

$$\mathbf{R} = \begin{bmatrix} \bar{\mathbf{R}} & \mathbf{0}_{3K*2K} & \dots & \mathbf{0}_{3K*2K} \\ \mathbf{0}_{3K*2K} & \bar{\mathbf{R}} & \dots & \mathbf{0}_{3K*2K} \\ \vdots & \vdots & \ddots & \mathbf{0}_{3K*2K} \\ \mathbf{0}_{3K*2K} & \mathbf{0}_{3K*2K} & \mathbf{0}_{3K*2K} & \bar{\mathbf{R}} \end{bmatrix}$$

Substituting Equations 4.30 and 4.36 into Equation 4.44,

$$\begin{aligned} & \mathbf{T} * \mathbf{A} * [\boldsymbol{\varepsilon}_1 * \mathbf{f} * \mathbf{u}_i + \boldsymbol{\varepsilon}_2 * \mathbf{s} * \mathbf{u}_i] + \mathbf{R} * \mathbf{A} * (\boldsymbol{\varepsilon}_1 \mathbf{u}_i + \boldsymbol{\varepsilon}_2 * \mathbf{f} * \mathbf{u}_i) \\ & = -\mathbf{T} * \mathbf{A} * \boldsymbol{\varepsilon}'_0(\mathbf{w}_i) - \mathbf{R} * \mathbf{A} * \boldsymbol{\varepsilon}_0(\mathbf{w}_i) - \mathbf{T} * \mathbf{B} * \boldsymbol{\kappa}'_0(\mathbf{w}_i) - \mathbf{R} * \mathbf{B} * \boldsymbol{\kappa}_0(\mathbf{w}_i) \quad \dots(4.46) \end{aligned}$$

or

$$\begin{aligned} & [\mathbf{T} * \mathbf{A} * [\boldsymbol{\varepsilon}_1 * \mathbf{f} + \boldsymbol{\varepsilon}_2 * \mathbf{s}] + \mathbf{R} * \mathbf{A} * (\boldsymbol{\varepsilon}_1 + \boldsymbol{\varepsilon}_2 * \mathbf{f})] * \mathbf{u}_i = \\ & -\mathbf{T} * \mathbf{A} * \boldsymbol{\varepsilon}'_0(\mathbf{w}_i) - \mathbf{R} * \mathbf{A} * \boldsymbol{\varepsilon}_0(\mathbf{w}_i) - \mathbf{T} * \mathbf{B} * \boldsymbol{\kappa}'_0(\mathbf{w}_i) - \mathbf{R} * \mathbf{B} * \boldsymbol{\kappa}_0(\mathbf{w}_i) \quad \dots(4.47) \end{aligned}$$

To solve for in-plane displacements \mathbf{u}_i , Equation 4.47 can be written in a simpler form as:

$$\mathbf{L} \mathbf{u}_i = \mathbf{H}(\mathbf{w}) \quad \dots(4.48)$$

Therefore \mathbf{u}_i can be obtained by;

$$\mathbf{u}_i = \mathbf{L}^{-1}\mathbf{H}(\mathbf{w}) \quad \dots(4.49)$$

Where superscript -1 denotes the inverse of the matrix.

From Equation 4.48, the matrix on the left hand side \mathbf{L} is square and contains only constant coefficients, whilst on the right hand side $\mathbf{H}(\mathbf{w})$ is a non-linear function of out-of-plane displacements which changes at every postbuckling cycle. To avoid repetitive calculations, the matrix \mathbf{L} is assembled and \mathbf{L}^{-1} calculated before starting the postbuckling analysis with \mathbf{L}^{-1} remaining constant throughout the whole calculation. Thus whenever the equilibrium equations are required to be solved, the calculations are simplified, finding the function of the out-of-plane displacements w , $\mathbf{H}(\mathbf{w})$, by multiplying with the pre-calculated matrix \mathbf{L}^{-1} .

Hence, the equilibrium equations in terms of u and v at the neutral surface are assembled. To finish the analysis, boundary conditions need to be considered before the equations are solved.

4.6. Boundary and loading conditions

To apply different in-plane boundary conditions, the equilibrium equations at the edges need to be modified correspondingly. Three in-plane boundary conditions are considered in this thesis: free edges, fixed edges and straight edges. In each case the longitudinal plate edges are constrained in the out-of-plane direction with no in-plane constraints applied to the transverse edges.

Unlike in-plane boundary conditions, out-of-plane boundary conditions are applied through the modified Newton iteration scheme rather than the equilibrium equations, more detail of which is provided in Chapter 5.

Free edges: The free edge case has no in-plane constraints applied i.e. the four boundaries are free to move and rotate in-plane as shown in Figure 4.3. Therefore the stress resultants N_x and

N_y are zero at the longitudinal boundaries. So in the equilibrium equations (Equations 4.42 and 4.43), the equations that represent the constraints along the four edges should be replaced by:

$$N_{x1} = 0 \text{ and } N_{xn} = 0 \quad \dots(4.50)$$

$$N_{y1} = 0 \text{ and } N_{yn} = 0$$

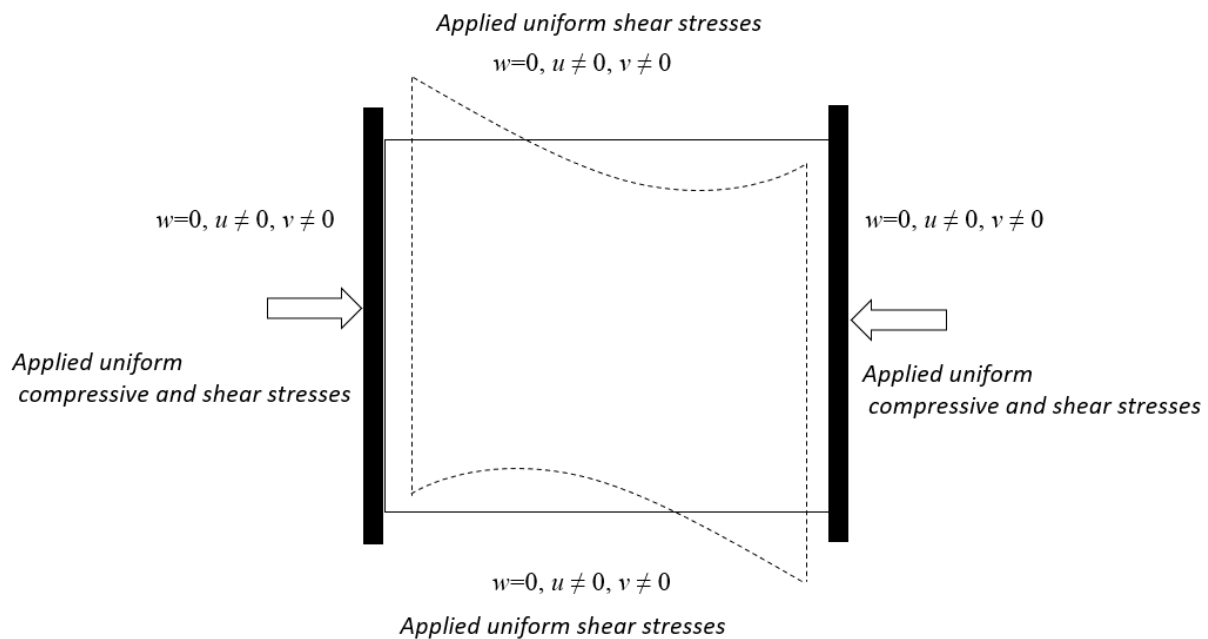


Figure 4.3. Initial postbuckling of a rectangular plate with longitudinal free edges under combined uniform compressive and shear stresses. The black rectangles indicate rigid bodies that control the displacements applied to the plate in the postbuckling analysis

Fixed edges: Fixed edges have displacement constraints applied to all the transverse components i.e. $u_1 \neq 0$, $u_n \neq 0$ and $v_1 = 0$, $v_n = 0$, see Figure 4.4. Therefore stress resultants N_x at the boundaries are zero and the following equations replace the equilibrium equations;

$$N_{x1} = 0 \text{ and } v_1 = 0 \quad \dots(4.51)$$

$$N_{y1} = 0 \text{ and } v_n = 0$$

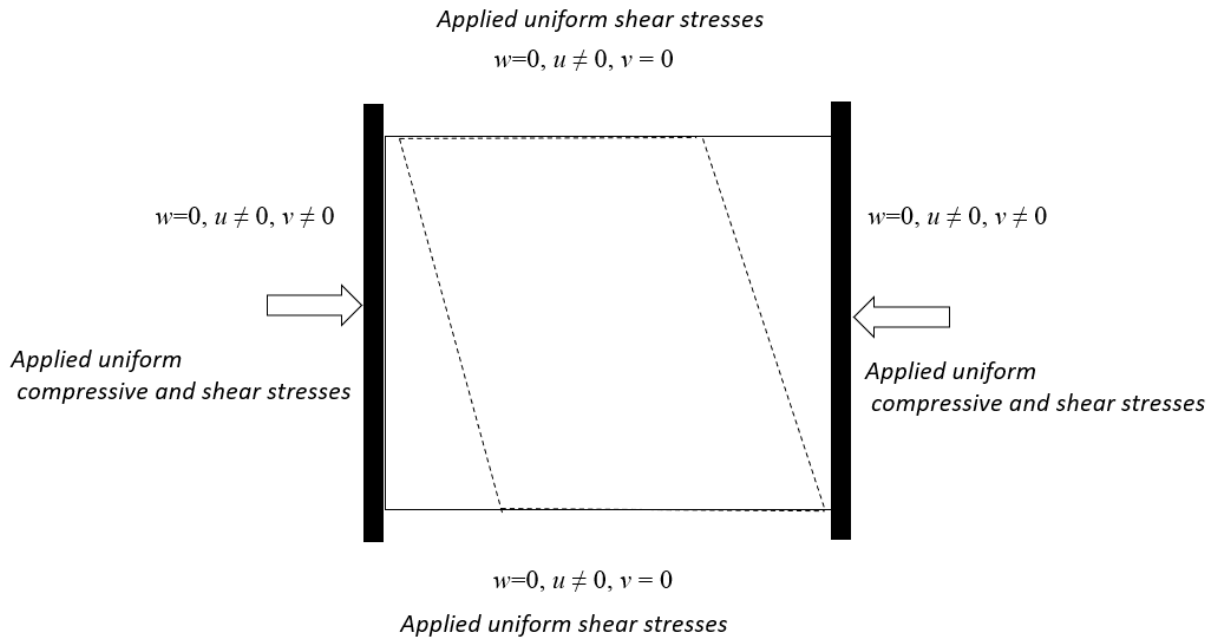


Figure 4.4. Initial postbuckling of a rectangular plate with longitudinal fixed edges under combined uniform compressive and shear stresses

Straight edges: This boundary condition requires the longitudinal edges to stay straight throughout the postbuckling analysis whilst allowing them to move towards or away from each other, see Figure 4.5. This results in the constant transverse displacement terms being nonzero, i.e. $v_{1,0} \neq 0$ and $v_{n,0} \neq 0$, the constant transverse stress terms being equal to zero, i.e. $N_{y1,0} = 0$ and $N_{yn,0} = 0$, and all other transverse displacement amplitudes on the edges, corresponding to the longitudinally varying terms, being equal to zero. Since the edges are allowed to move freely in the u direction, the equations for u displacements are replaced by:

$$N_{x1} = 0 \text{ and } N_{xn} = 0 \quad \dots(4.52)$$

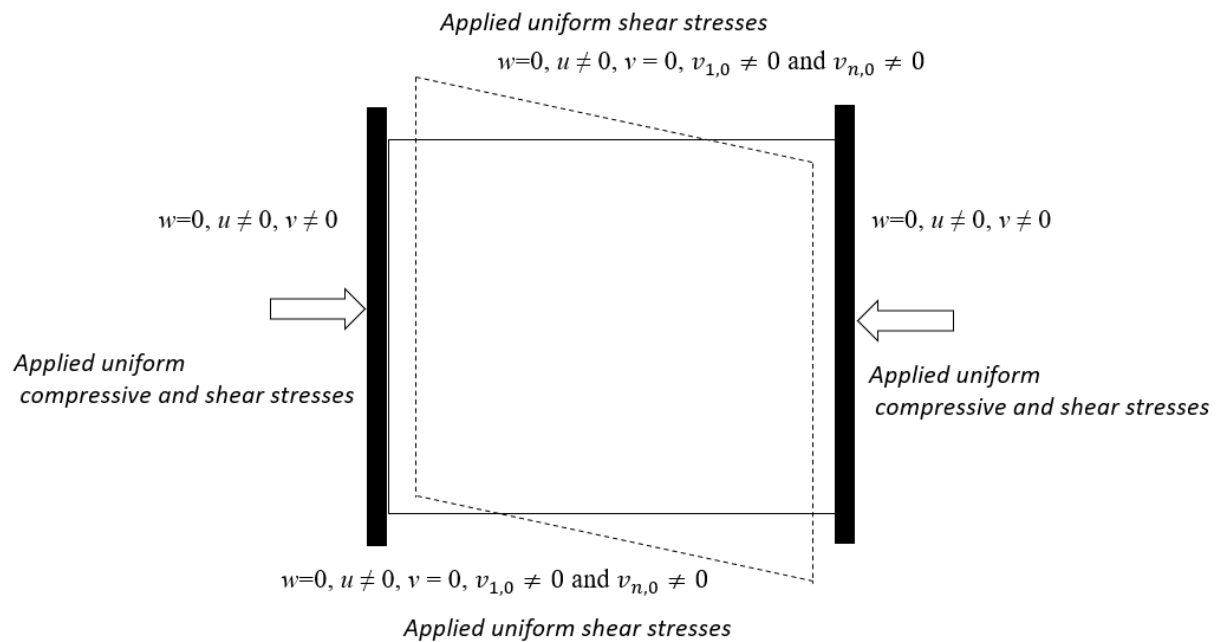


Figure 4.5. Initial postbuckling of a rectangular plate with longitudinal straight edges under combined uniform compressive and shear stresses

However these three cases all have the problem of free rigid body movement, causing the in-plane equilibrium equations to be singular. To avoid this, two alternative methods are proposed here:

1. Replace the equations representing all the displacement components terms at the central node by $\mathbf{v} = \mathbf{0}$ and $\mathbf{u} = \mathbf{0}$. or
2. Replace just two equations for the constant part of the in-plane displacement at edges $u_{1,0} = 0$ and $u_{n,0} = 0$.

The first method is easy to apply and efficiently avoids the problem. However it constrains all the displacements in both directions at the middle node, causing redundant constraints. This may lead to inaccurate results.

The second method is more accurate. It has been found that for the assembled equilibrium equations, rigid body movement is caused by the equations for the constant part of the in-plane displacements $u_{i,0}$ and $v_{1,0}$ which are singular at all nodes. The most efficient way to avoid this is to set one of these displacements to zero. In order to retain symmetry, two equations representing the constant part of the in-plane displacements at the first and last nodes respectively are replaced by $u_{1,0} = 0$ and $u_{n,0} = 0$.

In terms of loading conditions, three different loading conditions are considered along the transverse edges: compression, pure shear and combined shear and compression. In the method presented, compressive loading along the longitudinal edges is not considered. It is well known that with more shear or anisotropy in the plate, the mode shape becomes more skewed and this makes it hard to converge on the postbuckling mode. Therefore composite plates loaded in pure shear are considered as the most extreme case. CWPAN also gives a good agreement with other numerical techniques when solving these extreme cases. A model has been built and analysed in chapter 6.

When the equilibrium equations are fully assembled and modified, the in-plane displacements u and v can be solved analytically. Since u and v are expressions of a series of trigonometric terms multiplied by coefficients, see Equation 4.2, equilibrium equations are solved to obtain these coefficients for the in-plane displacements. After obtaining u and v , substituting solutions back into Equations 4.4-4.5 and Equations 4.30-31 the stress resultants, bending moments and strains can all be obtained. Stress resultants and bending moments can also be obtained by substituting strains into Equation 4.29. It is worth noting that all the outputs have the same format as the initial assumptions, which are trigonometric terms at node level. To illustrate and compare the results with other methods, all results need to be converted to actual values at specified points. Solving equilibrium Equations 4.42 and 4.33 involves the derivatives of stress resultants N_x , N_y and N_{xy} with respect to x or y . Those expressions for stress resultants consist of constant terms N_{x0} , N_{y0} , and N_{xy0} respectively, which are not included in the in-plane equilibrium equations, and sinusoidal terms relating to half-wavelengths that are calculated in the initial calculation, see Equation 4.2. By breaking down these constant terms, it can be seen that they are only related to the end shortening strains $\overline{\varepsilon_x}$ and strains $\overline{\gamma_{xy}}$ which contribute mostly to the in-plane displacements. Therefore there are no terms relating to end shortening stresses in the equilibrium equations, i.e. equations are only assembled to solve the sinusoidal part of the in-plane displacements (variation of displacements). Besides the strains and stresses are considered to be the second order derivatives of the in-plane displacements and the linear terms involving end shortening strain in Equation 4.2 are considered to be the first order of x and y . The end shortening strains therefore disappear in the equilibrium equations. To obtain the actual in-plane displacements, solutions solving the equilibrium equations are required to add end shortening stresses $\overline{\varepsilon_x}$ and strains $\overline{\gamma_{xy}}$ back into equation 4.2 based on the locations of the points in the plate. Similarly since strains and stresses are obtained from substituting u and v into equation 4.4, it is necessary to add end shortening strains into the expressions for strains

as well. For stress resultant calculations, they can be directly obtained from Equation 4.19 after calculations of the strains.

4.7. Conclusions

This chapter shows the full process of one iteration of postbuckling analysis from displacements assumptions to solving the in-plane equilibrium equations. Distributions of the stresses and strains can be obtained. Compared with the previous postbuckling analysis method the analysis assumes the component strips vary according to a sinusoidal series with a predefined set of half-wavelengths, rather than just two half-wavelengths. It achieves good accuracy when solving any anisotropic or shear load plates even for the most extreme cases like a plate under pure shear. With distributions of stresses obtained, uniform stress resultants can be calculated as the current equilibrium state's applied load. These calculations are essential for postbuckling stiffness with more details provided in the next chapter.

It is well known that postbuckling is normally considered as a large deflection regime in which non-linear terms in the governing equilibrium equations are required to capture the postbuckling mode accurately. Although von Kármán's large deflection theory is used and higher order terms are considered in this approach, the equilibrium equations are still linear since the out-of-plane displacements and rotations are taken as known variables, significantly increasing computational efficiency.

This process is referred to as the in-plane solutions for the rest of the thesis. However the in-plane solutions requires out-of-plane displacements including rotations as known quantities. A technique to obtain the out-of-plane mode for each cycle of postbuckling is therefore required and presented in the next chapter.

Chapter 5. CWPAN: Newton Iteration and Convergence Procedure

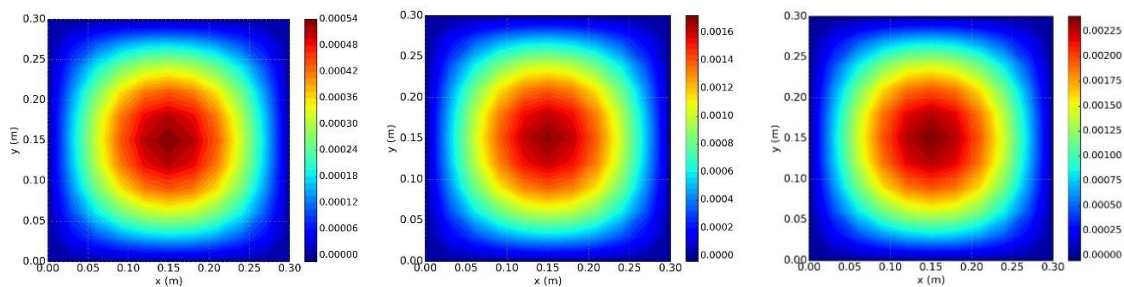
This chapter introduces a modified Newton iteration scheme and its supporting convergence procedure into CWPAN. Under the theory of the exact strip method, VICON assumes plate deformation varies as the sum of a series of sinusoidal terms with specified half-wavelengths, and solves the equilibrium equations analytically. It requires the out-of-plane buckling mode to be provided as input for each postbuckling cycle. The previously implemented Newton iteration schemes however only calculate the buckling mode for a single half-wavelength. Thus a new Newton iteration scheme is developed. The chapter is organized as follows. Section 5.1 introduces the general background. Sections 5.2-5.3 present an overview and detailed explanations of the convergence procedure and a short introduction to the strategies applied in the procedure. Section 5.4 introduces the predefined parameters. Section 5.5 illustrates the new VICON type Newton iteration scheme. Section 5.6 describes the method of obtaining the approximation amplitude for the buckling mode. Section 5.7 presents the formulations of the equivalent uniform stress resultant calculations. The last section concludes the chapter.

5.1. Overview

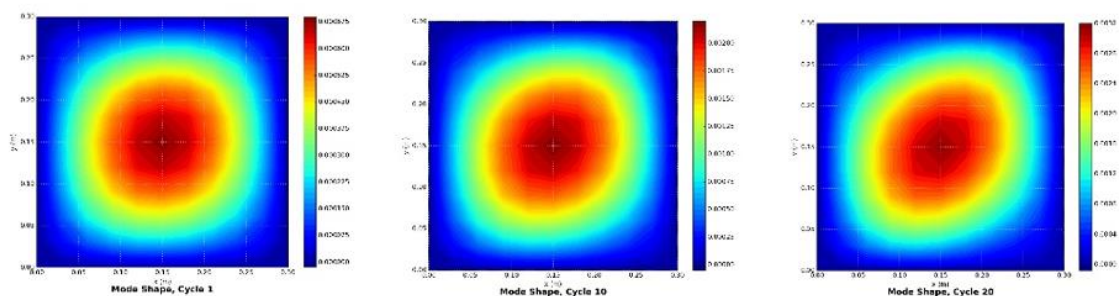
In the previous chapter, a postbuckling analysis based on the use of the distributions of out-of-plane displacements and the corresponding half-wavelengths for an assumed mode is presented. By solving the in-plane equilibrium equations analytically, the method can accurately capture the in-plane displacements and distributions of strains and stresses for any loading condition for symmetric laminates. However since out-of-plane displacements are required to obtain the

buckling mode at each cycle of the postbuckling process, a convergence method capable of calculating these out-of-plane displacements needs to be developed.

It is well known that the mode of postbuckling of a structure changes as the applied load increases. While for a rectangular flat structure that is isotropic and under only compressive load, the regions of maximum displacement expand from the centre of the plates towards the unloaded edges and the postbuckling mode merely changes in shape. For a composite or shear loaded plate however, the mode shape is increasingly skewed, due to the lack of symmetry within the structure, see Figure 5.1.



(a)



(b)

Figure 5.1. Postbuckling mode shape analysed by CWPAN at cycles 1,10 and 20, showing contour plots of growing out-of-plane displacements. (a) Isotropic plate under compression, no skewing at any point of postbuckling cycles. (b) Composite plate under compression with small amount of shear, growing skewed mode.

The previous postbuckling analysis, based on the theory of VIPASA, i.e. in which the buckling mode is assumed to vary sinusoidally with one half-wavelength λ , can capture non-skewed modes or small amounts of skew by applying the Newton iteration scheme, as described in

Section 3.7. However the coupled wavelengths postbuckling analysis assumes the plate to vary as the sum of sinusoidal terms with a series of half-wavelengths enabling it to represent more complex mode shapes. In this context the Newton iteration and previous convergence procedure is not suitable for CW PAN.

CW PAN comprises a number of cycles, each characterised by a pre-defined increment of longitudinal and/or shear strain, α/γ . Within each cycle, the total applied load, the variation of stress resultants across the plate, and the amplitude and shape of the postbuckling mode, are determined using in-plane solutions. In order to obtain an accurate postbuckling mode at each of these cycles, a recursive Newton method is introduced. The Newton iteration scheme was first developed to capture the buckling mode for VIPASA analyses where the buckling mode is assumed to vary sinusoidally with one half-wavelength, and is therefore not suitable for CW PAN. In this chapter, a detailed modified Newton iteration and its supporting convergence procedure is presented.

5.2. Convergence procedure overview

CW PAN assumes plates to be subjected to in-plane loading which can be compression, combined compression and shear or pure shear loading, with end shortening occurring uniformly across the width. The material can be either isotropic, anisotropic, a balanced or unbalanced composite. The method of analysis comprises a number of cycles, each characterised by a pre-defined increment α of longitudinal and/or shear strain, α/γ . Within each cycle the total applied load, the variation of stress resultants across the plate, and the amplitude and shape of the postbuckling mode are determined using the in-plane solutions. The essential part of the analysis is to obtain the mode shape before starting the in-plane calculations. The first cycle's out-of-plane displacements are obtained from a VICON initial buckling analysis. For subsequent cycles, the recursive Newton method and its supporting calculation are used.

Assume a plate has an initial critical buckling load, P_{cr} , its end shortening strain is ε_0 and its shear shortening strain is γ_0 . For the first cycle of the first iteration, the end shortening strain will be $\varepsilon_1 = (\alpha + 1) \times \varepsilon_0$ and the shear strain $\gamma_1 = (\alpha + 1) \times \gamma_0$. Note that in this analysis the

ratio between end shortening strain and end shortening shear strain remains the same as at the buckling point, where α is the postbuckling increment ratio. Importing ε_1 and the out-of-plane displacements into the in-plane solutions, the in-plane displacements, strains and stresses at the current cycle can be obtained. Then equivalent longitudinally invariant stresses can be obtained to facilitate the calculations in the next cycle.

For the following cycles, instead of subjecting the plate to a compressive load P , the equivalent uniform stresses are applied to the plate. Therefore, a new buckling load P_{cr} and out-of-plane displacements for the new cycle are obtained. Repeating the procedure above will result in a full postbuckling analysis.

5.3. Convergence procedure

A flow diagram illustrating the calculation procedure is shown in Figure 5.2. Each step is elaborated below:

- 1, Four predefined values are required to be defined including the number of out-of-plane half-wavelengths m , the number of strips/nodes, n , the ratio of the increment of end shortening strain, α (which determines the number of cycles required to reach a pre-defined maximum level of strain), and the tolerance in the Newton iteration, β .
- 2, The analysis starts with a VICON initial buckling analysis based on the plate properties and predefined variables including the number of half-wavelengths and the number of strips. The outputs from this stage are the out-plane displacements and rotations, the critical buckling load and the end shortening strains and possible shear strains.
- 3, The in-plane half-wavelengths are calculated, as described in Section 4.3.
4. The inverse matrix \mathbf{L}^{-1} in Equation 4.36 is then calculated as illustrated in Section 4.5. This will not change once the properties of the structure are decided. To efficiently proceed with the postbuckling analysis, this matrix is therefore considered as a constant matrix, and is calculated once, before the convergence starts.

5. The end shortening strain for a certain cycle is obtained by multiplying by the pre-defined variable α . This defines the postbuckling analysis and increases the strain by α at every cycle.
6. This step calculates an approximate amplitude for the buckling mode from the previous cycle which helps the Newton iteration scheme to converge more efficiently. The first cycle uses the VICON buckling mode. More detail will be provided in Section 5.4.
- 7-12. These steps constitute the in-plane solution which calculates the right hand side of Equation 4.34 in Chapter 4. The input values for this process are the out-of-plane displacements at the critical buckling load for the first cycle or the calculated out-of-plane displacements from the previous iteration or cycle, the properties of the plate and the end shortening strains.
13. The last chapter described a method to solve the equilibrium equations for postbuckling analysis using the exact strip method. This allows the calculation of the in-plane displacements and distributions of stresses and strains within the plate. However to find the applied load for the next cycle, these distributions cannot be used. Therefore this step calculates equivalent uniform stresses resultants using the previous distributions of stresses, see Section 5.6.
14. This step is a part of the VICON type Newton iteration scheme. As described in the Newton iteration scheme in Chapter 3, the stiffness matrix is assembled by coupling the stiffness matrices obtained by increasing the displacements at each degree of freedom by a small amount. Therefore, in the Newton iteration scheme, the in-plane solutions are run a number of times equal to the total number of degrees of freedom, counted over all the out-of-plane half-wavelengths, see Section 5.5.
15. Adjustments to the displacements \mathbf{d}^* are found by solving Equation 3.35 and added to the previous \mathbf{D} to get the new displacements \mathbf{D} .
16. The convergence check described in the VICON Newton iteration scheme in section 5.5 is applied.
17. The solutions from steps 11-13 are tabulated.

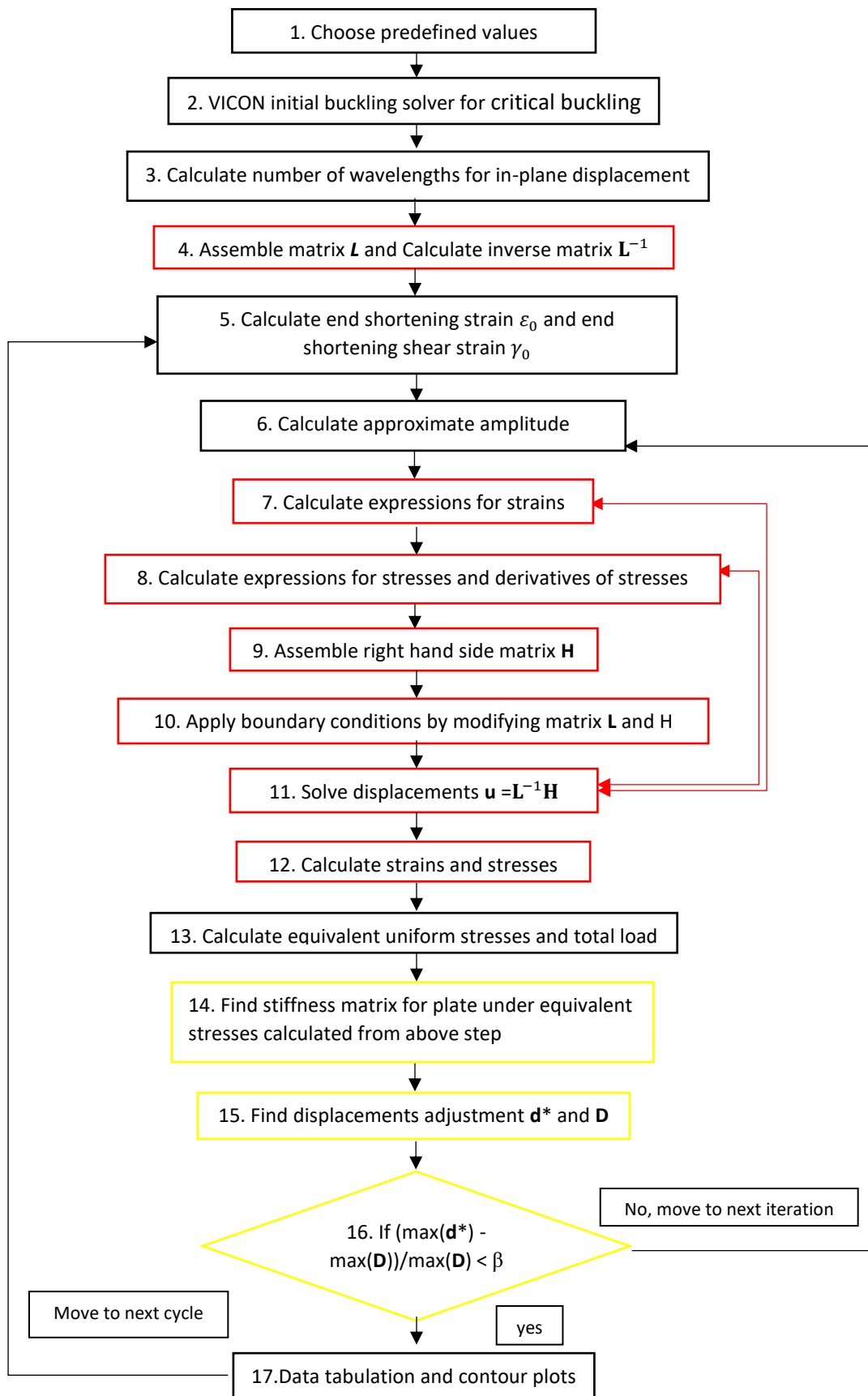


Figure 5.2. Flow of diagram for the method of analysis: red boxes indicate in-plane solutions, yellow boxes indicate Newton Iteration scheme

Steps 1 to 5 are completed before starting the analysis, calculating constants used throughout the whole analysis. Steps 4 to 12 are the series solution for postbuckling introduced in Chapter 4. This process can be used not only for capturing in-plane displacements and stress distributions but also equivalent uniform stress resultants to be used in the next cycle. It is worth noting that steps 6 and 14 also include the full process of the in-plane solutions in order to obtain the equivalent stress resultants. Steps 14 to 16 are the VICON Newton iteration scheme. The red arrows indicate that in the in-plane solutions the stresses and strains are obtained by substituting the solutions of the equilibrium equations back into the explicit expressions.

5.4. Pre-defined variables

Before starting the analysis, four pre-defined variables are required to be determined.

1. The number of half-wavelengths for the out-of-plane displacement, m , from the VICON analysis. The VICON analysis couples a series of wavelengths to represent more complex mode shapes using Lagrange multipliers which cannot be modelled using VIPASA analysis. Theoretically increasing the number of wavelengths leads to more accurate solutions. However it can be seen that, from Equation 4.2 - Equation 4.30, the addition of each half-wavelength results in an increase of the number of calculations and therefore the computational time. It is critical therefore to determine a suitable number of half-wavelengths in order to minimize the effect on the speed of the calculation. This is investigated in the next chapter.
2. The number of strips or the number of nodes. Plates are divided into $n-1$ strips of arbitrary width, identified by n nodes at the strip edges where n is a user defined parameter. The number of strips is equivalent to the mesh in the finite element method. Increasing the number of nodes n can increase accuracy but will decrease computational efficiency. The effect of the number of strips is also investigated in the next chapter.
3. The ratio of the linear strain increment, α , which controls the step size for postbuckling. If the chosen value of α is too big, the Newton iteration scheme may not capture changes in the mode. The right step size is therefore crucial especially for some extreme cases, e.g. composite

plates under pure shear loading. Combined with the number of cycles, the strain increment controls how far the postbuckling analysis goes. As we move further from initial buckling, mode jumping may occur. This has not been incorporated into this analysis. Therefore the number of cycles must be chosen to avoid the stage at which mode jumping might occur. Further investigation of this is presented in the next chapter.

4. The tolerance for the Newton iteration, β . This variable is explained in Section 5.5 and investigated in Chapter 6.

5.5. Newton Iteration scheme

As described in Chapter 4, out-of-plane displacements are considered as known variables and the first cycle's out-of-plane displacements are taken from a VICON initial buckling analysis. For the rest of the cycles, using VICON analysis to solve for buckling is inefficient as to do this VICON would have to be incorporated as a subroutine solver. To overcome this limitation, mode shapes are obtained through a VICON type Newton iteration scheme.

The Newton iteration scheme was first developed for VIPASA postbuckling analysis. It replaced the linear approximations applied in the first VIPASA postbuckling analyses and provided accurate convergence on critical buckling loads and associated buckling modes (see Section 3.7). However it was based on the assumption that the out-of-plane deformation varies sinusoidally along the longitudinal direction with a single half-wavelength. It is therefore unsuitable for complex buckling modes which need to be modelling with multiple half-wavelengths. Therefore a Newton iteration scheme based on VICON analysis is developed here enabling CWPAN by modifying the stiffness matrix, displacement and force vectors in Equation 3.34.

Since for CWPAN, more than one half-wavelength is needed to represent more complex mode shapes, the \mathbf{D} and \mathbf{K} matrices in Equation 3.34 are m times bigger than for VIPASA postbuckling (where m is the number of out-of-plane half-wavelengths) and need to be assembled using complex arithmetic. Convergence on the amplitude and shape of the mode

vector \mathbf{D} implies convergence on the adjustments \mathbf{d}^* to the stress resultants due to flexure, and hence the postbuckling in-plane displacements, stresses and strains can be calculated.

Since the new Newton iteration scheme is adopted within VICON analysis, there is also the possibility to include point supports at nodes on the transverse edges. Therefore the stiffness matrix in the new Newton iteration scheme has to be modified to take these point supports into account. Similar to VICON buckling analysis, the stiffness matrix is modified by adding zero displacements at points corresponding to the supports for all wavelengths. Figure 5.3 shows a three wavelength stiffness matrix example of a simply supported plate in the VICON Newton iteration scheme. Each identity matrix indicates corresponding point constraints on the transverse edges and all identity matrices have the same dimensions since the three half-wavelengths are coupled to create one mode. Boundary conditions on longitudinal edges are applied by deleting corresponding rows. In Figure 5.3, the null matrix is a square matrix and the RHS vector denotes the applied forces in Equation 3.35. The force vector also needs to be added to indicate the reaction forces. For other more general cases, i.e. point constraints applied at arbitrary location within plates, the identity matrices on the left hand side are modified accordingly.

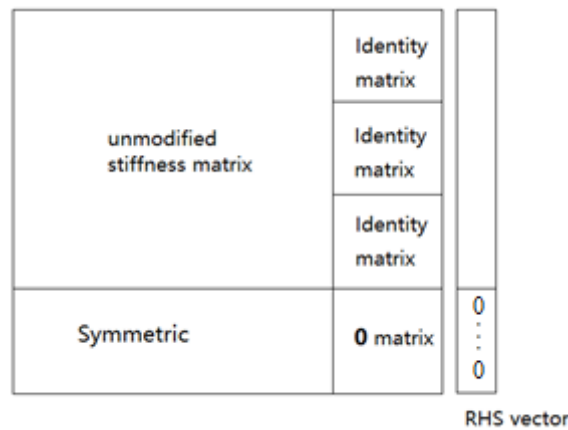


Figure 5.3. Three wavelength stiffness matrix transverse boundary conditions example

The purpose of the Newton iteration scheme is to obtain the mode shapes for each cycle except for the first one for which the out-of-plane displacements are obtained directly from a VICON buckling analysis. At each cycle, the Newton iteration solves Equation 3.35 by finding the stiffness matrix and the derivatives of the stiffness matrix using finite difference approximations to converge on the required adjustments to the displacements. To obtain these

stiffness matrices the equivalent uniform stresses which are considered as the loading conditions are required as shown in Figure 5.4. However the coupled wavelength postbuckling analysis only captures the distributions of the stresses within the plate. A series of calculations are therefore required to derive equivalent uniform stresses from the distribution of stresses within the plate.

The convergence of the Newton iteration procedure is achieved when the difference between the maximum of the displacement adjustments \mathbf{d}^* and the maximum of the previous displacements \mathbf{D} is small enough. It is assumed to occur when the criterion below is met;

$$\frac{|max(\mathbf{d}^*)-max(\mathbf{D})|}{max(\mathbf{D})} \leq \beta \quad \dots(5.1)$$

where β is a small positive number ($\beta \ll 0$), \mathbf{d}^* and \mathbf{D} are out-of-plane displacement adjustments and the out-of-plane displacements from the previous iteration respectively. $max()$ indicates a function of maximum value of given vector or matrix.

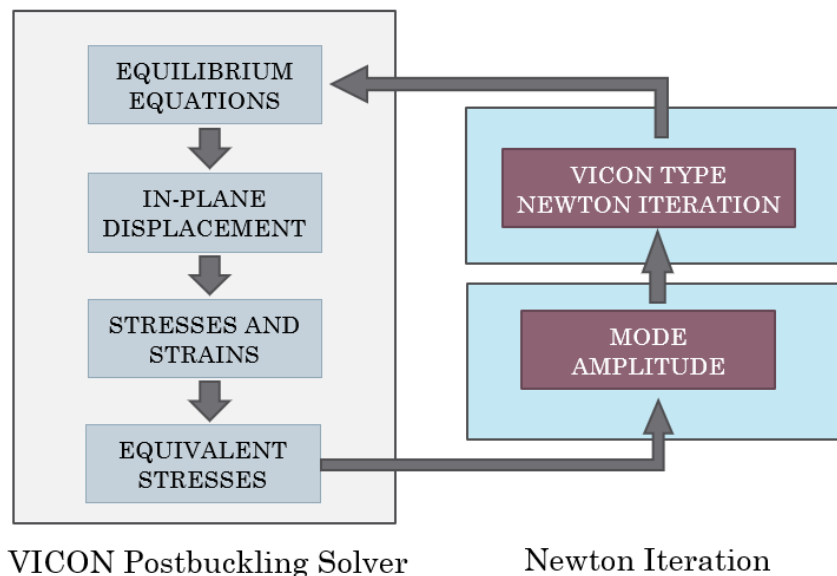


Figure 5.4. Implementation of Newton iteration in CWPAN

When the Newton iteration procedure has converged, the buckling mode for that particular cycle can be obtained. Compared with the previous Newton iteration scheme, the presented one can capture much more skewed mode shapes such as those resulting from anisotropy or shear load. However it has been found that if the shape of the buckling mode is not considered, the difference between the previous cycle's maximum displacement and the calculated one

may be too big, and the Newton iteration scheme will fail to converge or take a long time to converge. Therefore a convergence method to find the approximate amplitude is also required.

5.6. Approximate buckling mode amplitude

In CWPAN, the buckling mode for one cycle is used as a basis to converge on the next cycle's buckling mode. It has been found that the VICON type Newton iteration can converge only if the amplitude of buckling mode is not too far from the real buckling mode. Therefore it is necessary to find an approximate buckling mode before moving into the next Newton iteration.

The method for achieving this is based on a modified binary search which enables convergence on the buckling mode corresponding to a particular predefined end-shortening strain. To accurately locate the amplitude of the out-of-plane displacements, the W-W algorithm is used to examine whether the resulting applied load exceeds the actual buckling load. This process is illustrated in Figure 5.5 and corresponds to the following steps:

1. Out-of-plane displacements including rotations are obtained from VICON (for the first cycle) or from previous cycles.
2. A trial amplitude of the out-of-plane displacement is calculated from the previous iteration, either a lower bound or an upper bound. For the first iteration the trial amplitude is chosen as 1.
3. The resulting displacements are calculated from the displacements multiplied by the amplitude. This step only scales the buckling mode rather than changing the shape of it.
- 4-5. The resulting buckling mode is input into the in-plane solutions to obtain the stress distributions within the plate.
6. The equivalent stress resultants are calculated using the method described in section 5.7.
- 7-9. This calculation only utilizes a part of W-W algorithm to examine if the applied equivalent uniform stresses exceed the critical buckling load. If the applied load is higher than the critical buckling load, the corresponding amplitude will be taken as an upper bound and restored as Am_u and vice versa for convergence check 10. If both upper and lower bound are found, the

convergence check is able to proceed, evaluating the difference between the lower and upper bounds from the previous iterations. For the first iteration of every postbuckling cycle, the converged amplitude from the last cycle is taken as a lower bound as the increase in amplitude of the cycle decreases. Convergence is achieved if following criteria is met:

$$\frac{|Am_u - Am_l|}{Am_u} < 0.001 \quad \dots(5.16)$$

where 0.001 is a predefined default value. This value remains the same for all cycles and iterations since the purpose of the calculation is only to obtain an approximate buckling mode in order to converge on a better buckling mode during the Newton iteration procedure. Once convergence is achieved, the resulting buckling mode is used as a temporary mode for the Newton iteration scheme enabling it to converge on a final mode shape.

11.If the convergence check fails or either the upper or lower bound are not found, lower/upper bound is multiplied/divided by 1.5 for the next iteration.

By using the W-W algorithm and the in-plane solutions, the approximate amplitude is converged on at each postbuckling cycle. As described above, this solution cannot be used for postbuckling analysis directly since it fails to capture the progressive changes of mode shape caused by anisotropy or shear load. The purpose of this strategy is to reduce the computational time or possibility of failing to converge using the modified Newton iteration scheme due to large increment strains. Although such modes are only multiples of the previous cycle's postbuckling mode, the strategy can reduce the number of modified Newton iterations significantly while taking less than one second to converge itself. Furthermore since large increment strains are allowed during the analysis, fewer cycles are required to reach the target postbuckling equilibrium state, therefore reducing the execution time.

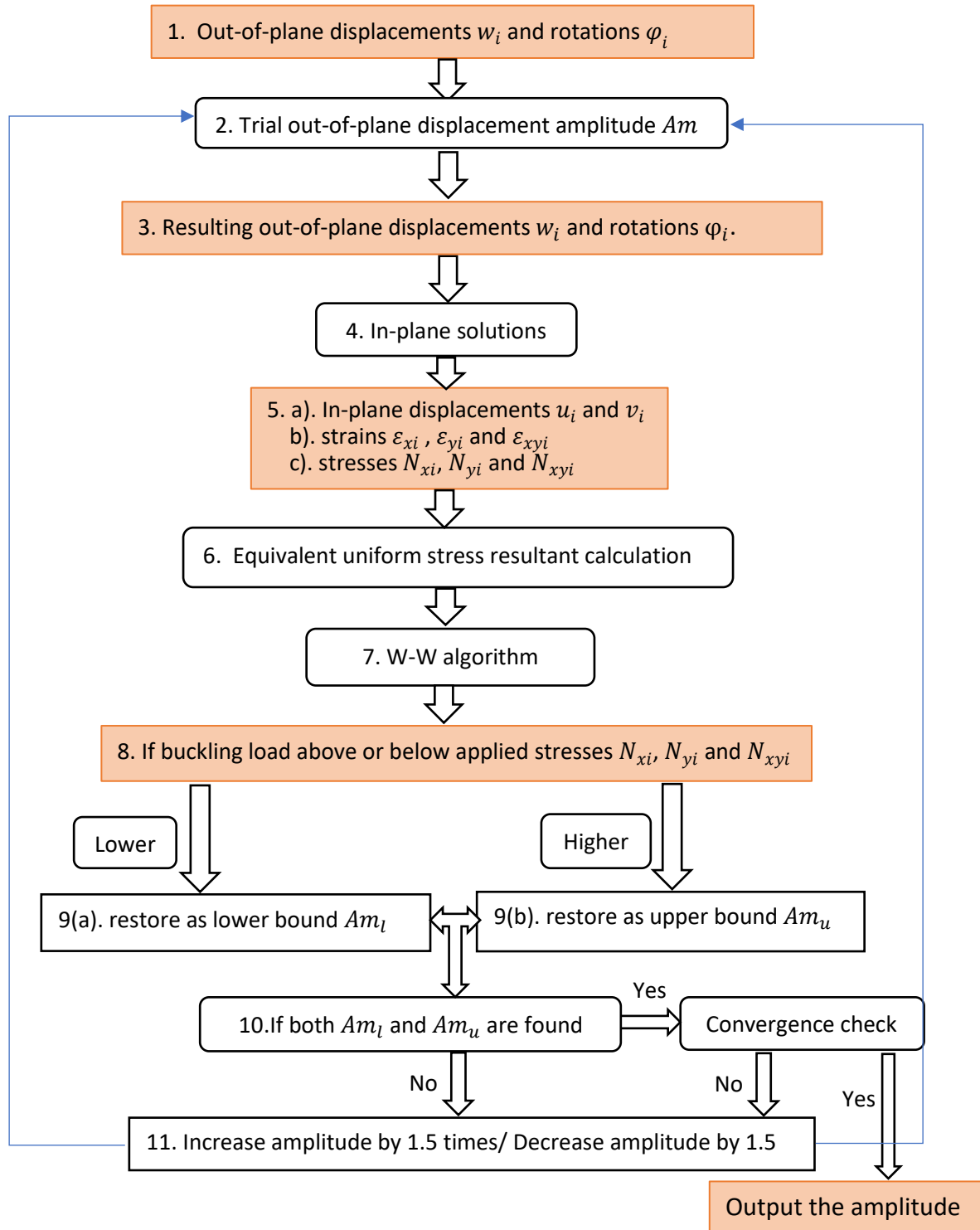


Figure 5.5. Flow diagram for the method of analysis

5.7. Stress resultants calculation

A stress redistribution occurs at each postbuckling cycle due to changes in the buckling mode. The loading condition therefore changes along with the stress redistribution. As shown in Figure 5.6 the applied stresses at the edges are normally continuous. To perform the Newton iteration however, these continuous stress resultants need to be converted into discontinuous equivalent stress resultants at strip level, see the dashed lines in Figure 5.5. Since the in-plane solutions captures a continuous distribution of stresses within the plate, an energy approach is provided to convert the stress distribution to a set of effective uniform stress resultants at each strip.

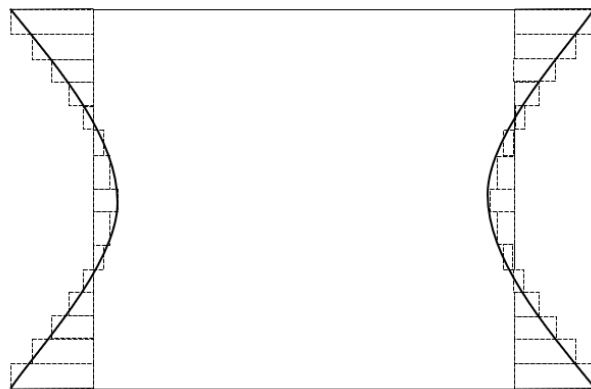


Figure 5.6. Stress distribution of a postbuckling analysis from a rectangular flat plate where solid line indicates normal stress distribution and dashed line is the equivalent uniform stress distribution.

In the buckling analysis, the work done by the applied loading can be obtained from

$$V = V_{xi} + V_{yi} + V_{xyi} \quad \dots(5.2)$$

where the components of total energy V at each node are written as:

$$V_{xi} = \bar{N}_x \int_0^L \varepsilon_x dx = \int_0^L N_x \varepsilon_x dx \quad \dots(5.3)$$

$$V_{yi} = \bar{N}_y \int_0^L \varepsilon_y dx = \int_0^L N_y \varepsilon_y dx \quad \dots(5.4)$$

$$V_{xyi} = \bar{N}_{xy} \int_0^L \gamma_{xy} dx = \int_0^L N_{xy} \gamma_{xy} dx \quad \dots(5.5)$$

where \bar{N}_x , \bar{N}_y and \bar{N}_{xy} are uniform longitudinal, transverse and shear stresses respectively. N_x , ε_x , N_y , ε_y , N_{xy} and γ_{xy} , can be written as

$$N_x = \sum_{n=0}^{\infty} \left(N_{xnc} \cos \frac{n\pi x}{L} + N_{xns} \sin \frac{n\pi x}{L} \right) \quad \dots(5.6)$$

$$\varepsilon_x = \sum_{m=0}^{\infty} \left(\varepsilon_{xmc} \cos \frac{m\pi x}{L} + \varepsilon_{xms} \sin \frac{m\pi x}{L} \right) \quad \dots(5.7)$$

$$N_y = \sum_{n=0}^{\infty} \left(N_{ync} \cos \frac{n\pi x}{L} + N_{yns} \sin \frac{n\pi x}{L} \right) \quad \dots(5.8)$$

$$\varepsilon_y = \sum_{m=0}^{\infty} \left(\varepsilon_{ymc} \cos \frac{m\pi x}{L} + \varepsilon_{yms} \sin \frac{m\pi x}{L} \right) \quad \dots(5.9)$$

$$N_{xy} = \sum_{n=0}^{\infty} \left(N_{xync} \cos \frac{n\pi x}{L} + N_{xyns} \sin \frac{n\pi x}{L} \right) \quad \dots(5.10)$$

$$\gamma_{xy} = \sum_{m=0}^{\infty} \left(\gamma_{xymc} \cos \frac{m\pi x}{L} + \gamma_{xyms} \sin \frac{m\pi x}{L} \right) \quad \dots(5.11)$$

Note that all the results (displacements, strains and stresses) can be represented by sinusoidal components.

Substituting Equations 5.6-5.11 into Equations 5.3-5.5 gives

$$\begin{aligned} \bar{N}_x & \\ &= \frac{\int_0^L \sum_{n=0}^{\infty} \sum_{m=0}^{\infty} \left(N_{xnc} \cos \frac{n\pi x}{L} + N_{xns} \sin \frac{n\pi x}{L} \right) \left(\varepsilon_{xmc} \cos \frac{m\pi x}{L} + \varepsilon_{xms} \sin \frac{m\pi x}{L} \right) dx}{\int_0^L \sum_{m=0}^{\infty} \left(\varepsilon_{xmc} \cos \frac{m\pi x}{L} + \varepsilon_{xms} \sin \frac{m\pi x}{L} \right) dx} \quad \dots(5.12) \end{aligned}$$

$$\begin{aligned} \bar{N}_y & \quad \dots(5.13) \\ &= \frac{\int_0^L \sum_{n=0}^{\infty} \sum_{m=0}^{\infty} \left(N_{ync} \cos \frac{n\pi x}{L} + N_{yns} \sin \frac{n\pi x}{L} \right) \left(\varepsilon_{ymc} \cos \frac{m\pi x}{L} + \varepsilon_{yms} \sin \frac{m\pi x}{L} \right) dx}{\int_0^L \sum_{m=0}^{\infty} \left(\varepsilon_{ymc} \cos \frac{m\pi x}{L} + \varepsilon_{yms} \sin \frac{m\pi x}{L} \right) dx} \end{aligned}$$

$$\begin{aligned} \bar{N}_{xy} & \quad \dots(5.14) \\ &= \frac{\int_0^L \sum_{n=0}^{\infty} \sum_{m=0}^{\infty} \left(N_{xync} \cos \frac{n\pi x}{L} + N_{xyns} \sin \frac{n\pi x}{L} \right) \left(\gamma_{xymc} \cos \frac{m\pi x}{L} + \gamma_{xyms} \sin \frac{m\pi x}{L} \right) dx}{\int_0^L \sum_{m=0}^{\infty} \left(\gamma_{xymc} \cos \frac{m\pi x}{L} + \gamma_{xyms} \sin \frac{m\pi x}{L} \right) dx} \end{aligned}$$

Thus the equivalent uniform stress distribution is calculated at node level based on the stress distribution within the plate for the current cycle. To apply these stresses at the strip level, they have to be transformed into equivalent uniform stresses by averaging the two adjacent nodes for that strip:

$$\bar{N}_k = \frac{\bar{N}_i + \bar{N}_{i+1}}{2} \quad \dots(5.15)$$

Once the current loading conditions are defined they are used as the next cycle's trial applied load for the Newton iteration scheme in order to converge on the next cycle's buckling mode.

5.8. Conclusions

This chapter introduces a convergence procedure that allows the analysis to observe progressive postbuckling equilibrium states of balanced and unbalanced laminated composite plates. The analysis consists of a number of cycles, each defined by an applied constant longitudinal or shear strain. At each cycle, the in-plane solution is utilized to find the distributions of in-plane displacements, strains and stresses, and further transform these into equivalent uniform stress resultants as the current cycle's applied load. The postbuckling

stiffness and out-of-plane displacements can thus be obtained based on a modified Newton iteration scheme. To accelerate the execution time of the Newton iteration scheme, an amplitude calculation is developed incorporating the binary search and W-W algorithms.

The proposed convergence approach is used to obtain the postbuckling modes corresponding to a particular value of end shortening strain input into the in-plane displacement calculations for each postbuckling cycle. This is in contrast to the previous postbuckling analysis by Che (2010; Zhang 2018) based on assumptions regarding out-of-plane displacements and requires the modification of the previous Newton iteration scheme to make it suitable for the analysis of complex composite structures and loading conditions. Compared with the previous method, the modified Newton iteration scheme allows not only formulations of single half-wavelength but also a series of half-wavelengths coupled together. In this way CWPAN can capture any shape of buckling mode accurately. An amplitude calculation is developed to assist the modified Newton iteration scheme. With such a strategy, it is possible to significantly reduce the number of iterations in the scheme, and convergence problems due to large strain increments are avoided allowing a small number of cycles to reach the target postbuckling equilibrium state.

By implementing the above methods into the VICON in-plane solutions, the out-of-plane displacements in the governing equations are no longer unknown variables. The equilibrium equations are transformed into linear equations but retain the nature of non-linearity by using von Kármán's large deflection theory. Hence the computational time is significantly reduced.

As described in this chapter, four re-defined variables affect the speed and accuracy of the analysis significantly. In the next chapter, more explorations and explanations will be presented to understand the effect of changes to these variables.

Chapter 6. Parameter Selection

Chapters 4 and 5 describe the development of a method for carrying out postbuckling analysis for composite plates. To apply this method four parameters, not related to the properties of the structures being analysed, are required to be selected. Before investigating the postbuckling behaviour of a range of different structures using CWPAN, it is therefore necessary to evaluate the optimum values for these predefined parameters for different scenarios. This chapter is organized as follows: Section 6.1 discusses the calculation of in-plane half-wavelengths and their influence on the governing equilibrium equations. The influence of the selected number of half-wavelengths on computational efficiency is also investigated as part of the search for the optimal out-of-plane half-wavelengths for certain problems. Section 6.2 investigates the influence of the number of strips that plates are divided into. Finally Sections 6.3 and 6.4 illustrate the effect of strain increment ratio and iteration tolerance of the Newton iteration scheme. The last section concludes the chapter.

6.1. Number of half-wavelengths

One of the key differences between the previous postbuckling analysis and CWPAN is the number of half-wavelengths used to represent the out-of-plane deflections resulting in differences in in-plane half-wavelengths.

Based on the theory in VICON, the selection of half-wavelengths is mainly related to the parameter ξ . Theoretically, ξ can be any number between zero and one and VICONOPT evaluates all these possibilities to search for the minimum buckling factor. The corresponding half-wavelengths for the out-of-plane displacements can be found from Equation 3.13 and for the in-plane displacements, by counting unique values of summations and subtractions from the out-of-plane half-wavelengths as follows.

For a general value of ξ the out-of-plane half-wavelengths are given by $l = l/m$, with the values of m given by $\xi \pm 2q$ where q is an integer $0, 1, 2, \dots$, see Chapter 3. Taking $q = 0, \pm 1, \pm 2$ as an example, $\xi = 1$ and $\xi = 0$ are special cases because the negative values of q give the same values of m as the positive values (but with the opposite sign) so that only the positive values of m need to be considered in the VICON analysis.

When $\xi = 1$:

For out-of-plane half-wavelengths $l = l/m$ and l/n , for the 3 values $m, n = (1, 3, 5)$ the 9 unique resulting values are highlighted in Tables 6.1, 6.2 and 6.3.

Summations	$n=1$	$n=3$	$n=5$
$m=1$	2	4	6
$m=3$	4	6	8
$m=5$	6	8	10

Table 6.1. Summations of half-wavelengths l/m and l/n , $m, n = (1,3,5)$

Subtractions	$n=1$	$n=3$	$n=5$
$m=1$	0	-2	-4
$m=3$	2	0	-2
$m=5$	4	2	0

Table 6.2. Subtractions of half-wavelengths l/m and l/n , $m, n = (1,3,5)$

The out-of-plane half-wavelengths are then:

Own values	$m=1$	$m=3$	$m=5$
	1	3	5

Table 6.3. Out-of-plane half-wavelengths l/m , $m = (1,3,5)$

When $\xi = 0$:

For out-of-plane half-wavelengths $l = l/m$ and l/n , for the 3 values of $m, n = (0, 2, 4)$ there are now only 5 unique resulting values, again shown highlighted in Tables 6.4, 6.5 and 6.6.

Summations	$n=0$	$n=2$	$n=4$
$m=0$	0	2	4
$m=2$	2	4	6
$m=4$	4	6	8

Table 6.4. Summations of half-wavelengths l/m and l/n , $m, n = (0,2,4)$

Subtractions	$n=0$	$n=2$	$n=4$
$m=0$	0	-2	-4
$m=2$	2	0	-2
$m=4$	4	2	0

Table 6.5. Subtractions of half-wavelengths l/m and l/n , $m, n = (0,2,4)$

The out-of-plane half-wavelengths are then:

Own values	$m=0$	$m=2$	$m=4$
	0	2	4

Table 6.6. Out-of-plane half-wavelengths l/m , $m = (0,2,4)$

When $0 < \xi < 1$:

By analogy with the previous cases we consider q_m and $q_n = 0, -1, +1, -2, +2$, i.e. there are now 5 out-of-plane half-wavelengths instead of 3. Note that m and n are no longer integers.

For out-of-plane half-wavelengths $l = l/m$ and l/n , with the 5 values $m, n = (\xi, \xi \pm 2, \xi \pm 4)$ there are now 23 unique resulting values, again shown highlighted in Tables 6.7, 6.8 and 6.9.

Summations	$q_n=-2,$ $n=\xi-4$	$q_n=-1,$ $n=\xi-2$	$q_n=0,$ $n=\xi$	$q_n=+1,$ $n=\xi+2$	$q_n=+2,$ $n=\xi+4$
$q_m=-2, m=\xi-4$	$2\xi - 8$	$2\xi - 6$	$2\xi - 4$	$2\xi - 2$	2ξ
$q_m=-1, m=\xi-2$	$2\xi - 6$	$2\xi - 4$	$2\xi - 2$	2ξ	$2\xi + 2$
$q_m=0, m=\xi$	$2\xi - 4$	$2\xi - 2$	2ξ	$2\xi + 2$	$2\xi + 4$
$q_m=+1, m=\xi+2$	$2\xi - 2$	2ξ	$2\xi + 2$	$2\xi + 4$	$2\xi + 6$
$q_m=+2, m=\xi+4$	2ξ	$2\xi + 2$	$2\xi + 4$	$2\xi + 6$	$2\xi + 8$

Table 6.7. Summations of half-wavelengths l/m and l/n , $m, n = (\xi, \xi \pm 2, \xi \pm 4)$

Subtractions	$q_n=-2,$ $n=\xi-4$	$q_n=-1,$ $n=\xi-2$	$q_n=0,$ $n=\xi$	$q_n=+1,$ $n=\xi+2$	$q_n=+2,$ $n=\xi+4$
$q_m=-2, m=\xi-4$	0	-2	-4	-6	-8
$q_m=-1, m=\xi-2$	2	0	-2	-4	-6
$q_m=0, m=\xi$	4	2	0	-2	-4
$q_m=+1, m=\xi+2$	6	4	2	0	-2
$q_m=+2, m=\xi+4$	8	6	4	2	0

Table 6.8. Subtractions of half-wavelengths l/m and l/n , $m, n = (\xi, \xi \pm 2, \xi \pm 4)$

The out-of-plane half-wavelengths are then:

Own values	$q_m=-2,$ $m=\xi-4$	$q_m=-1,$ $m=\xi-2$	$q_m=0,$ $m=\xi$	$q_m=+1,$ $m=\xi+2$	$q_m=+2,$ $m=\xi+4$
	$\xi - 4$	$\xi - 2$	ξ	$\xi + 2$	$\xi + 4$

Table 6.9. Out-of-plane half-wavelengths l/m $m = (\xi, \xi \pm 2, \xi \pm 4)$

Resulting in total of 23 unique values: 9 from Table 6.7; 9 from Table 6.8 and 5 from Table 6.9.

These relationships between the number of in-plane and out-of-plane wavelengths are summarised in Table 6.10,

Case	Out-of-plane half-wavelengths	Summations	Subtractions	Out-of-plane half-wavelengths	In-plane half-wavelengths
$\xi = 1$	Q	$2Q-1$	1	Q	$3Q$
$0 < \xi < 1$	$2Q-1$	$2(2Q-1)-1 = 4Q-3$	$2(2Q-1)-1 = 4Q-3$	$2Q-1$	$10Q-7$
$\xi = 0$	Q	$2Q-1$	0	0	$2Q-1$

Table 6.10. Relationships between in-plane and out-of-plane half-wavelengths

The equilibrium equations are solving for the coefficients of a series of trigonometric terms representing in-plane displacements and the size of these coefficients is highly dependent on two parameters: the parameter Q defining the number of out-of-plane half-wavelengths and the number of nodes n . Considering both imaginary and real parts of the in-plane variables, noting there is no imaginary part if the half-wavelength is zero, the numbers of unknown variables including in-plane displacements in both the longitudinal and transverse directions are therefore:

$$\begin{aligned}
 2 * (6Q - 1) * n, & \quad \xi = 1 \\
 2 * (20Q - 15) * n, & \quad 0 < \xi < 1 \\
 2 * (4Q - 3) * n, & \quad \xi = 0
 \end{aligned}
 \tag{6.1}$$

The above equations indicate the extent to which the complexity increases as the number of out-of-plane half-wavelengths increases. To further investigate the influence on the computational efficiency of the number of half-wavelengths, two models, composite plates under combined loading and pure shear, are tested. To limit any effects noted to the choice of number of wavelengths, all plates are divided into 10 strips.

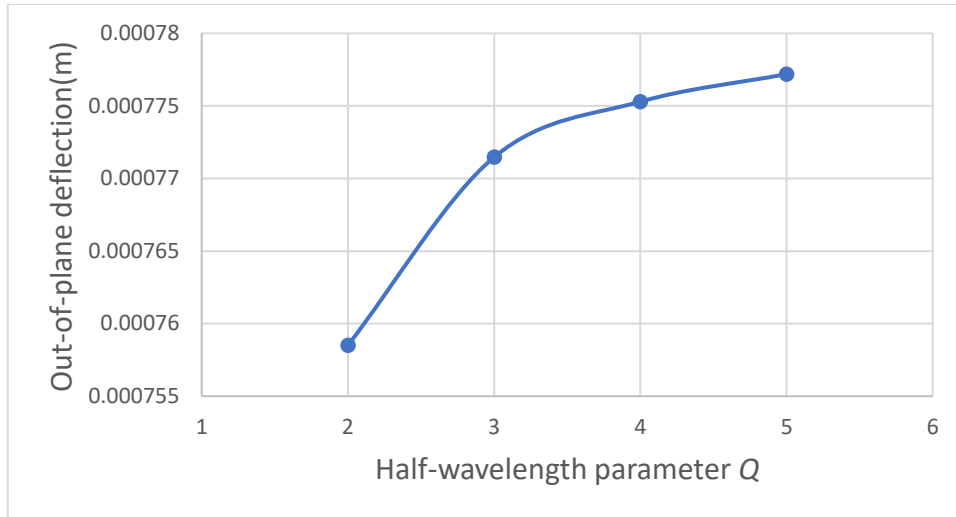


Figure 6.1. Out-of-plane deflections calculated using different numbers of half-wavelengths for a composite plate under combined loading, divided into 10 strips

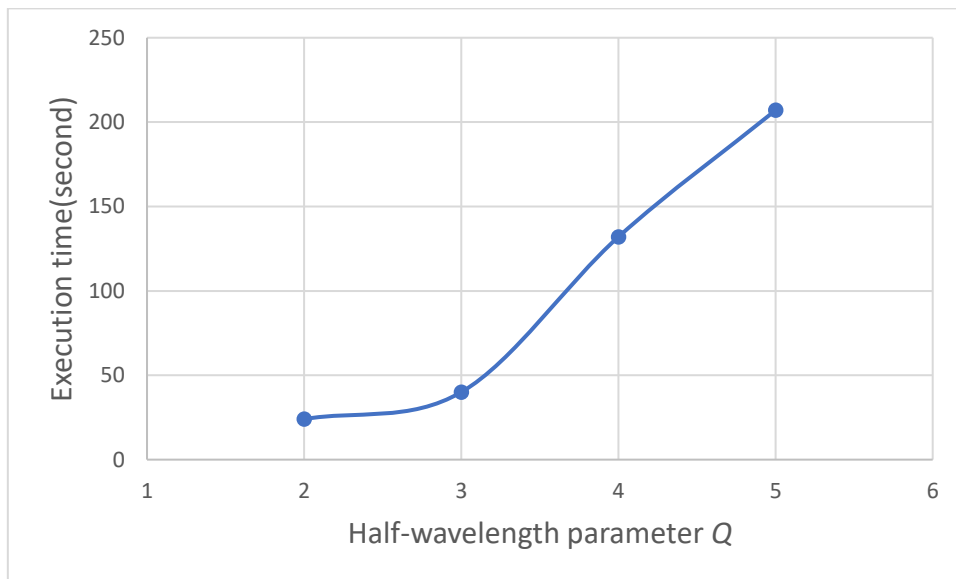


Figure 6.2. Execution time for different numbers of half-wavelengths from a composite plate under combined loading, divided into 10 strips

Figure 6.1 shows the out-of-plane deflection against the number of half-wavelengths, at 10% applied strain for a composite plate under combined loading for analysis with $\xi = 1$. Theoretically, increasing the number of half-wavelengths will result in more accurate results. From the figure the deflection increases as the number of wavelengths increases with a noticeable change of slope at $Q = 3$ above which the path tends to be flatter converging on a value of 0.78 mm which can therefore be taken as an estimate of the exact value in this case.

Equation 6.1 indicates a linear relationship between the unknown variables and out-of-plane half-wavelengths which can be seen in Figure 6.2. From $Q=2$ to $Q=3$, the execution time increases slightly and the accuracy increases the most, while when Q is 4 or 5, the accuracy does not alter much and the computational time increases almost three times, see Figures 6.1 and 6.2. It can be predicted that higher numbers of half-wavelengths will result in solutions which are very similar to those for $Q = 3, 4$ or 5 but which will incur significantly increased execution times and are therefore not worth being considered. Therefore for composite plates under compression or combined loading, three out-of-plane half-wavelengths can be considered adequate for postbuckling analysis.

For prebuckling analysis on the other hand for the above case of 5 half-wavelengths, the first half-wavelength $l/1$ makes 93% of the contribution to the buckling mode and $l/3$ and $l/5$ most of the other 7% between them. The rest of the half-wavelengths make less than 1% contribution to the buckling mode. It is therefore not surprising to see higher half-wavelengths, namely half-wavelengths smaller than $l/3$, only slow the computational efficiency.

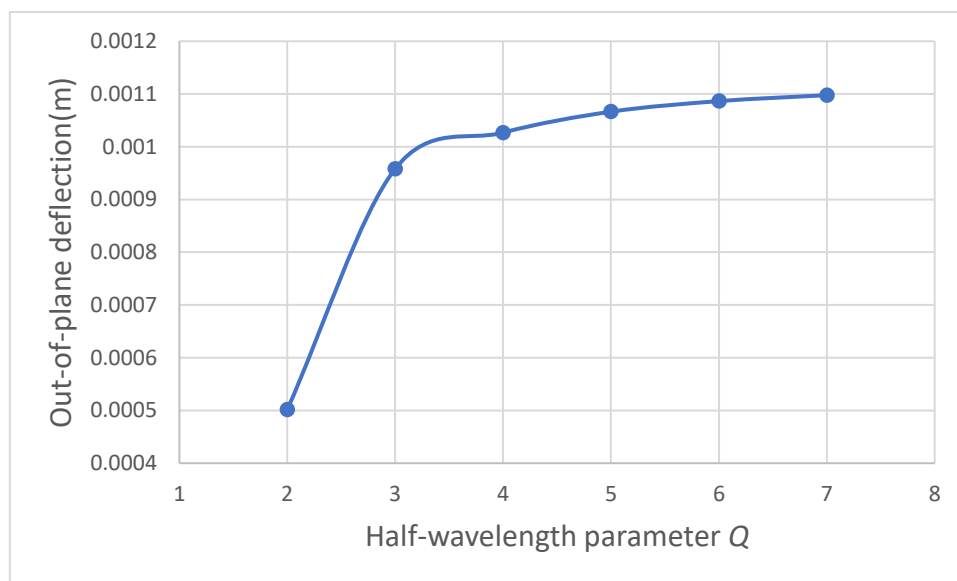


Figure 6.3. Out-of-plane deflections calculated by different half-wavelengths from a composite plate under shear loading, divided into 10 strips

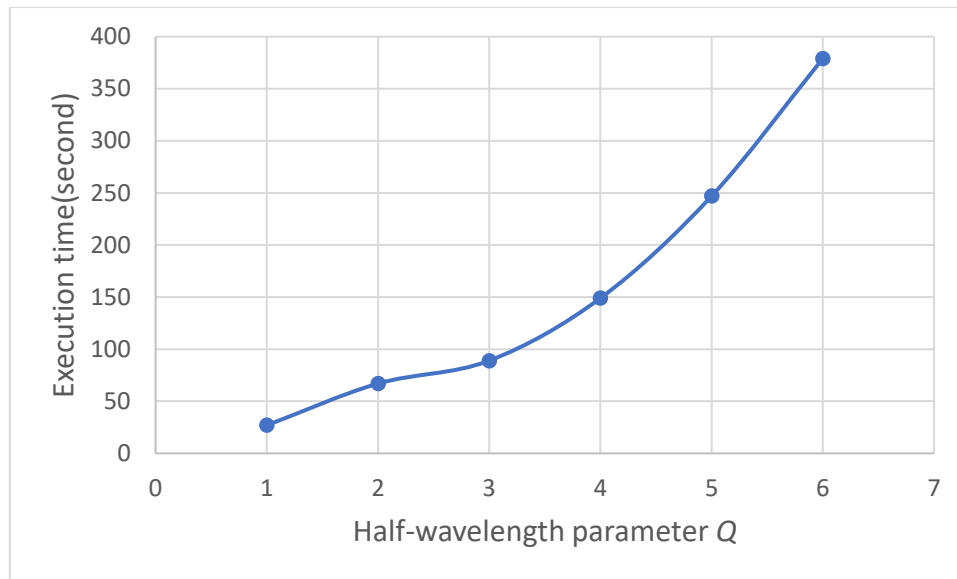


Figure 6.4. Execution time of different half-wavelengths from a composite plate under shear loading, divided by 10 strips

Figures 6.3 and 6.4 plot of out-of-plane deflection and execution time against the number of half-wavelengths respectively, at 5% constant strain above critical buckling for a composite plate under pure shear. The figures show very similar trends to those for the plate under combined loading with the deflection increasing rapidly up to a certain point and then levelling off. In the pure shear case, this happens at 4 half-wavelengths instead of the 3 found for the combined loading case. However, the increase in execution time between 4 and 5 half-wavelengths remains linear even though the increase in accuracy is quite small. From a prebuckling point of view, the fifth half-wavelength still makes a 3% contribution to the buckling mode (calculated from VICONOPT) and is therefore worth taking into account. This will be increasingly true as we move further along the postbuckling path and the contributions of each of the half-wavelengths will change with higher half-wavelengths making a higher contribution due to mode changes. Hence composite plates under pure shear require five out-of-plane half-wavelengths.

For unbalanced and unsymmetric composite plates where critical buckling has $\xi = 0$ or $0 < \xi < 1$, and the current analysis is only capable of analysing one cycle of postbuckling, recommendations on the required number of half-wavelengths cannot currently be made.

6.2. Number of nodes/strips

The number of nodes/strips is another important parameter which needs to be determined before analysis. Similar to the number of half-wavelengths, it influences the computational efficiency, see Equation 6.1, and accuracy. Observing Equations 4.13 and 4.38, the width of the strip determines the spacing of finite difference approximations between nodes. Decreasing the width of a strip, i.e. increasing the number of nodes, results in larger \mathbf{s} and \mathbf{f} matrices affecting the governing equilibrium equations, see Equations 4.46 and 4.47. Further influence on solutions, however, is hard to quantify based on explicit expressions. The number of strips required therefore, needs to be based on modelling experience.

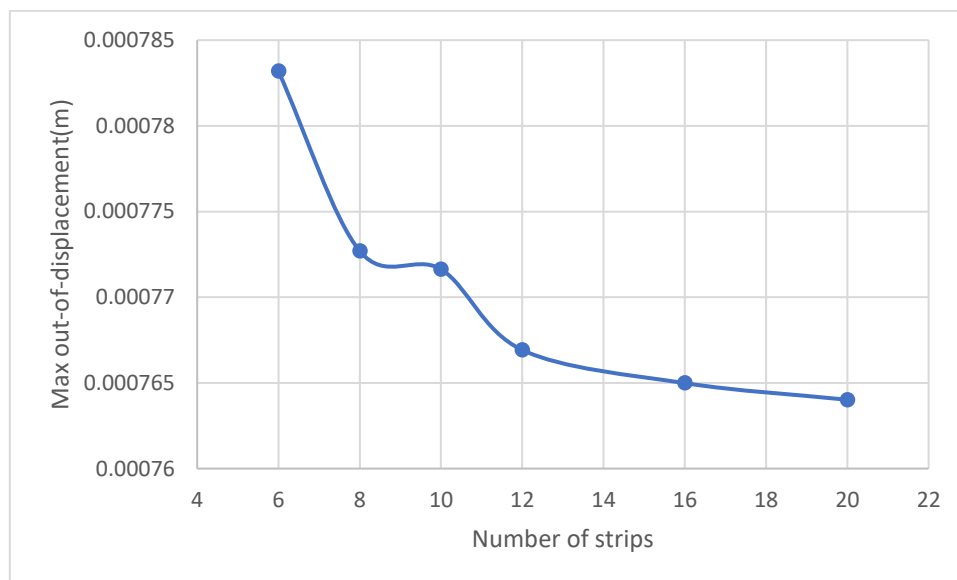


Figure 6.5. Max out-of-plane deflections calculated based on 3 half-wavelengths for a composite plate under combined loading, divided into different numbers of strips

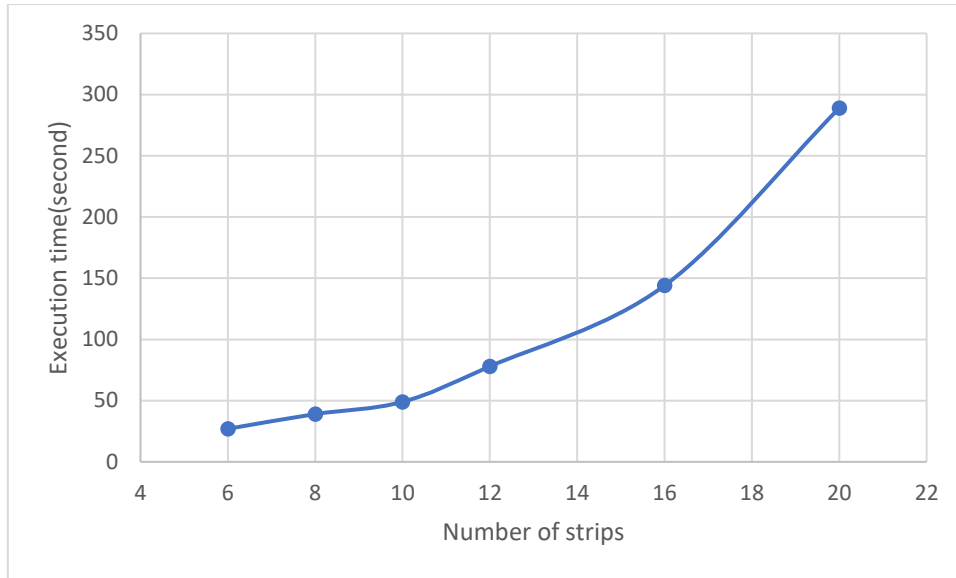


Figure 6.6. Execution time of 3 half-wavelengths for a composite plate under combined loading, divided into different numbers of strips

Figures 6.5 and 6.6 present curves of displacement and execution times against number of strips for a composite plate under combined load. As the exact solution of such a plate is around 0.78 mm, see Figure 6.1, the closest solution to this is when the plate is divided into 10 strips. Figure 6.5 shows that as the number of strips increases, the solutions converge on a value of 0.76 mm. Dividing the plate into more than 10 strips however changes the solution slightly at the cost of increased execution time, see Figure 6.6. For plates divided into less than 10 strips, the curve of the deflection against number of strips indicates that they are still unstable. Therefore 10 strips are found to be more than adequate to obtain the required accuracy and to represent postbuckling modes while retaining a comparably good efficiency. For other types of composite plates or under other loading conditions, 10 strips are also selected as the number of strips.

6.3. The ratio of linear strain increment α and the number of cycles

As described in Chapter 5, the increments along the postbuckling path are determined by an applied linear strain, defined by a ratio α . At each postbuckling equilibrium state, out-of-plane deflections are converged on the corresponding linear strain along which the in-plane displacements are found. The number of iterations required to converge on the equilibrium state is largely governed by the strain increment. If the increment is large, more iterations are required to converge and vice versa. An appropriate increment ratio α increases the computational efficiency and avoids convergence issues. Tests have shown that for composite plates under compression and combined loading, a 10% increment can achieve an average of two iterations to converge for all cycles (detailed solutions can be found in Chapter 7). 10% is, therefore, considered a suitable value for these types of loading. A similar investigation for pure shear has shown that 10% is too large for such cases to converge as the mode changes are more significant than for combined loading. A 5% strain increment ratio however has been found to be suitable for analysing such cases. Multiplying by the strain increment ratio, the number of cycles results in the farthest point of the postbuckling equilibrium state. It provides an option for researchers to select the range of the postbuckling regime.

6.4. The tolerance for Newton iteration scheme β

The modified Newton iteration scheme is developed to find out-of-plane displacements at certain applied strains, see Chapter 5. It uses the previous cycle's deflection as a trial value and accounts for changes in postbuckling stiffness to find the required adjustments to the displacements. Convergence is achieved when the difference between the maximum of the displacement adjustments \mathbf{d}^* and the maximum of the previous displacements \mathbf{D} is small enough as described in Chapter 5. Now bringing equation 5.1 here, this is assumed to occur when the criterion below is met.

$$\frac{|max(\mathbf{d}^*)-max(\mathbf{D})|}{max(\mathbf{D})} \leq \beta \quad \dots(6.2)$$

where β is a small positive number ($\beta \ll 0$), \mathbf{d}^* and \mathbf{D} , are the out-of-plane displacement adjustments and out-of-plane displacements from the previous iteration respectively.

β is a parameter that can be pre-set and has a default value of 0.1%. This value has been found to be small enough to converge on acceptable solutions with no convergence problems.

6.5. Conclusions

Similar to commercial simulation software, application of the coupled wavelength postbuckling analysis in this thesis requires a number of parameters to be selected when modelling. This chapter investigates the sensitivity of the results obtained to four parameters that have the potential to significantly affect accuracy and computational efficiency. The key findings are as follows.

The number of out-of-plane half-wavelengths is the most crucial parameter that affects the in-plane half-wavelengths and further decides the size of the governing equilibrium equations. For three values of ξ , it has been found that the influence of out-of-plane half-wavelengths is different. Investigations based on both explicit expressions and modelling experience are described in section 6.1. For plates under any in-plane loading other than pure shear, three out-of-plane half-wavelengths can achieve more than 99% accuracy without losing too much computational efficiency. For plates under pure shear, the optimal choice is increased to five out-of-plane half-wavelengths.

The number of strips that plates are divided by is equivalent to mesh size in finite element analysis. A similar analysis to that for the number of half-wavelengths has been conducted and found 10 strips to be adequate for the load cases tested.

Chapter 6

For the ratio of constant strain increment, 10% allows the solution to reach to the late stages of postbuckling at fastest rate without losing accuracy for non-pure shear plates while for plates under pure shear, since it is found that 10% would sometimes fail to converge, 5% is chosen.

Finally, 0.1% is selected as the tolerance for the Newton iteration scheme and no convergence problems are found.

Chapter 7. Illustrative Results and Validation

A study of sensitivity to parameter choices for the coupled wavelength postbuckling analysis was presented in chapter 6. CWPAN is capable of analysing the postbuckling behaviour of a wide range of composite plates with the desired speed and accuracy by adjusting predefined parameters, providing information on out-of-plane displacement, in-plane stress and strain distributions. In this chapter results for a number of illustrative cases are presented and validated against those obtained using the finite element analysis ABAQUS based on the Riks method. By comparing to the results obtained using the Riks method a deeper understanding of the capabilities and postbuckling behaviours of CWPAN can be gained. The chapter is organized as follows: Section 7.1 presents the problem definition for an isotropic plate under combined loading, Section 7.2 presents the solutions for such a plate and demonstrates the method's capability in terms of analysing various boundary conditions. Section 7.3 presents the modelling of symmetric and balanced composites plates under compression and validates the results obtained using FEA. Sections 7.4 and 7.5 solve the case of a composite plate under combined loading and pure shear respectively, which are again compared with results obtained from FEA. Section 7.6 illustrates the method's capability to analyse more general cases such as unsymmetric and unbalanced laminated composite. Section 7.7 presents the computational efficiency of the method for a range of typical composite plates. Section 7.8 concludes the chapter.

7.1. Overview

Chapters 4 and 5 presented CWPAN in which the buckling mode is represented by a series of sinusoidal terms with any predefined half-wavelengths. By combining different half-wavelengths to achieve the required mode shape, as in the VICON analysis, CWPAN is able

to analyse modes which are skewed due to anisotropy or shear loading. In this chapter, both isotropic and composite plates involving these skewed mode shapes are modelled and analysed using CWPAN. To compare different materials and loading conditions, all models have the same geometry - square plates with edge length 300mm, thickness 2mm, as shown in Figure 7.1.

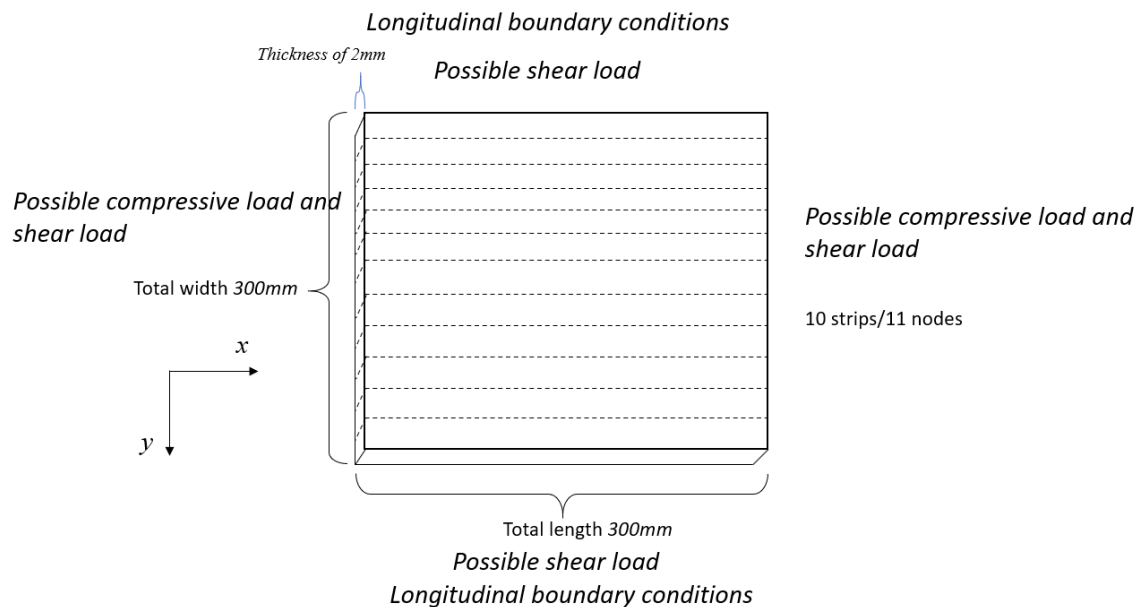


Figure 7.1. The CWPAN model: in-plane boundary conditions and loading conditions

Cases studied include isotropic plates, balanced symmetric composites, unbalanced symmetric composites and unbalanced unsymmetric composites, with each tested under three different in-plane longitudinal boundary conditions - free edges, straight edges and fixed edges, see Section 4.6. Focusing on cases where skewing is present, isotropic plates under compression and shear, composite plates under compression, composite plates under pure shear and unbalanced symmetric and unbalanced unsymmetric laminated composites are modelled and analysed in this chapter.

Before starting the analysis, as mentioned in the previous chapter, a number of parameters must be decided upon in order to ensure the optimum accuracy and speed. First is the number of half wavelengths to be used. All analysis is with $\xi = 1$ in VICON as it is adequate for most of the cases, and other choices of ξ are explained in the section 7.5. Three half-wavelengths are therefore selected for out-of-plane displacements which are $l/(1,3,5)$, the justification for such choices being explained in Section 6.1. The in-plane displacements are represented by $l/(0,1,2,3,4,5,6,8,10)$. Next is the number of strips in the model. Here 10 strips (11 nodes) are

considered to be sufficient for this size of plate. The ratio of the increment of end shortening strain is chosen as 10%, noting here that for the case of a plate under pure shear this is changed to 5% since 10% may not sufficiently capture the changing buckling modes and fail to converge. Finally 10 cycles and 0.1% are chosen as the number of cycles and the tolerance in the modified Newton iteration scheme. Detailed discussion regarding such choices is presented in Chapter 6.

All models are run in VICONOPT first to obtain the initial buckling mode to be used in the first iteration of the first cycle in the postbuckling analysis. In VICONOPT, the plate is modelled with the same boundary conditions as the postbuckling analysis to ensure consistency on both transverse and longitudinal edges.

7.2. Isotropic plate under combined loading

In this section, an isotropic plate under combined compression and shear loading is modelled to investigate the slightly skewed postbuckling mode. The material properties are Young's modulus $E = 110 \text{ kNmm}^{-2}$ and Poisson's ratio $\nu = 0.3$. Initial buckling is attained assuming a ratio of 50% between the shear and longitudinal stress resultants, followed by postbuckling analysis in which there is a constant ratio between the applied shear and longitudinal strains. The plate is simply supported (restricting out of plane displacement) along all four edges with three different in-plane boundary conditions applied along its longitudinal edges, see Figure 7.2.

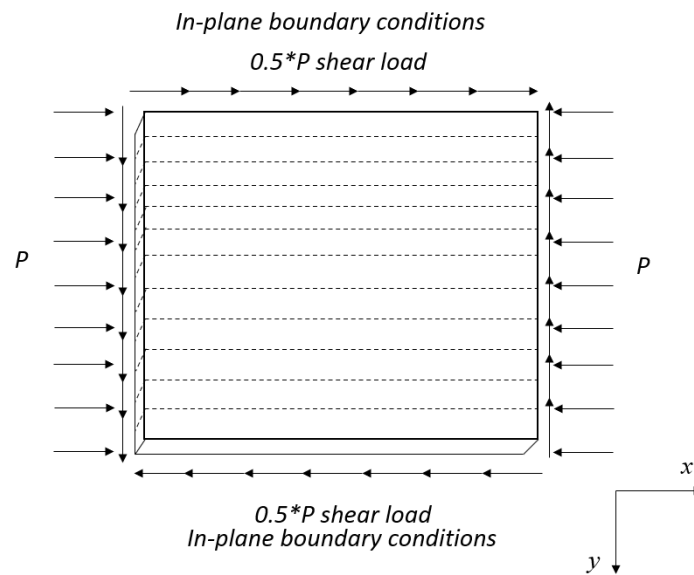


Figure 7.2. Load and boundary conditions for isotropic plate under combined load

VICON analyses are run first to extract the critical buckling modes, critical buckling loads and end shortening strains. For the case of in-plane free edges, the end shortening compressive and shear strains can be pre-determined by the ratio α as;

Cycle	0	1	2	3	...	19	20
$\overline{\varepsilon}_x$	-1.57E-4	-1.72E-4	-1.88E-4	-2.04E-4	...	-4.55E-4	-4.71E-4
$\overline{\gamma}_{xy}$	-2.04E-4	-2.24E-4	-2.45E-4	-2.65E-4	...	-5.92E-4	-6.13E-4
Normalized	1	1.1	1.2	1.3		2.9	3

Table 7.1. End shortening strains at postbuckling cycles, 0 indicates critical buckling point. For each postbuckling cycle, in-plane displacements u and v are obtained directly by solving the equilibrium equations. Then distributions of strains and stresses can be tabulated and plotted to observe their progression.

Terms Node	C0	C1	S1	C2	S2	C3	S3	C4	S4	C5	S5	C6	S6	C8	S8	C10	S10
1	0	0	0	-6.30E-22	-1.34E-21	0	0	2.06E-23	-1.27E-23	0	0	-1.74E-23	3.00E-24	9.08E-26	1.04E-24	-1.71E-27	-1.00E-26
2	-6.96E-07	0	0	5.22E-07	-9.43E-07	0	0	4.30E-07	-1.82E-08	0	0	6.08E-08	2.76E-08	-1.46E-09	1.69E-08	-2.46E-10	2.15E-09
3	-1.15E-06	0	0	7.38E-07	-3.11E-06	0	0	1.21E-06	5.10E-08	0	0	1.57E-07	7.53E-08	-7.51E-09	3.35E-08	-6.45E-10	3.77E-09
4	-1.13E-06	0	0	7.37E-07	-5.92E-06	0	0	1.53E-06	2.79E-07	0	0	1.70E-07	6.52E-08	-9.43E-09	2.52E-08	-4.46E-10	2.69E-09
5	-6.76E-07	0	0	4.71E-07	-8.24E-06	0	0	1.04E-06	4.98E-07	0	0	1.07E-07	1.47E-08	-5.64E-09	7.38E-09	-8.37E-11	8.03E-10
6	-7.60E-12	0	0	6.27E-12	-9.14E-06	0	0	7.72E-12	5.80E-07	0	0	8.84E-14	-1.26E-08	-3.15E-14	-9.43E-10	-7.11E-16	-4.35E-11
7	6.76E-07	0	0	-4.71E-07	-8.24E-06	0	0	-1.04E-06	4.98E-07	0	0	-1.07E-07	1.47E-08	5.64E-09	7.38E-09	8.38E-11	8.03E-10
8	1.13E-06	0	0	-7.37E-07	-5.92E-06	0	0	-1.53E-06	2.79E-07	0	0	-1.70E-07	6.52E-08	9.43E-09	2.52E-08	4.46E-10	2.69E-09
9	1.15E-06	0	0	-7.38E-07	-3.11E-06	0	0	-1.21E-06	5.10E-08	0	0	-1.57E-07	7.53E-08	7.51E-09	3.35E-08	6.45E-10	3.77E-09
10	6.96E-07	0	0	-5.22E-07	-9.43E-07	0	0	-4.30E-07	-1.82E-08	0	0	-6.08E-08	2.76E-08	1.46E-09	1.69E-08	2.46E-10	2.15E-09
11	0	0	0	-6.44E-21	-5.07E-21	0	0	-8.09E-22	-1.41E-21	0	0	-6.46E-23	3.97E-22	6.79E-23	3.01E-23	4.78E-25	7.44E-24

Table 7.2. Amplitudes of nodal in-plane displacement u from CWPAN for an isotropic plate under compression and shear with in-plane free edges at cycle 10

Terms Node	C0	C1	S1	C2	S2	C3	S3	C4	S4	C5	S5	C6	S6	C8	S8	C10	S10
1	2.12E-05	0	0	-7.22E-06	2.27E-07	0	0	-4.54E-08	-4.29E-07	0	0	3.01E-09	-1.65E-08	5.64E-09	-2.12E-09	5.29E-10	-1.85E-10
2	1.47E-05	0	0	-1.43E-06	-2.49E-06	0	0	9.35E-08	5.36E-07	0	0	-3.61E-08	1.89E-07	-1.48E-08	-3.33E-09	-1.32E-09	-2.76E-10
3	9.12E-06	0	0	2.54E-06	-3.39E-06	0	0	-7.02E-08	8.03E-07	0	0	-2.74E-08	2.06E-07	-3.31E-09	-3.81E-09	-7.33E-11	-6.03E-11
4	4.88E-06	0	0	3.89E-06	-2.71E-06	0	0	-2.38E-07	4.52E-07	0	0	6.23E-09	1.26E-07	8.34E-09	-8.60E-10	7.08E-10	1.39E-10
5	2.02E-06	0	0	2.70E-06	-1.62E-06	0	0	-1.98E-07	-3.95E-08	0	0	1.77E-08	4.57E-08	8.09E-09	1.03E-09	5.86E-10	5.87E-11
6	0	0	0	-9.20E-12	-1.13E-06	0	0	-2.77E-12	-2.52E-07	0	0	3.47E-13	1.41E-08	4.96E-14	1.27E-09	1.37E-15	-3.88E-11
7	-2.02E-06	0	0	-2.70E-06	-1.62E-06	0	0	1.98E-07	-3.95E-08	0	0	-1.77E-08	4.57E-08	-8.09E-09	1.03E-09	-5.86E-10	5.87E-11
8	-4.88E-06	0	0	-3.89E-06	-2.71E-06	0	0	2.38E-07	4.52E-07	0	0	-6.23E-09	1.26E-07	-8.34E-09	-8.60E-10	-7.08E-10	1.39E-10
9	-9.12E-06	0	0	-2.54E-06	-3.39E-06	0	0	7.02E-08	8.03E-07	0	0	2.74E-08	2.06E-07	3.31E-09	-3.81E-09	7.33E-11	-6.03E-11
10	-1.47E-05	0	0	1.43E-06	-2.49E-06	0	0	-9.35E-08	5.36E-07	0	0	3.61E-08	1.89E-07	1.48E-08	-3.33E-09	1.32E-09	-2.76E-10
11	-2.12E-05	0	0	7.22E-06	2.27E-07	0	0	4.53E-08	-4.29E-07	0	0	-3.01E-09	-1.65E-08	-5.64E-09	-2.12E-09	-5.29E-10	-1.85E-10

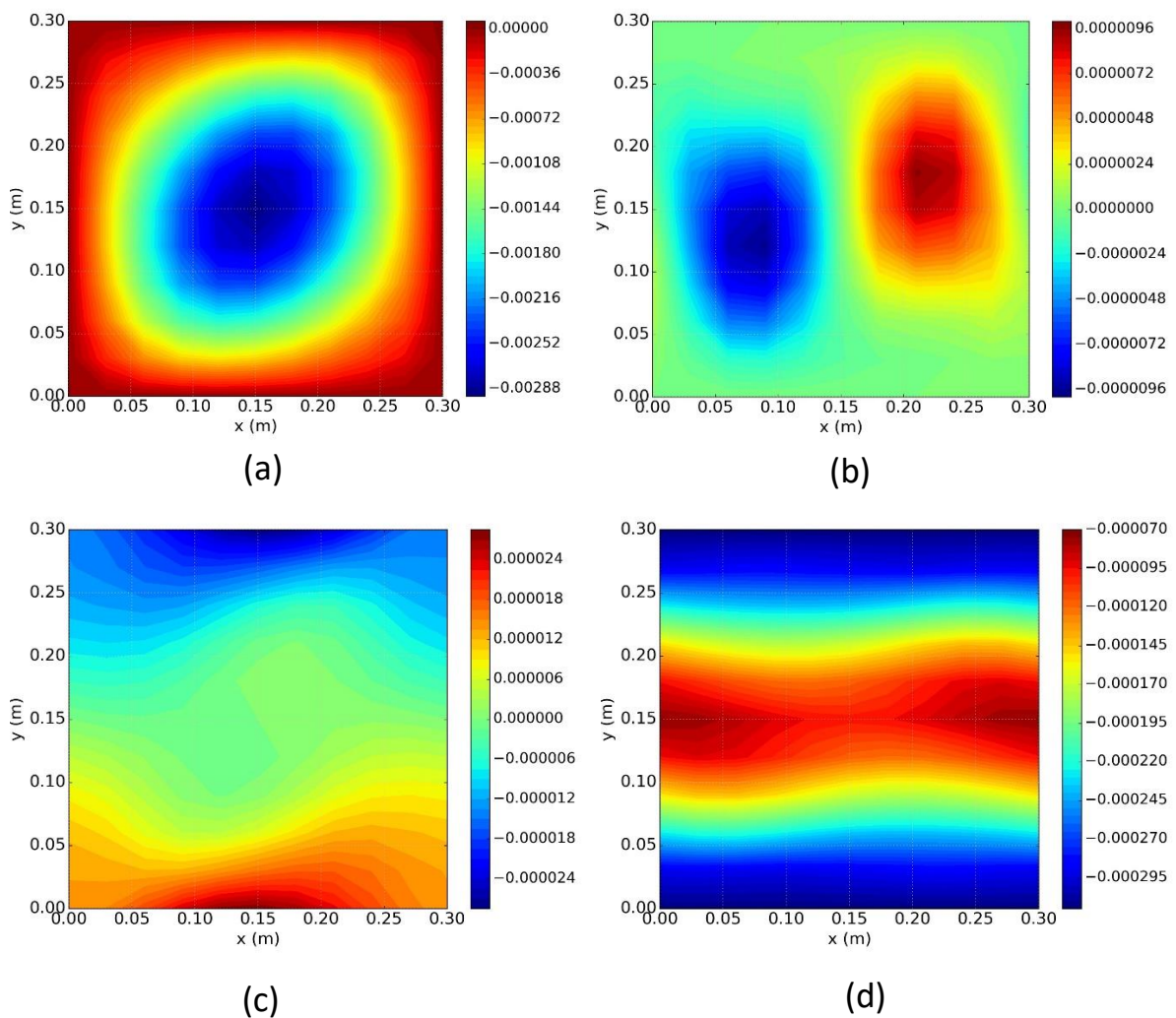
Table 7.3. Amplitudes of nodal in-plane displacement v from CWPAN for an isotropic plate under compression and shear with in-plane free edges at cycle 10

Terms Node	C1	S1	C3	C3	C5	S5
1	-0.00453	-0.02973	0.003613	2.67E-05	0.000673	2.42E-05
2	-0.00299	-0.02854	0.002598	0.000349	0.000419	4.48E-05
3	-0.00055	-0.02454	0.000534	0.000578	1.07E-05	1.04E-05
4	0.001509	-0.01787	-0.00125	0.000486	-0.00023	-2.75E-05
5	0.002724	-0.00937	-0.00234	0.000244	-0.00035	-3.16E-05
6	0.003112	-2.83E-08	-0.00269	2.48E-08	-0.00038	3.13E-09
7	0.002724	0.009371	-0.00234	-0.00024	-0.00035	3.16E-05
8	0.001509	0.017868	-0.00125	-0.00049	-0.00023	2.75E-05
9	-0.00055	0.024539	0.000534	-0.00058	1.07E-05	-1.04E-05
10	-0.00299	0.028541	0.002598	-0.00035	0.000419	-4.48E-05
11	-0.00453	0.029733	0.003613	-2.68E-05	0.000673	-2.42E-05

Terms Node	C1	S1	C3	S3	C5	S5
1	-0.00453	-0.02973	0.003613	2.67E-05	0.000673	2.42E-05
2	-0.00299	-0.02854	0.002598	0.000349	0.000419	4.48E-05
3	-0.00055	-0.02454	0.000534	0.000578	1.07E-05	1.04E-05
4	0.001509	-0.01787	-0.00125	0.000486	-0.00023	-2.75E-05
5	0.002724	-0.00937	-0.00234	0.000244	-0.00035	-3.16E-05
6	0.003112	-2.83E-08	-0.00269	2.48E-08	-0.00038	3.13E-09
7	0.002724	0.009371	-0.00234	-0.00024	-0.00035	3.16E-05
8	0.001509	0.017868	-0.00125	-0.00049	-0.00023	2.75E-05
9	-0.00055	0.024539	0.000534	-0.00058	1.07E-05	-1.04E-05
10	-0.00299	0.028541	0.002598	-0.00035	0.000419	-4.48E-05
11	-0.00453	0.029733	0.003613	-2.68E-05	0.000673	-2.42E-05

Table 7.4. Amplitudes of nodal out-of-plane displacement w (left) and rotation ϕ (right) by Newton iteration scheme for an isotropic plate under compression and shear with in-plane free edges at cycle 10

As shown in Tables 7.2 and 7.3, the solutions obtained by solving the equilibrium equations correspond to nine half-wavelengths with both real (cosine) and imaginary (sine) parts. It can be seen that the results for both u and v are perfectly antisymmetric in the transverse direction. This is because whilst both the geometry and material are symmetric, the loading condition is antisymmetric leading to an antisymmetric solution. Another observation is that the amplitudes of the sinusoidal terms decrease as the half-wavelength increases, with the amplitude of the $l/10$ term being approximately 0.1% of that of the $l/1$ one. The contributions of the $l/10$ term for the buckling mode are therefore insignificant, which means that its existence only slows down the calculations. However, it cannot be simply be neglected since the half-wavelength $l/10$ for the in-plane displacements is calculated from the half-wavelength $l/5$ for the out-of-plane displacements $l/(5+5)$, and $l/5$ makes a contribution to the out-of-plane displacements which cannot be ignored, see Table 7.4.



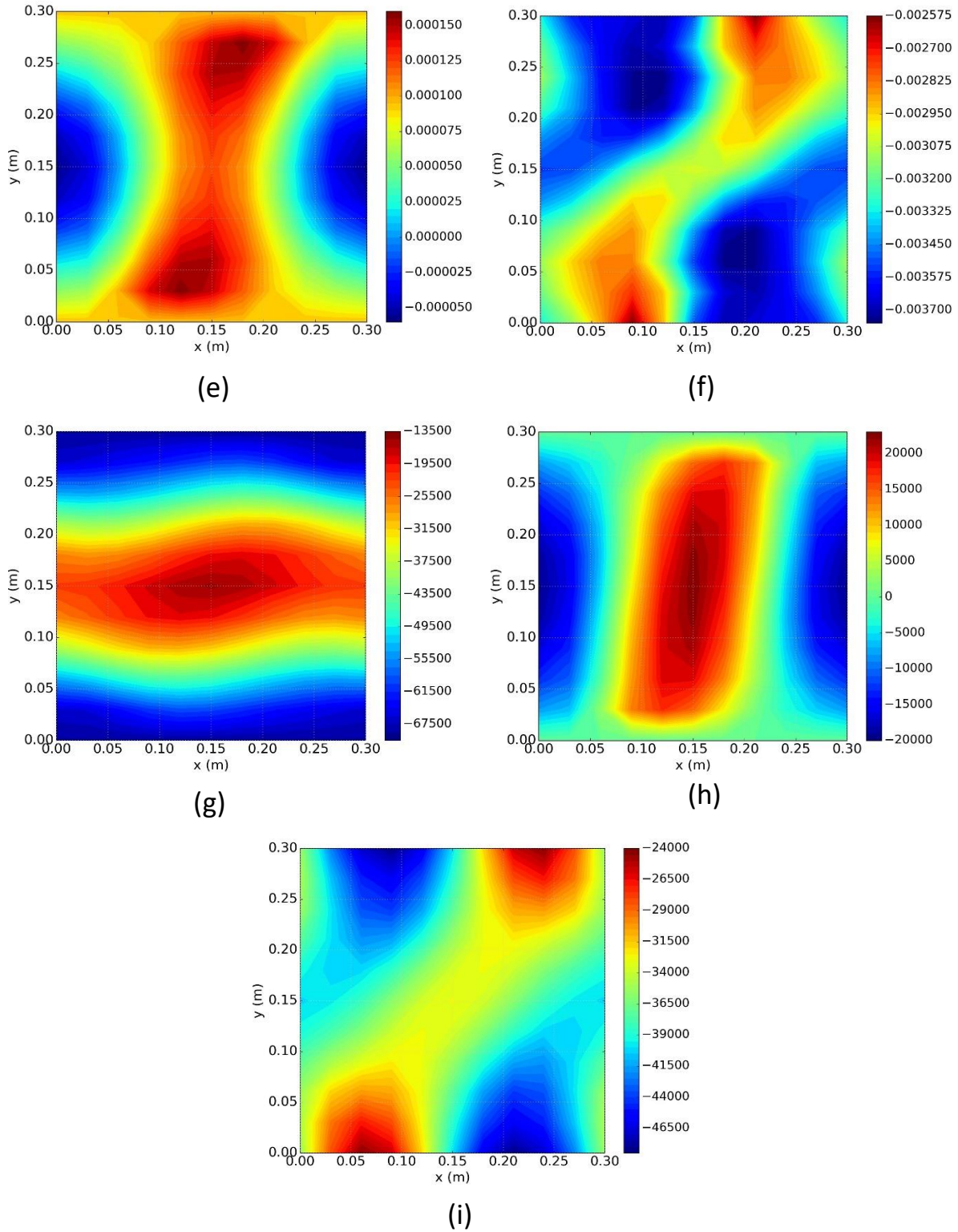


Figure 7.3. Contour plots of (a) out-of-plane displacements w (m); (b) in-plane displacements u (m); (c) in-plane displacements v (m); (d) strain ϵ_x ; (e) strain ϵ_y ; (f) strain γ_{xy} ; (g) stress resultant N_x ; (h) stress resultant N_y (N/m); (i) stress resultant N_{xy} (N/m), under compression and shear with free in-plane edge conditions, at cycle 10 (200% of initial end shortening strain)

After obtaining the displacements u and v by solving the in-plane equilibrium equations, stresses and strain can be calculated trigonometrically. To present the solutions visually, the trigonometric terms are required to be transformed to actual values at specific locations. Figure 7.3 illustrates the converged solutions for CWPAN at cycle 10. It is worth noting that in Figure 7.3 (b) and (c), the contours only plot the variations in the displacements, with the linear terms of Equation 4.2 excluded since they are very large compared to the variations which hence would be obscured. It can be seen that the contour plots are all skewed in the direction of the shear load and antisymmetric due to the antisymmetric solutions of the in-plane displacements. Figure 7.4 presents the postbuckling load paths for both compression and shear from cycle 1 to cycle 20. The path of the compression applied at the transverse edges increments in an approximately quadratic manner. On the other hand, the shear loading is approximately linear. Another observation is that the compression path decreases at a strain of about $4e-4$, i.e. around cycles 19 and 20. This is because, from Figures 7.5 and 7.6, the equivalent stress resultants redistribute at every cycle, with the stress in the middle strip starting to become negative at this point resulting in a decrease in the total load for the whole plate. Figure 7.7 shows the stress resultant path for each strip, from which it can be seen that strips 6-10 are symmetric to strips 1-5, where the dashed line represents the stress resultants at the critical buckling point. It can also be seen that the nearer the strips are to the edges, the more the stress increases. In the middle strips 5 and 6, the stress resultants decrease instead of increasing. Figure 7.6 shows the shear stress resultants at each postbuckling cycle.

The reason for the approximately linear increments in the shear in Figure 7.4 can be concluded from Figures 7.6 and 7.8, where the equivalent shear stress on each strip increases linearly. From a structural point of view, shear stress does not have the same effect of stress redistribution as occurs with longitudinal stress. Figure 7.9 presents the progressive out-of-plane deflection at each cycle obtained using the modified Newton iteration scheme.

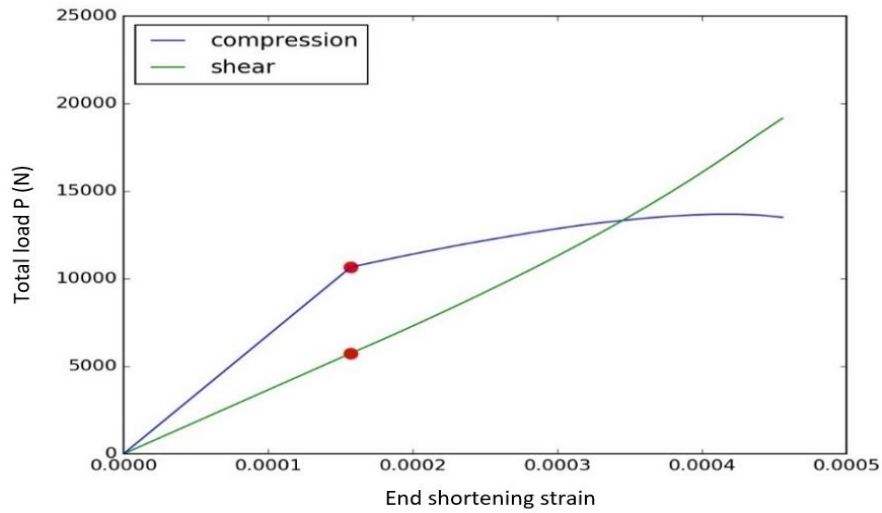


Figure 7.4 Postbuckling behaviour of load strain curve

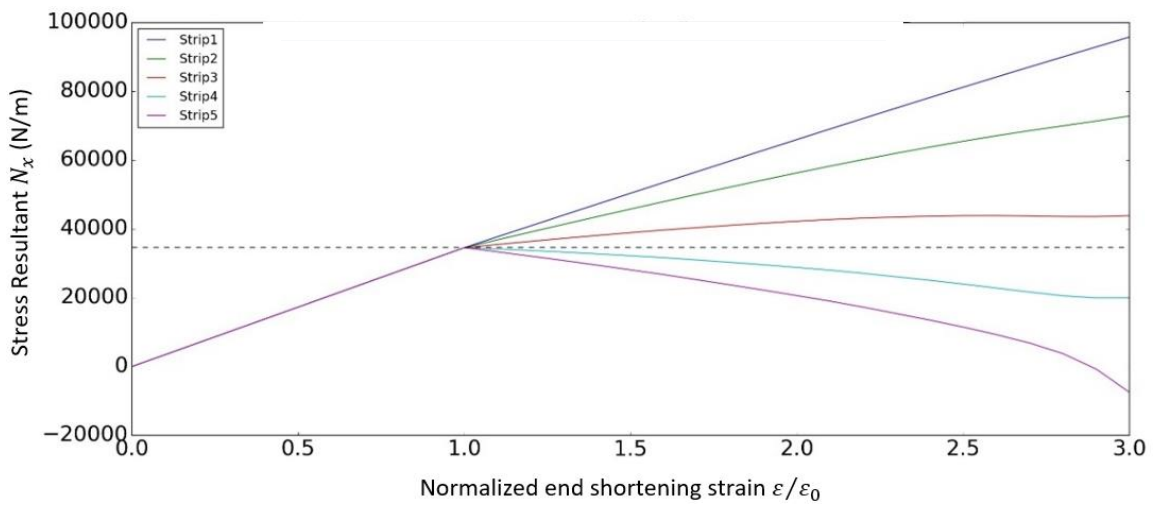


Figure 7.5 Equivalent uniform longitudinal stress at strip vs normalized end shortening strains

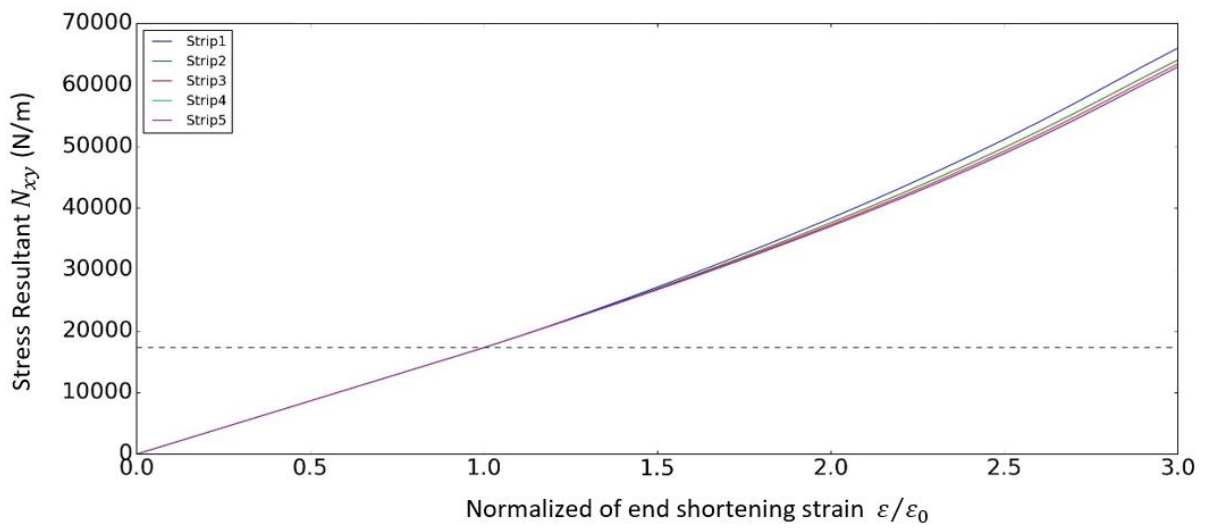
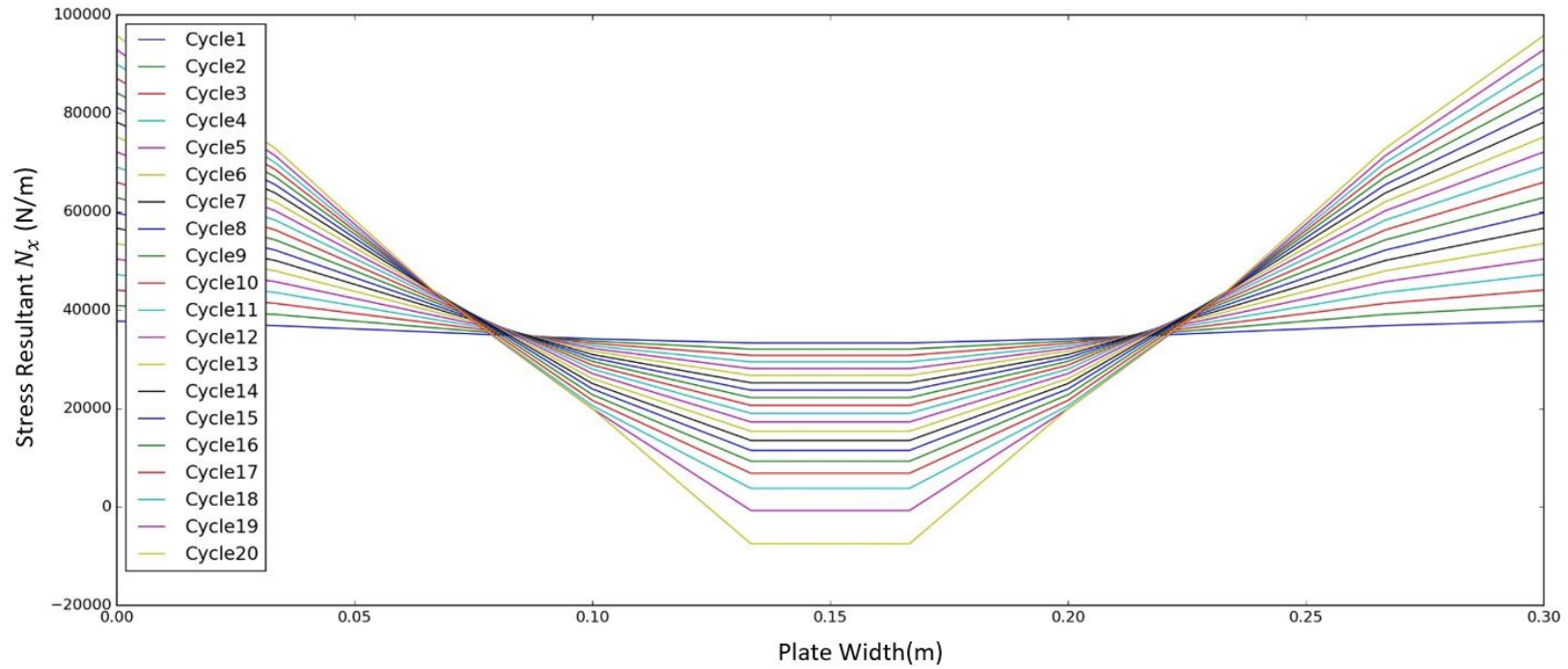
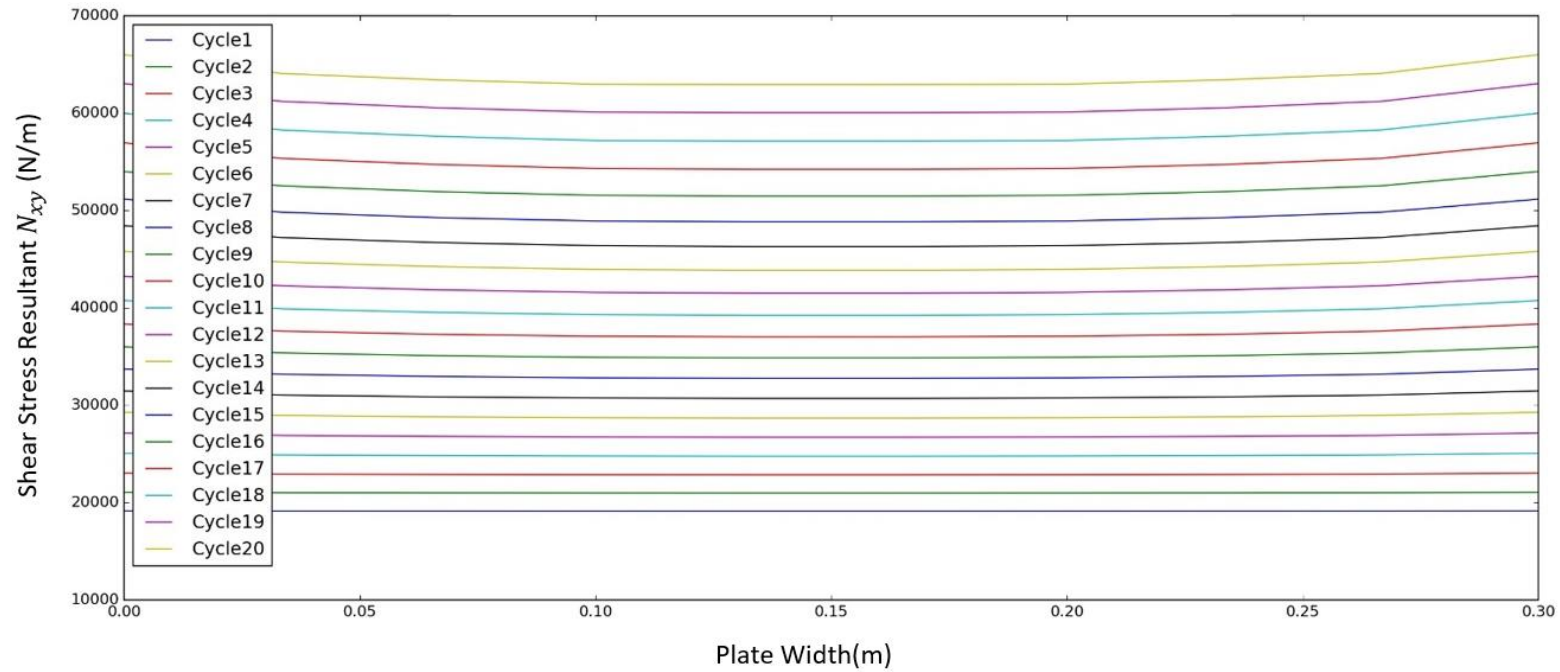


Figure 7.6. Equivalent uniform shear stress at strip vs normalized end shortening strains



Cycle	1	2	3	4	5	6	7	8	9	10	11	12	13	14	15	16	17	18	19	20
Strip 1	37756	40925	44089	47245	50395	53538	56667	59788	62900	65997	69082	72145	75186	78210	81207	84173	87109	90013	92910	95817
Strip 2	36864	39127	41376	43597	45796	47971	50099	52200	54274	56300	58285	60195	62028	63811	65504	67095	68586	69978	71375	72848
Strip 3	35513	36415	37295	38132	38935	39707	40398	41059	41688	42252	42766	43168	43462	43712	43850	43865	43779	43615	43596	43852
Strip 4	34174	33734	33274	32765	32222	31652	30983	30297	29594	28828	28030	27113	26092	25079	23985	22821	21656	20583	19976	19991
Strip 5	33350	32087	30808	29478	28117	26733	25239	23734	22219	20639	19027	17276	15394	13512	11491	9288	6844	3780	-714	-7465
Strip 6	33350	32087	30808	29478	28117	26733	25239	23734	22219	20639	19027	17276	15394	13512	11491	9288	6844	3781	-714	-7472
Strip 7	34174	33734	33274	32765	32222	31652	30983	30297	29594	28828	28030	27113	26092	25079	23984	22821	21657	20584	19978	19990
Strip 8	35513	36415	37295	38132	38935	39707	40398	41059	41688	42252	42766	43168	43461	43712	43848	43865	43780	43617	43600	43864
Strip 9	36864	39127	41376	43597	45796	47971	50099	52200	54274	56300	58285	60195	62028	63810	65502	67095	68586	69979	71378	72852
Strip 10	37756	40925	44089	47245	50395	53538	56667	59788	62900	65997	69082	72145	75186	78210	81207	84173	87109	90013	92910	95816

Figure 7.7. Equivalent uniform stress distribution at each postbuckling cycle



Cycle	1	2	3	4	5	6	7	8	9	10	11	12	13	14	15	16	17	18	19	20
Strip 1	19141	21058	23033	25064	27146	29278	31465	33703	35993	38343	40752	43236	45797	48435	51166	54002	56946	59988	63038	66000
Strip 2	19126	21007	22931	24897	26904	28952	31047	33186	35372	37612	39909	42273	44710	47224	49829	52535	55352	58270	61209	64073
Strip 3	19124	20991	22892	24827	26798	28807	30857	32950	35089	37280	39529	41844	44233	46701	49264	51932	54718	57615	60546	63415
Strip 4	19122	20981	22869	24786	26737	28721	30746	32812	34922	37085	39304	41589	43947	46386	48919	51559	54318	57190	60106	62968
Strip 5	19122	20977	22859	24769	26712	28688	30704	32761	34863	37018	39231	41510	43865	46302	48834	51477	54240	57119	60047	62930
Strip 6	19122	20977	22859	24769	26712	28688	30704	32761	34863	37018	39231	41510	43865	46302	48834	51477	54240	57119	60048	62934
Strip 7	19122	20981	22869	24786	26737	28721	30746	32812	34922	37085	39304	41589	43947	46386	48919	51559	54318	57190	60106	62975
Strip 8	19124	20991	22892	24827	26798	28807	30857	32950	35089	37280	39529	41844	44233	46701	49264	51932	54718	57614	60546	63417
Strip 9	19126	21007	22931	24897	26904	28952	31047	33186	35372	37612	39909	42273	44710	47224	49829	52535	55352	58270	61209	64072
Strip 10	19141	21058	23033	25064	27146	29278	31465	33703	35993	38343	40752	43236	45797	48435	51167	54002	56945	59988	63038	65999

Figure 7.8 Equivalent uniform shear stress distribution at each postbuckling cycle

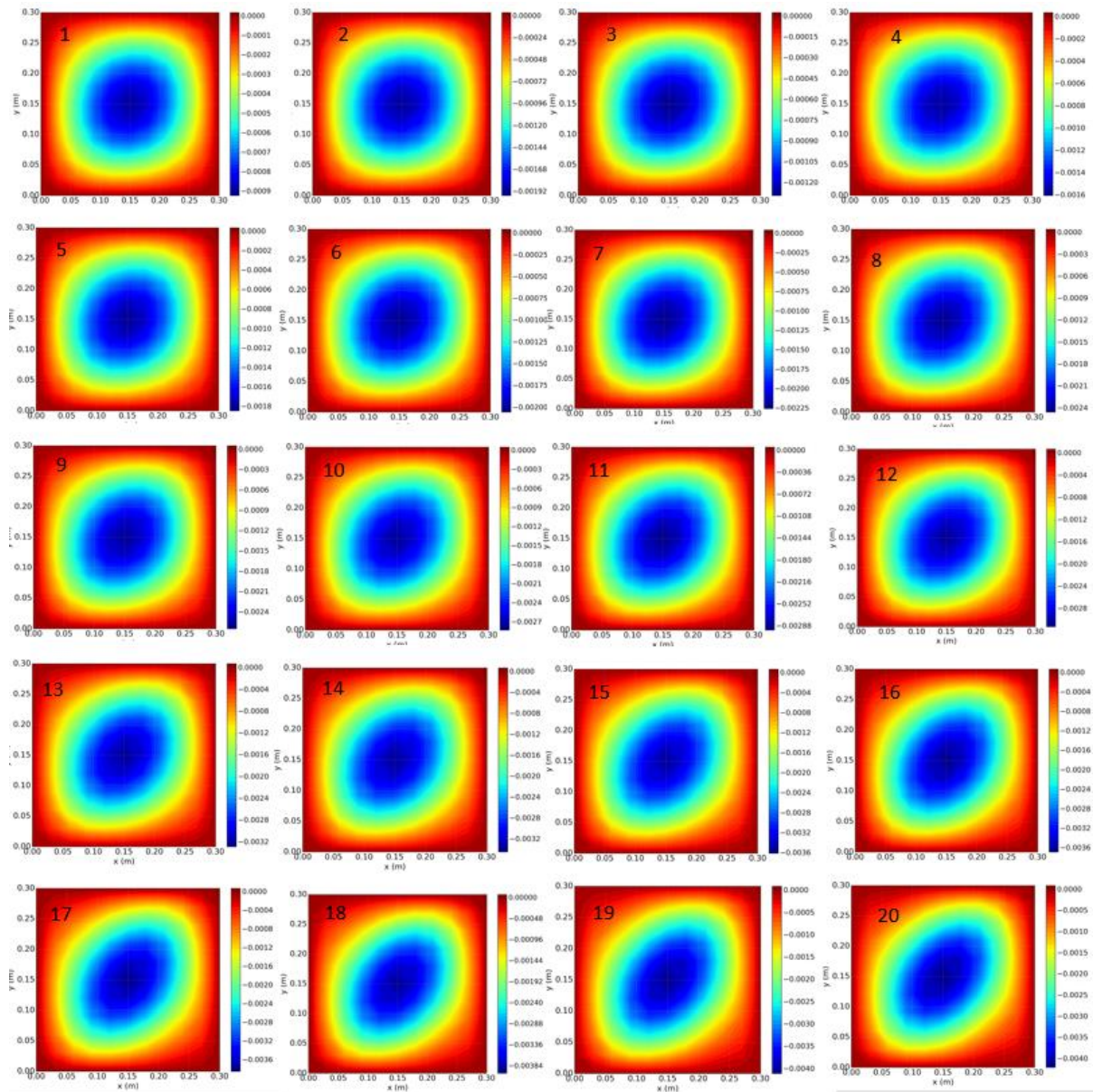


Figure 7.9. Contour plots of out-of-plane displacements at cycles 1 to 20, showing the progressive buckling mode.

If the boundary conditions in the longitudinal direction are changed to either fixed or straight edges, the v displacement contours are affected whilst the u displacements contours merely change shape. Figure 7.10 presents the v contour for each boundary condition at cycle 10. The plate with fixed edges is seen to have quite a different displacement distribution with two skewed contours and zero displacement along the longitudinal edges. For the straight edges plate, the v displacements at the edges are constant and the contours are in between those for the free and fixed edge plates.

Figures 7.11 and 7.12 show the equivalent uniform longitudinal stresses distributions from cycles 1 to 20 for plates with straight and fixed edges respectively. For the plate with straight edges, it can be seen that the stress resultants are all positive due to the Poisson effect. For the fixed edge plate, the stress resultants for each of the cycles show a much lower level of redistribution with no interaction occurring due to there being less difference between the stresses nearer the edge and in the middle. Another effect of changing the longitudinal v boundary conditions is that introducing constraint results in stresses N_y on the longitudinal boundaries which are zero for free and straight edges, see Figure 7.13. Figure 7.14 presents the load paths for each of the boundary conditions.

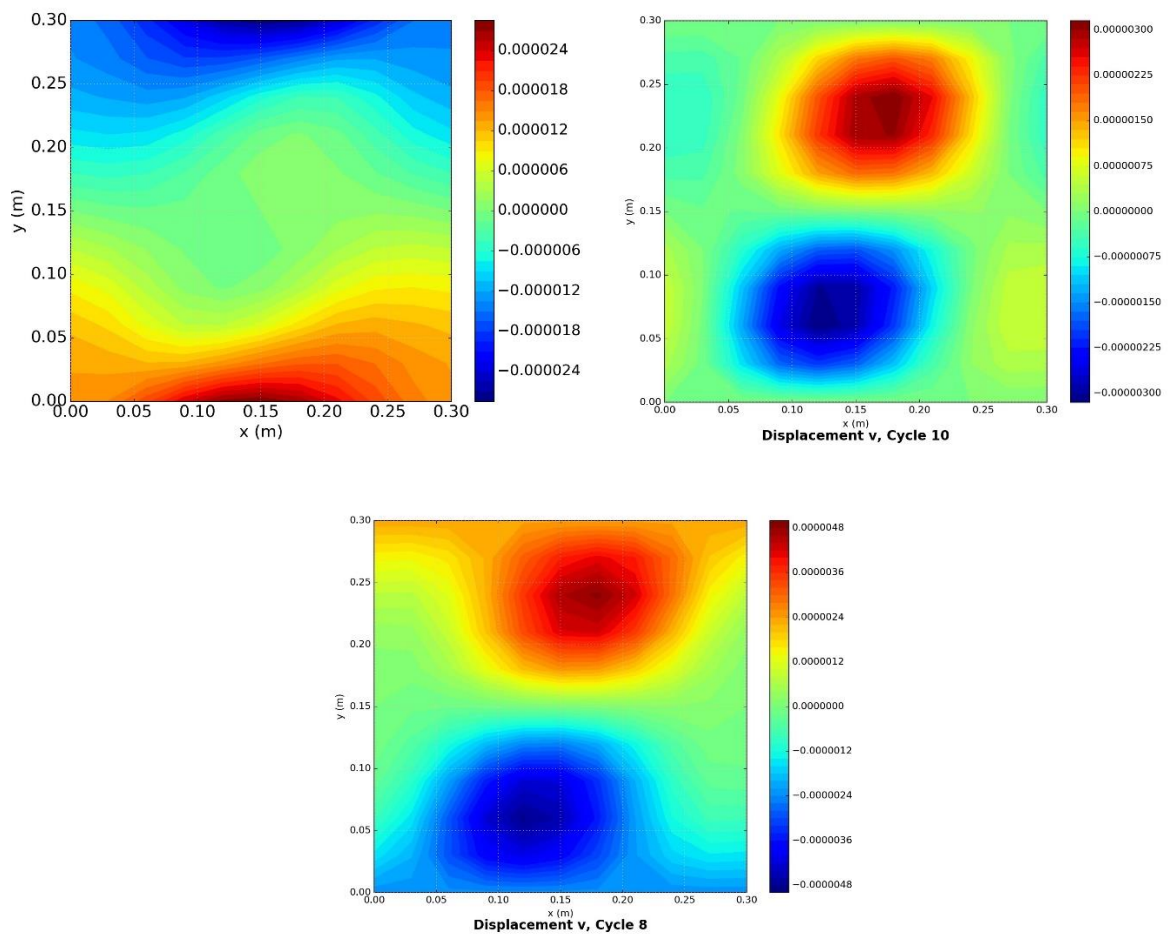
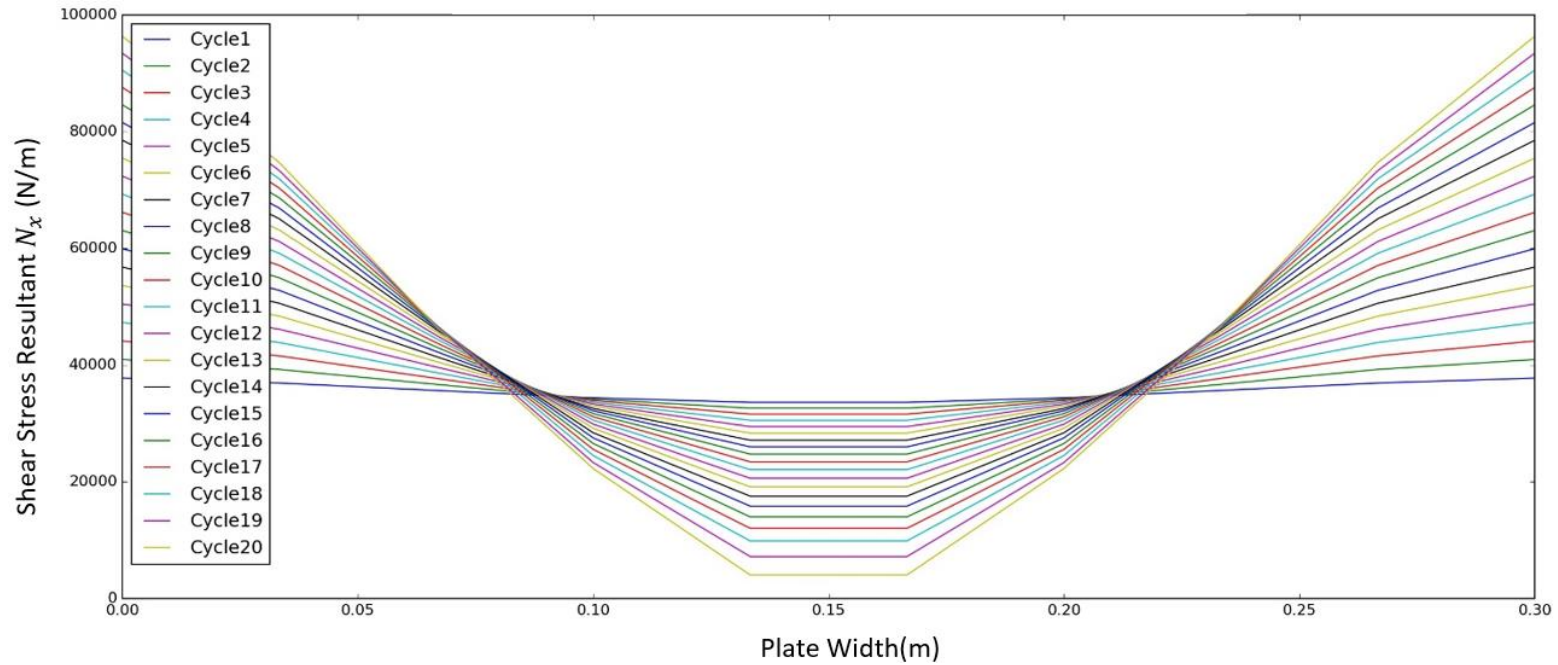
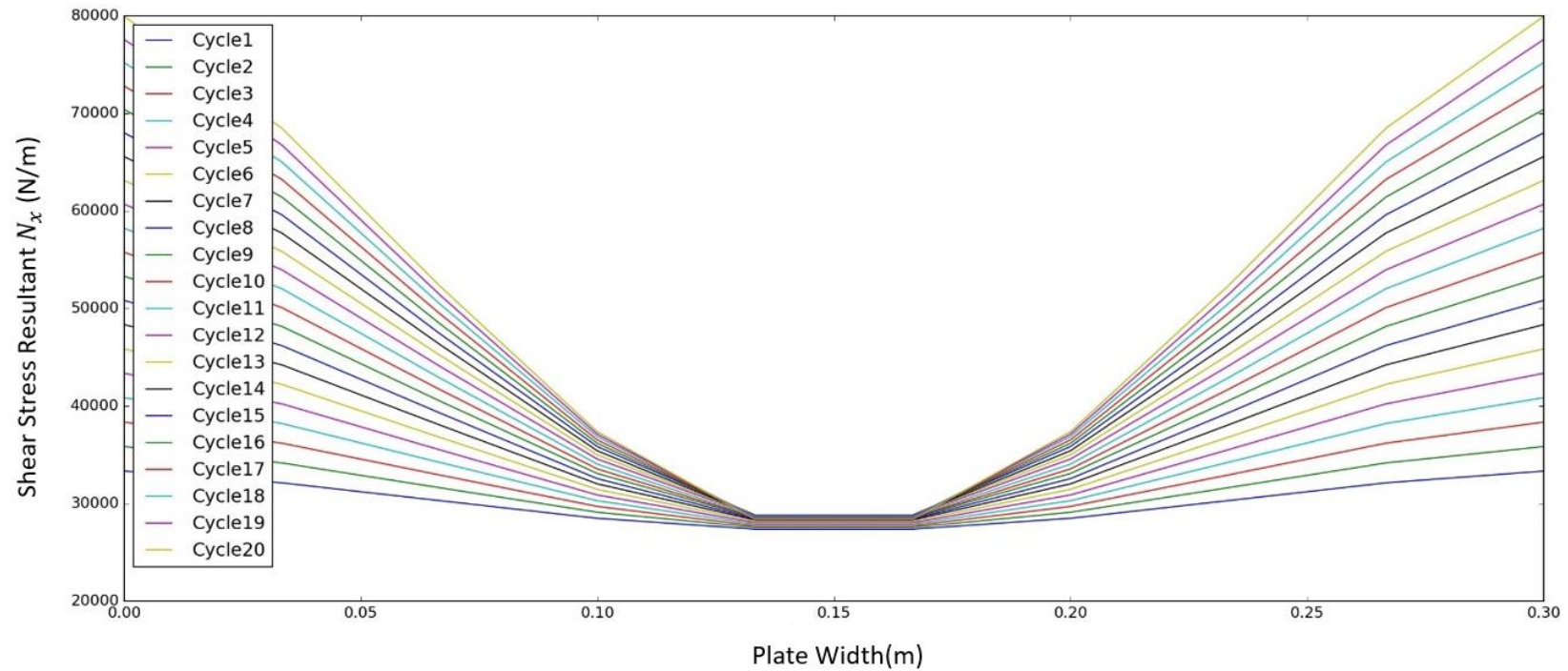


Figure 7.10. v displacement contour plots (m) from (a) free edges, (b) fixed edges and (c) straight edges



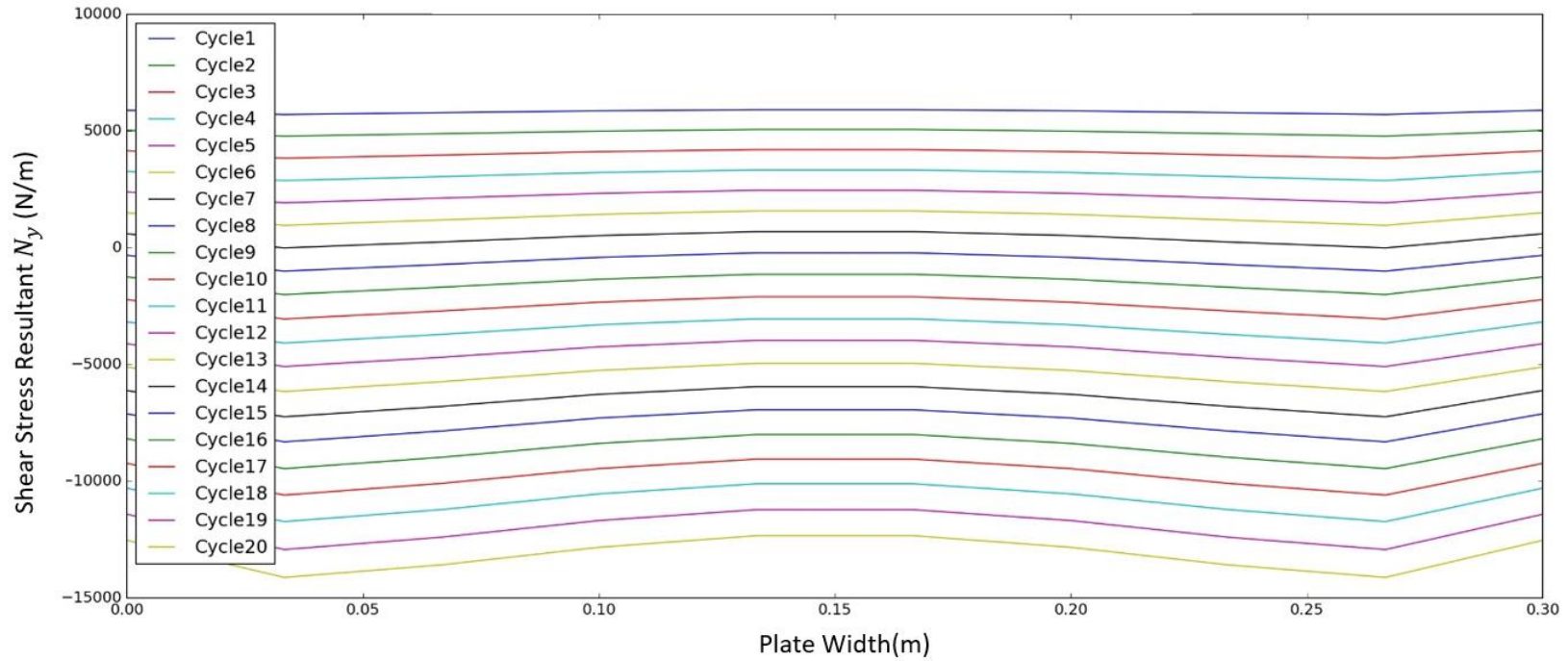
Cycle	1	2	3	4	5	6	7	8	9	10	11	12	13	14	15	16	17	18	19	20
Strip 1	37771	40956	44136	47309	50476	53637	56786	59933	63066	66187	69297	72389	75470	78531	81571	84586	87577	90540	93459	96354
Strip 2	36929	39260	41576	43869	46141	48393	50601	52807	54964	57080	59160	61175	63155	65066	66904	68659	70333	71911	73340	74699
Strip 3	35654	36700	37727	38715	39672	40602	41457	42326	43114	43842	44525	45105	45652	46103	46453	46698	46850	46895	46749	46589
Strip 4	34389	34168	33929	33646	33332	32994	32564	32178	31696	31153	30576	29885	29190	28403	27529	26568	25560	24505	23306	22285
Strip 5	33611	32612	31599	30541	29454	28347	27138	25993	24742	23427	22082	20606	19130	17542	15836	13996	12033	9878	7198	4038
Strip 6	33611	32612	31599	30541	29454	28347	27138	25993	24742	23427	22082	20606	19130	17542	15836	13996	12033	9878	7199	4040
Strip 7	34389	34168	33929	33646	33332	32994	32564	32178	31696	31153	30576	29885	29190	28403	27529	26568	25561	24506	23308	22289
Strip 8	35654	36700	37727	38715	39672	40602	41457	42326	43114	43842	44524	45105	45651	46102	46453	46698	46851	46897	46751	46594
Strip 9	36929	39260	41576	43869	46141	48393	50601	52807	54964	57080	59160	61175	63154	65066	66904	68659	70333	71911	73342	74702
Strip 10	37771	40956	44136	47309	50476	53637	56786	59933	63066	66187	69297	72389	75470	78531	81571	84586	87578	90540	93459	96355

Figure 7.11. Uniform longitudinal stress distribution at each postbuckling cycle for in-plane longitudinal straight edges



Cycle	1	2	3	4	5	6	7	8	9	10	11	12	13	14	15	16	17	18	19	20
Strip 1	33327	35841	38347	40849	43351	45847	48339	50820	53297	55756	58219	60687	63129	65563	67996	70401	72804	75201	77572	79937
Strip 2	32124	34162	36187	38204	40218	42221	44215	46190	48155	50086	52021	53961	55855	57730	59600	61415	63223	65014	66755	68476
Strip 3	30301	31624	32929	34222	35514	36791	38058	39296	40523	41699	42886	44087	45218	46326	47431	48457	49478	50482	51412	52322
Strip 4	28490	29108	29703	30289	30877	31452	32019	32553	33080	33546	34036	34557	34994	35410	35839	36173	36518	36858	37117	37371
Strip 5	27374	27559	27721	27874	28034	28181	28323	28432	28536	28574	28646	28761	28783	28790	28819	28745	28694	28646	28516	28392
Strip 6	27374	27559	27721	27874	28034	28181	28323	28432	28536	28575	28646	28761	28784	28791	28820	28746	28697	28645	28515	28390
Strip 7	28490	29108	29703	30289	30877	31452	32019	32554	33080	33547	34036	34558	34995	35412	35842	36176	36524	36856	37115	37368
Strip 8	30301	31624	32929	34222	35514	36791	38058	39296	40523	41700	42886	44088	45220	46328	47434	48461	49484	50481	51410	52318
Strip 9	32124	34162	36187	38204	40218	42221	44215	46190	48155	50087	52021	53962	55856	57731	59602	61417	63227	65014	66753	68473
Strip 10	33327	35841	38347	40849	43351	45847	48339	50820	53297	55756	58219	60687	63129	65563	67997	70401	72805	75201	77572	79936

Figure 7.12. Equivalent uniform longitudinal stress distribution at each postbuckling cycle for in-plane longitudinal fixed edges



Cycle	1	2	3	4	5	6	7	8	9	10	11	12	13	14	15	16	17	18	19	20
Strip 1	5889	5030	4155	3273	2391	1499	601	-321	-1249	-2220	-3176	-4109	-5103	-6111	-7109	-8177	-9234	-10294	-11410	-12526
Strip 2	5709	4780	3834	2880	1927	964	-7	-1001	-2003	-3049	-4079	-5085	-6154	-7238	-8312	-9457	-10591	-11727	-12922	-14116
Strip 3	5785	4887	3971	3048	2125	1192	251	-714	-1687	-2705	-3708	-4689	-5733	-6794	-7847	-8972	-10089	-11211	-12394	-13579
Strip 4	5865	4998	4114	3222	2332	1431	523	-409	-1347	-2330	-3298	-4244	-5252	-6276	-7292	-8378	-9456	-10540	-11682	-12827
Strip 5	5915	5067	4203	3331	2461	1580	692	-219	-1136	-2097	-3043	-3966	-4950	-5949	-6940	-8000	-9050	-10105	-11217	-12330
Strip 6	5915	5067	4203	3331	2461	1580	692	-219	-1136	-2097	-3043	-3966	-4950	-5950	-6940	-8000	-9050	-10105	-11217	-12330
Strip 7	5865	4998	4114	3222	2332	1431	523	-409	-1347	-2330	-3298	-4244	-5252	-6276	-7292	-8378	-9456	-10540	-11682	-12827
Strip 8	5785	4887	3971	3048	2125	1192	251	-714	-1687	-2705	-3708	-4689	-5733	-6794	-7847	-8972	-10089	-11211	-12394	-13580
Strip 9	5709	4780	3834	2880	1927	964	-7	-1001	-2003	-3049	-4079	-5084	-6154	-7237	-8311	-9456	-10590	-11728	-12923	-14117
Strip 10	5889	5030	4155	3273	2391	1499	601	-320	-1249	-2220	-3176	-4109	-5103	-6111	-7109	-8176	-9233	-10294	-11410	-12527

Figure 7.13. Equivalent uniform transverse stress distribution N_y at each postbuckling cycle for in-plane longitudinal fixed edges

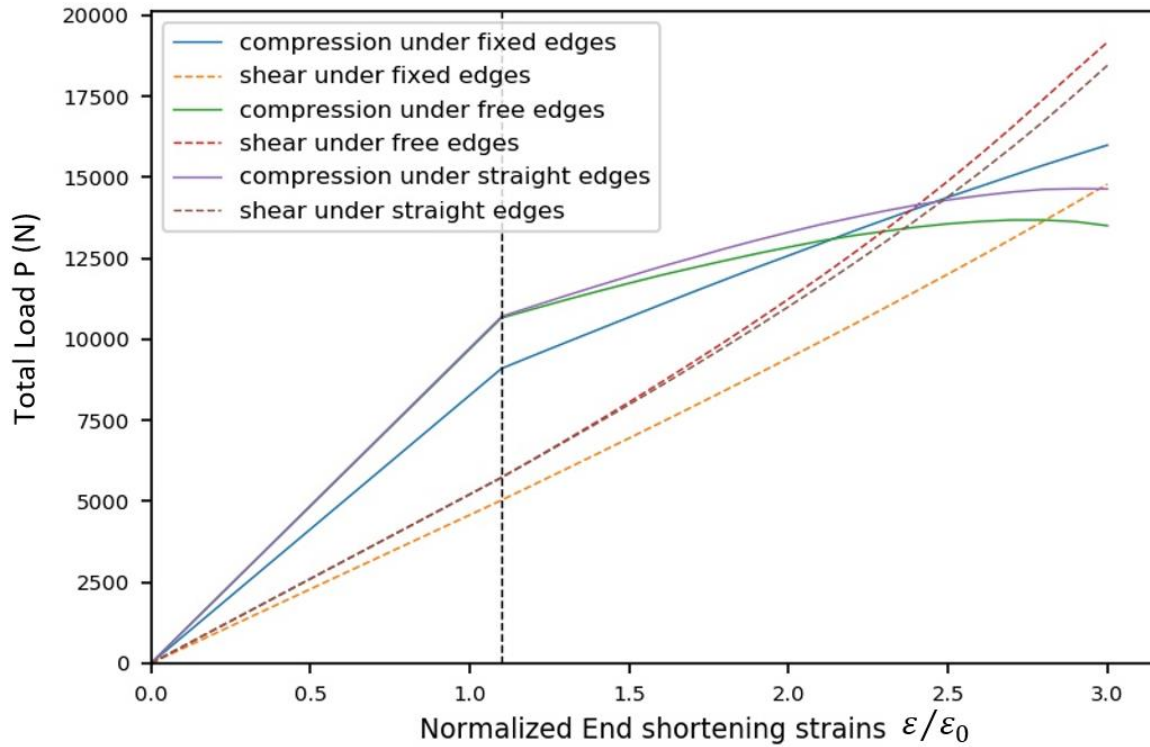


Figure 7.14. Postbuckling load paths for all boundary conditions for metal plate

7.3. Composites loaded in compression

In this section, to illustrate the capability of CWPAN in analysing composite plates under shear loading, a square plate with the same dimensions as the plate in the last section but manufactured from composite is modelled. The properties of the material are taken from Zhang (2018): $E_{11} = 131\text{kNmm}^{-2}$, $E_{22} = 13\text{kNmm}^{-2}$, $G_{12} = G_{13} = G_{23} = 6.41\text{kNmm}^{-2}$, $\nu_{12} = 0.38$. The plate consists of 16 plies with a ply thickness of 0.125mm a layup of $[0/0/+45/0/-45/0/90/90/90/90/0/-45/0/+45/0/0]$, see Figure 7.15. (This orientation is utilized by the models in all balanced and symmetric cases). This layup is balanced and symmetric resulting in $A_{16} = A_{26} = 0$, a zero \mathbf{B} -stiffness matrix with no extension bending or shear extension coupling. The membrane stiffness matrices of the laminates are as follows

A-Stiffness Matrix (Nm^{-1})			D-Stiffness Matrix (Nm)		
1.6222×10^8	2.3827×10^7	0	72.778	7.9425	2.1044
2.3827×10^7	1.0236×10^8	0	7.4974	15.415	2.1044
0	0	2.6624×10^7	2.1044	2.1044	8.8746

Table 7.5. Laminate stiffness of balanced and symmetric laminates

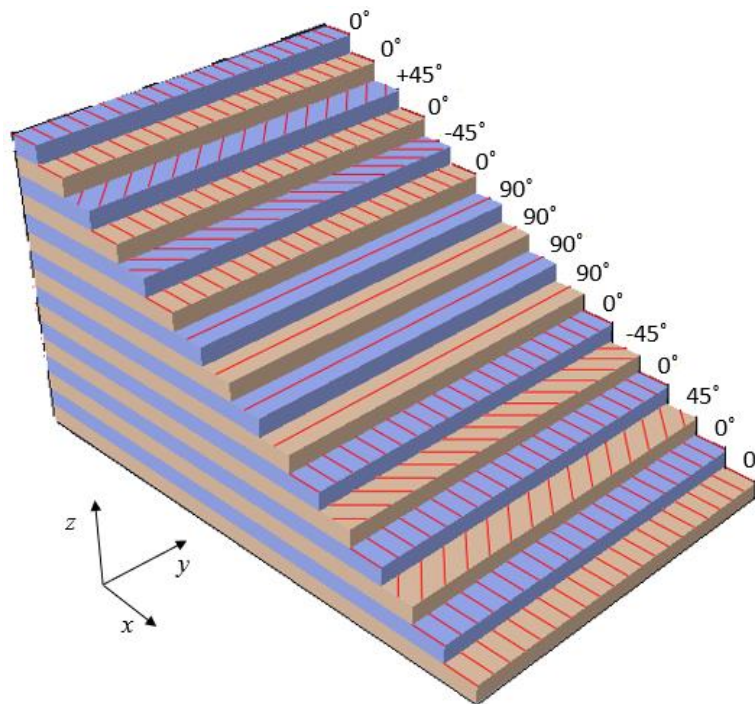
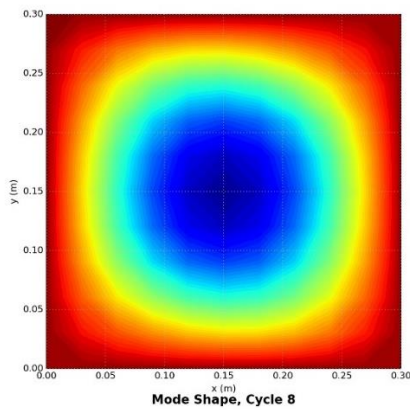


Figure 7.15 Laminate orientation example

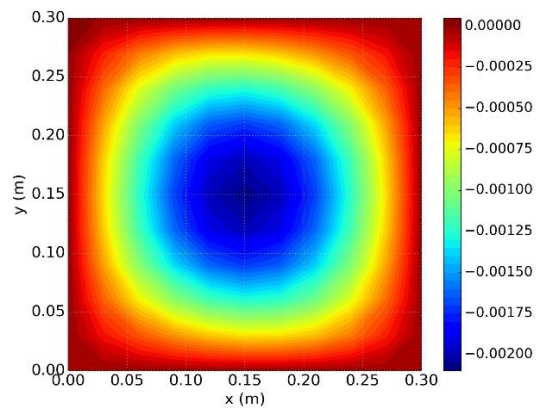
To validate CWPAN the critical buckling and postbuckling behaviour are compared with those from ABAQUS/Standard (ABAQUS 2014). The plate is modelled with 400 S4R 4-node general-purpose shell elements, with reduced integration and hourglass control, and three integration points through the thickness of each ply. For a 16 ply composite plate this corresponds to 48 integration points in total, with strains and stress resultants at the mid surface at integration point 24 (or 25 since these are coincident). A linear buckling perturbation is utilised to find the eigenvalues with the mode corresponding to the lowest positive eigenvalue selected to predict the postbuckling mode. Subsequently, the Riks method with a 0.01 curvature increment is chosen to perform a non-linear postbuckling analysis. The Riks method allows geometrically nonlinear static problems including buckling or collapse where the load-

displacement response shows a negative stiffness, and the structure must release strain energy to remain in equilibrium, to be solved. It is therefore particularly suitable for nonlinear, potentially unstable problems such as postbuckling.

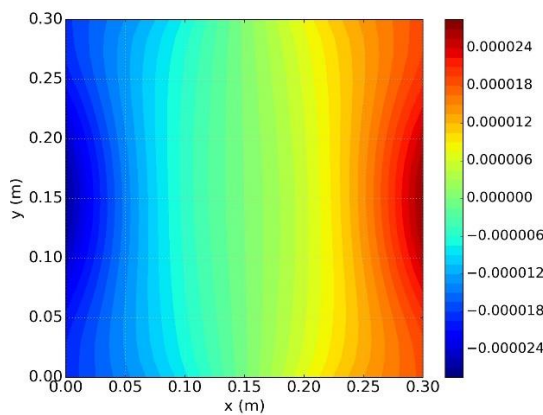
The model is analysed for the same three boundary conditions described in Section 7.1. However, to enable comparison with the improved exact strip method (Che, 2012), only free edges are presented here since this method is restricted to free edges only. Since CWPAN is controlled by end shortening strains which are increased by α at each postbuckling cycle, the FEA loading is controlled by displacements to provide the best comparison with CWPAN. This is achieved by applying equation constraints to the two loaded edges.



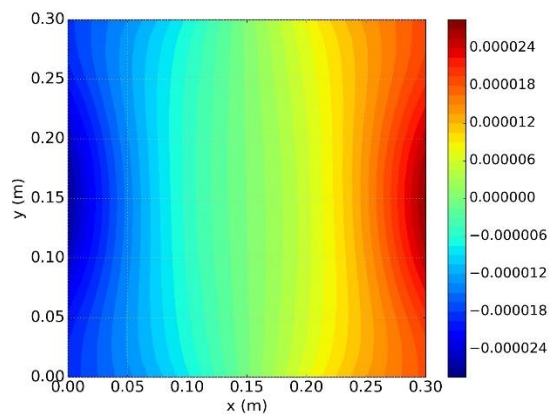
(a)



(b)



(c)



(d)

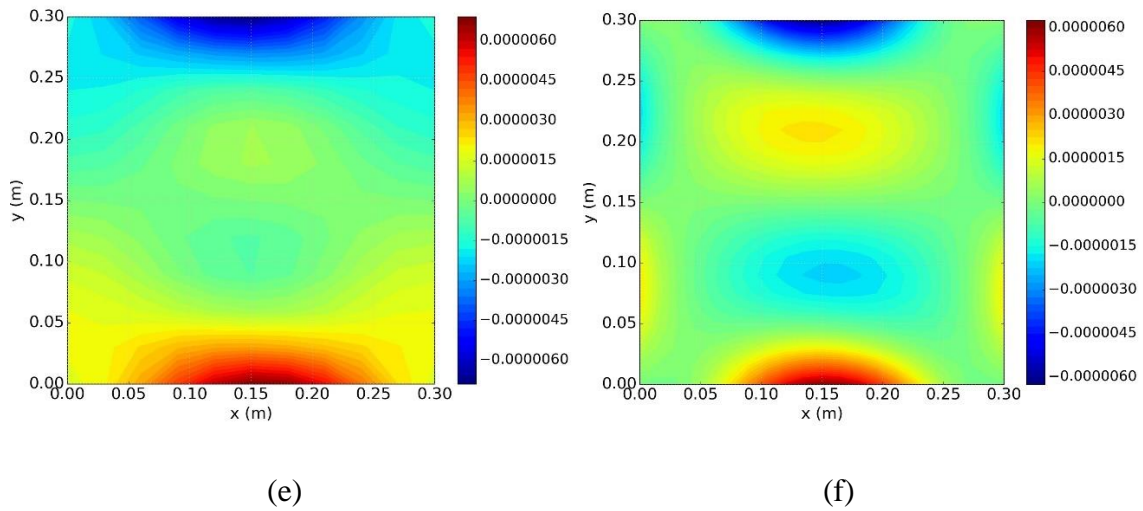
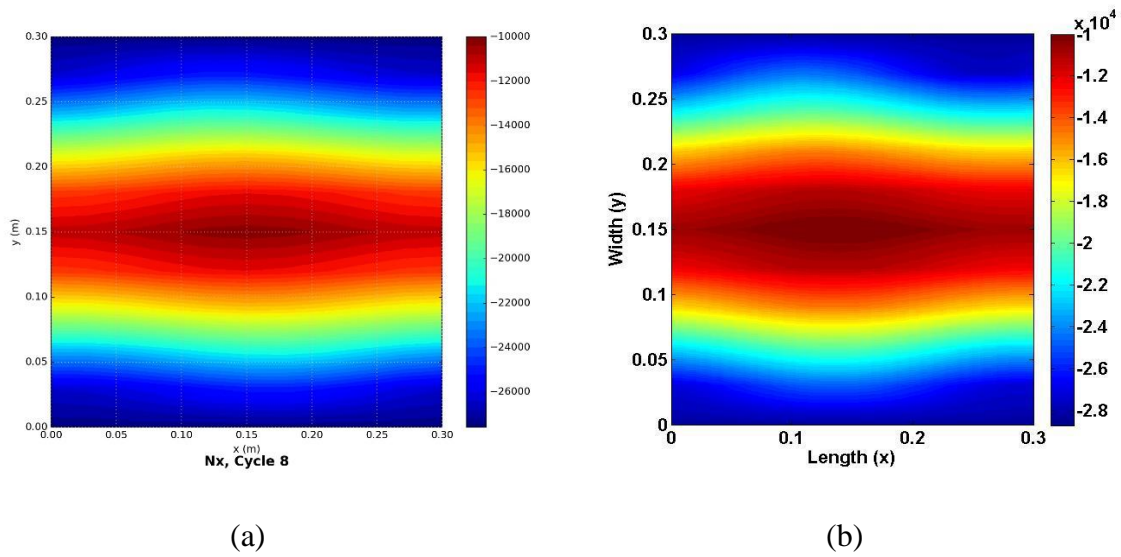
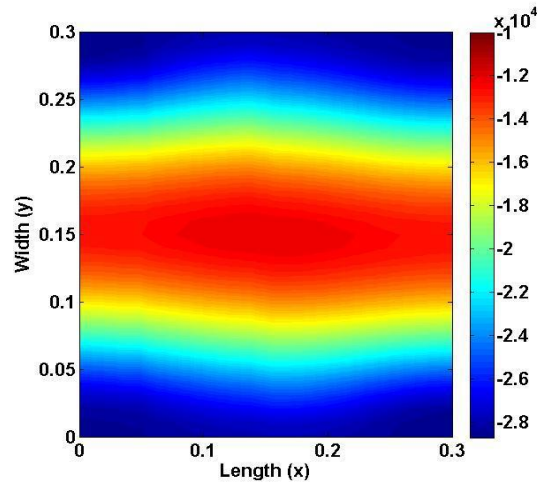


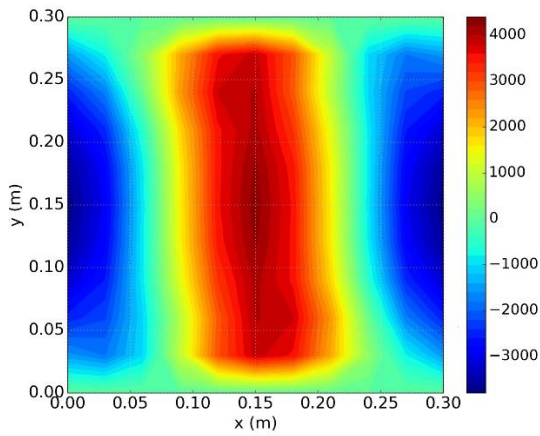
Figure 7.16. Contour plots of displacements (m) at cycle 8 of the composite plate under compression: (a) out-of-plane w , CWPAN (b) out-of-plane w , ABAQUS (c) in-plane u , CWPAN (d) in-plane u , ABAQUS (e) in-plane v , CWPAN (f) in-plane v , ABAQUS



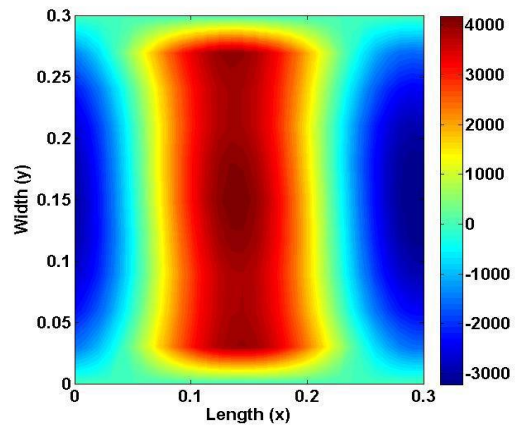


(c)

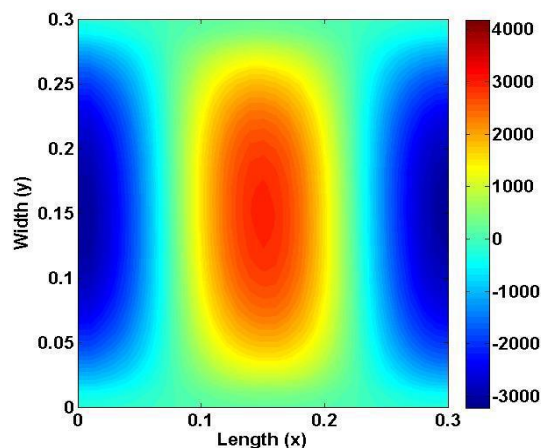
Figure 7.17. Contour plots of stress resultants N_x at cycle 8 of composite plate under compression (N/m): (a) series solution (b) improved exact strip method (Zhang, 2018) (c) ABAQUS solution



(a)



(b)



(c)

Figure 7.18. Contour plots of stress resultants N_y at cycle 8 of the composite plate under compression (N/m): (a) series solution (b) improved exact strip method (Zhang 2018) (c) ABAQUS solution

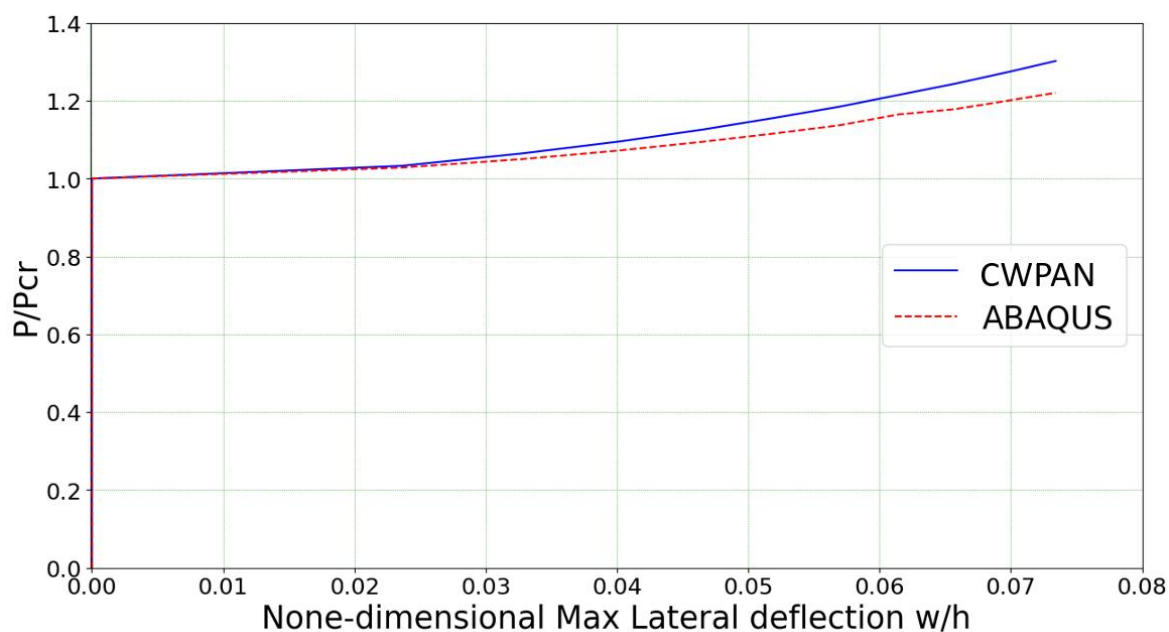


Figure 7.19. Normalized applied compressive load (P/P_{cr}) vs non-dimensional maximum deflection w/h

w/h	0.0235	0.0328	0.0402	0.0464	0.0519	0.0569	0.0614	0.0657	0.0696	0.0734
VPA	1.0327	1.0651	1.0956	1.1256	1.1557	1.1846	1.2149	1.2435	1.2728	1.3020
ABAQUS	1.0282	1.0503	1.0725	1.0944	1.1156	1.1368	1.1648	1.1782	1.1995	1.2204
Relative difference	0.0044	0.0140	0.0215	0.0285	0.0358	0.0419	0.0430	0.0554	0.0610	0.0668

Table 7.6. Normalized deflections from CWPAN and ABAQUS

Figure 7.16 compares contour plots of in-plane and out-of-plane displacements from CWPAN and FEA at cycle 8. A good agreement can be seen both in shape and values. Figures 7.17 and 7.18 compare contour plots of strain and stress resultants from CWPAN, improved exact strip method and finite element analysis at cycle 8 (1.8 times the critical buckling strain, chosen to coincide with the example from Che (2010)). It can be seen that the mode skews slightly due to the introduction of composite material resulting in bend twist coupling. The shape of the plots will continue to be distorted as the applied load increases due to stress redistribution. One observation is that CWPAN shows good agreement with the improved exact strip method (Che, 2010). As can be seen from the explicit expressions, the previous method represents the in-plane buckling mode using five half-wavelengths while ten are used for CWPAN. CWPAN is, therefore, closer to the actual solution. Since in this case, the level of anisotropy is small the difference between the two methods is fairly negligible. For higher levels of anisotropy however such as the introduction of shear load, the study of unbalanced laminate lay-ups or later into the postbuckling period, CWPAN will show much closer agreement with the actual solutions. Both methods show good agreement with ABAQUS although their contours are more angular than ABAQUS close to transverse edges for N_y . This is because the free boundary conditions on the transverse edges in ABAQUS cannot easily be modelled due to the resulting rigid body movement whilst the exact strip postbuckling analysis overcomes this by adding point supports at longitudinal strips explained in Section 4.6. Figure 7.19 compares the total load path from the CWPAN and FEA. The maximum error of 6.68% is found at the last equilibrium point shown in the figure.

7.4. Composite loaded under combined load

In this section, a composite plate under combined shear and compression is modelled to illustrate CWPAN's ability to analyse a composite under shear loading. The geometry and properties of the composite are the same as in the previous example whilst the load combines compression with a shear load having half its magnitude at initial buckling, applied as described in section 7.2 (see Figure 7.20). Again, only the results for in-plane fixed v displacements are presented. (This orientation is utilized by all models in this thesis).

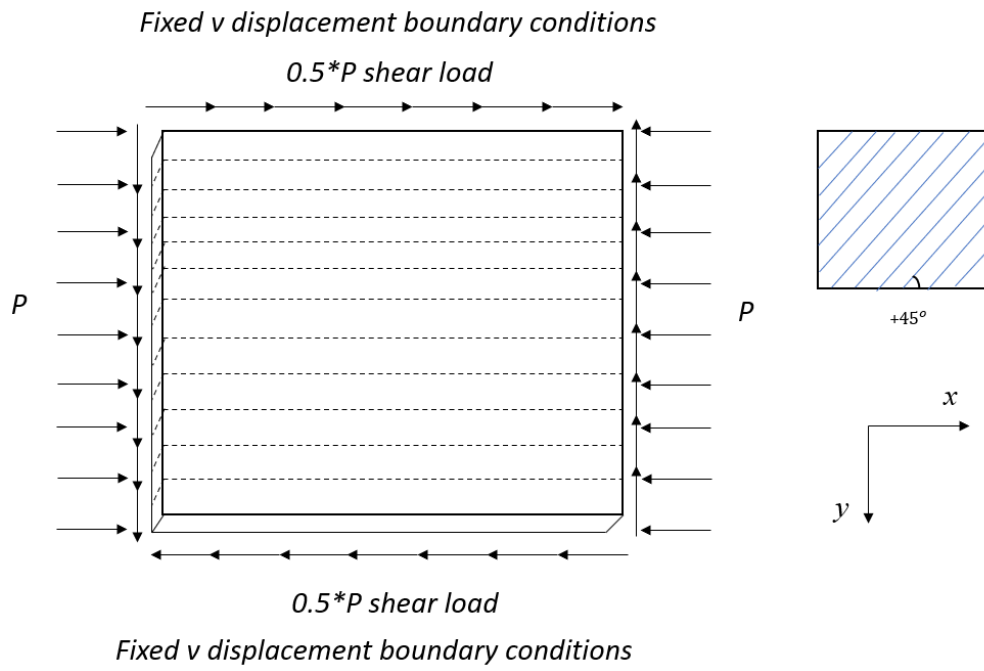
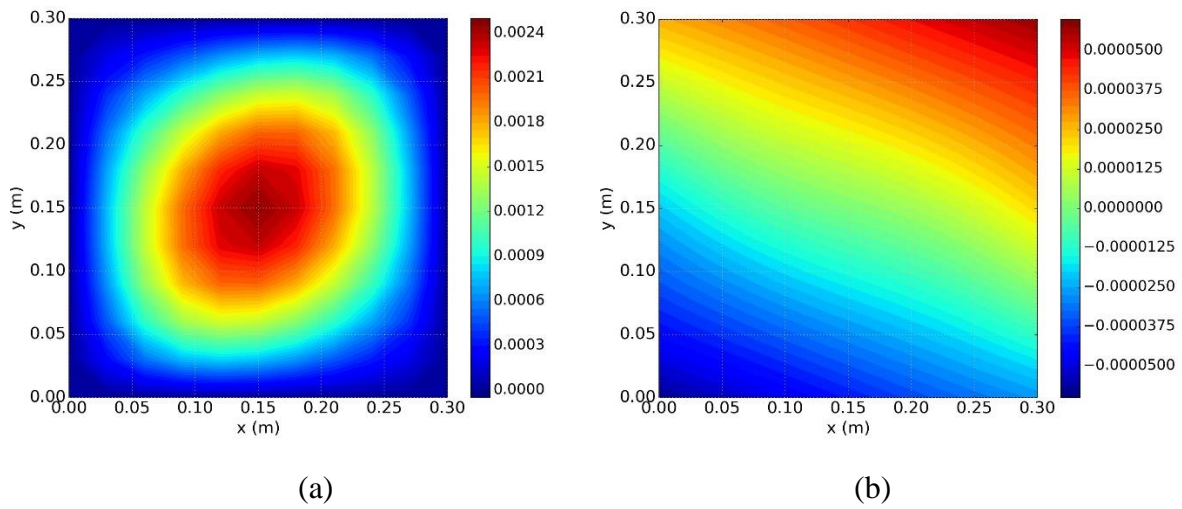
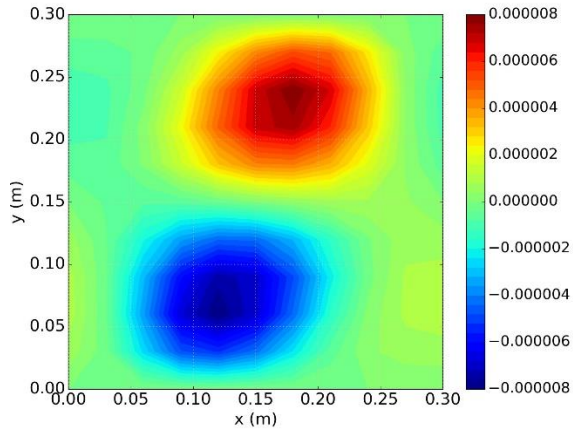
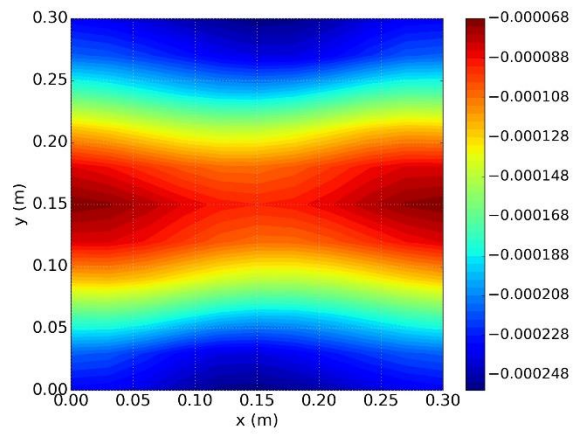


Figure 7.20. Load and boundary conditions

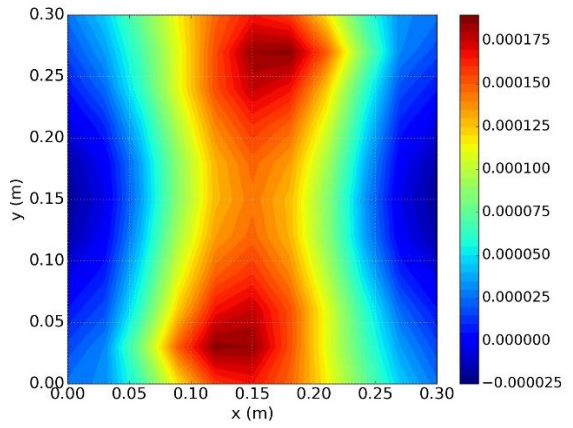




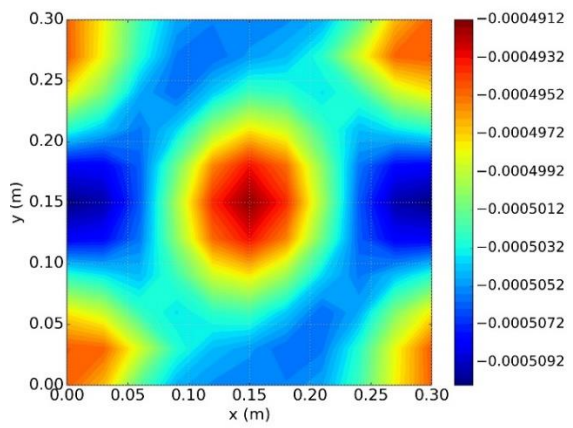
(c)



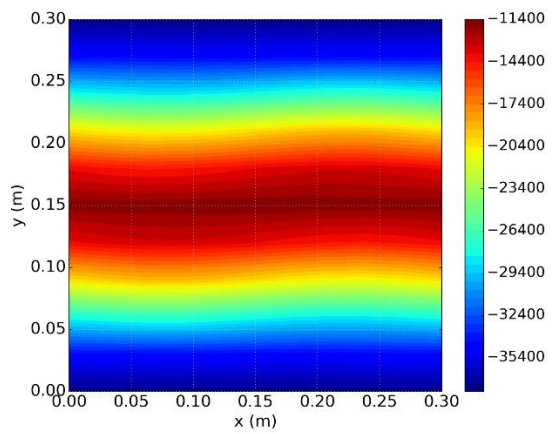
(d)



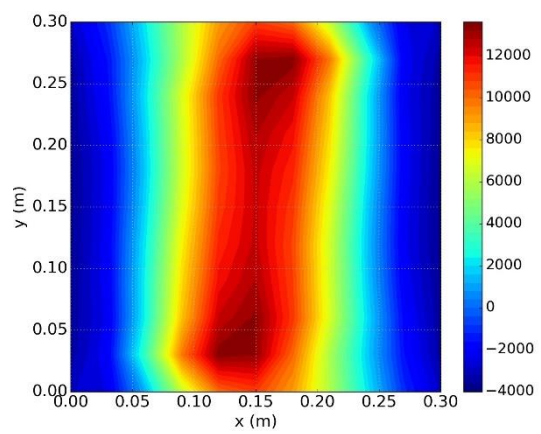
(e)



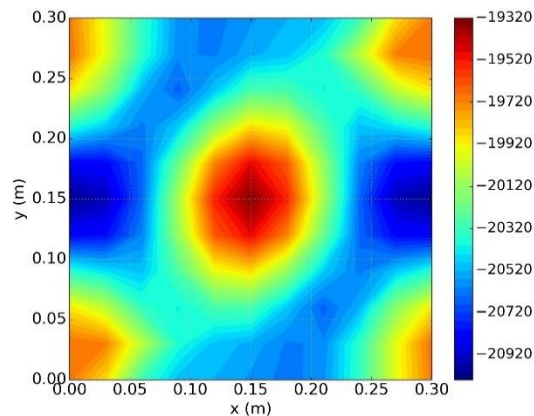
(f)



(g)



(h)



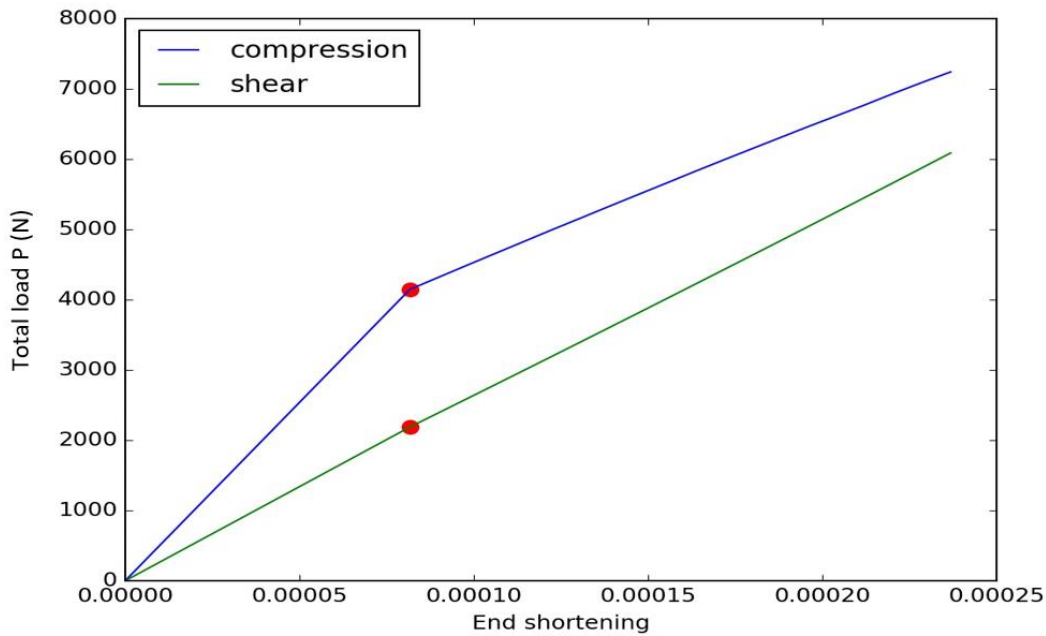
(i)

Figure 7.21. Combined loading case contour plots of: (a) out-of-plane displacement w (m) (b) in-plane displacement u (m) (c) in-plane displacement v (m) (d) strain ϵ_x (e) strain ϵ_y (f) strain γ_{xy} (g) stress resultant N_x (N/m) (h) stress resultant N_y (N/m) (i) stress resultant N_{xy} (N/m)

Figure 7.21 shows contour plots of displacements and stress and strain distributions for the plate. The inclusion of shear loading, can be clearly observed to increase the level of skew. This can be seen from the sinusoidal solutions to be due to the fact that the non-dominant (in-plane half-wavelength 0 is considered to be the dominant term) terms contribute more when compared to the compression only case. From a structural point of view, the shear loading will bring antisymmetry into the structure resulting in skewed mode shapes also validating CWPAN.

One observation from Figure 7.21(b) is that displacements u are approximately linearly distributed in both the longitudinal and transverse directions. This is caused by the constant ratio between the applied end shortening and shear strains applied to the structure at each postbuckling cycle, see Equation 4.2, while the non-linear parts of the displacements are caused by postbuckling stiffness. Another observation from Figure 7.21(c) is that since in-plane boundary conditions are only applied on the longitudinal edges, the distribution of v displacements along these edges will clearly be different in this case than for other boundary conditions. As shown in Figure 7.21(c), v displacements are zero at the longitudinal edges and the two contours in the upper and lower halves of the plate move in opposite directions. Figure 7.22 presents the buckling and postbuckling longitudinal and shear stress paths for composites under combined loading. It can be seen that at the beginning of the path, the ratio of shear to compression is 0.5. This ratio increases when the path goes into the later stages due to the assumptions of strain control in the postbuckling analysis. Another difference between the different boundary conditions is in the stress redistributions at each cycle, see Figure 7.23. For

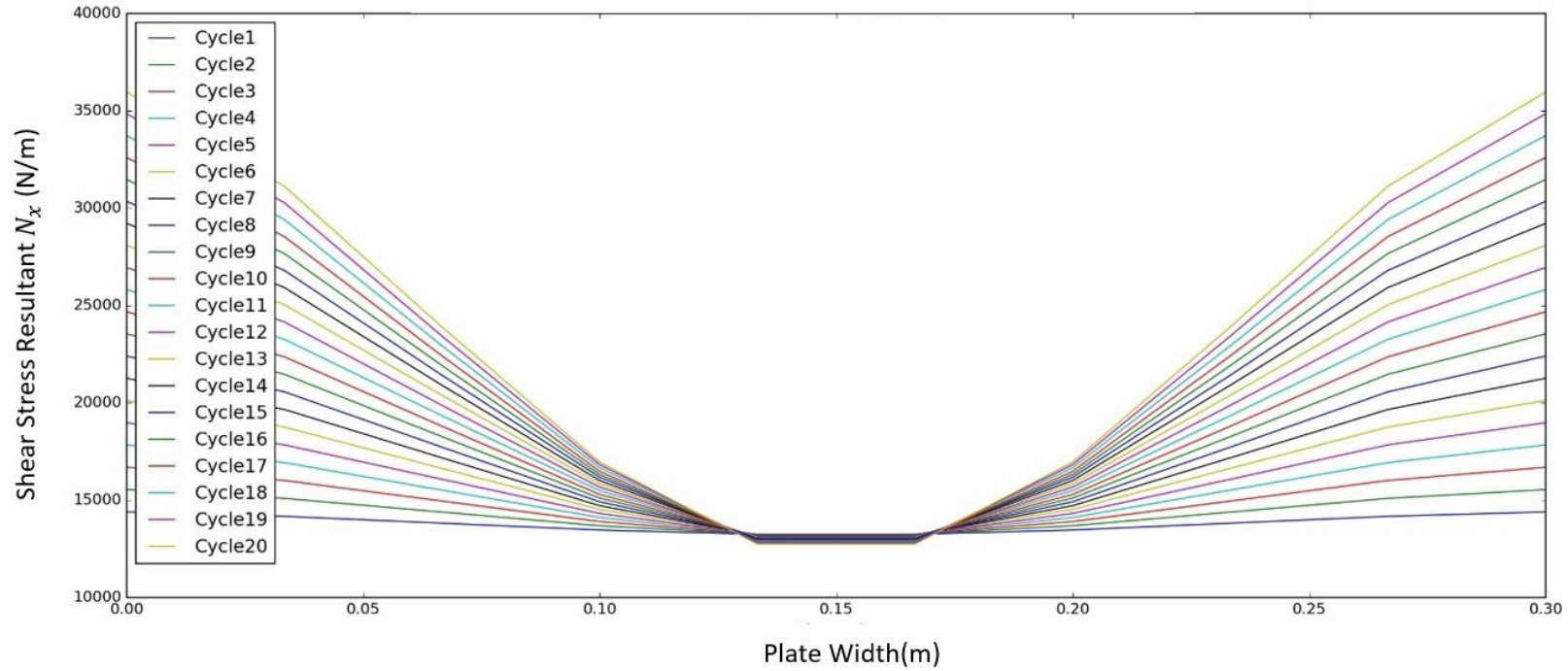
the fixed boundary conditions considered here, stress resultants on the edge strips increase more slowly than for ones under free boundary conditions whilst the stress resultants at the middle strips hardly reduce.



Cycle	0	1	2	3	4	5	6	7	8	9	10
Compression(N/m)	397 4	414 6	431 8	448 8	465 8	482 7	499 6	516 1	532 8	549 3	565 7
Shear(N/m)	198 7	218 7	238 8	258 9	279 1	299 3	319 5	339 8	360 2	380 6	401 0
Ratio	2	1.90	1.81	1.73	1.67	1.61	1.56	1.52	1.48	1.44	1.41

Figure 7.22 Postbuckling load paths and tabulation of shear and compression for a composite plate under combined loading and in-plane fixed boundary conditions

The solution for the combined loading case illustrates the main difference between the arc length method (Riks method), used in the finite element analysis, and CWPAN. The Riks method is a numerical technique which converges on an equilibrium state by increasing the applied load and displacements at the same time (Memon, 2004).



Cycle	1	2	3	4	5	6	7	8	9	10	11	12	13	14	15	16	17	18	19	20
Strip 1	14395	15542	16689	17834	18978	20122	21262	22403	23542	24680	25819	26954	28086	29217	30348	31473	32598	33728	34851	35968
Strip 2	14170	15092	16012	16927	17841	18754	19659	20565	21466	22364	23264	24155	25041	25923	26804	27671	28540	29418	30280	31129
Strip 3	13817	14388	14954	15514	16072	16630	17174	17722	18263	18799	19341	19869	20389	20904	21420	21914	22414	22932	23427	23899
Strip 4	13465	13685	13901	14109	14316	14525	14716	14915	15105	15292	15488	15668	15839	16008	16179	16324	16480	16667	16824	16953
Strip 5	13247	13252	13252	13244	13235	13230	13205	13191	13168	13142	13130	13100	13060	13019	12984	12919	12869	12859	12816	12741
Strip 6	13247	13252	13252	13244	13235	13230	13205	13191	13168	13142	13130	13100	13060	13019	12984	12919	12870	12859	12816	12742
Strip 7	13465	13685	13901	14109	14316	14525	14716	14915	15105	15292	15488	15668	15839	16008	16179	16324	16480	16667	16824	16953
Strip 8	13817	14388	14954	15514	16072	16630	17174	17722	18263	18799	19341	19869	20389	20904	21420	21914	22414	22932	23427	23899
Strip 9	14170	15092	16012	16927	17841	18754	19659	20565	21466	22364	23264	24155	25041	25923	26804	27671	28540	29418	30281	31129
Strip 10	14395	15542	16689	17834	18978	20122	21262	22403	23542	24680	25819	26954	28086	29217	30348	31473	32598	33728	34851	35968

Figure 7. 23 Equivalent uniform longitudinal stress distribution at each postbuckling cycle for a composite plate under combined loading and in-plane longitudinal fixed edges

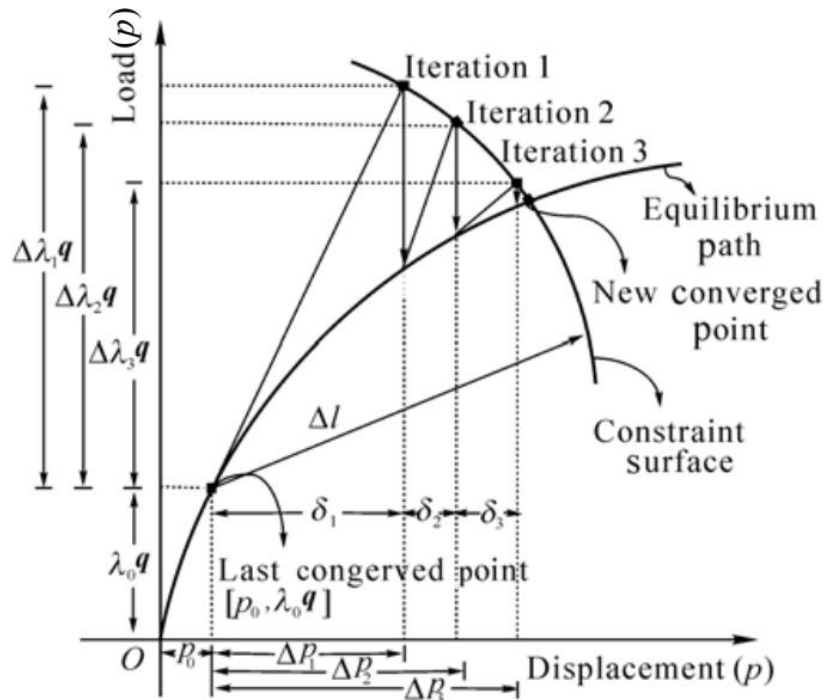


Figure 7.24. Arc length procedure for specific iteration (Memon, 2004)

As shown in Figure 7.24, the increment of displacement is written as Δp while for the applied load, instead of using load directly, a load proportionality factor (LPF) $\Delta \lambda$ is used. The applied load at each equilibrium state is

$$Q = \Delta \lambda_c q \quad \dots(7.1)$$

where q is the reference load applied when modelling and c is the cycle number. From Equation 7.1, it can be concluded that the load during a Riks step is always proportional to the reference load. (ABAQUS 2014).

If the applied load is a combined load instead of a single force, this combined load will be incremented and the ratio between the two individual loads will remain the same, see Figure 7.25(a). On the contrary, for CWPAN, as the increment at each cycle is controlled by the level of strain, it is the strain ratio which remains unchanged rather than the applied force ratio, see Figure 7.25(b). Thus, the applied forces will not be in the same ratio as for the initial input load, see Figure 7.21. In this case, comparison with the Riks method will naturally show poor agreement.

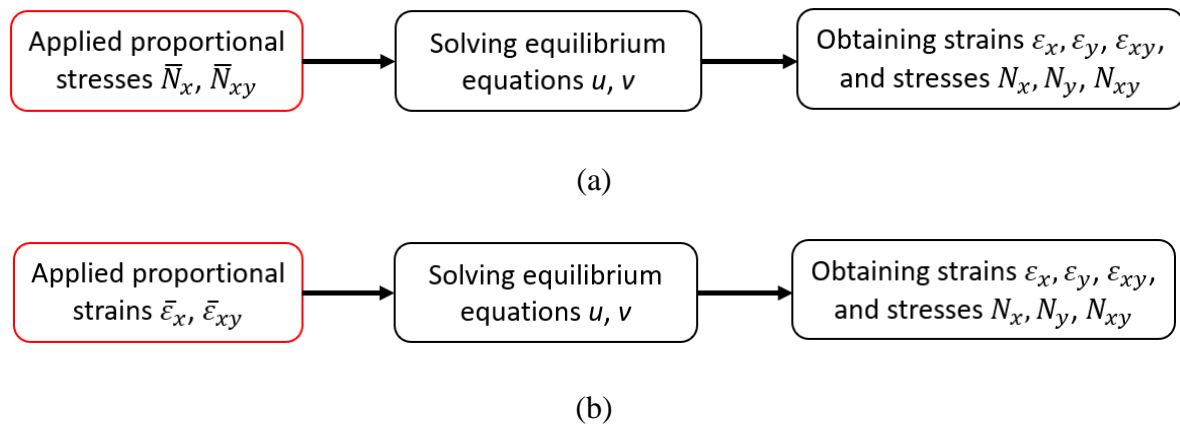


Figure 7.25. The inputs and outputs of a postbuckling analysis using: (a) the ABAQUS Riks method; (b) CWPAN

Such phenomena also occur for an unsymmetric laminate because the coupling of in-plane and out-of-plane stiffness matrices has not been incorporated into the stiffness calculation, see Section 5.5. In all of these cases therefore the Riks method cannot be used to validate the results from CWPAN.

7.5. Composite loaded in pure shear

Composite plates under pure shear have been studied extensively (Xu et al., 2013; Gousal et al., 2015). However, many numerical methods incur very high computational costs or even fail to converge due to high levels of nonlinearity. Using CWPAN, composite plates under pure shear can be analysed efficiently and convergence problems can be overcome by solving the equilibrium equations analytically.

In this section, a plate under pure shear is modelled and validated using ABAQUS. In-plane fixed boundary conditions are applied on the longitudinal edges and pure shear load is applied on all four edges. The properties of the plate are as described in section 7.3. As the complexity of the problem is increased, three out-of-plane half-wavelengths may no longer accurately capture the in-plane and out-of-plane displacement distributions. Instead therefore, five out-of-plane half-wavelengths and a 5% shear strain increment ratio are selected. Other predefined parameters are as described in section 7.1.

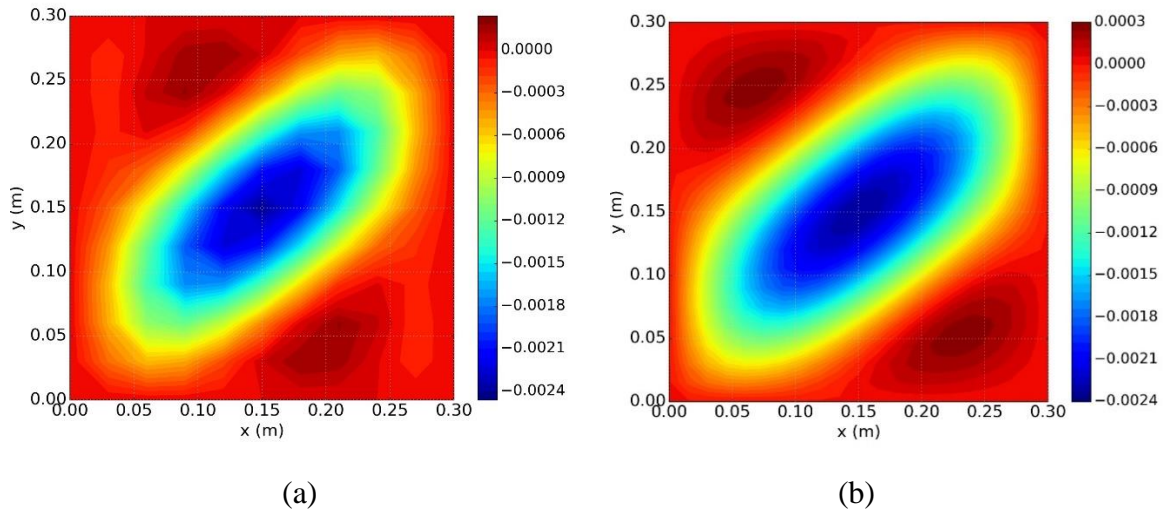


Figure 7.26 Contour plots of out-of-plane displacements w at initial buckling for pure shear case (m): (a) CWPAN. (b) ABAQUS

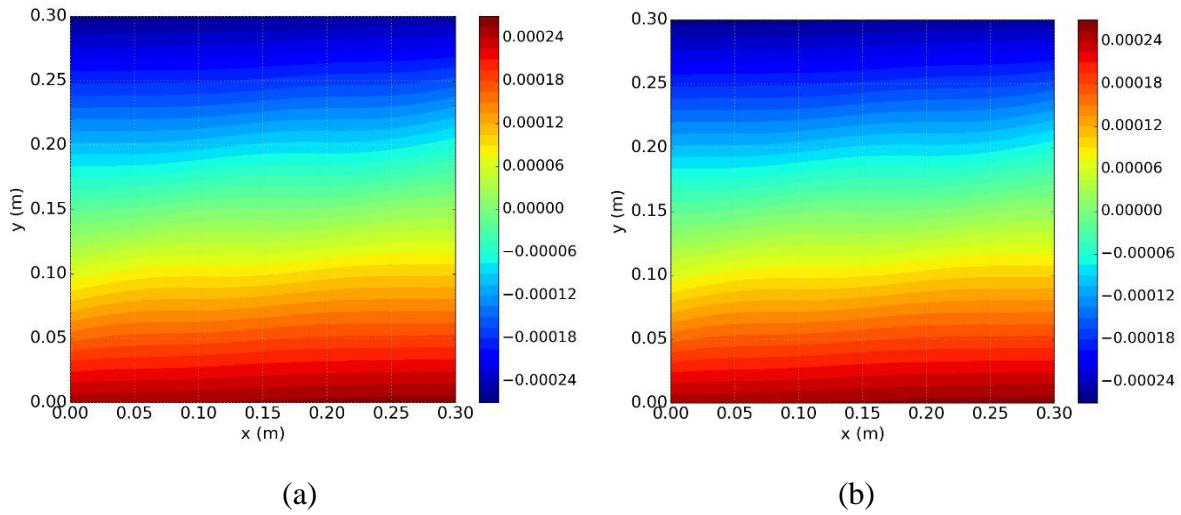


Figure 7.27. Contour plots of out-of-plane displacements u for pure shear case at cycle 5 (m): (a) CWPAN. (b) ABAQUS

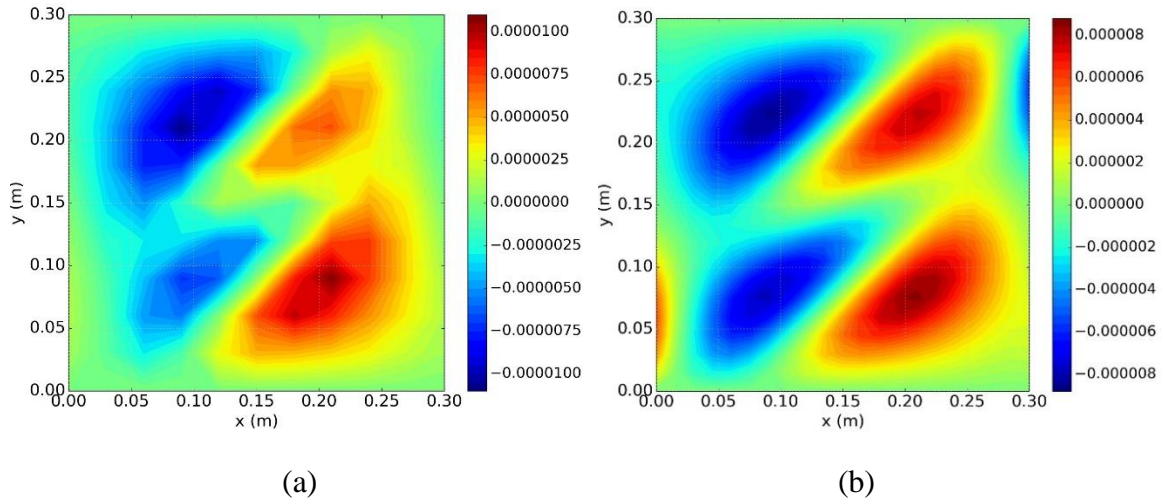


Figure 7.28. Contour plots of out-of-plane displacements v for pure shear case at cycle 5 (m): (a) CWPAN. (b) ABAQUS

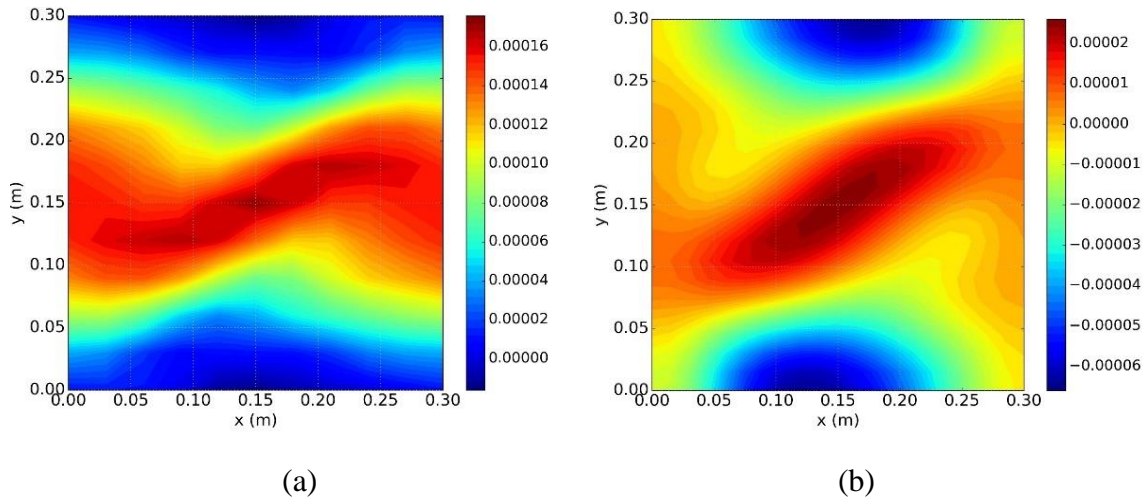


Figure 7.29. Contour plots of strain ϵ_x for pure shear case at cycle 5: (a) CWPAN. (b) ABAQUS

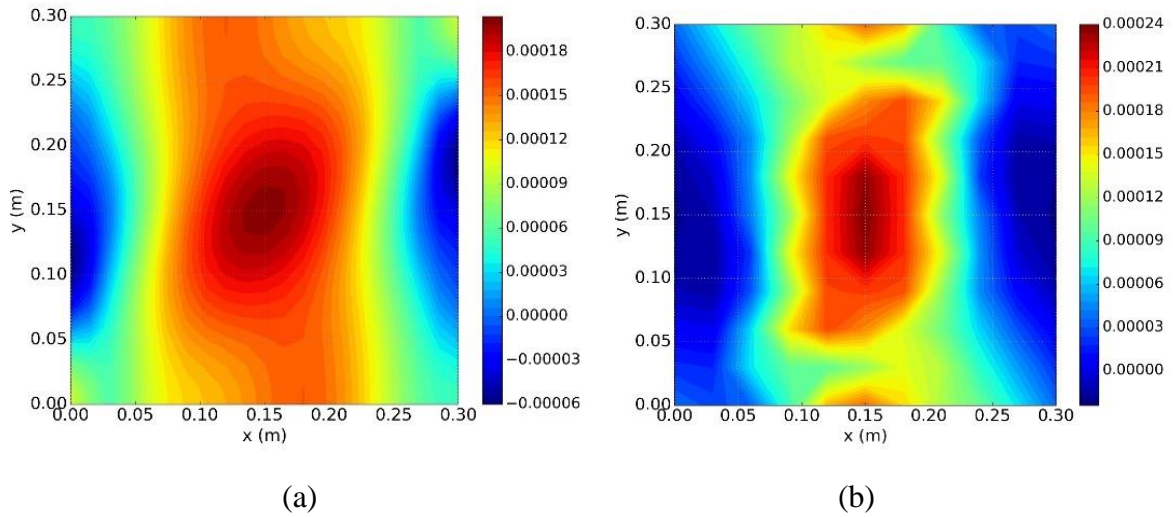


Figure 7.30. Contour plots of strain ϵ_y for pure shear case at cycle 5: (a) CWPAN. (b) ABAQUS

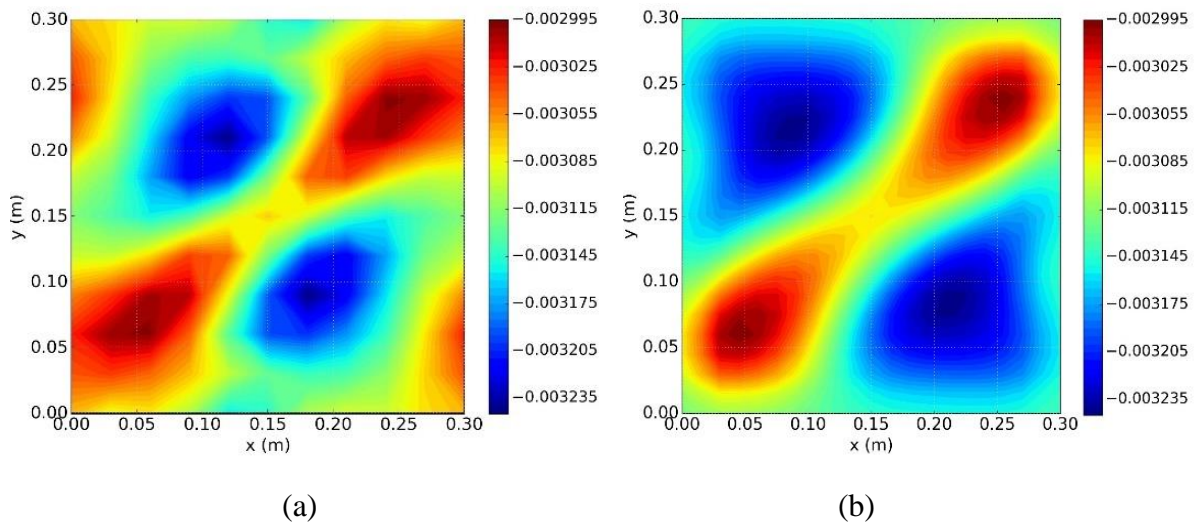


Figure 7.31. Contour plots of strain γ_{xy} for pure shear case at cycle 5: (a) CWPAN. (b) ABAQUS

Figures 7.26, 7.27 and 7.28 present the distribution of displacements at cycle 5, i.e. at 125% of the initial shear strain (5% strain increment times 5 cycles), compared with ABAQUS Riks analysis. From these figures, it can clearly be seen that very good agreement has been achieved. Displacements w (Figure 7.26) are skewed significantly and symmetrical along the diagonal due to the coupling of the effects of the pure shear loading and the composite material. This

kind of solution cannot be obtained by the previous postbuckling analysis by Che (2010) due to it being limited to one out-of-plane half-wavelength.

Figures 7.29, 7.30 and 7.31 show strain distributions at cycle 5. Solutions from both CWPAN and ABAQUS Riks analysis are largely in agreement with each other. However, there are differences in the strain ε_x contour on its longitudinal edges, the strain ε_y contour on its transverse edges and the shear strain γ_{xy} at its corners. These differences can be explained by another major mechanism difference between CWPAN and the ABAQUS Riks method.

This difference originates from the initial buckling analysis which is solved by VICON. As described in Chapter 3, VICON analysis assumes plates as infinitely long with the end supports repeating at longitudinal intervals over their length l . The mode shapes are therefore assumed to repeat in the longitudinal direction at intervals of $L = 2l/\xi$, where ξ is a parameter in the range $0 \leq \xi \leq 1$ and can therefore be represented (Anderson et al., 1983) by a series of responses with half-wavelengths $l/(\xi + 2m)$ where m is any integer.

In the modelling process, parameter ξ is selected to find the interval giving the lowest eigenvalue and the mode shape corresponding to this is taken as the initial buckling mode for the postbuckling analysis. Such a method is advantageous for thin slender structures like an aeroplane wing which can be considered as an infinitely long stiffened plate providing an accurate representation of the boundary conditions along the length (Diaconu and Weaver, 2006).

Figure 7.32 shows a finite number of bays from a repetitive infinitely long panel from VICON's initial buckling solutions when $\xi = 1, 0.5$ and 0.25 . It is worth noting that the total length of the repeat intervals is $L = 2l/\xi$, the number of repeating bays M is therefore $L/l = 2/\xi$. Thus, when $\xi = 1$, the number of repeating bays M is 2 bays. Similarly, when $\xi = 0.5$, $M = 4$ and when $\xi = 0.25$, $M = 8$. For each ξ , although the buckling mode extends across all of the repeating bays, with each displaying a slightly different mode shape, only the first one is chosen as the postbuckling start point. In this case $\xi = 0.5$ gives the lowest critical buckling load $P_{cr} = 12,712 N$. Thus, the mode corresponding to the first of the four repeating bays will be taken as the initial buckling mode shape.

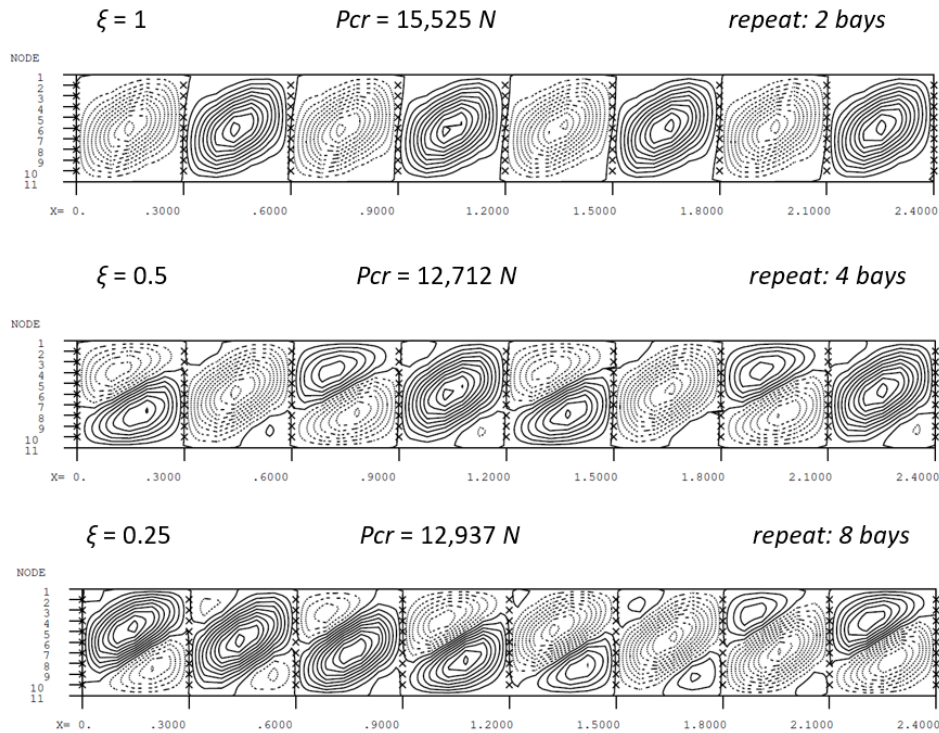


Figure 7.32. Initial buckling solution from VICON for pure shear case

In the ABAQUS model however, the analysis is based on a single bay rather than an infinitely long plate. In this case the lowest buckling mode is as shown in Figure 7.26(b), corresponding to a critical buckling load $P_{cr} = 11,540 \text{ N}$ which shows very poor agreement with the lowest buckling mode and load $P_{cr} = 12,712 \text{ N}$ when $\xi = 0.5$ from the VICON analysis. (The ABAQUS solution is closer to the mode when $\xi = 1$, see Figure 7.26(a)). Unsurprisingly, results from the two methods lead to differences in strain distributions.

The advantage of assuming infinite long plates in the coupled wavelength postbuckling analysis is that the computational efficiency remains the same regardless of the length of plate, i.e. the complexity of analysing one bay or multiple bays plate is the same, is inherited from VICON analysis. This is very different from FEA. Furthermore, for CWPAN, the infinitely long plate model allows for moment equilibrium where there is continuity with other parts of a larger structure, and is therefore more representative of aircraft wing panels with intermediate transverse stiffeners, i.e. ribs.

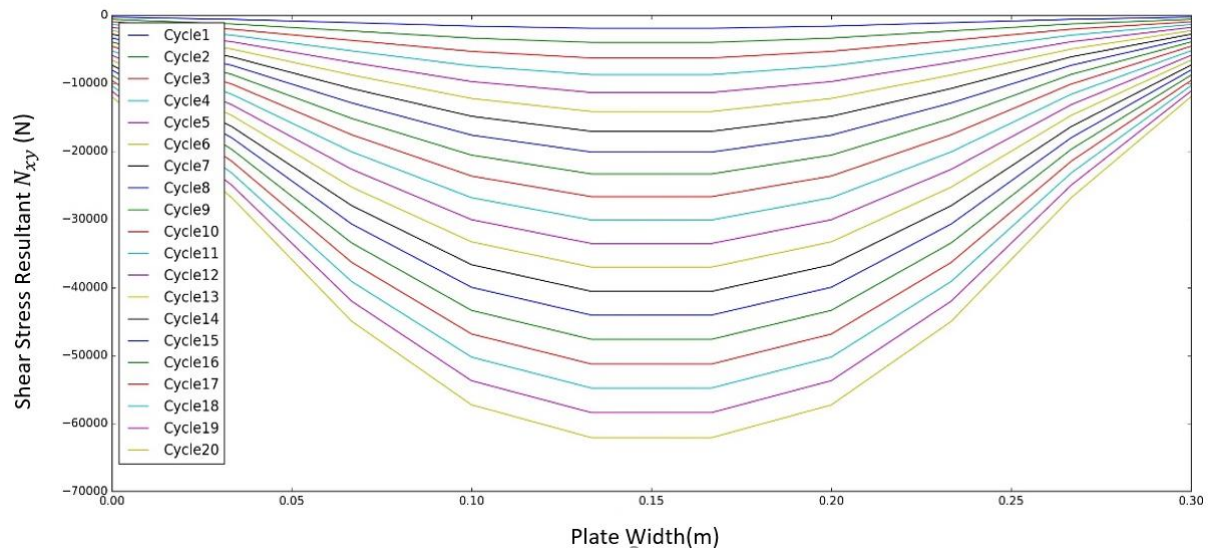


Figure 7.33. Shear stress redistribution from pure shear model

Figure 7.33 illustrates the shear stress redistribution observed over 20 cycles of CWPAN. Compared to the stress redistribution seen for example for a plate under compression, redistribution of the shear stress resultants occurs in the opposite direction with the stress resultants in the middle of the strips increasing whilst the ones closer to the edges decrease. From a structural point of view, for pure shear cases, large deflections are located in areas of high stress. As the largest deflections are found in the centre of the plate, see Figure 7.26, the large stresses are therefore also located in the centre as shown in Figure 7.33. Such phenomena can also be validated based on the ABAQUS postbuckling analysis.

7.6. Unbalanced and unsymmetric composites

In this section, unbalanced symmetric and unbalanced unsymmetric laminated composites are modelled to illustrate the capability of CWPAN in analysing more general cases.

As described in chapter 2, for unbalanced composite materials, shear-extension coupling occurs during both the buckling and postbuckling regimes, with the A_{16} and A_{26} terms in the stiffness matrix becoming non-zero. For these lay-ups in-plane normal stresses N_x and N_y cause shear strain γ_{xy} and twist stress N_{xy} causes elongations.

A lack of symmetry brings another level of complexity for postbuckling analysis, introducing coupling of out-of-plane curvatures κ including twist κ_{xy} and bending moments \mathbf{M} . Furthermore, since the stiffness elements B_{ij} are non-zero, in-plane stresses N_x, N_y, N_{xy} cause out-of-plane curvatures and bending moments M_x, M_y, M_{xy} cause in-plane strains.

These coupling effects need to be incorporated for accurate postbuckling analysis. To include both the \mathbf{B} and the \mathbf{D} elements of the stiffness matrix, expressions for curvatures and moments are required to form the correct equilibrium equations as described in Chapter 4. When solving these equilibrium equations - Equations 4.46 and 4.47, it can be seen that expressions for curvatures are only related to out-of-plane deflections w , considered to be constants appearing on the right hand side of the equations, whilst moments M_x, M_y, M_{xy} are irrelevant to those equations. From a computational point of view, the time taken to solve such equations is therefore more or less the same as for balanced and symmetric composites. However as the structural stiffness matrix is required for the Newton iteration scheme, the technique for obtaining symmetric composite stiffness cannot be used for unsymmetric cases. This is because out-of-plane stiffness for symmetric composites has no coupling with in-plane stiffness, namely only stiffness matrix \mathbf{A} and \mathbf{D} are required and are embedded into the theory. To consider the in-plane coupling effect caused by unsymmetric laminates, further stiffness calculations would have to be developed. Therefore, in this section, only the first cycle of the postbuckling analysis for unsymmetric composite is presented since the mode shapes for the rest of the cycles will be inaccurate.

The plates in this section are subject to in-plane compression and under fixed boundary conditions. The configurations studied are presented below:

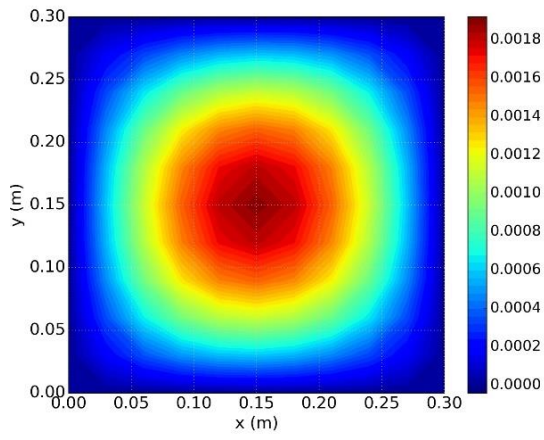
A: [0/-45/+45/0/-45/0/90/90/90/90/0/-45/0/+45/-45/0]

B: [0/90/+45/0/-45/0/-45/90/90/90/0/-45/-45/0/0/+45]

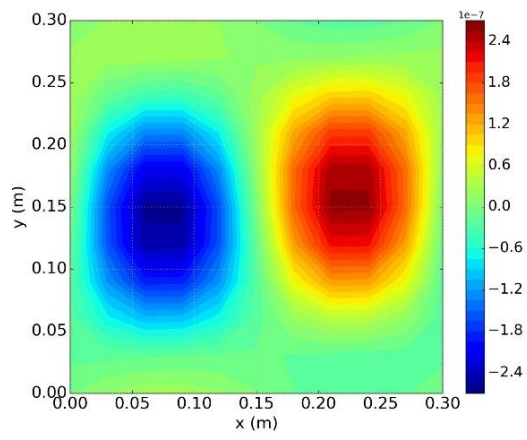
Based on the level of complexity of the mode shape, the predefined parameters chosen for the balanced and symmetric composites i.e. three out-of-plane half-wavelengths, ten strips and 10% strain increments are also used here. Since as discussed in section 7.5, it is not possible

Chapter 7

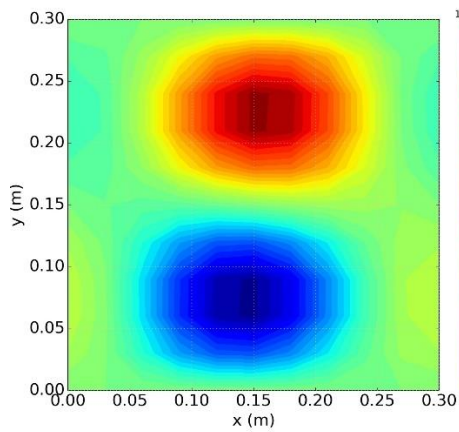
to generate a comparable load case using FEA for unbalanced cases, comparison with FEA is not presented here.



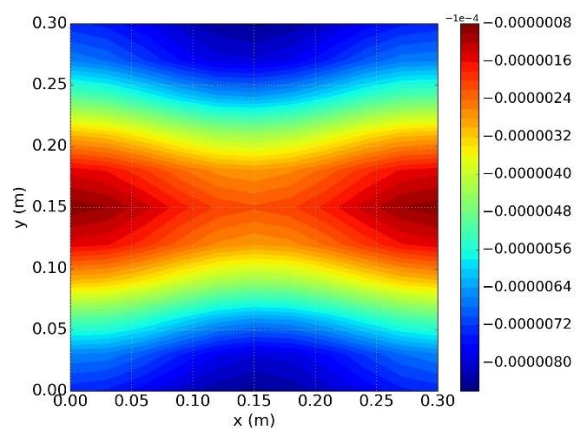
(a)



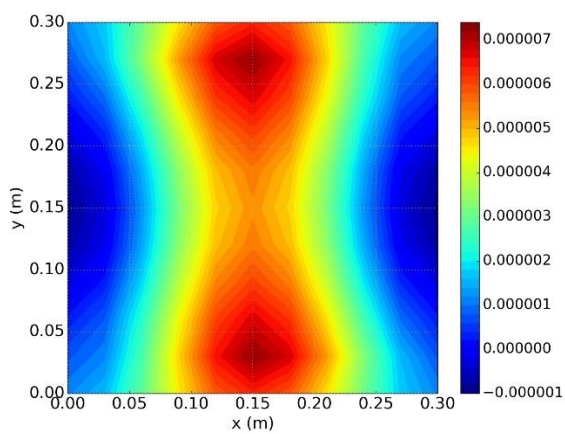
(b)



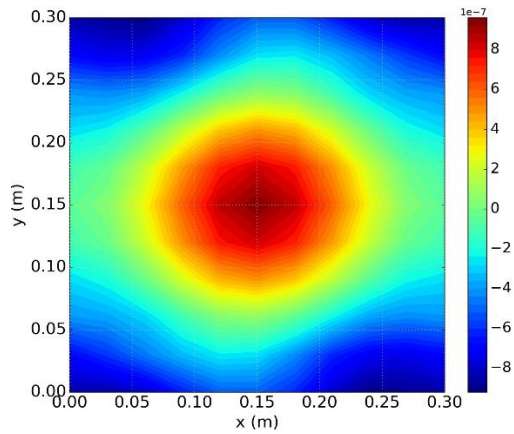
(c)



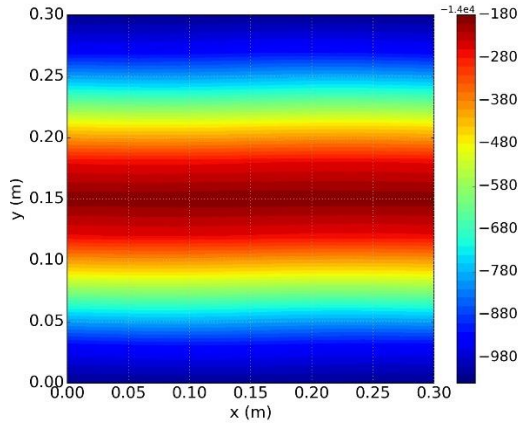
(d)



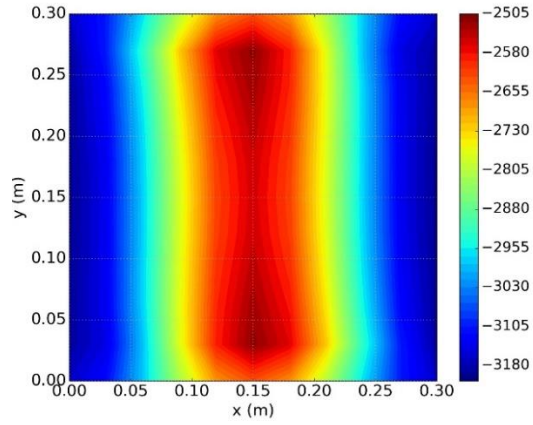
(e)



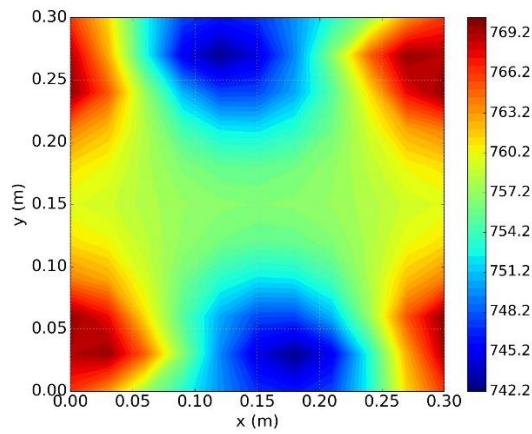
(f)



(g)



(h)



(i)

Figure 7.34. Symmetric unbalanced laminated composite under in-plane compression and fixed boundary condition at cycle 1 (110% of buckling end shortening strain), contour plots of: (a) out-of-plane deflection w (m); (b) in-plane longitudinal deflection u (m); (c) in-plane transverse deflection v (m); (d) strain ϵ_x ; (e) strain ϵ_y ; (f) strain γ_{xy} ; (g) stress resultant N_x (N/m); (h) stress resultant N_y (N/m); (i) stress resultant N_{xy} (N/m).

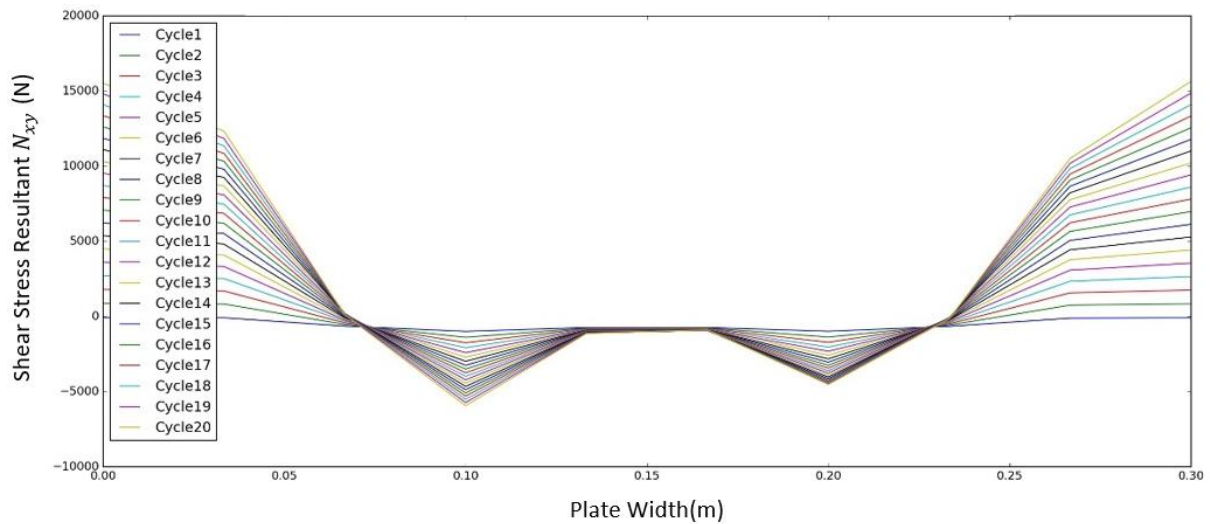


Figure 7.35. Equivalent shear uniform stress distribution at each postbuckling cycle

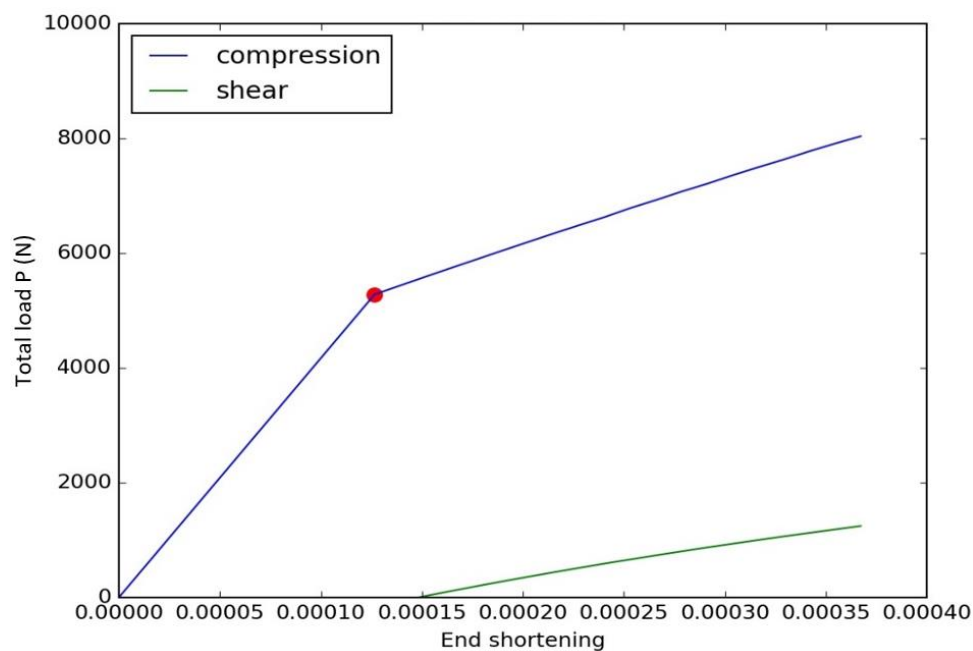


Figure 7.36. Postbuckling load paths for unbalanced symmetric composite under compression, free edges

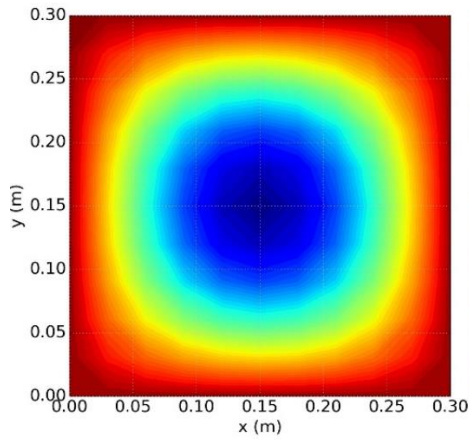
Figure 7.34 presents the displacement, stress and strain distributions for a symmetrical unbalanced composite plate under compression with fixed in-plane boundary conditions. It can be seen that most of the contours are twisted in one direction, caused by the unbalanced lay-up. Another observation is that compared to balanced composites, the shape and maximum amplitudes of the shear stress (N_{xy}) contour plots are very different, with stresses concentrated on the edges unlike those from a balanced composite. The stress redistribution is therefore much more obvious due to the coupling of direct and shear stresses and strains.

Figure 7.35 shows the equivalent shear stress resultants at strip level at each postbuckling cycle for the unbalanced composite. The graph shows that the shear stress resultants fluctuate along the transverse direction in which positive extrema are located at both ends while negative ones are located at the quarter points of the plate, and they are unsymmetric and increasing. These patterns are very different to the balanced cases, see Figures 7.13 and 7.33. As for total shear stress, an interesting phenomenon can be seen in Figure 7.36 where shear stress does not appear straight after the critical buckling point as shear loading is not applied. Instead, it starts to show after the first postbuckling cycle and then keeps increasing. From a structural point of view, these effects are due to the involvement of stiffness elements A_{16} and A_{26} which results in in-plane normal forces N_x and N_y causing twist of the laminate κ_{xy} , and a twist force N_{xy} causing elongations in the x and y directions. A more detailed solution for unbalanced symmetric case is presented in Appendix B.

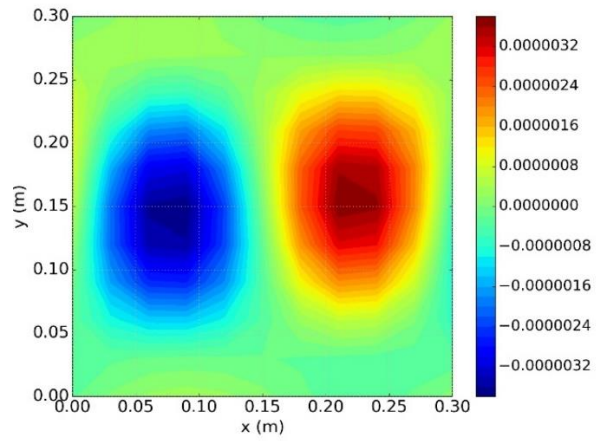
Figure 7.37 presents the displacement, stress and strain distributions for an unsymmetric unbalanced laminated composite plate under compression and fixed boundary conditions. Compared with the symmetric cases, the shear strains and stresses here are clearly very different. This is largely due to the involvement of stiffness matrices **B** and **D**.

Figure 7.38 shows the curvatures κ and bending moments **M**, which have not been presented in the previous cases. As solutions are shown only for the first cycle of the postbuckling analysis, i.e. 110% of buckling constant strain, there is not too much skewing, and the bending moments caused by the unsymmetric layups are relatively small. These are likely to be more significant further along the postbuckling path.

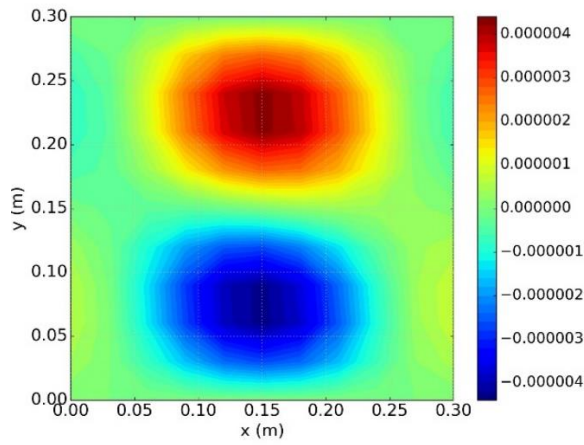
Chapter 7



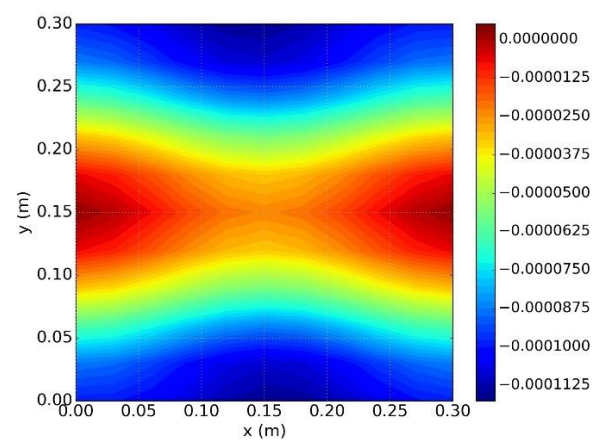
(a)



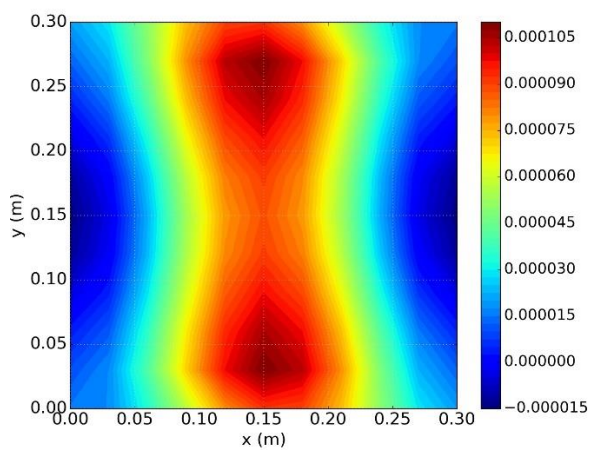
(b)



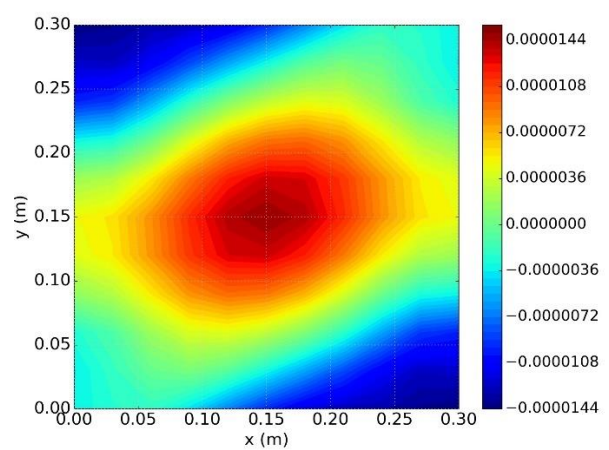
(c)



(d)



(e)



(f)

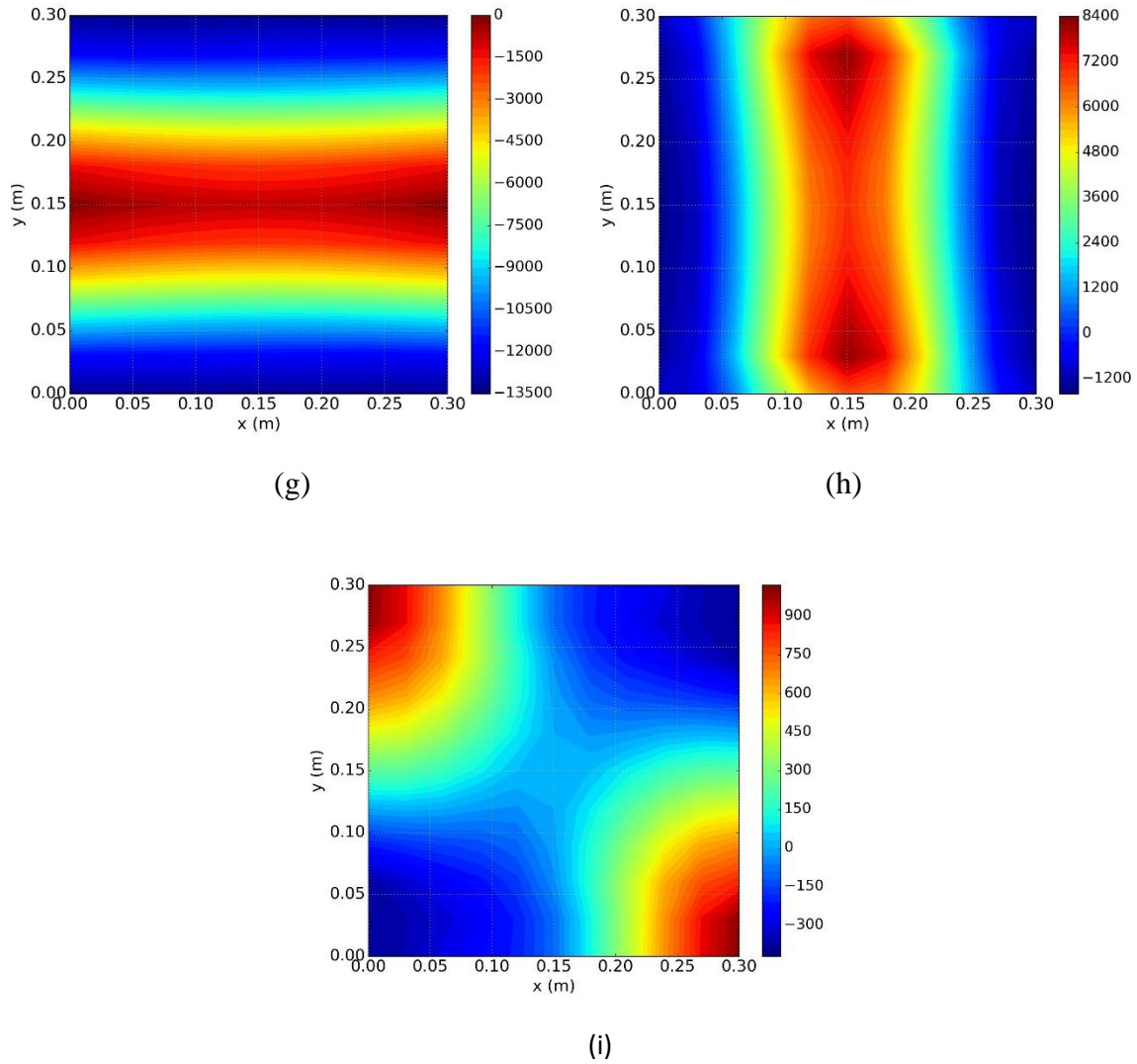


Figure 7.37. Unsymmetric unbalanced laminated composite model under in-plane compression and fixed boundary conditions at cycle 1 (110% of buckling end shortening strain), contour plots of: (a) out-of-plane deflection w (m); (b) in-plane longitudinal deflection u (m); (c) in-plane transverse deflection v (m); (d) strain ϵ_x ; (e) strain ϵ_y ; (f) strain γ_{xy} ; (g) stress resultant N_x (N/m); (h) stress resultant N_y (N/m); (i) stress resultant N_{xy} (N/m).

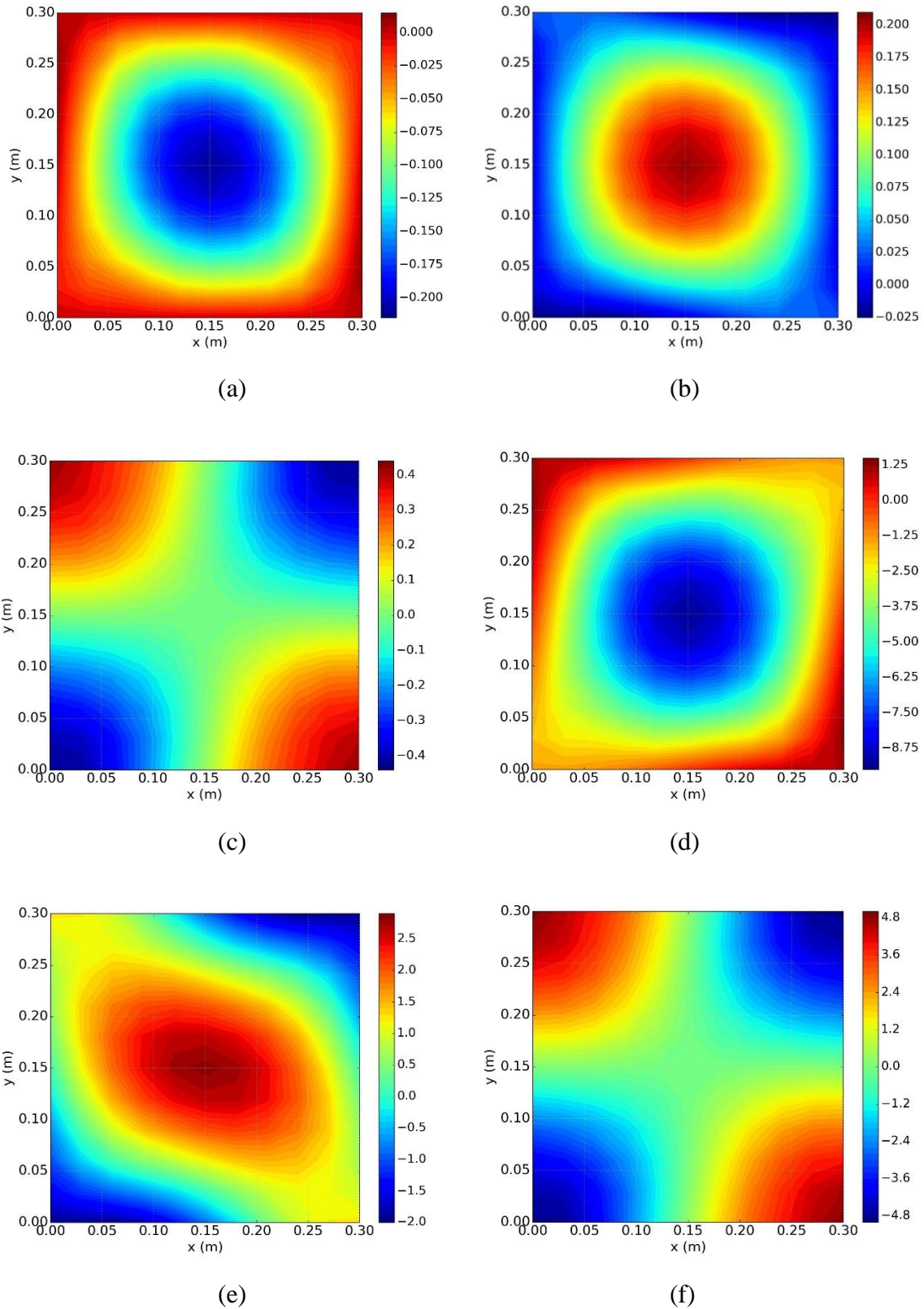


Figure 7.38. Unsymmetric unbalanced laminated composite model under in-plane compression and fixed boundary condition at cycle 1 (110% of buckling end shortening strain), contour plots of: (a) curvature κ_x ; (b) curvature κ_y ; (c) curvature κ_{xy} ; (d) bending moment M_x (Nm); (e) bending moment M_y (Nm); (f) bending moment M_{xy} (Nm).

7.7. Computational Efficiency Evaluation

Computational efficiency is an important consideration for numerical modelling techniques. Reducing the computational cost of composite modelling for large aerospace projects is highly beneficial particularly for preliminary design where many different design scenarios must be considered, and optimization which may take months for conventional FEA to solve. In these cases, a fast and reliable numerical technique is of great value. In this section, an evaluation of the computation efficiency of CWPAN for different cases is presented.

The most time-consuming calculation process in the postbuckling analysis is the solution of the equilibrium equations which are large linear equations. The size of these equations is highly dependent on the number of in-plane half-wavelengths and the number of strips. Since these are solved using the modified Newton iteration scheme more than 50 repeats are required which exacerbates the problem. Therefore, to improve the computational efficiency, reducing the computational effort required to solve large equations becomes the priority problem.

For a plate divided into 10 strips, using three and five half-wavelengths, it takes 0.35 minutes and 0.9 minutes to run one Newton iteration respectively using a 4 cores i7 and 16 RAM computer, . Such differences result in the computational times shown in Table 7.7.

Cycle number	Compression with free edges(3 half-wavelengths)	Compression with fixed edges(3 half-wavelengths)	Compression with straight edges(3 half-wavelengths)	Combined load with free edges(3 half-wavelengths)	Combined load with fixed edges(3 half-wavelengths)	Combined load with straight edges(3 half-wavelengths)	Pure shear(5 half-wavelengths)
1	2	1	2	2	2	2	3
2	2	1	1	2	2	2	3
3	2	1	1	2	2	2	4
4	2	1	1	2	2	2	4
5	2	1	1	2	2	2	5
6	2	1	1	2	2	2	5
7	2	1	1	2	2	2	6
8	2	1	1	2	2	2	7
9	2	1	1	2	2	2	8
10	2	1	1	2	2	2	8
Total	20	10	11	20	20	20	53
Time(mins)	8	4	5	8	8	8	47

Table 7.7 Approximate computational efficiency of CWPAN, showing iteration counts and solution times.

Table 7.7 shows the average number of iterations required to converge on a postbuckling mode using the modified Newton iteration scheme and the total run time. It can be seen that the run time increases when the complexity of the case increases, for example for shear. In this case this is due to the combination of the fact that shear loading adds instability to the structure resulting in more iterations for convergence, and that the use of 5 out-of-plane half-wavelengths increases the size of the linear equations. However for simpler cases, the analysis reaches double the critical buckling constant strain (10 cycles), within a maximum of 8 minutes.

For the ABAQUS Riks method, the run time is relatively hard to measure since it is dependent on many factors such as the number of elements, arc lengths, imperfection, etc. For a simple square composite plate under non-pure-shear loading, an approximation has been made that around 10 minutes are required to reach the same stage as CWPAN by using 900 elements. Even for these simple cases, CWPAN achieves the same level of accuracy with a 20% execution time reduction by dividing the plate into 10 strips. As described in section 7.5, as plates are assumed to be infinitely long, the computational complexity of the square plate is the same as plates of rectangular shape. This means that when analysing long plates, CWPAN will be significantly more efficient than Riks analysis to achieve the same level of accuracy.

Since the long execution time is associated with solving the large linear equations, applying suitable techniques based on key features of the resulting matrix could reduce the computational time significantly. For CWPAN, the target equations are found to form a banded matrix. This would allow them to be transformed into upper and a lower triangular matrices (LU decomposition) and solved accordingly, saving a significant amount of time. There are other techniques for solving such a matrix that can further reduce computational time such as the Gaussian elimination method (Maa et. al. 1997). Applying one of those techniques, the computational efficiency of CWPAN could be further reduced.

7.8. Conclusion

In this chapter, different types of isotropic laminated composite plates are modelled and presented to illustrate the capabilities of the coupled wavelength postbuckling analysis and modified Newton iteration scheme. The modelling examples start with isotropic plate under combined loading illustrating the particular data structures by CWPAN. For the case of a balanced symmetric laminate under pure compression and pure shear force, results are validated using the ABAQUS Riks method and the differences between the results for the two methods have been discussed. The modelling of unbalanced and unsymmetric composite plates is presented in the Section 7.6 to illustrate the ability of analysing general composite plates. Finally, a study of computational efficiency is presented. Some key conclusions are made.

Based on combining a number of half-wavelengths, a series solution for postbuckling analysis has been developed to enable any kind of laminated composites and in-plane loading conditions to be studied. To capture out-of-plane deflections for each postbuckling cycle, a modified Newton iteration has been introduced. These two techniques have been validated for a selection of different types of laminated composite plates with good results. Compared with previous postbuckling analysis using VIPASA analysis, CWPAN overcomes the limitations of compression loading and conservative solutions for composite materials.

Comparison of the results with those from ABAQUS Riks analyses shows good agreement has been achieved in terms of both contour plots of in-plane and out-of-plane displacements (u , v , w), strains (ε_x , ε_y , γ_{xy}), stress resultants (N_x , N_y , N_{xy}) and postbuckling paths where the maximum difference between the two methods has reached approximately 7%. As the two methods have some key differences, a discussion of these has been included.

A study has been presented to illustrate the computational efficiency of CWPAN for different combinations of loading and material anisotropy. In comparison with FEA, CWPAN has achieved a 20% reduction in execution time for square composite plates. For longer plates, however, CWPAN has an obvious advantage since as it already assumes an infinitely long plate the size of the model stays the same which is clearly not the case for FEA.

Chapter 8. Conclusions and Future Work

8.1. General conclusions

The literature on numerical solutions for shell structure postbuckling is extensive. Many of these studies focus on the finite element or finite strip methods as they provide highly robust and accurate solutions for structures with complex geometries, loading and boundary conditions. However, researchers and engineers have sometimes found those methods unsuitable for preliminary design due to their computational cost particularly when examining large numbers of different scenarios. To overcome these difficulties, other researchers are looking for analytical solutions or semi-analytical solutions which can provide fast analysis processes while retaining the required accuracy for certain problems.

The coupled wavelengths postbuckling presented in this thesis provides an efficient and reliable technique to allow researchers and engineers to observe postbuckling behaviours for composite plates under any in-plane loading. Based on the exact strip method, the theory represents out-of-plane displacements with a series of user-defined terms which are trigonometric in the longitudinal direction, and in-plane displacements with another enhanced set of trigonometric terms to account for the effect of large deflections. Such assumptions regarding displacements bring several advantages when compared to previous work. Firstly, composite plates and plates under shear load which causes skewed mode shapes can be accurately captured. This cannot be done using the previous postbuckling analysis which assumes plate deformation varies with only one half-wavelength. Secondly, by naturally regarding plates as infinitely long the method provides advantages for slender structures like an aircraft's wings and fuselage because solving for square plates and plates with multiple bays results in the same execution time. Thirdly dividing plates into strips rather than elements

results in a relatively small stiffness matrix. Compared to the conventional finite element method, retaining the desired accuracy using CWPAN is more efficient. By having explicit expressions for displacements, governing equilibrium equations can be assembled and solved analytically. The distributions of displacements, stresses and strains can therefore be captured.

These advantages have been illustrated by considering composite plates under a number of different in-plane boundary and loading conditions corresponding to particular engineering scenarios. Solutions have been compared with finite element analysis and previous postbuckling analyses, and the maximum difference between the presented method and FEA has reached approximately 7%. Results are seen to correlate well.

The series solutions used are inspired by previous postbuckling analyses based on VIPASA finite exact strip analysis. However, instead of representing the out-of-plane displacements with a single half-wavelength, any number of half-wavelengths can be coupled to represent complex postbuckling behaviours. The postbuckling solutions are therefore more accurate than those obtained previously for cases involving composite plates and skewed loading, and allow solutions to be obtained for cases which could not be solved using the previous version of the analysis.

The series solutions representing in-plane variables are based on taking out-of-plane displacements as known quantities. To employ the method in postbuckling analysis, several convergence strategies have been developed to find progressive changes in out-of-plane displacement, including a general convergence strategy, calculation of effective uniform stress resultants, approximate buckling amplitude calculation and a modified Newton iteration scheme. An effective uniform stress resultants calculation employs an energy approach to find the current postbuckling stage's applied load. Based on this, the postbuckling stiffness used for the Newton iteration scheme can be calculated. The Newton iteration scheme was first developed for VICONOPT postbuckling analysis to provide accurate convergence on critical buckling loads and associated buckling modes with a single half-wavelength. The modified version extends the technique to enable any number of half-wavelengths to be considered for complex buckling modes such as composite plates under shear loading. By considering postbuckling stiffness, the out-of-plane displacements are therefore captured accurately. The strategy of approximate buckling amplitude calculation is developed to assist the Newton iteration scheme to converge more efficiently.

Validation studies are performed to compare the progressive postbuckling mode with that obtained using the Riks method in the FE software ABAQUS. Solutions are seen to replicate classical plate phenomena like stress redistribution, validating the method. The method is also seen to be capable of predicting the correct distributions of in-plane and out-of-plane displacements at any strain level. Comparisons of displacements, stresses and strains using contour plots show good agreement for the majority of cases. Those where there is less agreement are a result of the infinitely long plate assumption and the method of controlling the linear strains, which are not directly replicated in FE. In both cases however CWPAN is considered to be closer to real structural behaviour. A study of computational efficiency showed CWPAN achieved a 20% reduction in execution time for square composite plates. For longer plates, however, it has an even greater advantage since as it already assumes an infinitely long plate so that the size of the model stays the same which is clearly not the case for FEA.

The following objectives have been achieved in this research:

1. A peer review on stability of plate structures has been completed and limitations and gaps in the research on the postbuckling analysis of composite plates have been found.
2. Based on the exact strip method, a postbuckling analysis using coupled wavelengths (CWPAN) has been developed allowing researchers and engineers to observe postbuckling of composite plates in a fast and reliable way.
3. To further enable a full postbuckling analysis and increase the robust features of the technique, a convergence procedure has been developed.
4. A sensitivity study has been conducted to select the optimal parameters in the coupled wavelength postbuckling analysis.
5. A validation has been done against FEA to further study the speed and accuracy of CWPAN.

8.2. Future work

Further improvements have been identified throughout the course of this study which may bring additional benefits and which should be considered for implementation in the future.

Some recommendations for future development based on the improved analysis are discussed below.

1. Large linear matrices are required to be solved in both the series solutions and the Newton iteration scheme. Currently a method of LU decomposition is employed to achieve this. However, it has been found that the features of the target matrix, such as the fact that the equilibrium equations are found to form a banded matrix, have not been fully exploited in the solution techniques. A suitable linear equation solving technique would reduce the computational time significantly.
2. Although unsymmetric and unbalanced laminates can be analysed in the series solutions, convergence strategies are still not able to cover these cases. The stiffness matrix calculation utilized in the modified Newton iteration scheme is based on the method developed by Anderson et al. (1983). Such a method is particularly designed for the exact strip method and enables the exact stiffness to be found for balanced and symmetric composites for buckling problems. It would be worth studying a structure's stiffness for unsymmetric and unbalanced laminates in the exact strip method.
3. One limitation of the study in this thesis is that it is restricted to simple geometries. Assemblies like stiffened and curved panels are not able to be analysed by the series solution. This is because as the half-wavelengths for the in-plane displacements are generalized from the out-of-plane displacements, they naturally cannot be represented by the same set. However, for stiffened panels, the skins' out-of-plane displacements are the stiffeners' in-plane displacements and vice versa. This cannot be achieved in explicit expressions for the current method. To overcome this limitation, the in-plane and out-of-plane displacements have to be represented by one set of half-wavelengths. One solution would be to neglect the extra half-wavelengths in the in-plane displacements to make them identical to the out-of-plane ones. Zhang (2018) did a similar study using VIPASA postbuckling analysis by neglecting two extra half-wavelengths. The solutions were compared with ABAQUS but discrepancies were noted due to oversimplification. Such an assumption may lead to an even larger discrepancy for the series solutions as the target structures are more complex. Another solution would be to establish completely new assumptions for both in-plane and out-of-plane displacements with out-of-plane displacements being no longer known quantities in the equilibrium equations. The equilibrium equations would then be non-linear instead of linear. Consequently,

convergence strategies for obtaining out-of-plane displacements may not be necessary. Such a hypothesis could be less efficient than the presented one due to the involvement of highly non-linear equations. But it is almost certain that it will increase the accuracy and most importantly overcome the stiffened panel problem. More studies are required to achieve such hypothesis.

4. Another limitation is concerned with the fact that only in-plane boundary conditions can be applied to the structure. Out-of-plane boundary conditions are designed to represent simple support in CWPAN. To enable the flexible application of out-of-plane edge conditions in series solutions, the stiffness matrix for the particular edge conditions in the Newton iteration scheme would be required to be modified considering extra Lagrange Multipliers. Such a technique already exists in VICONOPT. Implementing extra Lagrange Multipliers, point supports are able to be added at any location on the plate. Furthermore, unsymmetrical edge conditions can be achieved which may then be helpful for the analysis of stiffened panels.

References

- ABAQUS. 2014. *User's Manual, Version 6.11*. Dassault Systems Inc., Paris.
- Almroth, B.O., Brogan, F.A. and Stanley, G.M. 1981. *Structural analysis of general shells*. Volume 2: User instructions for STAGSC-1.
- Anderson, M.S. and Kennedy, D. 2008. Post-buckling of composite stiffened panels using exact strip analysis with Newton iteration. *Proceedings of the 49th AIAA/ASME/ASCE/AHS/ASC Structures, Structural, Dynamics and Materials Conference*, Schaumburg, AIAA-2008-2184, 1-8.
- Anderson, MS. and Williams, F.W., Wright CJ. 1983. Buckling and vibration of any prismatic assembly of shear and compression loaded anisotropic plates with an arbitrary supporting structure. *International Journal of Mechanical Sciences*, 25(8), 585-596.
- Beslin, O. and Nicolas, J. 1997. A hierarchical functions set for predicting very high order plate bending modes with any boundary conditions. *Journal of Sound and Vibration*, 202(5), pp.633-655.
- Bisagni, C. and Vescovini, R. 2009. Analytical formulation for local buckling and post-buckling analysis of stiffened laminated panels. *Thin-Walled Structures*, 47(3), pp.318-334.
- Bisagni, C. and Vescovini, R. 2009. Fast tool for buckling analysis and optimization of stiffened panels. *Journal of Aircraft*, 46(6), pp.2041-2053.
- Bloom, F. and Coffin, D. 2000. *Handbook of Thin Plate Buckling and Postbuckling*. CRC Press.
- Bryan, G.H. 1890. On the stability of a plane plate under thrusts in its own plane, with applications to the "buckling" of the sides of a ship. *Proceedings of the London Mathematical Society*, 1(1), pp.54-67.
- Butler, R and Williams F.W. 1992. Optimum buckling design of compression panels using VICONOPT. *Structural Optimization*, 6(3), 160-165.
- Che, B, Kennedy, D and Featherston, C.A. 2010. Improved exact strip postbuckling analysis for anisotropic plates. *Proceedings of 2nd Royal Aeronautical Society Conference on Aircraft Structural Design*, London, Paper 37.
- Chen, Q. and Qiao, P. 2021. Buckling and postbuckling of rotationally-restrained laminated composite plates under shear. *Thin-Walled Structures*, 161, p.107435.
- Coan, J.M. 1951. Large-deflection theory for plates with small initial curvature loaded in edge compression. *Journal of Applied Mechanics-Transactions of the ASME* 18(2), pp. 143–151.
- Cox, H.L. 1933. The Buckling of Thin Plates in Compression. British Ministry of Aviation, Aeronautical Research Council, Reports and Memoranda, 1554,.
- Diaconu, C.G. and Weaver, P.M. 2005. Approximate solution and optimum design of compression-loaded, postbuckled laminated composite plates. *AIAA Journal*, 43(4), pp.906-914.
- Diaconu, C.G. and Weaver, P.M. 2006. Postbuckling of long unsymmetrically laminated composite plates under axial compression. *International Journal of Solids and Structures*, 43(22-23), pp.6978-6997.

- Dong, S.B., Pister, K.S. and Taylor, R.L. 1962. On the theory of laminated anisotropic shells and plates. *Journal of the Aerospace Sciences*, 29(8), pp.969-975.
- D'Ottavio, M. and Polit, O. 2017. Classical, first order, and advanced theories. In *Stability and Vibrations of Thin Walled Composite Structures* (pp. 91-140). Woodhead Publishing.
- Dym, C.L. 1974. *Stability Theory and Its Applications to Structural Mechanics*, Noordhoff Int. Publ., Leyden.
- Euler, L. 1759. Sur la force des colonnes. *Memoires de L'Academie des Sciences et Belles-Lettres* 13, pp. 252–282.
- Fafard, M. and Massicotte, B. 1993. Geometrical interpretation of the arc-length method. *Computers and Structures*, 46(4), pp.603-615.
- Ferreira, J.V. and Serpa, A.L. 2005. Application of the arc-length method in nonlinear frequency response. *Journal of Sound and Vibration*, 284(1-2), pp.133-149.
- Fleming, G.G. and De Lepinay, I. 2019, Environmental Trends in Aviation to 2050, International Civil Aviation Organization.
- Gibson, R.F., 2016. *Principles of Composite Material Mechanics*. CRC press.
- Gousel, M., Kumbar, R. and Madhusudhan, T. 2015, Review on Investigation of “Buckling Behaviour of Composite Plate” *International Journal of Engineering Research and General Science* 3(2:2), pp.190-193.
- Grossmann, C., Roos, H.G. and Stynes, M. 2007. *Numerical Treatment of Partial Differential Equations* (Vol. 154). Berlin: Springer.
- Hanna, N.F. and Leissa, A.W. 1994. A higher order shear deformation theory for the vibration of thick plates. *Journal of Sound and Vibration*, 170(4), pp.545-555.
- Harris, G.Z. 1975. The buckling and post-buckling behaviour of composite plates under biaxial loading. *International Journal of Mechanical Sciences*, 17(3), pp.187-202.
- Herakovich, C.T. 2012. Mechanics of composites: a historical review. *Mechanics Research Communications*, 41, pp.1-20.
- Hutchinson, J.W. and Koiter, W.T. 1970. Postbuckling theory. *Applied Mechanics Reviews*, 23(12), pp.1353-1366.
- Johns, D.J. 1970. Shear buckling of isotropic and orthotropic plates a review. *Ministry of Defence Reports and Memoranda*, 3677.
- Jones, J.M. 1973. A composite heterogeneous model for brand choice behavior. *Management Science*, 19(5), pp.499-509.
- Kantorovich, L.V. and Krylov, VI. 1958, *Approximate Methods of Higher Analysis*. Interscience, New York.
- Kim, K. and Voyiadjis, G.Z. 1999. Non-linear finite element analysis of composite panels. *Composites Part B: Engineering*, 30(4), pp.365-381.
- Koiter, W.T. 1943. De meedragende breedte bij groote oversehrijding der dnikspanning voor versehillende inklemming der plaatranden. (The effective width of in finitely long, flat rectangular plates under various conditions of edge restraint) *Report S.287. Nationaal Luchtvaartlaboratorium*, Amsterdam.

References

- Lekhnitskii, S.G. 1968. *Anisotropic Plates*. Gordon and Breach, New York.
- Lentini, M. and Pereyra, V. 1977. An adaptive finite difference solver for nonlinear two-point boundary problems with mild boundary layers. *SIAM Journal on Numerical Analysis* 14(1), pp. 91–111.
- Levy, S. 1942. Bending of rectangular plates with large deflections. *NACA Technical Note 846*, pp. 1–46.
- Li, D.M., Featherston, C.A. and Wu, Z. 2020. An element-free study of variable stiffness composite plates with cutouts for enhanced buckling and post-buckling performance. *Computer Methods in Applied Mechanics and Engineering*, 371, p.113314.
- Librescu, L. and Stein, M. 1991. A geometrically nonlinear theory of transversely isotropic laminated composite plates and its use in the post-buckling analysis. *Thin-Walled Structures*, 11(1-2), pp.177-201.
- Liszka, T. and Orkisz, J. 1980. The finite difference method at arbitrary irregular grids and its application in applied mechanics. *Computers and Structures*, 11(1-2), pp.83-95.
- Lo, K.H., Christensen, R.M. and Wu, E.M. 1977. A high-order theory of plate deformation—Part 1: Homogeneous plates. *Journal of Applied Mechanics*, 44(4), pp.663-668.
- Love, A.E.H. 1888. XVI. The small free vibrations and deformation of a thin elastic shell. *Philosophical Transactions of the Royal Society of London.(A.)*, (179), pp.491-546.
- Maa, J.P., Maa, M.H., Li, C. and He, Q. 1997. *Using the Gaussian Elimination Method for Large Banded Matrix Equations*. Special Scientific Report 135, Virginia Institute of Marine Science.
- Marshall, I.H., Rhodes, J. and Banks, W.M. 1977. The nonlinear behaviour of thin, orthotropic, curved panels under lateral loading. *Journal of Mechanical Engineering Science*, 19(1), pp.30-37.
- Memon, B.A. and Su, X. 2004. Non-linear analysis of reinforced concrete members with ANSYS. *Quaid-e-Awam University Research Journal of Engineering, Science and Technology*, 5(1), pp.37-46.
- Memon, B.A., 2004. Arc-length technique for nonlinear finite element analysis. *Journal of Zhejiang University-Science A*, 5(5), pp.618-628
- Mindlin, R.D. 1951. Influence of rotatory inertia and shear on flexural motions of isotropic, elastic plates. *Journal of Applied Mechanics* 18(1), pp.31-38.
- Mrazova, M., 2013. Advanced composite materials of the future in aerospace industry. *Incas bulletin*, 5(3), p.139.
- Mukhopadhyay, M. 2005. *Mechanics of Composite Materials and Structures*. Universities Press, Hyderabad.
- Nagavally, R.R. 2017. Composite materials-history, types, fabrication techniques, advantages, and applications. *International Journal of Mechanical and Production Engineering*, 5(9), pp.82-7.
- Oliveri, V. and Milazzo, A. 2018. A Rayleigh-Ritz approach for postbuckling analysis of variable angle tow composite stiffened panels. *Computers and Structures*, 196, pp.263-276.

- Pister, K.S. and Dong, S.B. 1959. Elastic bending of layered plates. *Journal of the Engineering Mechanics Division*, 85(4), pp.1-10.
- Pister, K.S. 1959. Flexural vibration of thin laminated plates. *Journal of the Acoustical Society of America*, 31(2), pp.233-234.
- Powell, S., Williams, F., Askar, A.S. and Kennedy, D. 1998. Local postbuckling analysis for perfect and imperfect longitudinally compressed plates and panels. *Proceedings of 39th AIAA/ASME/ASCE/AHS/ASC Structures, Structural Dynamics, and Materials Conference*, Long Beach, 595-603.
- Raju, G., Wu, Z. and Weaver, P.M. 2013. Postbuckling analysis of variable angle tow plates using differential quadrature method. *Composite Structures*, 106, pp.74-84.
- Raju, G., Wu, Z. and Weaver, P.M. 2015. Buckling and postbuckling of variable angle tow composite plates under in-plane shear loading. *International Journal of Solids and Structures*, 58, pp.270-287.
- Ramm, E., 1981. Strategies for tracing the nonlinear response near limit points. In *Nonlinear Finite Element Analysis in Structural Mechanics* (ed. W Wunderlich, E Stein and KJ Bathe), Springer, Berlin, Heidelberg, pp.63-89.
- Reissner, E. and Stavsky, Y. 1961. Bending and stretching of certain types of heterogeneous aeolotropic elastic plates. *Journal of Applied Mechanics* 28(3), pp.402-408.
- Reissner, E. 1961. On finite pure bending of cylindrical tubes. *Österreich Ingenieur Archiv*, 15, pp.165-172.
- Riks, E. 1972. The application of Newton's method to the problem of elastic stability. *Journal of Applied Mechanics* 39(4), pp.1060-1065.
- Riks, E. 1979. An incremental approach to the solution of snapping and buckling problems. *International Journal of Solids and Structures*, 15(7), pp.529-551.
- Song, M., Yang, J., Kitipornchai, S. and Zhu, W. 2017. Buckling and postbuckling of biaxially compressed functionally graded multilayer graphene nanoplatelet-reinforced polymer composite plates. *International Journal of Mechanical Sciences*, 131, pp.345-355.
- Sousa, C.A. and Pimenta, P.M. 2010. A new parameter to arc-length method in nonlinear structural analysis. *Mecánica Computacional*, 29(17), pp.1841-1848.
- Stein, M. 1985. Analytical results for post-buckling behaviour of plates in compression and in shear. In: *Aspects of the analysis of plate structures, A volume in honour of W. H. Wittrick* (ed. DJ Dawe, RW Horsington, AG Kamtekar and GH Little), Clarendon Press, Oxford, pp.205-223.
- Stein, M. 1959a. Loads and deformations of buckled rectangular plates. *Technical Report R-40*, NASA (19980235521).
- Stein, M. 1959b. The phenomenon of change in buckle pattern in elastic structures. *Technical Report R-39*, NASA (19980228195).
- Stein, M. 1983. Postbuckling of orthotropic composite plates loaded in compression. *AIAA Journal* 21(12), pp. 1729–1735.
- Stein, M. 1985. Postbuckling of long orthotropic plates in combined shear and compression. *AIAA Journal* 23(5), pp. 788–794.

References

- Stroud, W.J. Greene, W.H. and Anderson, M.S. 1984. Buckling loads of stiffened panels subjected to combined longitudinal compression and shear: results obtained with PASCO, EAL, and STAGS computer programs. *Technical Paper 2215*, NASA..
- Sundaresan, P.B.A.V.S.S.C., Singh, G.B.A.V.S.S.C. and Rao, G.V. 1996. Buckling and post-buckling analysis of moderately thick laminated rectangular plates. *Computers and Structures*, 61(1), pp.79-86.
- Teng, J.G. and Luo, Y.F. 1998. A user-controlled arc-length method for convergence to predefined deformation states. *Communications in Numerical Methods in Engineering*, 14(1), pp.51-58.
- Timoshenko, S. and Krieger, S.W. *Theory of Plates and Shells*. McGraw-Hill, New York.
- Timoshenko, S.P. 1936. *Theory of Elastic Stability*. McGraw-Hill, New York.
- Uflyand, Y.S., 1948. Wave propagation associated with the transverse vibrations of beams and plates. *Prikladnaya Matematika i Mekhanika* 12(3), pp.287-300.
- Vescovini, R. and Bisagni, C. 2012. Buckling analysis and optimization of stiffened composite flat and curved panels. *AIAA Journal*, 50(4), pp.904-915.
- Vescovini, R. and Bisagni, C. 2016. Fast analysis of non-symmetric panels using semi-analytical techniques. *Composites Part B: Engineering*, 99, pp.48-62.
- Viswanathan, A. V and Tamekuni, M. 1973. Elastic buckling analysis for composite stiffened panels and other structures subjected to biaxial in-plane loads. *Contractor Report 2216*, NASA.
- Viswanathan, A.V. Tamekuni, M. and Baker, L. L. 1974. Elastic stability of laminated, flat and curved, long rectangular plates subjected to combined in-plane loads. *Contractor Report 2230*, NASA.
- Vlasov, V.Z., 1957a, On the equations of bending of plates (in Russian), *Doklady Akademiiia Nauk Azerbaidzhanskoi SSR*, 13(9), pp.955-959.
- Vlasov, V.Z. 1957b. The method of initial function in problems of theory of thick plates and shells. *Proceeding of the 9th International Congress of Applied Mechanics, University of Bruxelles* 6, pp.321-330.
- Von, Kármán, T, Sechler, E.E. and Donnell L.H. 1932. The strength of thin plates in compression. *Transactions of ASME*, 54, pp.53-57.
- Wang, C.M. 2007. Relationships between vibration frequencies of higher-order plate theories and classical thin plate theory. In *Analysis and Design of Plated Structures* (ed. NE Shanmugam and CM Wang), pp.275-292. Woodhead Publishing, Sawston.
- Wang, Y. and Qiao, P. 2021. Postbuckling analysis of orthogonally-stiffened plates by a simplified spline finite strip method. *Thin-Walled Structures*, 166, p.108122.
- Weaver, P. 2004. On optimisation of long anisotropic flat plates subject to shear buckling loads. *Proceedings of 45th AIAA/ASME/ASCE/AHS/ASC Structures, Structural Dynamics & Materials Conference*, p. 2053.
- Williams, F.W. and Anderson MS. 1983. Incorporation of Lagrange multipliers into an algorithm for finding exact natural frequencies or critical buckling loads. *International Journal of Mechanical Sciences*, 25(8), 579-584.

- Williams, F.W. Anderson, M.S. Kennedy, D. Butler, R. Aston, G. and Hoh, S.M. 1990. User manual for VICONOPT: An exact analysis and optimum design program covering the buckling and vibration of prismatic assemblies of flat in-plane loaded, anisotropic plates, with approximations for discrete supports, and transverse stiffeners, Cardiff University
- Williams, F.W. Kennedy, D. Anderson, M.S and Butler, R. 1991. VICONOPT: Program for exact vibration and buckling analysis or design of prismatic plate assemblies. *AIAA Journal* 29(11), pp.1927-1928.
- Winter, G. 1947. Strength of thin steel compression flanges. *Transactions of the American Society of Civil Engineers*, 112(1), pp.527-554.
- Wittrick, W.H. 1968a. A unified approach to the initial buckling of stiffened panels in compression. *The Aeronautical Quarterly* 19(3), pp.265–283.
- Wittrick, W.H. 1968b. General sinusoidal stiffness matrices for buckling and vibration analyses of thin flat-walled structures. *International Journal of Mechanical Sciences* 10(12), pp.949–966.
- Wittrick, W.H. and Curzon. P.L.V. 1968. Stability functions for the local buckling of thin flat-walled structures with the walls in combined shear and compression. *The Aeronautical Quarterly* 19(4), pp.327–351.
- Wittrick, W.H and Williams F.W. 1971. A general algorithm for computing natural frequencies of elastic structures. *Quarterly Journal of Mechanics and Applied Mathematics*, 24(3), pp.263-284.
- Wittrick, W.H. and Williams. F.W. 1973. An algorithm for computing critical buckling loads of elastic structures, *Journal of Structural Mechanics*. 1(4), pp.497-518.
- Wittrick, W.H. and Williams F.W. 1974. Buckling and vibration of anisotropic or isotropic plate assemblies under combined loadings. *International Journal of Mechanical Sciences*, 16(4), pp.209-239.
- Xu, J., Zhao, Q. and Qiao, P. 2013. A critical review on buckling and post-buckling analysis of composite structures. *Frontiers in Aerospace Engineering*, 2(3), pp.157-168.
- Yamaki, N. 1960. Postbuckling behavior of rectangular plates with small initial curvature loaded in edge compression—(continued). *Journal of Applied Mechanics* 27(2), pp.335–342.
- Zhang, C. 2018. Postbuckling analysis of isotropic and anisotropic plate assemblies under combined loading. *PhD thesis*, Cardiff University.
- Zhao, K., Kennedy, D. and Featherston, C.A. 2019. Exact strip postbuckling analysis of composite plates under compression and shear. *Aeronautical Journal*, 123(1263), pp.658-677.

Appendices

Appendix A

This appendix presents programming codes written in Python to achieve highly robust calculations in this thesis.

Calculation of the list of in-plane half-wavelengths

```
NOwavlth = list(abs(self.lambda1))
for i in self.lambda1:
    for j in self.lambda1:
        NOwavlth.append(abs(i + j))
        NOwavlth.append(abs(i - j))
NOwavlth = np.unique(NOwavlth)
NOwavlth.sort()
NOwavlth = np.asarray(NOwavlth)

K = 2 * NOwavlth.size - 1
```

Calculation of Equation 4.17

```
epioNSC = empty([n, NOwavlth.size])
epioNSS = empty([n, NOwavlth.size])
epioCX = empty([n, K])

for i in range(0, n):
    for j in range(0, NOwavlth.size):
```

```

epioNSC[i, j] = 0
epioNSS[i, j] = 0
for m in range(0, lambda1.size):
    for k in range(0, lambda1.size):
        if lambda1[m] + lambda1[k] == NOWavlth[j]:
            epioNSC[i,j] = epioNSC[i,j] + lambda1[m] *
lambda1[k]*\ (-w[i,m*2]*w[i,k*2]+w[i,m*2+1]*w[i,k*2+1])
            epioNSS[i,j] = epioNSS[i,j] + lambda1[m] *
lambda1[k]*\ (-w[i,m*2]*w[i,k*2+1]-w[i,m*2+1]*w[i,k*2])
            elif np.absolute(lambda1[m] - lambda1[k]) == NOWavlth[j]:
                epioNSC[i,j] = epioNSC[i,j] + lambda1[m] *
lambda1[k]*\ (w[i,m*2]*w[i,k*2]+w[i,m*2+1]*w[i,k*2+1])
                if lambda1[m] - lambda1[k] > 0:
                    epioNSS[i, j] = epioNSS[i, j] + lambda1[m] *\
lambda1[k]*(-w[i,m*2] * w[i,k*2+1] + w[i,m*2+1]*w[i,k*2])
                elif lambda1[m] - lambda1[k] < 0:
                    epioNSS[i, j] = epioNSS[i, j] + lambda1[m] *\
lambda1[k]*(w[i,m*2]*w[i,k*2+1]-w[i,m*2+1]*w[i,k* 2])

        epioCX[i, 2 * j - 1] = epioNSC[i, j]
        epioCX[i, 2 * j] = epioNSS[i, j]

for i in range(0, n):
    epioCX[i, 0] = epioNSC[i, 0]
epioCX = ((0.25 * pi * pi) / (1 * 1)) * epioCX # multiply constants for the all matrix

```

Calculation of Equation 4.18

```
epioCYC = empty([n, NOwavlth.size])
```

```
epioCYS = empty([n, NOwavlth.size])
```

```
epioCY = empty([n, K])
```

```
for i in range(0, n):
```

```
    for j in range(0, NOwavlth.size):
```

```
        epioCYC[i, j] = 0
```

```
        epioCYS[i, j] = 0
```

```
        for m in range(0, lambda1.size):
```

```
            for k in range(0, lambda1.size):
```

```
                if lambda1[m] + lambda1[k] == NOwavlth[j]:
```

```
                    epioCYC[i, j] = epioCYC[i, j] + phi[i, m * 2] * phi[i, k * 2] - phi[i, m * 2 + 1] * phi[i, k * 2 + 1]
```

```
                    epioCYS[i, j] = epioCYS[i, j] + phi[i, m * 2] * phi[i, k * 2 + 1] + phi[i, m * 2 + 1] * phi[i, k * 2]
```

```
                elif np.absolute(lambda1[m] - lambda1[k]) == NOwavlth[j]:
```

```
                    epioCYC[i, j] = epioCYC[i, j] + phi[i, m * 2] * phi[i, k * 2] + phi[i, m * 2 + 1] * phi[i, k * 2 + 1]
```

```
                if lambda1[m] - lambda1[k] > 0:
```

```
                    epioCYS[i, j] = epioCYS[i, j] - phi[i, m * 2] * phi[i, k * 2 + 1] + phi[i, m * 2 + 1] * phi[i, k * 2]
```

```
                elif lambda1[m] - lambda1[k] < 0:
```

```
                    epioCYS[i, j] = epioCYS[i, j] + phi[i, m * 2] * phi[i, k * 2 + 1] - phi[i, m * 2 + 1] * phi[i, k * 2]
```

```
        epioCY[i, 0] = epioCYC[i, 0]
```

```
        epioCY[i, 2 * j - 1] = epioCYC[i, j]
```

```
        epioCY[i, 2 * j] = epioCYS[i, j]
```

```
epioCY = 0.25 * epioCY
```

Calculation of Equation 4.19

```
epioCXYC = empty([n, NOWavlth.size])
epioCXYS = empty([n, NOWavlth.size])
epioCXY = empty([n, K])
```

```
for i in range(0, n):
    for j in range(0, NOWavlth.size):
        epioCXYC[i, j] = 0
        epioCXYS[i, j] = 0
        for m in range(0, lambda1.size):
            for k in range(0, lambda1.size):
                if lambda1[m] + lambda1[k] == NOWavlth[j]:
                    epioCXYC[i, j] = epioCXYC[i, j] + lambda1[m] * (w[i, m \
2 + 1] * phi[i, k * 2] + w[i, m * 2] * phi[i, k * 2 + 1])
                    epioCXYS[i, j] = epioCXYS[i, j] + lambda1[m] * (-w[i, m \
2] * phi[i, k * 2] + w[i, m * 2 + 1] * phi[i, k * 2 + 1])
                elif np.absolute(lambda1[m] - lambda1[k]) == NOWavlth[j]:
                    epioCXYC[i, j] = epioCXYC[i, j] + lambda1[m] * (w[i, m \
2 + 1] * phi[i, k * 2] - w[i, m * 2] * phi[i, k * 2 + 1])
                    if lambda1[m] - lambda1[k] > 0:
                        epioCXYS[i, j] = epioCXYS[i, j] + lambda1[m] * (-w[i, m \
2] * phi[i, k * 2] - w[i, m * 2 + 1] * phi[i, k * 2 + 1])
                    elif lambda1[m] - lambda1[k] < 0:
                        epioCXYS[i, j] = epioCXYS[i, j] + lambda1[m] * (w[i, m \
2] * phi[i, k * 2] + w[i, m * 2 + 1] * phi[i, k * 2 + 1])

        epioCXY[i, 0] = epioCXYC[i, 0]
        epioCXY[i, 2 * j - 1] = epioCXYC[i, j]
        epioCXY[i, 2 * j] = epioCXYS[i, j]
```

```
epioCXY = ((0.5 * pi) / l) * epioCXY
epioC = empty([n, K * 3])
```

Calculation of effective uniform stress resultants (Equations 5.12-5.14)

`def EffStres(AdStrainsX, AdStressesX):`

```

    EfStresX = np.zeros(N/m)
    for k in range(0, n):
        for i in range(0, K + 1):
            for j in range(0, K + 1):
                if i % 2 == 0 and j % 2 == 0:
                    if NOWavlth[i // 2] == NOWavlth[j // 2] and NOWavlth[i
// 2] == 0:
                        EfStresX[k] = AdStressesX[k, i] * AdStrainsX[k, j] +
EfStresX[k]
                    elif NOWavlth[i // 2] == NOWavlth[j // 2] and
NOWavlth[i // 2] != 0:
                        EfStresX[k] = AdStressesX[k, i] * AdStrainsX[k, j] / 2 +
EfStresX[k]
                    elif i % 2 == 1 and j % 2 == 1:
                        if NOWavlth[(i - 1) // 2] == NOWavlth[(j - 1) // 2] and
NOWavlth[(i - 1) // 2] != 0:
                            EfStresX[k] = AdStressesX[k, i] * AdStrainsX[k, j] / 2 +
EfStresX[k]
                    elif i % 2 == 1 and j % 2 == 0:
                        if NOWavlth[(i - 1) // 2] % 2 == 0 and NOWavlth[j // 2] %
2 == 1:
                            EfStresX[k] = AdStressesX[k, i] * AdStrainsX[k, j]
* (2 * NOWavlth[(i - 1) // 2]) / (pi * (np.power(NOWavlth[(i - 1) // 2], 2) -
np.power(NOWavlth[j // 2], 2))) + EfStresX[k]
                        elif NOWavlth[(i - 1) // 2] % 2 == 1 and NOWavlth[j //
2] % 2 == 0:
                            EfStresX[k] = AdStressesX[k, i] * AdStrainsX[k, j] \
* (2 * NOWavlth[(i - 1) // 2]) / (pi * (np.power(NOWavlth[(i - 1) // 2], 2) -
np.power(NOWavlth[j // 2], 2))) + EfStresX[k]
                    elif j % 2 == 1 and i % 2 == 0:
                        if NOWavlth[(j - 1) // 2] % 2 == 0 and NOWavlth[i
// 2] % 2 == 1:
                            EfStresX[k] = AdStressesX[k, i] *
AdStrainsX[k, j] * (2 * NOWavlth[(j - 1) // 2]) / (pi * (np.power(NOWavlth[(j - 1) // 2],
NOWavlth[i // 2], 2))) + EfStresX[k]
                    elif NOWavlth[(j - 1) // 2] % 2 == 1 and

```

```

NOWavlth[i // 2] % 2 == 0:
    EfStresX[k] = AdStressesX[k, j] *
AdStrainsX[k, i] * (2 * NOWavlth[(j - 1) // 2]) / (pi * ( np.power(NOWavlth[(j - 1) // 2], 2) -
np.power(NOWavlth[i // 2], 2))) + EfStresX[k]

EfStraX = np.zeros(N/m)
for i in range(0, n):
    EfStraX[i] = AdStrainsX[i, 0]
for k in range(0, n):
    for j in range(0, K + 1):
        if j % 2 == 1:
            if NOWavlth[(j - 1) // 2] == 0:
                EfStraX[k] = EfStraX[k] + AdStrainsX[k, j]
            elif NOWavlth[(j - 1) // 2] % 2 == 1:
                EfStraX[k] = EfStraX[k] + 2 * AdStrainsX[k, j]
(NOWavlth[(j - 1) // 2] * pi)

Efs = np.zeros(N/m)

for i in range(0, n):
    if abs(EfStraX[i]) < 10e-10:
        Efs[i] = AdStressesX[i, 0]
    else:
        Efs[i] = EfStresX[i] / EfStraX[i]

```

Local stiffness matrix calculation. This process is adopted from Wittrick and Williams (1983) for the calculation of stiffness matrix for a symmetric composite.

```

alfa11 = D11 / D22
alfa12 = D12 / D22
alfa33 = D66 / D22
alfa13 = D16 / D22
alfa23 = D26 / D22
vudash = alfa12 - alfa23**2

```

```

def EStiff(Nl, Ns, Nt, wlen):
    Lm = l / lambda1[wlen]
    w = lambda1[wlen]*(pi * B)/l
    T = (alfa12) + (2 * alfa33) - (3 * alfa23**2) - ((Lm**2 * Nt) / (2 * pi**2 * D22))
    S = ((Lm**2 * Ns) / (pi**2 * D22)) + (2 * ((alfa23 * T) + (alfa23**3) - (alfa13)))
    L = ((Lm**2 / (pi**2 * D22)) * Nl) - (2 * alfa23 * S) + (T + alfa23**2)**2 - (alfa11)
    Tt = ((S**2) / 4) + (T * L / 3) - ((T**3) * 8 / 27)

```

Appendices

```

Delta = (((T**2) * 4 / 3) - L)**3 - (27 * Tt**2)
if Delta > 0:
    xii = np.arccos(27 * Tt * ((4 * T ** 2) - (3 * L)) ** -1.5)
    beta = np.sqrt((((4 * T**2) - (3 * L))**0.5 * np.cos(xii / 3)) - T) / 3

elif Delta < 0:
    if (Tt - (np.sqrt(-Delta / 27))) >= 0:
        beta = np.sqrt((0.5 * pow((Tt + (np.sqrt(-Delta / 27))), 1 / 3)) + (0.5 * pow((Tt
- (np.sqrt(-Delta / 27))), 1 / 3)) - (1 / 3 * T))
    elif (Tt - (np.sqrt(-Delta / 27))) < 0:
        beta = np.sqrt((0.5 * pow((Tt + (np.sqrt(-Delta / 27))), 1/3)) + (0.5 * -pow((-
(Tt - (np.sqrt(-Delta / 27))), 1/3)) - (1 / 3 * T))
    if (T + beta ** 2 + (S / (2 * beta))) > 0:
        alfa = np.sqrt(T + beta ** 2 + (S / (2 * beta)))
        s1 = (1 / alfa) * np.sinh(w * alfa)
        c1 = np.cosh(w * alfa)
    elif (T + beta ** 2 + (S / (2 * beta))) < 0:
        alfa = np.sqrt(-(T + beta ** 2 + (S / (2 * beta))))
        s1 = (1 / alfa) * np.sin(w * alfa)
        c1 = np.cos(w * alfa)
    if (T + beta ** 2 - (S / (2 * beta))) > 0:
        gama = np.sqrt(T + beta ** 2 - (S / (2 * beta)))
        s3 = (1 / gama) * np.sinh(w * gama)
        c3 = np.cosh(w * gama)
    elif (T + beta ** 2 - (S / (2 * beta))) < 0:
        gama = np.sqrt(-(T + beta ** 2 - (S / (2 * beta))))
        s3 = (1 / gama) * np.sin(w * gama)
        c3 = np.cos(w * gama)

s2 = np.sin(w * beta)
c2 = np.cos(w * beta)
A = T + (2 * beta ** 2)
F = L + (8 * T * beta ** 2) + (12 * beta ** 4)
B2 = S / (2 * beta)
B1 = (2 * beta ** 2) + B2
B3 = (2 * beta ** 2) - B2
Z = ((A + beta ** 2) * s1 * s3) - (c1 * c3) + ((2 * c2 ** 2) - 1)
R1 = (B1 * c1 * s3) + (B3 * c3 * s1) - (4 * beta * s2 * c2)
R2 = (4 * A * beta * s2 * c2) + ((F - (A * B1)) * c1 * s3) + ((F - (A * B3)) * c3 * s1)
R3 = F * s1 * s3
R4 = (2 * beta * s2 * (c1 + c3)) - (c2 * ((B1 * s3) + (B3 * s1)))
R5 = c2 * (s1 + s3)
R6 = (B2 * c2 * (c1 - c3)) + (beta * s2 * ((s1 * (T + A + B1)) + (s3 * (T + A + B3))))
I3 = (2 * B2 * s2 * c2) + (beta * c1 * s3 * (T + A + B3)) - (beta * c3 * s1 * (T + A + B1))
I4 = (s2 * ((B1 * s3) - (B3 * s1))) - (2 * beta * c2 * (c1 - c3))
I5 = s2 * (s1 - s3)
I6 = (B2 * s2 * (c1 + c3)) + (beta * c2 * ((s3 * (T + A + B3)) - (s1 * (T + A + B1))))
Smm = ((pi * D22) / Lm) * Z ** -1 * R1
Sqq = ((pi ** 3 * D22) / Lm ** 3) * Z ** -1 * (R2 + (alfa23 ** 2 * R1) - (2 * alfa23 * I3))

```

```

Smq = (pi ** 2 * D22 / Lm ** 2) * (((A - vudash) - (Z ** -1 * R3)) + ((1j * Z ** -1) * (I3 - (alfa23
* R1))))
cSmq = (pi ** 2 * D22 / Lm ** 2) * (((A - vudash) - (Z ** -1 * R3)) + ((-1j * Z ** -1) * (I3 -
(alfa23 * R1))))
Fmm = (pi * D22 / Lm) * Z ** -1 * (R4 - (I4 * 1j)) * np.exp(1j * alfa23 * w)
cFmm = (pi * D22 / Lm) * Z ** -1 * (R4 - (-I4 * 1j)) * np.exp(-alfa23 * 1j * w)
Fqq = (pi ** 3 * D22 / Lm ** 3) * Z ** -1 * (((A - alfa23 ** 2) * R4) + (F * R5) - (2 * alfa23 *
I6)) - (1j * (((A - alfa23 ** 2) * I4) + (F * I5) + (2 * alfa23 * R6))) * np.exp(alfa23 * 1j * w)
Fmq = -(pi ** 2 * D22 / Lm ** 2) * Z ** -1 * ((R6 - (alfa23 * I4)) - (1j * (I6 + (alfa23 * R4)))) *
np.exp(1j * alfa23 * w)
cFqq = (pi ** 3 * D22 / Lm ** 3) * Z ** -1 * (((A - alfa23 ** 2) * R4) + (F * R5) - (2 * alfa23 *
I6)) - (-1j * (((A - alfa23 ** 2) * I4) + (F * I5) + (2 * alfa23 * R6))) * np.exp(-1j * alfa23 * w)
cFmq = -(pi ** 2 * D22 / Lm ** 2) * Z ** -1 * ((R6 - (alfa23 * I4)) - (-1j * (I6 + (alfa23 * R4)))) *
np.exp(-1j * alfa23 * w)
KLminf1 = np.array( [[Smm, -Smq, Fmm, Fmq], [-cSmq, Sqq, -Fmq, -Fqq], [cFmm, -cFmq,
Smm, cSmq], [cFmq, -cFqq, Smq, Sqq]])

return KLminf1

```

Assembly of local stiffness matrices into a global stiffness matrix

```

gstiff = np.array([], dtype=complex)
for i in range(0, lambda1.shape[0]):
    Aestiff = np.zeros((2, 2), dtype=complex)
    for j in range(0, n-1):
        estiff = EStiff(stress_resultants[j], shear_stress[j], EfssY[j], i)
        Aestiff[-1, -1] = Aestiff[-1, -1] + estiff[1, 1]
        Aestiff[-1, -2] = Aestiff[-1, -2] + estiff[1, 0]
        Aestiff[-2, -1] = Aestiff[-2, -1] + estiff[0, 1]
        Aestiff[-2, -2] = Aestiff[-2, -2] + estiff[0, 0]
        Aestiff = block_diag(Aestiff, estiff[2:4, 2:4])
        Aestiff[-4, -2] = Aestiff[-4, -2] + estiff[0, 2]
        Aestiff[-4, -1] = Aestiff[-4, -1] + estiff[0, 3]
        Aestiff[-3, -2] = Aestiff[-3, -2] + estiff[1, 2]
        Aestiff[-3, -1] = Aestiff[-3, -1] + estiff[1, 3]
        Aestiff[-2, -4] = Aestiff[-2, -4] + estiff[2, 0]
        Aestiff[-2, -3] = Aestiff[-2, -3] + estiff[2, 1]
        Aestiff[-1, -4] = Aestiff[-1, -4] + estiff[3, 0]
        Aestiff[-1, -3] = Aestiff[-1, -3] + estiff[3, 1]
    gstiff = block_diag(gstiff, Aestiff)

gstiff = gstiff[1:, :]

```

The following presents the programming structure of the amplitude calculation

```

Effective_stress_resultants = postbuckling_solver(trial_displacements)
Upper_Lower_Bound = W-W_algorithm(Effective_stress_resultants)
Initialize Upper_bound=0, Lower_bound, Amplitude

While true:
    If Upper_Lower_Bound ==0:
        Upper_bound = Amplitude
        If abs(Upper_bound - Lower_bound)/Upper_bound < 0.001;
            break
        if Lower_bound == 0:
            Amplitude = Amplitude /1.5
        elif Lower_bound != 0:
            Amplitude = (Upper_bound + Lower_bound)/2
        Effective_stress_resultants = postbuckling_solver(Amplitude * trial_displacements)
        Upper_Lower_Bound = W-W_algorithm(Effective_stress_resultants)
    else:
        Lower_bound = Amplitude
        if abs(Upper_bound - Lower_bound)/Upper_bound < 0.001:
            break
        if Upper_bound > 10e5:
            Amplitude = Amplitude *1.5
        elif Upper_bound < 10e5:
            Amplitude = (Upper_bound + Lower_bound)/2
        Effective_stress_resultants = postbuckling_solver(Amplitude * trial_displacements)
        Upper_Lower_Bound = W-W_algorithm(Effective_stress_resultants)

```

The following presents the structure of the whole postbuckling analysis

```

Displacements = VICONOPT(structure_properties)
Initialize predefined parameters

```

Initial constant strain, cycle = 0, iteration

While true:

 Cycle += Cycle

 If cycle > number_cycles:

 break

 Amplitude = Amplitude_Calculation(constants_strain[cycle])

 Displacements = Amplitude * Displacements

 While true:

 Effective_stress_resultants = postbuckling_solver(Displacements)

 Stiffness = Global_Stiffness_matrix(Effective_stress_resultants)

 displacements_adjustments = Modified_Newton_iteration(Stiffness)

 trial_displacements = Displacements + Displacements_adjustments

 If max(displacements_adjustments) < 0.001 * max(trial_displacements):

 Effective_stress_resultants = postbuckling_solver(trial_displacements)

 Print solutions

 Displacements = trial displacements

 Iteration += 1

 Break

 Else:

 Iteration += iteration

 Continue

Appendix B

Some solutions from composite plates that are not discussed in Chapter 7 are presented in this appendix.

B.1. Balanced and symmetric composite plate under combined loading, straight edges

The layups are shown as follows:

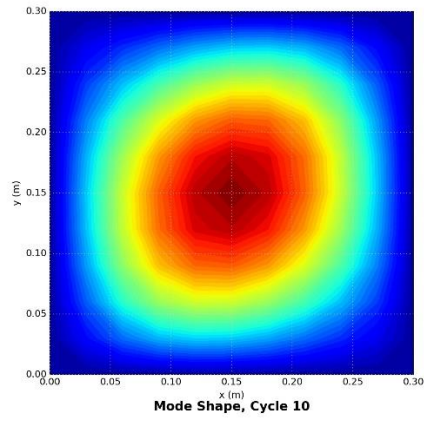
[0/0/+45/0/-45/0/90/90/90/90/0/-45/0/+45/0/0]

Other properties of the plate and predefined variables are shown in Figure B.1. Results are shown in Figures B.2, B.3 and B.4.

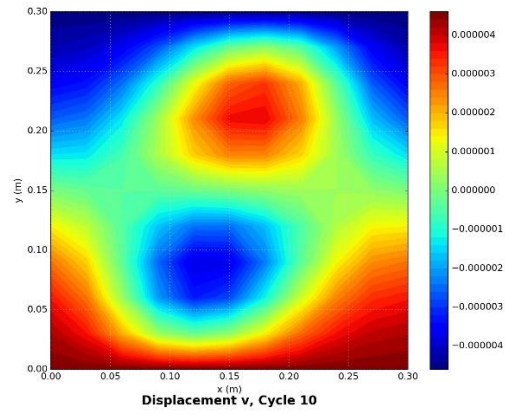
```

model_name
name, value
half-wavelength, 1 3 5
length, 0.3
number of nodes, 11
thickness of plate, 0.002
Poisson's ratio, 0.38
Boundary conditions, free edges
A matrix(Composite)
A11, 1.6222E+08
A12, 2.3827E+07
A22, 1.0236E+08
A16, 0
A26, 0
A66, 2.6624E+07
D11, 7.2778E+01
D12, 7.9425E+00
D22, 1.5415E+01
D16, -2.1044E+00
D26, -2.1044E+00
D66, 8.8746E+00
B11, 0
B12, 0
B22, 0
B16, 0
B26, 0
B66, 0
Buckling load, 4.5432E+03
linear strain, -10.6661E-05
linear shear strain, 0
increment ratio, 0.1
number of cycles, 20
    
```

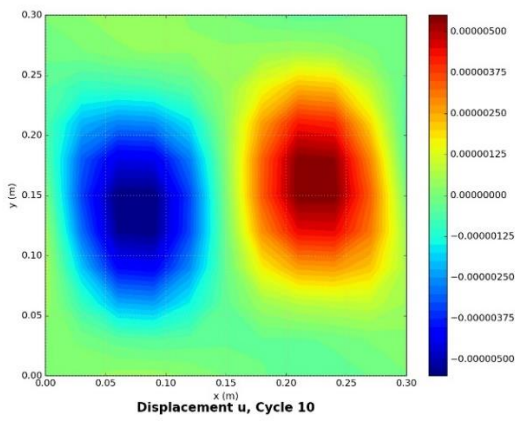
Figure B.1. Input data for balanced and symmetric composite plate under combined loading, straight edges.



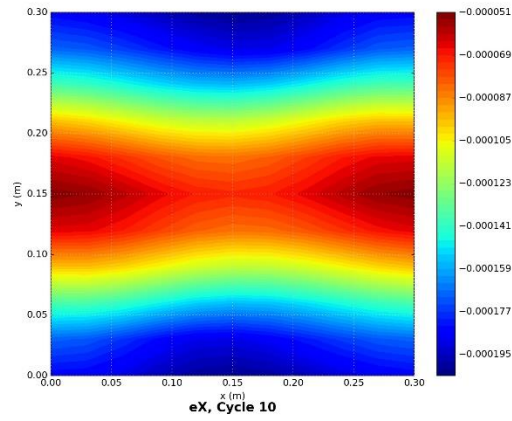
(a)



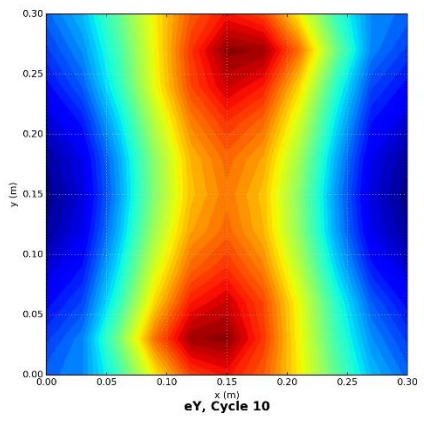
(b)



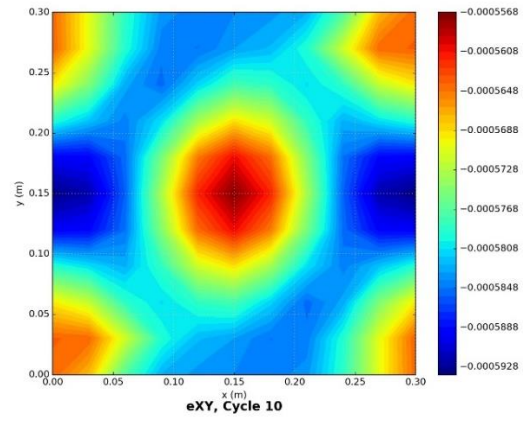
(c)



(d)



(e)



(f)

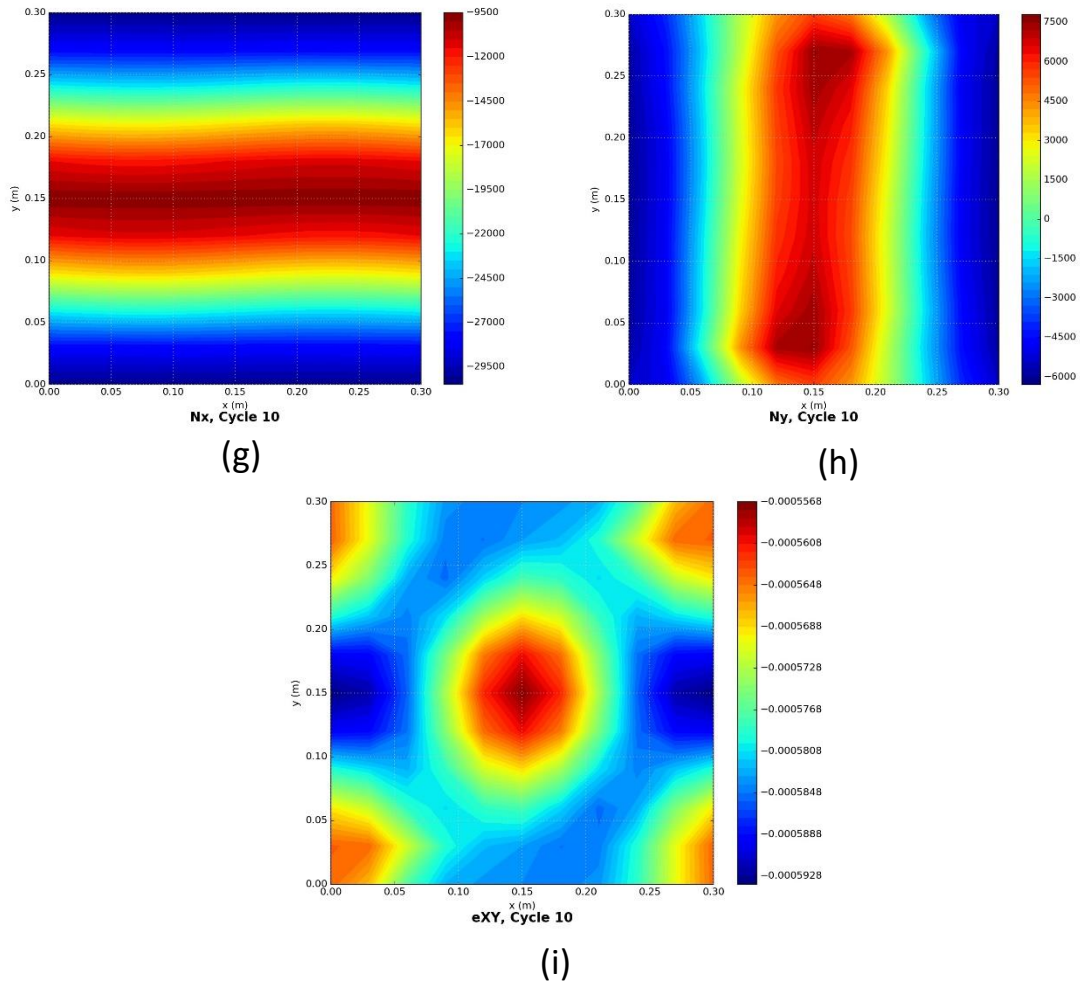


Figure B. 2. Contour plots of (a) out-of-plane displacements w (m); (b) in-plane displacements u (m); (c) in-plane displacements v (m); (d) strain ε_x ; (e) strain ε_y ; (f) strain γ_{xy} ; (g) stress resultants N_x (N/m); (h) stress resultants N_y (N/m); (i) stress resultants N_{xy} (N/m), for composite plate under compression and shear with free in-plane edge conditions, at cycle 10 (200% of initial end shortening strain)

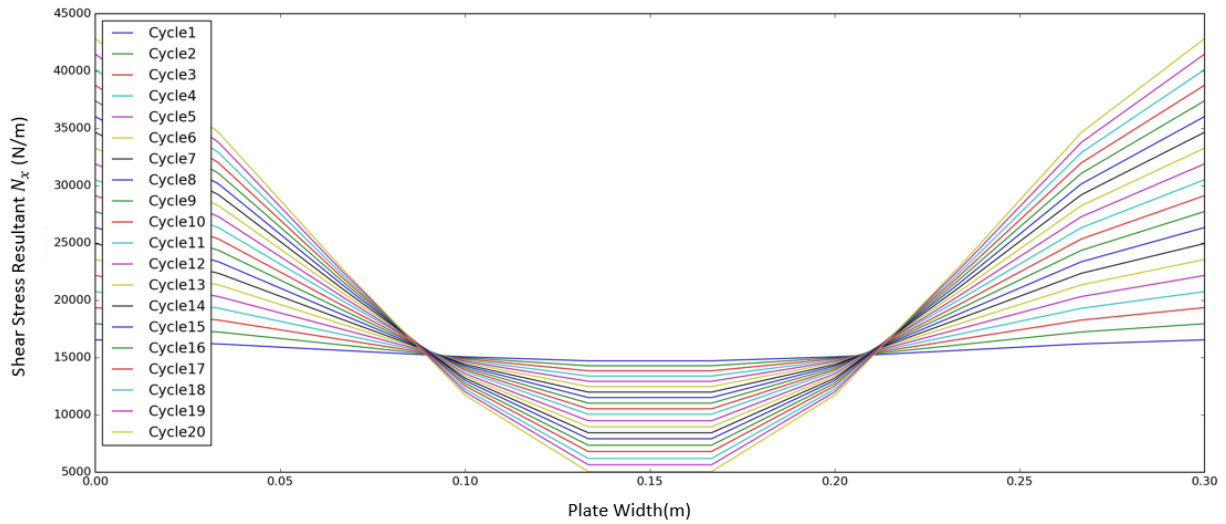


Figure B.4. Uniform stress resultant distribution at each postbuckling cycle for composite plate under combined loading, in-plane longitudinal straight edges

B.2. Unbalanced and symmetric composite plate under compression, fixed edges

The layups are shown as follows:

[0/-45/+45/0/-45/0/90/90/90/90/0/-45/0/+45/-45/0]

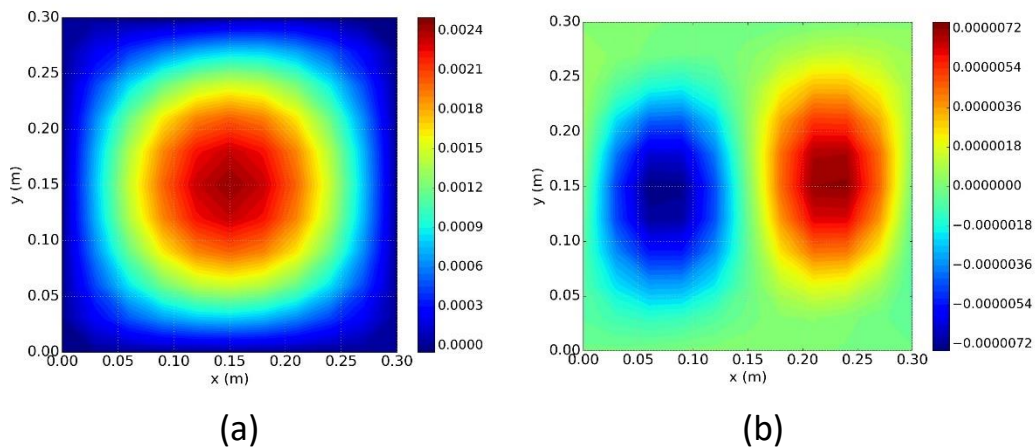
Other properties of the plate and predefined variables are shown in Figure B.5.

Results are shown in Figures B.6 to B.8.

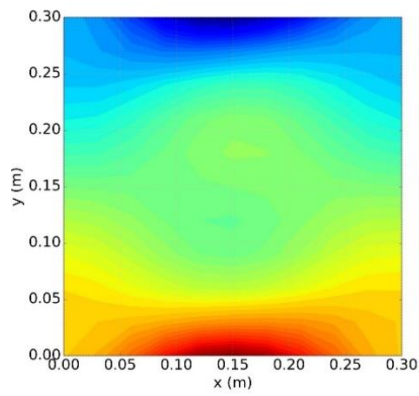
```

model_name
name, value
half-wavelength, 1 3 5
length, 0.3
number of nodes, 11
thickness of plate, 0.002
Poisson's ratio, 0.38
Boundary conditions, free edges
A matrix(Composite)
A11, 1.4035E+08
A12, 3.0729E+07
A22, 1.1042E+08
A16, -7.4822E+06
A26, -7.4822E+06
A66, 3.3526E+07
D11, 5.8315E+01
D12, 1.2508E+01
D22, 2.0748E+01
D16, -2.8448E+00
D26, -2.8448E+00
D66, 1.3440E+01
B11, 0
B12, 0
B22, 0
B16, 0
B26, 0
B66, 0
Buckling load, 5.1769049E+03
linear strain, -12.6661E-05
linear shear strain, 0
increment ratio, 0.1
number of cycles, 20
    
```

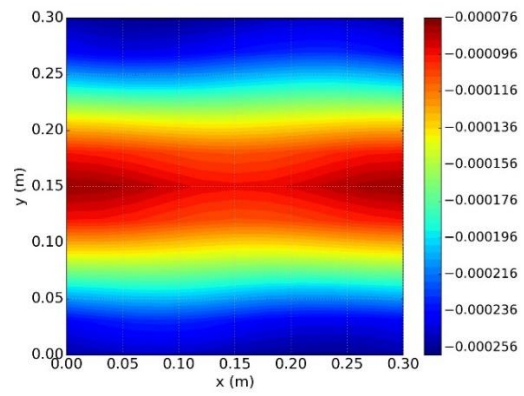
Figure B.5. Input data for unbalanced and symmetric composite plate under compression, free edges.



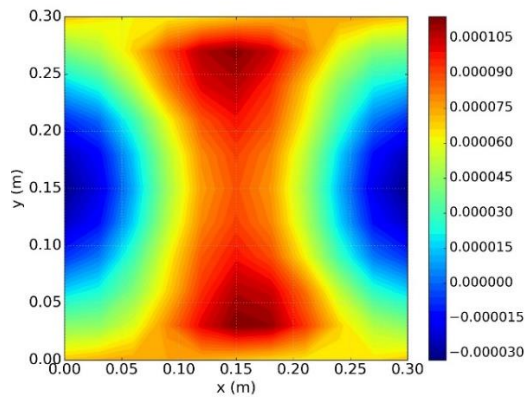
Appendices



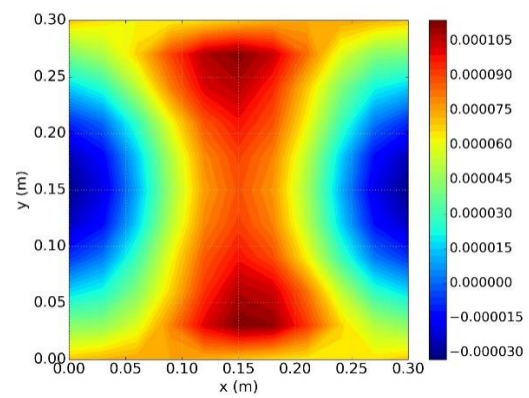
(c)



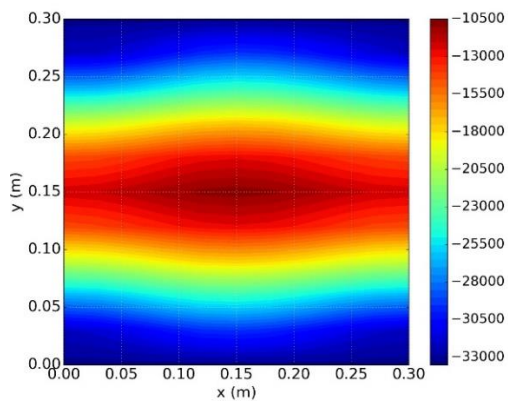
(d)



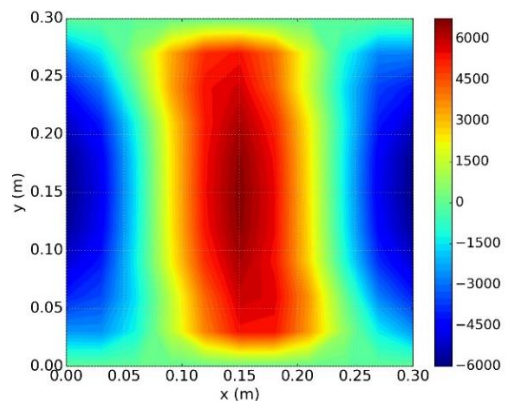
(e)



(f)



(g)



(h)

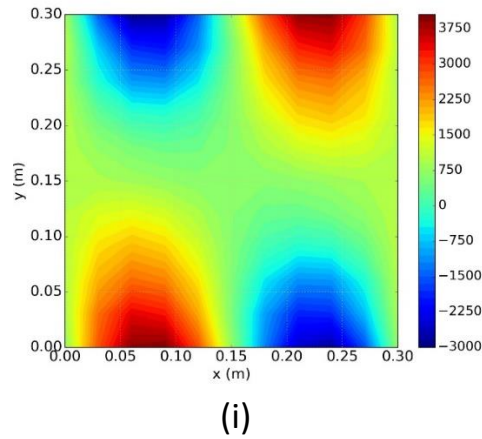
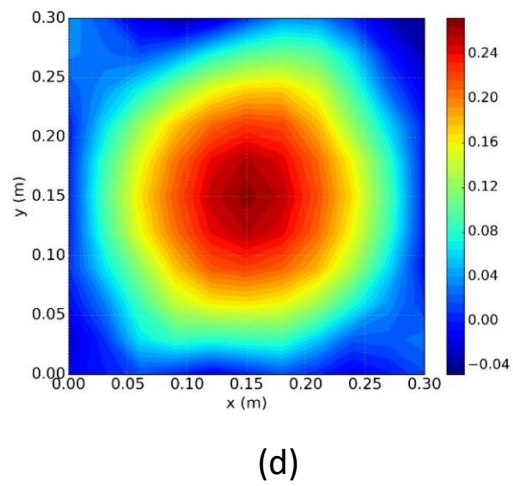
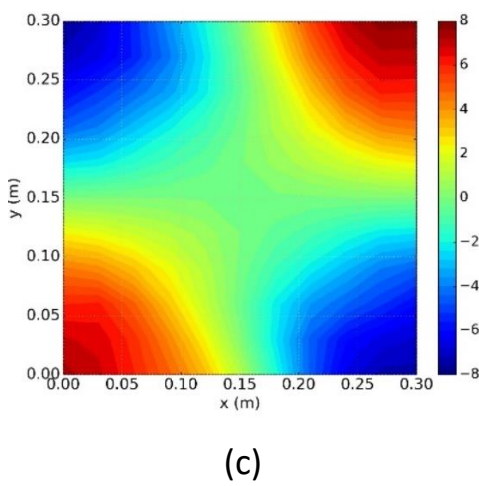
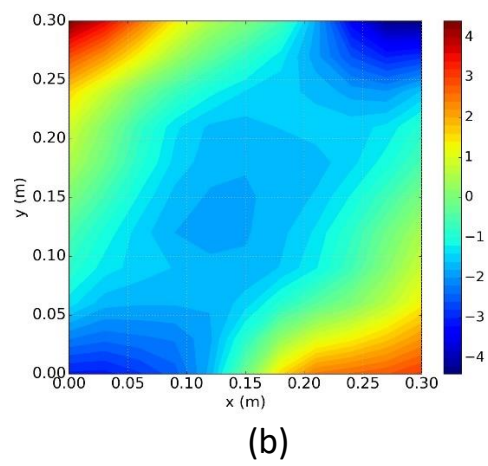
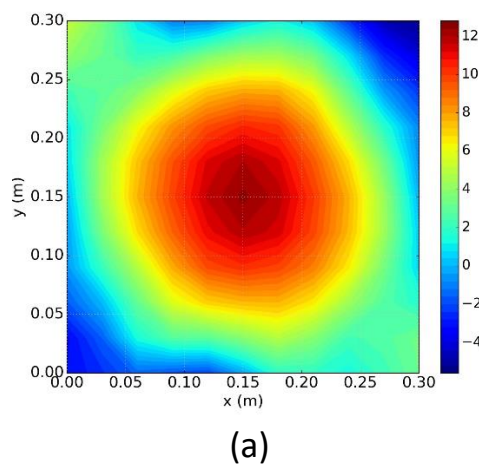


Figure B.6. Contour plots of (a) out-of-plane displacements w (m); (b) in-plane displacements u (m); (c) in-plane displacements v (m); (d) strain ϵ_x ; (e) strain ϵ_y ; (f) strain γ_{xy} ; (g) stress resultants N_x (N/m); (h) stress resultants N_y (N/m); (i) stress resultants N_{xy} (N/m), for unbalanced symmetric composite under compression with free in-plane edge conditions, at cycle 10 (200% of initial end shortening strain)



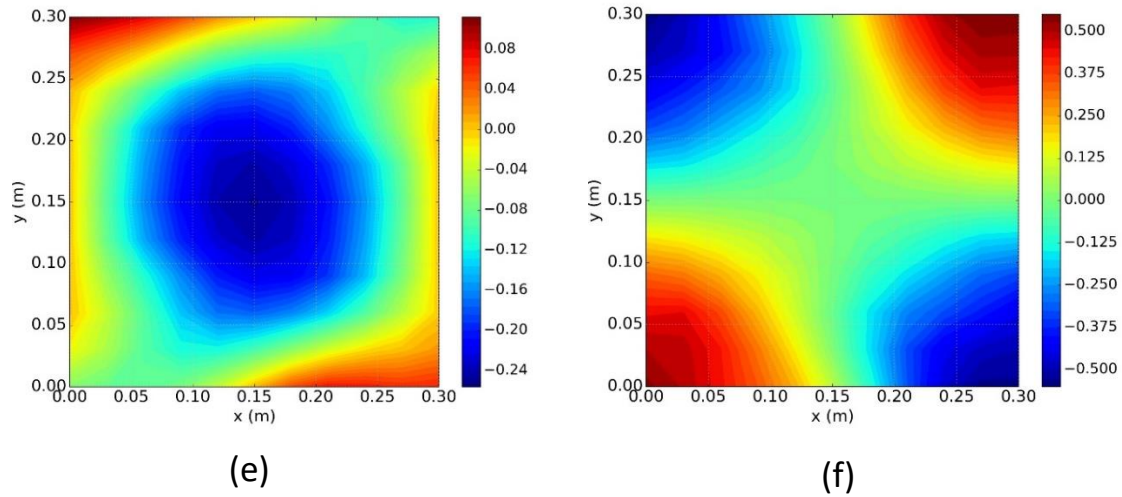


Figure B.7. Contour plots of (a) Moment M_x (Nm); (b) Moment M_y (Nm); (c) Moment M_{xy} (Nm); (d) curvature κ_x ; (e) curvature κ_y ; (f) curvature κ_{xy} for unbalanced symmetric composite under compression with free in-plane edge conditions, at cycle 10 (200% of initial end shortening strain)

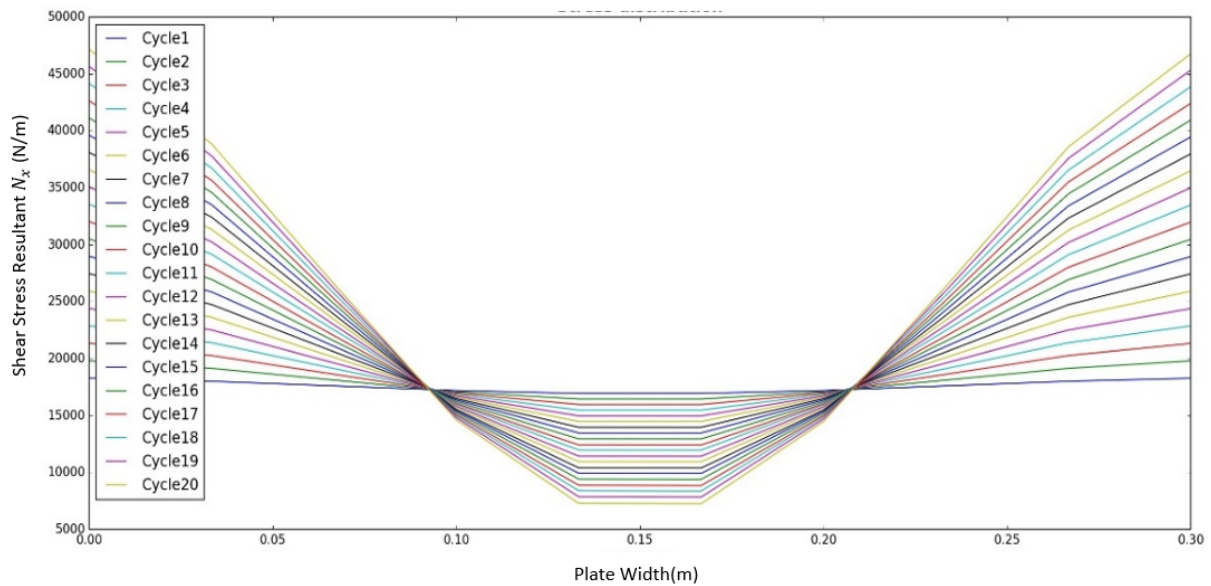


Figure B.8. Equivalent uniform longitudinal stress resultant distribution at each postbuckling cycle